On-line Analysis of Bacterial Metabolism by Modern Spectroscopic Laser Techniques

George Derek Metcalfe

A thesis submitted in partial fulfilment of the requirements
for the degree of Doctor of Philosophy

The University of Sheffield
Faculty of Science
Department of Chemistry

March 2022

Acknowledgements

First and foremost, I would like to thank my supervisor **Dr Michael Hippler** for his encouragement and support throughout my PhD. It has been a pleasure working with him for the last four years and I will miss our daily conversations and jokes. Also from the Hippler group, I wish to thank **Dr Saeed Alahmari**, **Dr Muneera Alrasheedi** and **Maryam Aldoghaim** for their help during collaborative projects, as well as their kindness throughout. A very special thanks goes to former group member **Dr Thomas W. Smith** who submitted his PhD thesis back in 2017 but has remained very helpful since then and has been a brilliant co-author on three publications.

I would like to thank **Dr Jim Reid**, my independent advisor, for his support and help. I would also like to thank the Reid group for allowing me to use their lab to prepare bacterial samples.

I would like to thank all the support staff from the Department of Chemistry. In particular, thank you to **Dan Jackson** for his excellent glassblowing work, **James Berry** for teaching me a procedure for nitrite colorimetry and **Rob Hanson** for the assistance with gas chromatography.

I wish to thank **Prof Frank Sargent** from Newcastle University for his help and co-authoring a publication on hydrogen production in the presence of oxygen by *E. coli* K-12.

I would like to thank **Prof Jeff Green** for advice and discussions as well as providing some *E. coli* strains.

I wish to thank the Engineering and Physical Sciences Research Council (**EPSRC**) for funding my PhD studentship. I would also like to thank the Association of British Spectroscopists (**ABS**) Trust for providing financial support to allow me to present my research at the 118th Bunsentagung in Jena, Germany.

I would like to thank my friends, especially **Alex**, **Calum**, **Charlie**, **Dan** and **Jean**, for helping me get through the PhD with their great support and shared laughter.

Finally, I would like to thank my parents, **David** and **Teresa**, and sister **Emily** for their unconditional love and support. I would also like to thank my late grandma **Margaret** whose wisdom and sense of humour was invaluable and is greatly missed. Thank you to my entire family, I couldn't wish for a better one.

Abstract

In order to best determine how bioprocesses develop and how to run bioreactors most efficiently, innovative new analytical techniques are required to supplement, or even supersede, conventional methods, many of which are invasive, require sampling and/or do not provide on-line data analysis. Spectroscopic laser techniques are powerful analytical tools that are capable of real-time, non-invasive monitoring of multiple variables simultaneously. Furthermore, spectroscopy offers high selectivity and sensitivity, including the ability to distinguish different isotopomers and isotopologues, which enables isotopic labelling studies to provide greater mechanistic insights into metabolic pathways.

This thesis describes the development of several spectroscopic techniques and their applications in studying different metabolic modes of *Escherichia coli* batch cultures. On-line analysis is achieved in the gas-phase using cavity-enhanced Raman spectroscopy (CERS), White cell FTIR spectroscopy and photoacoustic detection in a differential Helmholtz resonator (DHR) as well as in the liquid-phase using Raman spectroscopy. The spectral analysis and quantitation of over twenty parameters is discussed, including growth substrates such as glucose and ammonia, metabolites such as acetate, ethanol and formate, headspace gases such as H_2, O_2 and CO_2, and other process variables measured *in situ* such as the pH and optical density (OD).

The first bacterial study conducted is a revisitation of the classical *E. coli* experiment of glucose-lactose diauxie. A new approach for studying mixed sugar metabolism is presented using both the CERS and DHR techniques to distinguish $^{13}CO_2$ produced from ^{13}C-glucose metabolism from the subsequent production of $^{12}CO_2$ from unlabelled lactose. Next, gas-phase FTIR and liquid-phase Raman are developed for batch culture analysis and applied to monitoring mixed-acid fermentation. Finally, two further isotopic labelling studies are conducted by using CERS alongside FTIR and liquid-phase Raman analysis. Nitrate and nitrite reduction by *E. coli* to the major and minor end-products of ammonium and nitrous oxide is studied, respectively. ^{15}N-labelling is used to give mechanistic insights through interpretation of the different $^{14}N/^{15}N$-isotopomer products. The final study focuses on the fermentative pathways of *E. coli* in the absence and presence of O_2. Using ^{13}C- and D-labelled formate, evidence is found that the formate hydrogenlyase (FHL) complex can be assembled and functional under micro-aerobic conditions, which could remove some barriers to biotechnological applications such as biohydrogen generation.

List of Publications

Cavity-Enhanced Raman and Helmholtz Resonator Photoacoustic Spectroscopy to Monitor the Mixed Sugar Metabolism of E. coli
George D. Metcalfe, Saeed Alahmari, Thomas W. Smith and Michael Hippler (2019).
Analytical Chemistry. **91**, 13096-13104.
https://doi.org/10.1021/acs.analchem.9b03284

Using Activities to Correct the Henderson-Hasselbalch Equation
Michael Hippler and George D. Metcalfe (2020).
Bunsen-Magazin. **22**, 102-105.
https://doi.org/10.26125/y7p7-an56

On-line Analysis and in situ pH Monitoring of Mixed Acid Fermentation by Escherichia coli Using Combined FTIR and Raman Techniques
George D. Metcalfe, Thomas W. Smith and Michael Hippler (2020).
Analytical and Bioanalytical Chemistry. **412**, 7307-7319.
https://doi.org/10.1007/s00216-020-02865-5

Advanced Spectroscopic Analysis and ^{15}N-Isotopic Labelling Study of Nitrate and Nitrite Reduction to Ammonia and Nitrous Oxide by E. coli
George D. Metcalfe, Thomas W. Smith and Michael Hippler (2021).
Analyst. **146**, 7021-7033.
https://doi.org/10.1039/D1AN01261D

Hydrogen Production in the Presence of Oxygen by Escherichia coli K-12
George D. Metcalfe, Frank Sargent and Michael Hippler (2022).
Microbiology. **168**, 3.
https://doi.org/10.1099/mic.0.001167

Abbreviations

$1\ \sigma$	Noise-equivalent detection limit
$3\ \sigma$	Limit of detection
$5\ \sigma$	Limit of quantification
A^-	Conjugate base
AckA	Acetate kinase
ADP	Adenosine diphosphate
ADH	Alcohol dehydrogenase
ATP	Adenosine triphosphate
ATR	Attenuated total reflection
CCD	Charge coupled device
CCR	Carbon catabolite repression
CEAS	Cavity-enhanced absorption spectroscopy
CERS	Cavity-enhanced Raman spectroscopy
CoA	Co-enzyme A
CRDS	Cavity ring-down spectroscopy
cw	Continuous wave
DHR	Differential Helmholtz resonator
DNRA	Dissimilatory nitrate reduction to ammonia
ED	Entner Doudoroff
EMP	Embden-Meyerhof-Parnas
ETC	Electron transport chain
$FADH_2$	Flavin adenine dinucleotide
FDH-H	Formate dehydrogenase-H
FDH-N	Nitrate-inducible formate dehydrogenase

FERS	Fiber-enhanced Raman spectroscopy
FHL	Formate hydrogenlyase
FocA	Formate channel
Frd	Fumarate reductase
FTIR	Fourier-transform infrared
FWHM	Full width at half maximum
GC	Gas chromatography
HA	Brønsted-Lowry acid
HC-PCF	Hollow core photonic crystal fiber
HITRAN	High resolution transmission
Hyd-3	Hydrogenase-3
IR	Infrared
LB	Lysogeny broth
LC	Liquid chromatography
LDH	Lactate dehydrogenase
MIMS	Membrane inlet mass spectrometry
MIR	Mid-infrared
MS	Mass spectrometry
m/z	Mass-to-charge ratio
NADH	Nicotinamide adenine dinucleotide
NADPH	Nicotinamide adenine dinucleotide phosphate
Nap	Periplasmic nitrate reductase
NIR	Near-infrared
NirB	NADH-dependent nitrite reductase
NRA	Nitrate reductase A
NrfA	Periplasmic nitrite reductase

OD	Optical density
OFFL	Optical feedback frequency-locking
OPP	Oxidative pentose phosphate
Pck	PEP carboxykinase
PDH	Pyruvate dehydrogenase
PDHFL	Pound-Drever-Hall frequency-locking
PEP	Phosphoenolpyruvate
PFL	Pyruvate formate lyase
PNNL	Pacific Northwest National Laboratory
ppmv	Parts per million volume
Pta	Phosphate acetyltransferase
PTS	Phosphotransferase system
Pyk	Pyruvate kinase
Q	Quinone
QH_2	Quinol
RQ	Respiratory quotient
SDH	Succinate dehydrogenase
SERS	Surface enhanced Raman spectroscopy
TCA	Tricarboxylic acid
TMAO	Trimethylamine N-oxide
UQ	Ubiquinone
UV-Vis	Ultraviolet-visible
WC	White cell

Contents

Chapter 1 – An Introduction to Key Concepts in Vibrational Spectroscopy, Bacterial Metabolism and Bioreactor Sensors

Chapter 2 – A New Approach for a Classical *E. coli* Experiment: $^{13}CO_2$ Distinction of Glucose-Lactose Diauxie by Raman and Photoacoustic Spectroscopies

Chapter 3 – On-line Analysis and *in situ* pH Monitoring of *E. coli* Mixed-Acid Fermentation by FTIR and Raman Spectroscopies

Chapter 4 – ^{15}N-Isotopic Labelling Study of Nitrate and Nitrite Reduction to Ammonia and Nitrous Oxide by *E. coli*

Chapter 5 – Hydrogen Production in the Presence of Oxygen by *E. coli* K-12

Chapter 1

An Introduction to Key Concepts in Vibrational Spectroscopy, Bacterial Metabolism and Bioreactor Sensors

Abstract

This chapter is an introduction to background information and key literature relevant throughout the entire thesis. First, the fundamentals of vibrational spectroscopy are discussed, including IR and Raman selection rules, rotational and vibrational term values and associated approximations. Other essential concepts for understanding the IR and Raman spectra of molecules studied throughout this thesis are also introduced; including the distinction between fundamental bands, overtones and combination bands, how nuclear spin statistics influence the intensities of alternating rotational lines, the origin of the $v_1/2v_2^0$ Fermi resonance pair of CO_2 and spectral line broadening effects.

Next, a brief history of the importance of the model organism *E. coli* in molecular biology and cell physiology is discussed and then followed by an overview of bacterial metabolism pathways. Aerobic respiration during growth on glucose is detailed, including a summary of glycolysis, pyruvate decarboxylation, the citric acid cycle and oxidative phosphorylation. Anaerobic mixed-acid fermentation is then described and compared with aerobic respiration, including the notable differences in the metabolic pathways such as the production of organic acids, the branched citric acid cycle and how ATP is produced solely by substrate-level phosphorylation. The disproportionation of formate to H_2 and CO_2 by the formate hydrogenlyase (FHL) complex is also discussed.

Finally, a brief overview of bioreactor sensors is provided. Conventional techniques such as mass spectrometry (MS), gas chromatography (GC), liquid chromatography (LC) and invasive probes are discussed. Spectroscopic sensors have the advantage of offering real-time and non-invasive monitoring of numerous variables simultaneously. An overview of UV-Vis, IR and Raman spectroscopic techniques for bioreactor analysis is then covered. Furthermore, a more detailed explanation of Fourier-transform infrared (FTIR) spectroscopy and cavity-enhanced Raman spectroscopy (CERS) is provided as these are the two complementary gas-sensing techniques utilised the most throughout the research presented in this thesis.

1.1 Fundamentals of Vibrational Spectroscopy

1.1.1 IR Absorption and Raman Scattering

Optical spectroscopy is a key experimental tool in numerous interdisciplinary fields, with notable applications in analytics, structure determination, kinetics, dynamics, theory and practical applications such as lasers. Light is composed of photons with energy $E = h\nu$ where h is Planck's constant and ν is the frequency of light. Frequency ν and wavelength λ are connected *via* the wave equation $\lambda\nu = c$ where c is the speed of light. Photon energy is typically expressed as a function of wavenumber $\tilde{\nu} = 1/\lambda$ in units of cm^{-1}. According to Einstein, absorption, spontaneous emission and stimulated emission are the three fundamental processes by which light interacts with matter, as shown in Figure 1.1. The absorption of a photon with energy $h\nu$ can induce the transition from a lower energy state E_i to an excited state E_f with an energy difference $\Delta E = E_\mathrm{f} - E_\mathrm{i} = h\nu$. An excited state can emit a photon to decay to a lower energy level (spontaneous emission) or the emission can be induced when an incoming photon interacts with an exited state causing a second photon to be emitted with the same energy, direction and phase as the incident photon (stimulated emission).

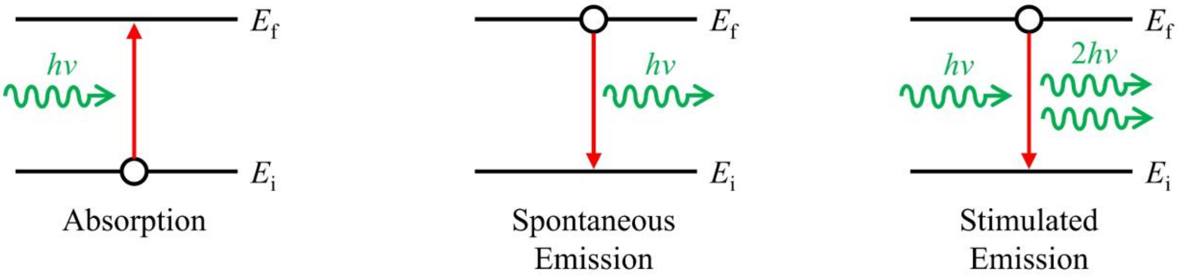

Figure 1.1 – The three fundamental processes according to Einstein whereby light interacts with matter *via* a lower energy state E_i and an excited state E_f.

In order of increasing energy, molecules contain rotational, vibrational and electronic energy levels. Every electronic state has a set of associated vibrational levels with each vibrational state, in turn, having a set of associated rotational levels. Pure rotational transitions are generally found in the microwave and far-IR regions (0.1 – 10 cm^{-1}), vibrational transitions in the mid-IR region (400 – 4000 cm^{-1}) and electronic transitions in the visible and UV regions (12000 – 70000 cm^{-1}). Multiple energy states can change in a single transition, such as a rovibrational transition when both vibrational and rotational states change or a rovibronic transition when electronic, vibrational and rotational states all change simultaneously. Vibrational spectroscopy is the study of the interaction of light with vibrational energy levels. As a rule, a linear molecule with N atoms has $3N - 5$ normal modes of vibration, while a non-linear molecule has $3N - 6$ modes. Molecular vibrations can be excited by the one-photon absorption of light (IR spectroscopy) or the two-photon inelastic scattering of light (Raman spectroscopy), provided that certain selection rules are obeyed in each case.

Solution of the Schrödinger equation $\hat{H}\psi = E\psi$ for a molecule gives a set of wavefunctions ψ_n and their corresponding energies E_n. These quantum states characterise the constituent particles of a given molecule. The Hamiltonian operator $\hat{H}$ and wavefunction ψ depend on many interacting degrees of freedom, with every coordinate and distance r between two charged particles being a variable. Hence, only the two-particle hydrogen atom has been solved analytically and only approximate solutions are possible for all other larger chemical species. The Born-Oppenheimer approximation supposes that the nuclei, being much heavier and slower than electrons, are stationary relative to fast electron motion. This means that the electrons approximately create a mean force field (chemical bond) that can be incorporated into a potential energy function $V(r)$ for the nuclear motion (vibrations and rotations). Also, external centre-of-mass motion (translation) of molecules is separate from the internal motion, which includes rotation, vibration and electronic excitation. Molecular rotation is assumed to not influence vibrations greatly according to the rigid rotor approximation. These approximations enable the energy levels a molecule can occupy to be estimated with high accuracy.

In a quantum chemical description, the transition matrix element $\int \psi_\mathrm{i}{}^* \vec{\mu}\, \psi_\mathrm{f}\, \mathrm{d}\vec{r}$ determines whether a transition from an initial quantum state ψ_i to a final state ψ_f is allowed, where $\vec{\mu}$ is the operator of the transition and $\vec{r}$ is the displacement of the internuclear distance r from the equilibrium configuration *i.e.* $(r - r_\mathrm{e})$. The transition probability is proportional to the square of this matrix element. In the electric dipole approximation, a molecule must possess, or at least transiently, an electric dipole moment oscillating at the frequency of a transition for it to interact with the electromagnetic light field and absorb or emit a photon. The strongest transitions are induced by electric dipole moment oscillations where the transition operator is given as $\vec{\mu} = \sum q_\mathrm{i}\vec{r}_\mathrm{i}$, which is essentially the electric dipole moment of a molecule with partial charges q separated by a distance $\vec{r}$. By evaluating the transition matrix element with the appropriate wavefunctions, the selection rules for allowed transitions can be evaluated [1].

An IR photon can induce a vibrational transition provided that the photon energy $h\nu$ matches the energy gap ΔE and the molecular electric dipole moment changes during the vibration. For an allowed electric dipole moment transition, this selection rule is expressed mathematically as $\mathrm{d}\mu/\mathrm{d}\vec{r} \neq 0$ if the vibration is IR active. The electric dipole moment of an uncharged molecule derives from partial charges q on the atoms, which can be determined from molecular orbital calculations or estimated by a comparison of the electronegativities of the atoms. Homonuclear diatomic molecules (*e.g.* H_2, N_2 and O_2) do not have an electric dipole moment in their equilibrium configuration, due to both their atoms having the same electronegativity, nor does their lone vibrational mode ($3N - 5 = 1$) induce a transient dipole moment. Hence, $\mathrm{d}\mu/\mathrm{d}\vec{r} = 0$ and these molecules cannot absorb an IR photon to excite vibrational motion, so they are referred to as IR inactive. In contrast, heteronuclear diatomic molecules (*e.g.* CO, HCl and NO) are IR active as the two atoms have different electronegativities creating a permanent dipole moment with a magnitude that changes as the bond is stretched and compressed, hence, $\mathrm{d}\mu/\mathrm{d}\vec{r} \neq 0$.

In an IR spectrum, absorbance A is proportional to the sample concentration C (molecules m^{-3}) according to the Beer-Lambert law for one-photon absorptions

$$A = \ln\left(\frac{I_0}{I}\right) = \sigma C l \tag{1.1}$$

where I is the light intensity measured in a sample transmission spectrum, I_0 is the intensity measured in a background transmission spectrum without the sample, σ is the absorption cross section (m^2) and l is the pathlength of light through the sample (m). Note that this is the natural logarithmic form of A, which will be used throughout this thesis, and not the decadic logarithmic form $\log_{10}(I_0/I) = \varepsilon c l$ where ε is the decadic molar absorptivity ($\mathrm{m}^2\ \mathrm{mol}^{-1}$) and c is molar concentration ($\mathrm{mol\ m}^{-3}$). The Beer-Lambert law allows quantitation in IR spectroscopy if the σ of the analyte and l of the measurement cell are known. However, the law is an approximation and linearity can be limited by chemical and instrumental factors. Non-linearity can occur at high analyte concentrations as there may be changes in the refractive index or deviations in absorption cross sections due to electrostatic interactions between the molecules in close proximity. Furthermore, scattering of light by particulates in the sample, fluorescence or phosphorescence of the sample and too intense incident light can lead to non-linearity effects. The Beer-Lambert law is most valid for dilute media when all the matter remains approximately in the ground state so that no spontaneous or stimulated emission can occur.

Theoretically predicted in 1923 by A. Smekal [2] and experimentally discovered in 1928 by C.V. Raman and K. S. Krishnan [3], the Raman effect refers to the inelastic scattering of photons by matter. By irradiating matter with intense monochromatic light (often in the visible or UV region), photons will be both elastically and inelastically scattered. The majority of light will be elastically scattered at the same frequency as the incident light (Rayleigh scattering). However, around 1 in 10^7 of the incident photons that collide with the matter will be inelastically scattered, losing some of their energy, and emerging with a lower frequency (Stokes scattering). If an excited vibrational level of the molecule is thermally populated, incident photons may gain energy and emerge with a higher frequency (anti-Stokes scattering).

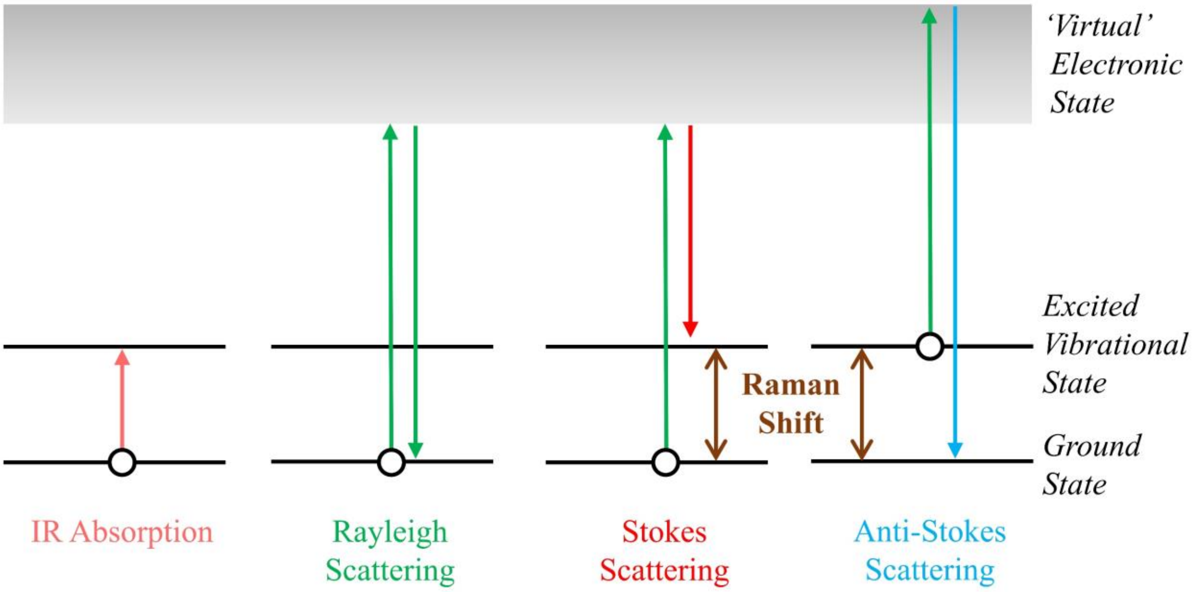

Figure 1.2 – Energy level diagram comparing IR absorption (one-photon process) with Rayleigh, Stokes and anti-Stokes scattering (two-photon process).

Light scattering is a two-photon process. First, a molecule must absorb a photon to excite from the ground state to a broad 'virtual' electronic state (a mixture of many electronically excited states), as shown in Figure 1.2. The 'virtual' state can either decay back to the ground state by emitting a Rayleigh scattered photon or to a vibrationally excited state by producing a Stokes scattered photon. Raman shift $\Delta\tilde{\nu}$ (cm^{-1}) is calculated from the difference in wavenumbers between the incident light and the measured Stokes scattered light. It is an indirect measurement of the wavenumber difference between two vibrational states which can be measured directly by IR spectroscopy if the vibration is also IR active. Raman spectroscopy is fundamentally less sensitive than IR spectroscopy as only around 1 in 10^7 photons that interact with a Raman active molecule will be inelastically scattered and contribute towards a Raman signal. Despite this, IR and Raman are complementary techniques as certain molecules or transitions can only be studied by one technique and not the other, due to the differences in the selection rules that govern them.

The intensity of Raman scattered radiation I_R is given by

$$I_R \propto v^4 I_0 \, N \left(\frac{d\boldsymbol{\alpha}}{d\vec{r}}\right)^2 \tag{1.2}$$

where v is the frequency of the exciting laser, I_0 is the incident laser intensity, N is the number of scattering molecules in a given state and α is the polarizability. This expression indicates the key parameters that determine Raman signal intensity. First, the signal is concentration dependent which allows sample quantitation. Secondly, using shorter wavelength excitation and/or increasing the laser power will increase the Raman intensity. Finally, only molecular vibrations which cause a change in polarizability are Raman active, unlike IR spectroscopy where a change in electric dipole moment is required for vibrational excitement. Polarizability α is a measure of the capability of inducing an electric dipole moment μ by an electric field E as defined by $\mu = \alpha E$ [4].

When monochromatic radiation falls on a molecule, the oscillating electric field generates an induced electric dipole as the positively-charged nuclei are attracted towards the negative pole of the field while the negatively-charged electron cloud is attracted towards the positive pole of the field. Essentially, polarizability determines the extent to which the electron cloud of a molecule can be displaced from the nucleus by an external electric field. The vibration of heteronuclear and homonuclear diatomic molecules is Raman active as the stretching and compression of the bond distorts the electron cloud, causing a change in polarizability *i.e.* $d\boldsymbol{\alpha}/d\vec{r} \neq 0$. Thus, heteronuclear diatomic molecules can be detected by either IR or Raman techniques, but the vibration of homonuclear diatomic molecules can only be probed by a Raman based technique.

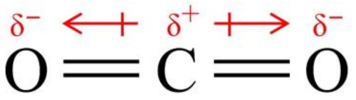

Equilibrium configuration
No net electric dipole moment

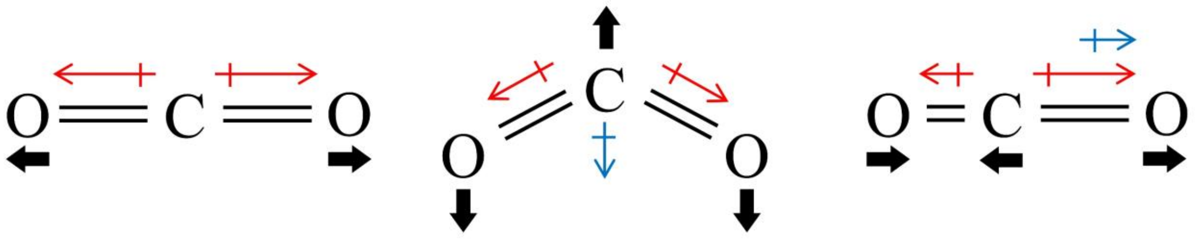

Symmetric stretching v_1
IR inactive
Raman active

Doubly degenerate bending v_2
IR active
Raman inactive

Asymmetric stretching v_3
IR active
Raman inactive

Figure 1.3 – Normal modes of vibration for CO_2. Black arrows indicate atomic motion. Red arrows indicate individual bond electric dipole moments which cancel out for the equilibrium configuration and symmetric stretching vibration. The bending and asymmetric stretching vibrations induce a net transient electric dipole moment as indicated by the blue arrows.

Like homonuclear diatomic molecules, other highly symmetric polyatomic molecules that possess an inversion centre *i* will have Raman active bands that are IR inactive for symmetric vibrations to *i*, while asymmetric vibrations to *i* are IR active but Raman inactive. This is known as the mutual exclusion rule which states that for a molecule with an inversion centre, no transition is allowed in both its IR and Raman spectrum, but only in one or the other or neither. For instance, the linear triatomic molecule CO_2 has an inversion centre. It has four normal modes of vibration ($3N - 5 = 4$), as shown in Figure 1.3. The equilibrium configuration of CO_2 has no net electric dipole moment, however, the asymmetric stretching and doubly degenerate bending vibrations induce net transient electric dipole moments which enables IR activity. The symmetric stretching vibration of CO_2 lengthens the two bonds making both become more polarizable, hence, this vibration is Raman active. For molecules with little to no symmetry, such as heteronuclear diatomic molecules, their vibrations are likely to be both IR and Raman active.

1.1.2 Rotational Term Values

The rotation of a diatomic molecule can be approximated as a rigid rotor in which the chemical bond is considered a fixed, weightless rod with the distance between the two nuclei remaining constant. Using a Hamiltonian operator for rotational energy and solving the Schrödinger equation for a rigid rotor gives the angular momentum as

$$P_J = \frac{h}{2\pi}[J(J+1)]^{\frac{1}{2}} \tag{1.3}$$

where the rotational quantum number $J = 0, 1, 2, \dots$ for a normal molecule with all electrons paired. In general, J is associated with total angular momentum excluding nuclear spin *i.e.* rotational + orbital + electron spin. Hence, when there is no orbital or electron spin angular momentum, it refers simply to rotation. The approximate molecular rotational energy levels are equal to

$$F(J) = BJ(J+1) \tag{1.4}$$

where $F(J)$ is the rotational term value (cm^{-1}) and B is the rotational constant (cm^{-1}). For $J = 0, 1, 2, 3, \dots$, $F(J) = 0, 2B, 6B, 12B, \dots$ [1].

The moment of inertia is $I = \mu r^2$ for a diatomic molecule where the reduced mass is $\mu = m_1 m_2/(m_1 + m_2)$ for nuclei of masses m_1 and m_2 separated by distance r. The rotational constant B is inversely proportional to the moment of inertia I as

$$B = \frac{h}{8\pi^2 cI} \tag{1.5}$$

Hence, if B is known from spectroscopy, it allows the determination of intramolecular distances and molecular structure. However, it is observed in pure rotational spectra of diatomic molecules that there is a small decrease in transition spacings with increasing J, not the constant spacing expected from the rigid rotor approximation. The non-rigid rotor approximation accounts for this deviation by more accurately representing the bond as a weightless spring between nuclei. The two main consequences of this approximation are as follows.

Firstly, with increasing vibrational excitation, the spring (chemical bond) gets extended (until it breaks) resulting in B effectively becoming smaller. Typically, many hundreds of vibrations occur in the time the molecule rotates once. Therefore, the rotation sees only the averaged effect of the vibrations. Each vibrational state υ has, therefore, its own effective (averaged) rotational constant

$$B_\upsilon = B_e - \alpha\left(\upsilon + \tfrac{1}{2}\right) \tag{1.6}$$

where B_e is the rotational constant without vibration with the molecule at the equilibrium bond length r_e, υ is the vibrational quantum number and α is a vibration-rotation interaction constant. In order to obtain B_e and r_e, B_υ must be obtained for at least two vibrational states.

The second consequence of the non-rigid rotor approximation is that with increasing rotational excitation, the spring (chemical bond) extends due to centrifugal forces. Therefore, a centrifugal distortion constant D_υ is introduced into the calculation of the rotational term value $F_\upsilon(J)$

$$F_\upsilon(J) = B_\upsilon J(J+1) - D_\upsilon J^2(J+1)^2 \tag{1.7}$$

The centrifugal distortion constant D_υ depends on the stiffness of the bond, is always positive for diatomic molecules and has a slight vibrational dependence, but not to the extent of B_υ [1].

Alongside rotational energy levels $F_\upsilon(J)$, corresponding wavefunctions ψ_J are obtained from the solution of the Schrödinger equation for molecular rotations. Calculating the transition matrix element using these wavefunctions determines if a rotational transition is allowed ($\neq 0$) or not ($= 0$). Firstly, for electric dipole allowed pure rotational transitions, the transition matrix element is only $\neq 0$ if the molecule has a permanent electric dipole moment, hence, there are pure rotational transitions for heteronuclear diatomic molecules but not for homonuclear ones. Furthermore, the wavefunctions ψ_i and ψ_f must have different parities (Laporte rule) and the rotational quantum number must change by $\Delta J = \pm 1$, which mathematically satisfies the parity rule.

The $\Delta J = \pm 1$ selection rule applies to pure rotational transitions. For transitions where the vibrational state υ (rovibrational transitions) is also changing, $\Delta J = 0$ may also be possible. *P*-lines refer to transitions when $\Delta J = -1$, *Q*-lines when $\Delta J = 0$ and *R*-lines when $\Delta J = +1$. For pure rotational transitions, *R*-lines are only found in absorption spectra while *P*-lines are only found in emission spectra. Based upon the rigid rotor approximation, the transition spacings between successive lines in pure rotational spectra are expected to be the same ($2B$), as shown in Figure 1.4.

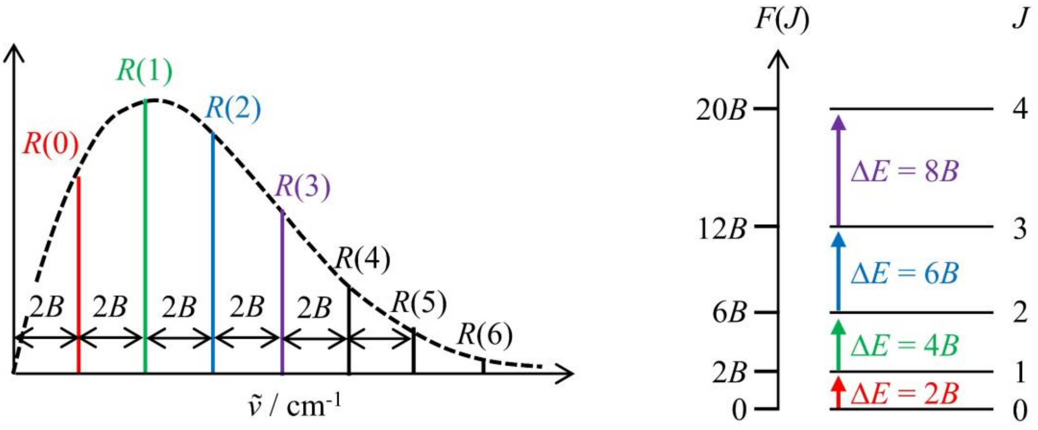

Figure 1.4 – The pure rotational absorption spectrum of a heteronuclear diatomic molecule with equally spaced *R*-lines (2*B*) and the rotational energy levels *F*(*J*) for the first four transitions, based on the rigid rotor approximation.

The individual rotational line intensities are proportional to the population of the rotational levels. The population depends on the number of molecules in a rotationally excited state N_J relative to the number in the ground state N_0 as described by the Boltzmann distribution

$$\frac{N_J}{N_0} = (2J + 1)\, e^{-\frac{E_J}{kT}} \tag{1.8}$$

where E_J is the energy of the excited rotational level, k is the Boltzmann constant and T is the temperature. The orientation of the angular momentum vector J leads to degeneracy of the J^{th} upper level $M_J = (2J + 1)$. As J increases, the degeneracy factor increases but the exponential Boltzmann factor decreases. At high J, the exponential factor wins out and N_J/N_0 approaches zero [1].

The selection rules for Raman rotational spectra are different to one-photon absorption transitions in the microwave/IR region. Raman scattering can be considered as effectively two one-photon transitions each with $\Delta J = \pm 1$. Hence, for pure rotational transitions to be Raman active, $\Delta J = 0, \pm 2$. *O*-lines refer to transitions when $\Delta J = -2$ and *S*-lines when $\Delta J = +2$. Furthermore, in contrast to one-photon absorption, the parity of the wavefunctions ψ_i and ψ_f must stay the same but the polarizability must change for the rotation to be Raman active [4]. Therefore, unlike pure rotational spectroscopy, which requires a permanent electric dipole moment, rotational Raman transitions can be observed for homonuclear diatomic molecules. The typical appearance of a rotational Raman spectrum for a diatomic molecule is shown in Figure 1.5.

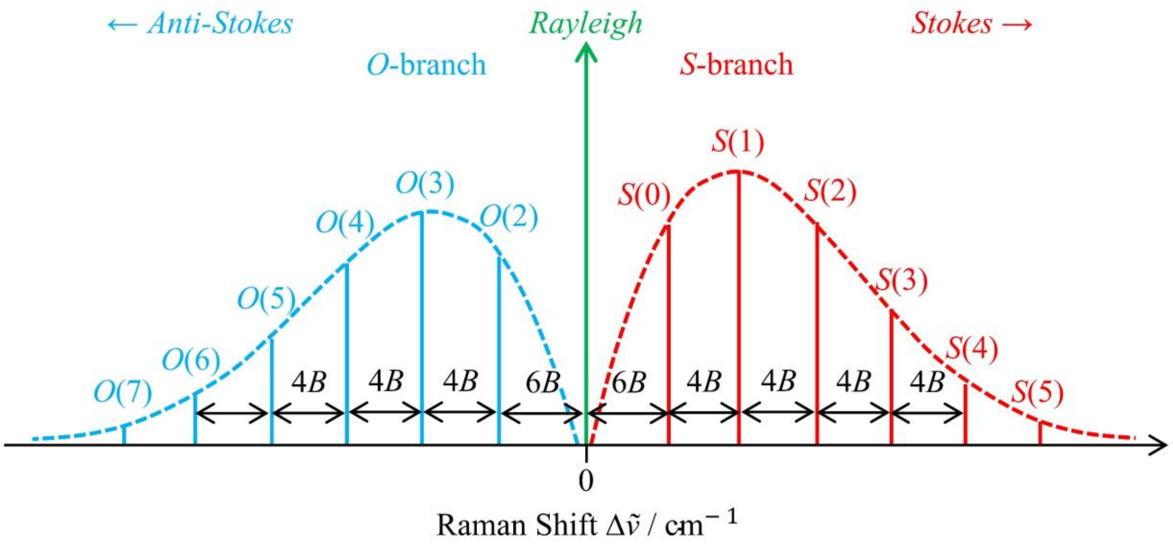

Figure 1.5 – The rotational Raman spectrum of a diatomic molecule (neglecting centrifugal distortion).

In highly symmetric molecules, exchange of undistinguishable nuclei (permutation) is a symmetry operation subject to the Pauli principle leading to nuclear spin statistic effects and alternating line intensities depending on J. In the rotational and rovibrational spectra of homonuclear diatomic molecules and molecules with a centre of inversion i, characteristic intensity differences are typically observed between lines originating from an even J as compared to odd J due to the influence of nuclear spin statistics. One such example is the rotational and rovibrational spectrum of H_2 which has an alternating intensity ratio of 3:1 between lines depending on whether the transition starts from an odd or even J, as shown in Figure 1.6. Molecular H_2 is composed of two equivalent, identical protons which are nuclear Fermions with spin $I = 1/2$. According to the Pauli principle, the total wavefunction of particles with half-integral spins (Fermions) must be antisymmetric with respect to exchange of identical particles. In the case of particles with integral spins (Bosons, *e.g.* ^{16}O with $I = 0$), the total wavefunction must be symmetric under exchange of identical particles. The spins of the two protons in H_2 may be parallel ↑↑ (ortho H_2) or antiparallel ↑↓ (para H_2). Ortho H_2 is a triplet state as it has a total nuclear spin $I = 1$ which can be orientated to give three possible values for the magnetic spin quantum number $M_I = -1$, 0 or 1. Para H_2 is a singlet state as $I = 0$ can only be orientated to give $M_I = 0$. There is, therefore, a statistical weight of 3 for ortho H_2 and 1 for para H_2. At room temperature and thermal equilibrium, thermal excitation gives such a ratio of approximately 3:1 ortho and para H_2.

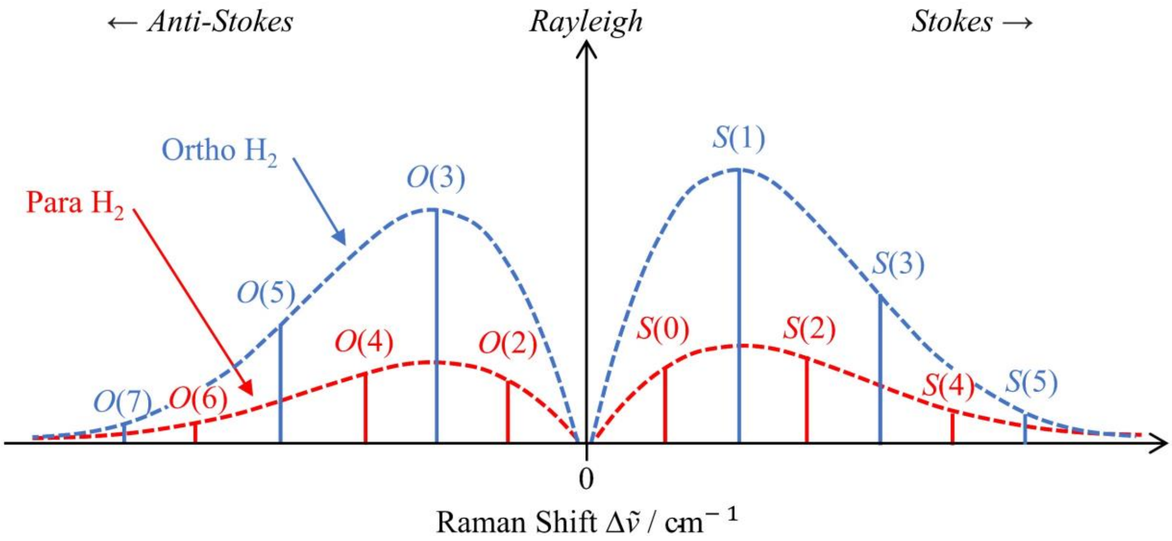

Figure 1.6 – The rotational Raman spectrum of H_2 which is a superposition of the spectra of ortho and para H_2, with the intensity ratio 3:1.

Due to the Pauli principle, the total wavefunction of either H_2 spin isomer must be antisymmetric with respect to the exchange of the two protons. The total wavefunction is the product of the electronic, vibrational, rotational and nuclear wavefunctions. The ${}^1\Sigma_g^+$ electronic ground state of H_2 and vibrational wavefunction are both symmetric. In the case of diatomic molecules, rotational wavefunctions for odd J values are antisymmetric, but symmetric for even J values. The nuclear wavefunction for ortho H_2 is symmetric so only rotational states with odd J are allowed so that the total wavefunction is antisymmetric. For para H_2, the nuclear wavefunction is antisymmetric so only transitions from rotational states with even J are allowed. Consequently, the rotational Raman spectrum of H_2 has lines with alternating 3:1 intensities, as shown in Figure 1.6. For the isotopomer HD, the deuterium nucleus ^{2}H is distinguishable from the hydrogen nucleus ^{1}H, thus, the molecule does not obey the Pauli principle and there is no intensity variation in the rotational spectrum due to nuclear spin statistics. Hence, the spectrum of HD resembles Figure 1.5, and not Figure 1.6.

For other molecules, nuclear spin statistics may also result in lines from certain J levels being missing in rotational and rovibrational spectra. For instance, ${}^{16}O_2$ is composed of two Bosons which ultimately results in rotational states and lines from odd J values being present, but rotational states and lines originating from even J not being observed. Another example is $C^{16}O_2$ where only even J exists in the symmetric vibrational modes.

1.1.3 Vibrational Term Values

The harmonic oscillator model can be used to approximate the normal mode of vibration for a diatomic molecule treated as two point masses connected by a massless spring of length r. The stretching and compression of the bond can be described by Hooke's law

$$F_s = \frac{dV(r)}{dr} = -k\,(r - r_e) \tag{1.9}$$

where F_s is the force acting on the spring, V is the potential energy, and k is the force constant that reflects the bond strength in magnitude. Integrating this equation gives $V(r) = \frac{1}{2}k\,(r - r_e)^2$ which has a parabolic relationship when plotting a potential energy curve of $V(r)$ against r, as shown in Figure 1.7 [1].

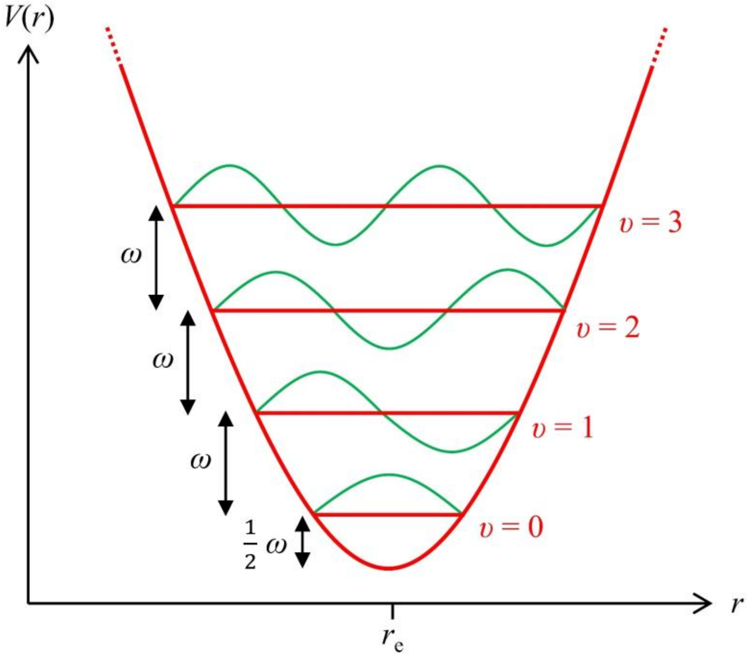

Figure 1.7 – The harmonic oscillator model for the vibration of a diatomic molecule. The potential energy curve contains equally spaced vibrational energy levels υ with their corresponding wavefunctions also shown in green.

Solution of the Schrödinger equation for the harmonic approximation gives vibrational energy levels which can be expressed as vibrational term values (cm^{-1})

$$G(\upsilon) = \omega\left(\upsilon + \tfrac{1}{2}\right) \tag{1.10}$$

where υ is the vibrational quantum number and ω is the wavenumber of the harmonic oscillator (cm^{-1}) which is related to the bond force constant k and the reduced mass μ by

$$\omega = \frac{1}{2\pi c}\sqrt{\frac{k}{\mu}} \tag{1.11}$$

For $\upsilon = 0, 1, 2, 3, \ldots$, $G(\upsilon) = \frac{1}{2}\,\omega, \frac{3}{2}\,\omega, \frac{5}{2}\,\omega, \frac{7}{2}\,\omega\ \ldots$. These energy levels are non-degenerate, equally spaced by ω and all have the same equilibrium bond length r_e. The zero-point energy is the energy of the lowest state ($\upsilon = 0$) equal to $\frac{1}{2}\,\omega$.

The harmonic approximation reasonably describes vibrational behaviour when a molecule is close to its equilibrium configuration, however, it fails to adequately describe higher vibrational modes, when r is far from r_e. The true potential energy curve should be far steeper when moving to smaller r compared to increasing to greater lengths as there are extra repulsion effects between the electron clouds when two nuclei are in close proximity. Furthermore, the harmonic oscillator model predicts that the nuclei can never separate, even at infinite internuclear separation, which is unphysical.

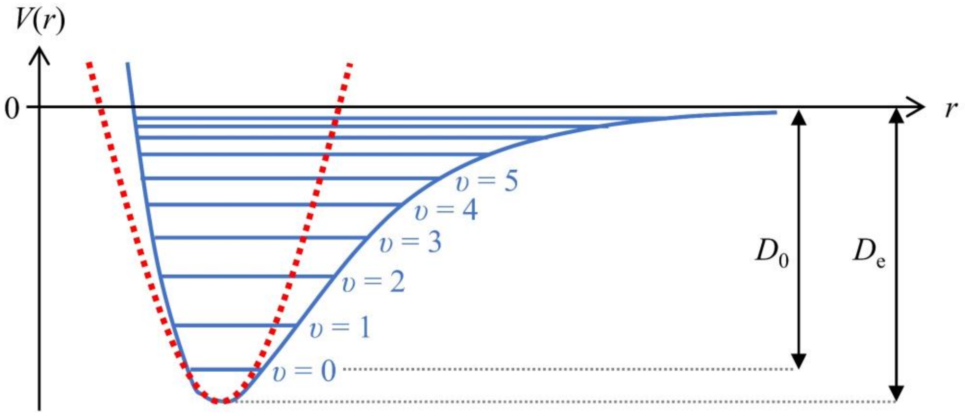

Figure 1.8 – The Morse potential energy curve for the vibration of a diatomic molecule. The harmonic potential energy curve is given for comparison as a red dashed line.

The anharmonic oscillator model considers these factors and more accurately models the potential energy curve of a vibrating diatomic molecule using the Morse potential

$$V(r) = D_e\,(1 - e^{-\alpha\,(r - r_e)})^2 \tag{1.12}$$

where D_e is the potential energy well depth and $\alpha = \sqrt{k/2D_e}$. The potential energy $V(r)$ rapidly increases as r approaches zero and becomes flat as r approaches infinity implying finite bond dissociation energy D_e, as shown in Figure 1.8. The 'true' bond dissociation energy D_0 is typically measured from the lowest vibrational term with $D_e - D_0$ equal to the zero-point energy [1].

By inserting the Morse potential into the Hamiltonian operator, the vibrational term values become

$$G(\upsilon) = \omega\left(\upsilon + \tfrac{1}{2}\right) - \frac{\omega^2}{4D_e}\left(\upsilon + \tfrac{1}{2}\right)^2 \tag{1.13}$$

Unlike the harmonic approximation, the additional quadratic term causes the separation between vibrational states to decrease with increasing υ. In IR absorption spectra, the band origin $\tilde{\nu}_0$ is the wavenumber difference between the vibrationally excited state $G(\upsilon')$ and the vibrational ground state $G(\upsilon'')$ for a hypothetical vibrational transition without any rotational excitation *i.e.* $J'' = 0 \rightarrow J' = 0$ (which is never allowed, but $\Delta J = 0$ is under certain conditions).

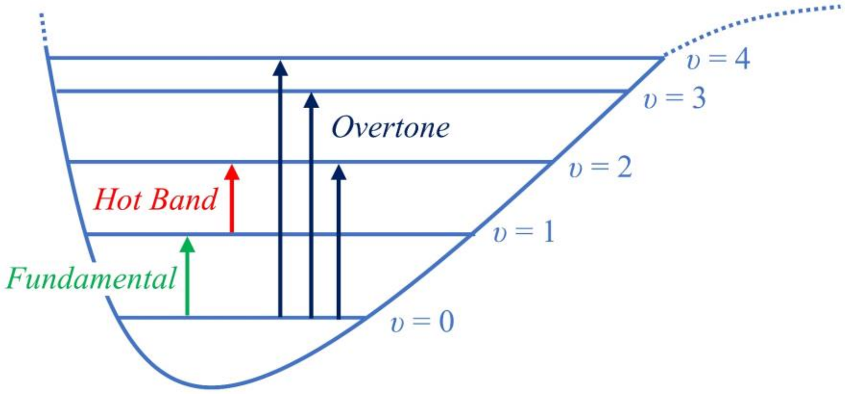

Figure 1.9 – Vibrational energy level diagram to illustrate the differences between fundamental transitions ($\Delta\upsilon = \pm 1$), overtone transitions ($\Delta\upsilon = \pm 2, 3, 4, \ldots$) and hot bands.

Solution of the Schrödinger equation for molecular vibrations gives vibrational term values $G(\upsilon)$ and corresponding wavefunctions ψ_υ. By evaluating the transition matrix element with vibrational wavefunctions it is found that strong fundamental transitions with $\Delta\upsilon = \pm 1$ are

IR active if the vibration gives rise to an oscillating electric dipole moment. For a vibration to be Raman active there must be a change in polarizability of the molecule. Compared to the rotational selection rules for ΔJ, the $\Delta \upsilon = \pm 1$ vibrational selection rule is somewhat less rigorous. Mainly due to anharmonicity, this rule is relaxed so that higher overtone transitions where $\Delta \upsilon = \pm 2, 3, 4, \ldots$ are also possible, however, overtone bands are typically orders of magnitude weaker than fundamental bands. Hot bands are observed when an already vibrationally excited level is further excited *e.g.* $\upsilon'' = 1 \rightarrow \upsilon' = 2$. Hot bands are called such as these transitions are temperature dependent. Due to the Boltzmann distribution, at room temperature only the vibrational ground state is highly populated, but with increasing temperature excited vibrational states become more thermally populated and, thus, the intensity of a hot band increases. To illustrate the differences between these different types of transitions, a vibrational energy level diagram is shown in Figure 1.9.

Polyatomic molecules have many vibrational modes. To an approximation they can be considered as independent harmonic or anharmonic vibrations (normal modes). Polyatomic molecules may also have weak combination bands which correspond to the simultaneous one-photon excitation of multiple normal modes of vibration together. As an example, in the IR absorption spectrum of CO_2, the combined excitation of the first overtone of the bending vibration $2\nu_2$ ($\tilde{\nu}_0 = 1334\ \mathrm{cm}^{-1}$) and the asymmetric stretching fundamental vibration ν_3 ($\tilde{\nu}_0 = 2349\ \mathrm{cm}^{-1}$) results in a combination band $2\nu_2 + \nu_3$ ($\tilde{\nu}_0 \approx 1334 + 2349\ \mathrm{cm}^{-1}$).

IR absorption may cause rovibrational transitions where vibrational υ and rotational J states change at the same time. To an approximation, rovibrational term values $T(\upsilon, J)$ are the sum of vibrational $G(\upsilon)$ and rotational $F_\upsilon(J)$ term values. The wavenumber difference between two rovibrational states is equal to

$$T(\upsilon', J') - T(\upsilon'', J'') = \tilde{\nu}_0 + B_\upsilon{}' J'(J' + 1) - B_\upsilon{}'' J''(J'' + 1) \qquad (1.14)$$

When the change in vibrational angular momentum is $\Delta l = 0$, $\Delta J = 0$ is not allowed for a rovibrational transition. However, degenerate vibrations have an angular momentum, such as the doubly degenerate bending vibration ν_2 of CO_2 which has $l = 1$, hence, for this transition from the non-degenerate $l = 0$ vibrational ground state, $\Delta J = 0$ is allowed. This results in a Q-branch at $\tilde{\nu}_0 = 667\ \mathrm{cm}^{-1}$ being observed for this vibration of CO_2, as shown in Figure 1.10.

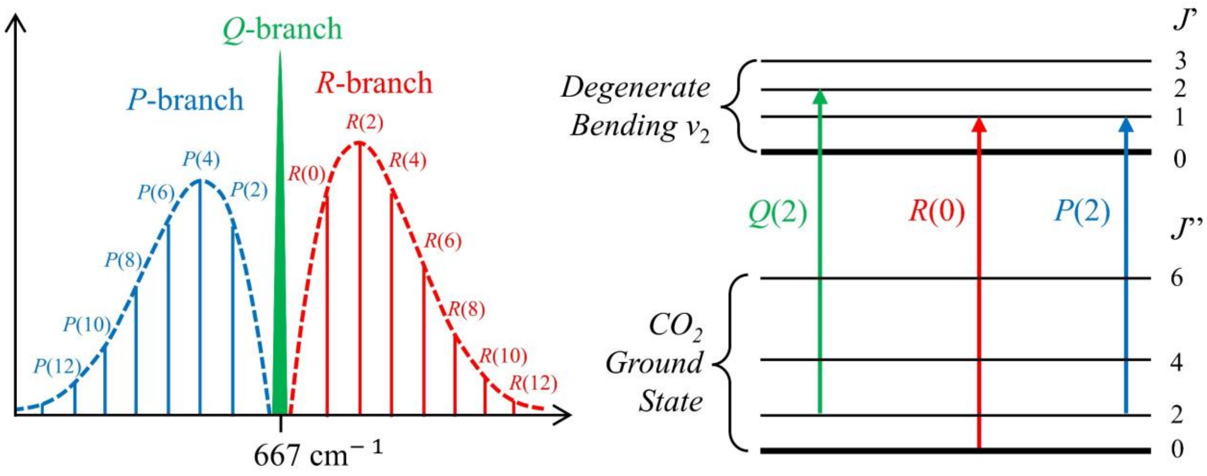

Figure 1.10 – The IR absorption spectrum of the CO_2 bending v_2 fundamental with allowed *J* values of the rotational energy levels displayed for the bending and ground states. Due to nuclear spin statistics, only even *J* exists in the ground state of $C^{16}O_2$.

Only even *J* values are allowed for the vibrational ground state in $^{12}C^{16}O_2$ as the two ^{16}O nuclear Bosons are identical and equivalent, so the Pauli principle applies here. The total wavefunction must be totally symmetric and as the electronic, vibrational and nuclear wavefunctions are symmetrical, odd *J* values (antisymmetric rotational wavefunction) are not allowed in the ground state. Due to the degeneracy of the bending vibrational state, the vibrational wavefunction can be both symmetric and antisymmetric which allows both even and odd *J* values, as shown in Figure 1.10. In comparison, the non-degenerate asymmetric stretching vibration v_3 of CO_2 ($\tilde{v}_0$ = 2349 cm^{-1}) has no Q-branch as the state has an antisymmetric vibrational wavefunction, hence, only odd *J* values are allowed and no $\Delta J = 0$ transitions from the ground state are possible.

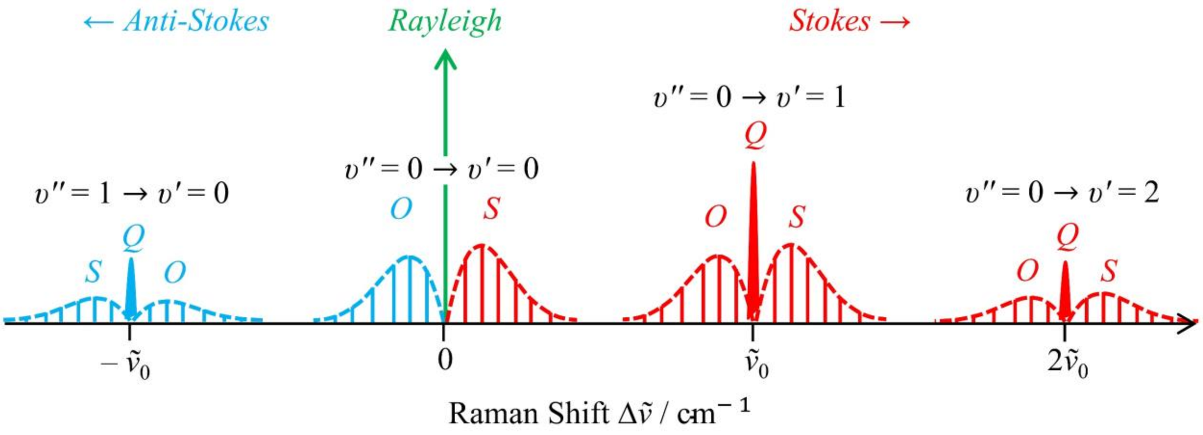

Figure 1.11 – The total Raman spectrum of a diatomic molecule.

In contrast to IR absorption spectroscopy where rovibrational lines are typically grouped into *P*, *Q* (if $\Delta l \neq 0$) and *S*-branches, the rotational selection rule for Raman spectroscopy is $\Delta J = 0, \pm 2$ which leads to *O*, *Q* and *S*-branches. A typical Raman spectrum of a diatomic molecule is shown in Figure 1.11. Note that Figure 1.5 previously introduced only the rotational lines while Figure 1.11 includes both rotational and rovibrational lines.

In the IR absorption or Raman spectrum of a molecule, if two (or more) vibrational states have the same symmetries and similar energies then the wavefunctions for the states can interact and mix compared to the independent harmonic oscillator approximation resulting in the transition of a weaker mode gaining intensity from the stronger mode and both vibrations moving away from their unperturbed position. This effect is called anharmonic resonance. In the special case of one quantum of one mode interacting with two quanta of another one it is called a Fermi resonance, named after the Italian physicist Enrico Fermi, who used CO_2 to explain the phenomenon [5].

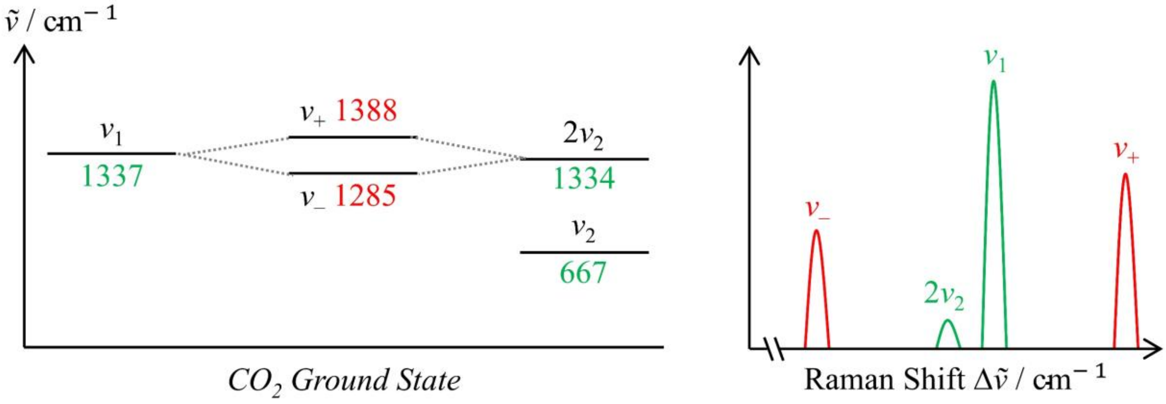

Figure 1.12 – The $\nu_1/2\nu_2^0$ Fermi resonance pair of CO_2. An energy level diagram shows how the ν_1 and $2\nu_2$ states have similar energy and undergo a Fermi resonance with the resulting splitting and sharing of intensity of the individual ν_1 fundamental and $2\nu_2$ overtone states (in green) to give the observed Fermi resonance pair (in red).

The symmetric stretching ν_1 vibration of CO_2 ($\tilde{\nu}_0 = 1337\ \text{cm}^{-1}$) is Raman active and strong. The symmetric component of the bending vibration first overtone $2\nu_2$ ($\tilde{\nu}_0 = 1334\ \text{cm}^{-1}$) is also Raman active, but weak. The $2\nu_2$ overtone is degenerate with vibrational angular momentum $l = 0, 2$ leading to the state having two components $2\nu_2^0$ and $2\nu_2^2$ with different symmetries, where the superscript denotes the vibrational angular momentum. The $2\nu_2^0$ component and the ν_1 fundamental have the same symmetry and similar energy which allows the modes to interact ($\nu_1/2\nu_2^0$ Fermi resonance pair). The weak $2\nu_2^0$ component gains intensity from the strong ν_1 fundamental, as shown in Figure 1.12.

1.1.4 Spectral Linewidths

An energy transition between two states $\Delta E = hc\tilde{\nu}_0$ does not simply have a sharp spectral line at the wavenumber of the transition $\tilde{\nu}_0$. In reality, spectral lines are broadened due to a number of factors. Firstly, each measuring instrument has a limited spectral resolution. Monochromators are typically limited by, among other factors, the camera resolution, the resolving power of the prism or grating and the entrance aperture width. Secondly, there may be inhomogeneous broadening of numerous sharp lines that blend together and give the appearance of one broad feature.

In gaseous samples, an important broadening process is the Doppler effect which states that the frequency of a wave changes in relation to an observer who is moving relative to the wave source. Molecules move rapidly in all directions meaning a stationary observer (spectrometer) detects the corresponding Doppler-shifted range of frequencies ν in the form of a Gaussian line shape (bell curve) around ν_0 [6]. The temperature T (K) can be determined by measuring the Doppler line shape according to

$$\frac{\Delta\nu}{\nu_0} = \frac{\Delta\tilde{\nu}}{\tilde{\nu}_0} = 7.16 \times 10^{-7}\sqrt{\frac{T}{m}} \tag{1.15}$$

where $\Delta\nu$ and $\Delta\tilde{\nu}$ are the full width at half maximum (FWHM) of the peak measured in frequency and wavenumber, respectively, and m is the molecular mass (u). Doppler broadening increases with temperature as the molecules acquire a wider range of speeds, hence, sharper spectral lines can be achieved with cooler samples.

Spectral lines are not infinitely sharp, even when working with samples at low temperatures to minimise Doppler broadening [6]. This residual broadening is due to quantum mechanical effects and is termed lifetime broadening, as described by the Heisenberg uncertainty principle. When solving the Schrödinger equation, time-independent stationary states are found which have a well-defined exact energy. However, if an excited state has a limited lifetime Δt then its energy ΔE is not perfectly defined according to the Heisenberg uncertainty principle of

$$\Delta E\,\Delta t \geq \frac{h}{4\pi} \tag{1.16}$$

This means that it is impossible to specify simultaneously, with precision, both the energy and lifetime of an excited state and that there is a fundamental limit to the accuracy with which these values can be obtained ($h/4\pi$). Thus, there will be a distribution of excited state energies ΔE resulting in a distribution of wavenumbers around $\tilde{\nu}_0$ in a spectrum [6]. If the excited state follows an exponential decay time law, as in first order kinetics, then the spectral line shape will be Lorentzian where the mean half-life of the excited state τ is related to the FWHM ($\delta\nu$ or $\delta\tilde{\nu}$) by

$$\tau = \frac{1}{2\pi\,\delta\nu} = \frac{1}{2\pi c\,\delta\tilde{\nu}} \tag{1.17}$$

The shorter the lifetimes of the states involved in a transition, the broader the corresponding spectral lines. Measuring Lorentzian spectral line shapes thus allows the determination of lifetimes when studying dynamics. No excited state has an infinite lifetime, so all spectral lines are subject to some amount of lifetime broadening. As an ultimate limit, every excited state will decay eventually to a lower sate by emitting a photon by spontaneous emission, this gives rise to the ‘natural linewidth’. Furthermore, the energy deposited in an excited molecule may cause the breaking of a chemical bond by dissociation or predissociation causing predissociation broadening.

The lifetime of excited states can also be limited by collisions with other molecules. This is a particular issue in the condensed phases where collisions are very frequent. This typically gives rise to very broad absorptions in liquids and solids, where rotational fine structure is not resolvable anymore.

Molecular collisions also occur in the gas phase. Here, the collision frequency is proportional to the pressure, hence, this phenomenon is called pressure broadening [7]. To an approximation, pressure broadening line shapes are Lorentzian, which is a bell shape but with feet extending further than a Gaussian, with FWHM $\delta\tilde{\nu} = \gamma\, p$, where γ is the pressure broadening coefficient depending on the collisional species ($\text{cm}^{-1}\ \text{atm}^{-1}$), which can be found in spectral databases such as the High Resolution Transmission (HITRAN) database [8], and p is the pressure.

If different broadening mechanisms apply, each line shape contribution adds up and convolutes to the total, effective line shape. The convolution of a Gaussian shape (as in Doppler broadening) and a Lorentzian shape (as in pressure broadening) results in a so-called Voigt line shape.

1.2 *Escherichia coli*

1.2.1 A Model Organism

In 1884, while studying infant gut microbes and their role in digestion and disease, Theodore Escherich discovered *Bacterium coli commune* [9], or as it is now known as *Escherichia coli* (*E. coli*). In the early twentieth century, interest in *E. coli* as model organism began with work such as Charles Clifton's studies on its oxidation-reduction reactions [10] and Felix d'Herelle's investigations into its interactions with bacteriophages [11]. *E. coli* became the most studied model organism in terms of gene regulation and expression as well as being the cornerstone of many important findings in molecular biology and cell physiology. The bacterium has been included in many Noble prize winning discoveries, including how bacteria can mate and exchange genes (bacterial conjugation) [12], the mechanisms of replication for DNA and RNA [13], the molecular structure of nucleic acids and their significance for encoding genetic information [14], gene organisation and regulation for controlling enzyme synthesis (operons) [15] and the creation of the first genetically engineered (recombinant) DNA [16, 17]. Furthermore, of significant importance to the work presented in this thesis, hydrogenases (enzymes which catalyse proton reduction and/or the oxidation of dihydrogen) were first discovered in the 1930s by Marjory Stephenson, once again with *E. coli* used as a model organism [18].

E. coli, which is a Gram-negative **γ**-proteobacterium, can grow in a variety of environmental conditions; it is commonly found in the lower intestines of many animals (an anaerobic environment) [19], but it is also found in estuaries (where micro-aerobic environments can be found) [20] and, in addition, is associated with plant tissues and other aerobic environments [21]. As a result, *E. coli* has evolved a genome equipped for almost every eventuality and can adapt, primarily through regulating gene expression, to changing environmental and nutritional conditions [22]. *E. coli* is easy to work with because of this metabolic versatility, alongside its rapid replication and the extensive tools available for its genetic manipulation [23].

A typical *E. coli* cell is rod-shaped, measuring only about 1 µm long by 0.35 µm wide, and will elongate during the cell cycle before dividing. Some strains are capable of growing even larger, up to 750 µm in length, while still remaining viable [24]. Many strains are motile, possessing multiple flagella for cell movement towards nutrient sources (chemotaxis). *E. coli* is a Gram-negative bacterium with an outer membrane that encompasses the entire cell volume and an inner membrane that divides the cell into the periplasm and the inner cytoplasmic compartment. Depending on the strain, *E. coli* cells contain a single circular chromosome of between 4.5 to 5.5 Mbp (mega base pairs) in length. Notably, *E. coli* K-12 MG1655 was one of the first organisms to have its complete genome sequenced in 1997 [25]. This strain is considered an approximation of wild-type *E. coli* with minimal genetic manipulation. *E. coli* K-12 is not a health risk to work with as it is unable to colonize the human gut [26].

1.2.2 Ethanol and Hydrogen as Biofuels

With increasing energy consumption and greenhouse gas emissions alongside depleting petroleum reserves, there is a demand for alternate renewable energies, such as biofuels. Currently, bioethanol dominates the biofuel industry despite its limitations such as high vapour pressure, corrosiveness due to high hygroscopicity and low energy density [27]. Lignocellulosic feedstock material is hydrolysed to hexose and pentose sugars and then converted to bioethanol by fermentation using organisms such as the yeast *Saccharomyces cerevisiae* or the bacterium *Zymomonas mobilis* [28]. However, these organisms cannot consume pentoses naturally and require metabolic engineering for improved bioethanol yields, such as the xylose-utilising *S. cerevisiae* strains that have been produced [29]. *E. coli* is also studied for its bioethanol production as it can use both hexose and pentose sugars with some strains capable of producing similar ethanol yields to *S. cerevisiae* [30]. However, more work is required for *E. coli* to be industrially viable as the feedstock contains toxic compounds which inhibit the growth of *E. coli* more than *S. cerevisiae* [30].

Dihydrogen (H_2) also holds promise as a renewable, carbon-neutral source of energy but the development of efficient storage, distribution and production methods remains a challenge. Powered by renewable energy sources, H_2 can be produced from water (by electrolysis, thermolysis, splitting, etc), but further improvement is needed for its wide-scale implementation [31]. Derived from biomass by fermentative, biophotolytic or electrolytic processes, biohydrogen has the potential to have an even smaller environmental impact than other production methods [32]. *E. coli* produces H_2 predominantly under fermentative conditions using the formate hydrogenlyase (FHL) complex (see Section 1.2.4), but at a relatively low yield. One possible approach for increasing H_2 yield is the heterologous expression of non-native enzymes, such as hydrogenases dependent on nicotinamide adenine dinucleotide (NADH) [33], which would not compete directly with the native pathways for H_2 production and link the new hydrogenase activity directly into the anaerobic fermentation of the host organism by recycling NADH. Despite challenges, the large toolbox available for its genetic engineering ensures that *E. coli* continues to be studied as a model organism for its biofuel production [34], as is the case for many other research topics in molecular biology and cell physiology.

1.2.3 Aerobic Respiration

As a facultative anaerobe, *E. coli* can utilise either aerobic respiration, anaerobic respiration or anaerobic fermentation metabolic modes, depending on the availabilities of certain electron donors and acceptors. The inner membrane contains many redox active, multi-subunit enzymes which form electron transport chains (ETCs) in order to generate a proton motive force for driving the phosphorylation of adenosine diphosphate (ADP) to adenosine triphosphate (ATP). These ETCs are composed of many different dehydrogenases and terminal reductases and oxidases linked by membrane-soluble quinones (Q) and quinols (QH_2) [35]. Electron carriers, such as NADH, nicotinamide adenine dinucleotide phosphate (NADPH) and flavin adenine dinucleotide ($FADH_2$), also store and transfer electrons between enzymes in the cytoplasm.

Aerobic respiration is generally preferred to anaerobic respiration and fermentation. When O_2 is present, growth substrates can be completely oxidised to CO_2 for producing energy as ATP. The equation for aerobic respiration with glucose as the carbon source is

$$C_6H_{12}O_6 + 6\ O_2 \rightarrow 6\ CO_2 + 6\ H_2O + \text{Energy}\ (<38\ \text{ATP}) \qquad (1.18)$$

For growth on glucose, both aerobic and anaerobic metabolic modes begin with glucose uptake followed by glycolysis. *E. coli* can transport glucose into the cytoplasm by several systems, but the main system involves the coupling of sugar transport with sugar phosphorylation (translocation) [36]. The phosphotransferase system (PTS) depends on phosphoenolpyruvate (PEP, the final glycolytic intermediate) as the phosphoryl (PO_3^{2-}) donor which creates a direct link between the uptake and glycolysis of sugars [37].

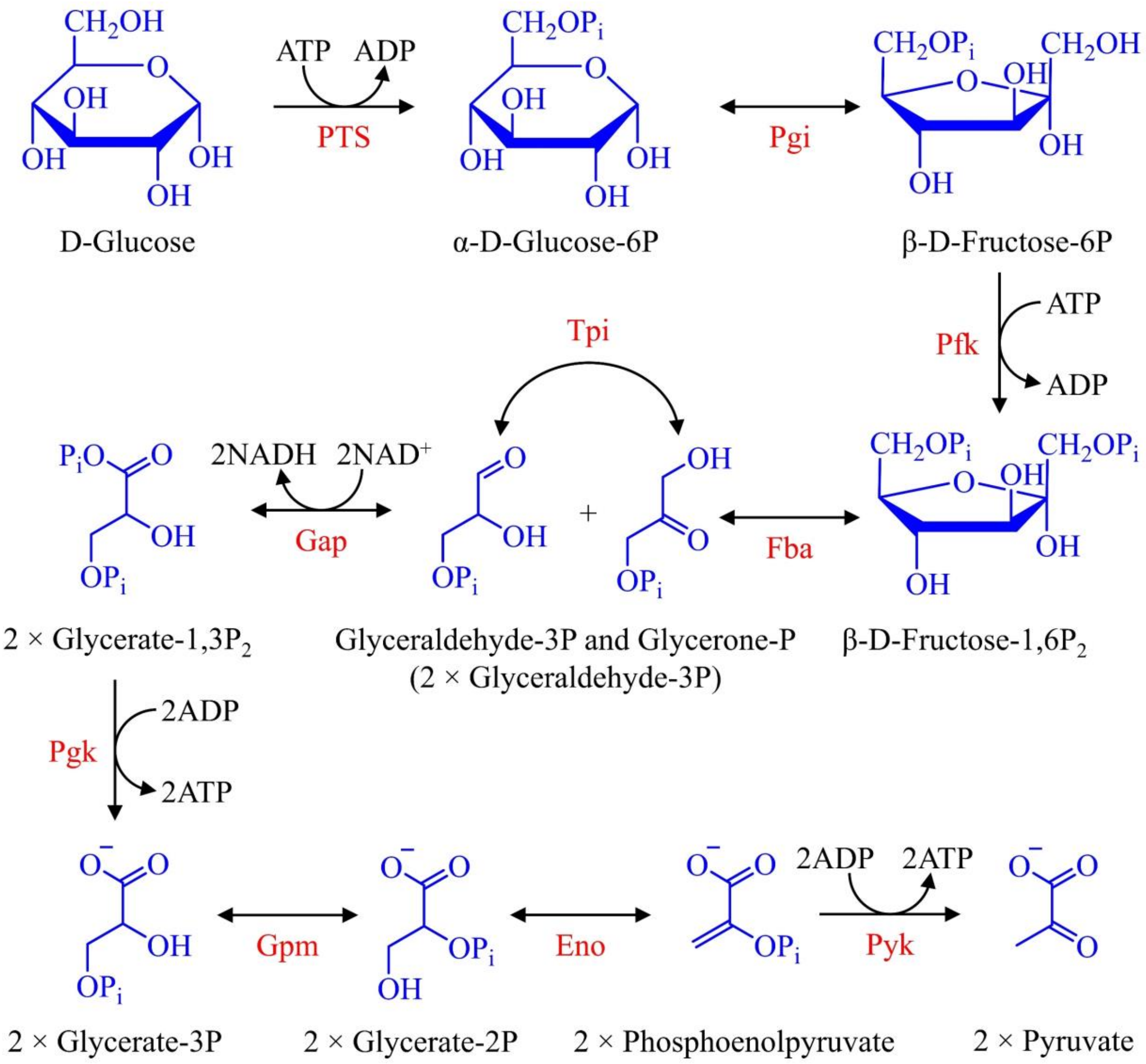

Figure 1.13 – Glycolysis by the Embden-Meyerhof-Parnas (EMP) pathway. P_i indicates phosphoryl (PO_3^{2-}) groups. Enzymes (in red) in order of the glycolytic steps: **PTS**, glucose-specific phosphotransferase system; **Pgi**, phosphoglucose isomerase; **Pfk**, phosphofructokinase; **Fba**, fructose-biphosphate aldolase; **Tpi**, triosephosphate isomerase; **Gap**, glyceraldehyde-3P dehydrogenase; **Pgk**, phosphoglycerate kinase; **Gpm**, phosphoglycerate mutase; **Eno**, enolase; **Pyk**, pyruvate kinase.

E. coli has three native glycolytic pathways: the Embden-Meyerhof-Parnas (EMP), Entner Doudoroff (ED) and oxidative pentose phosphate (OPP) pathways [38]. *E. coli* mainly uses the EMP and OPP pathways as the ED pathway remains inactive, except during growth with gluconate [39]. The EMP pathway includes ten enzymatic steps to yield two pyruvates, two ATP and two NADH per glucose molecule, as shown in Figure 1.13. The first phase of the pathway is energy-requiring, needing two ATP per glucose molecule in order to restructure the six-carbon backbone so that it can be efficiently cleaved to give two three-carbon isomers (glyceraldehyde-3P and glycerone-P) which can interconvert *via* an isomerase. The two glyceraldehyde-3P molecules then continue into the second phase of the EMP pathway in order to generate two pyruvate. This phase is energy-releasing, yielding four ATP (a net total of two) by substrate-level phosphorylation as well as two NADH.

The OPP pathway operates parallel to the EMP pathway, but its primary role is anabolic rather than catabolic by providing the cell with intermediates for the biosynthesis of amino acids, vitamins, nucleotides and cell wall constituents [38]. This pathway is also an important source of NADPH which is an essential reducing equivalent needed for biosynthesis. Briefly, the OPP pathway has an oxidative portion which converts glucose-6P to ribulose-5P by releasing a CO_2 molecule, followed by a non-oxidative portion which, through a series of transaldolase and transketolase reactions, produces fructose-6P and glyceraldehyde-3P.

Aerobically, pyruvate is decarboxylated to acetyl co-enzyme A (CoA) and CO_2, alongside the reduction of NAD^+, in a series of reactions catalysed by the pyruvate dehydrogenase (PDH) complex [40], as summarised by

$$\mathrm{CH_3COCO_2^- + CoA\text{-}SH + NAD^+ \rightarrow CH_3CO\text{-}S\text{-}CoA + CO_2 + NADH} \qquad (1.19)$$

Acetyl-CoA can then enter the tricarboxylic acid (TCA) cycle, which is the final pathway for the oxidation of growth substrates, as shown in Figure 1.14 [38]. The two-carbon acetyl group is transferred to the four-carbon intermediate oxaloacetate to give six-carbon citrate. In a series of enzymatically-catalysed reactions, two carbons in one citrate molecule are oxidised to two CO_2 molecules while also generating three NADH, one $FADH_2$ and one ATP per each revolution of the cycle. As well as the catabolism of organic molecules, the TCA cycle also produces intermediates for anabolic reactions, such as 2-oxoglutarate.

Aerobically, O_2 serves as the final electron acceptor of the ETC. Dehydrogenases catalyse the oxidation of cytoplasmic electron donors (NADH, $FADH_2$ and succinate) by coupling to the reduction of ubiquinone (UQ) to ubiquinol (UQH_2) [41]. Terminal oxidases then re-oxidise ubiquinol by coupling to the terminal reduction of O_2 to water. The ETC is needed for creating a concentration and charge gradient by translocating protons (H^+) from the cytoplasm to the periplasm *via* the inner membrane, which is impermeable towards ions except through dedicated channels. The H^+ gradient (proton motive force) can be used for ATP synthesis by oxidative phosphorylation or for other energy consuming processes linked to the membrane, such as nutrient transport or flagella motion. The H^+ gradient is mediated by certain dehydrogenases and reductases with H^+ pumps, the reduction of O_2 which removes four H^+

from the cytoplasm and the quinone/quinol redox reactions which take H^+ from the cytoplasm for quinone reduction and release H^+ into the periplasm during quinol oxidation.

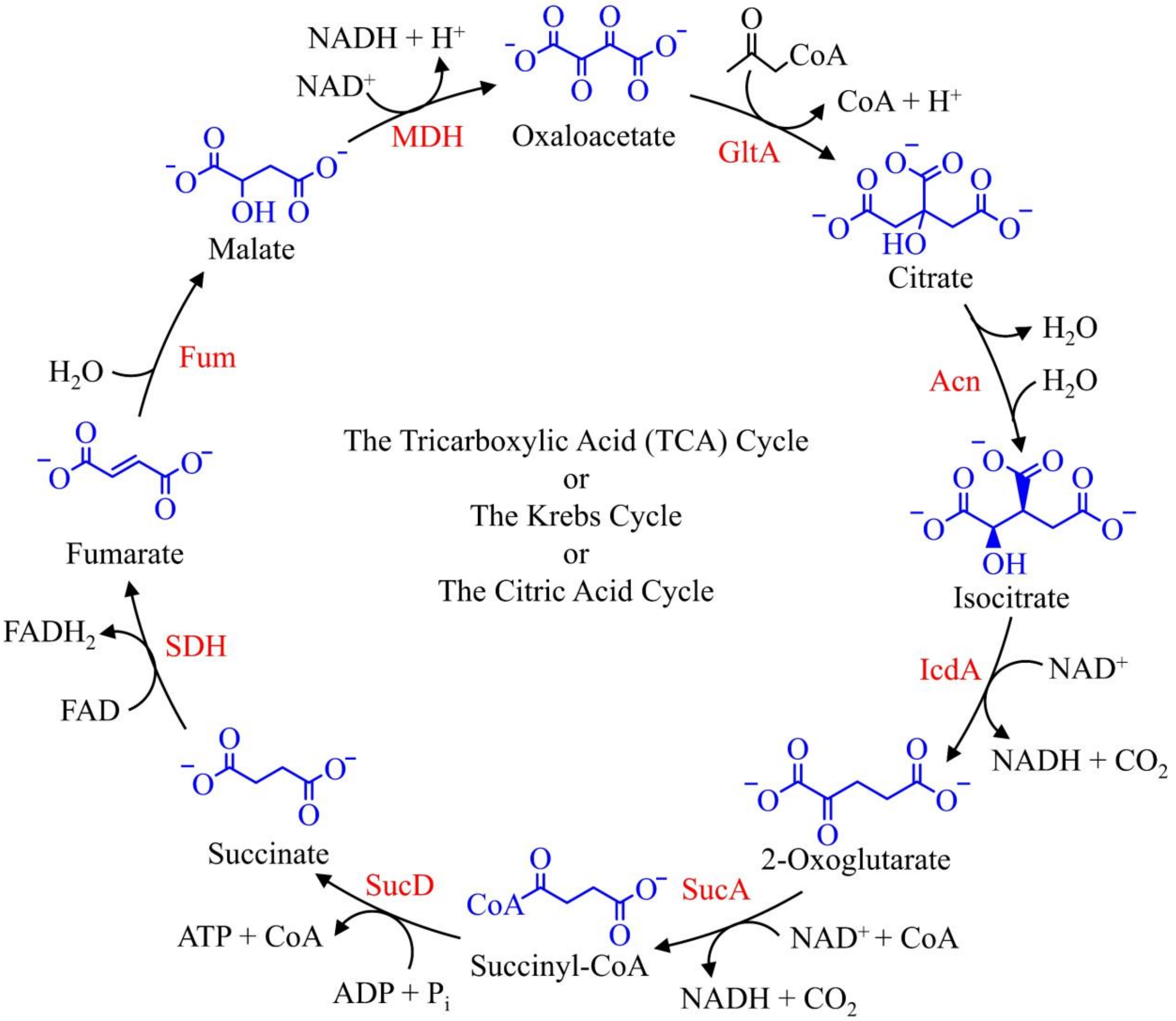

Figure 1.14 – The tricarboxylic acid (TCA) cycle. Enzymes (in red) moving clockwise from oxaloacetate: **GltA**, citrate synthase; **Acn**, aconitase; **IcdA**, isocitrate dehydrogenase; **SucA**, 2-oxoglutarate decarboxylase; **SucD**, succinyl-CoA synthase; **SDH**, succinate dehydrogenase; **Fum**, fumarase; **MDH**, malate dehydrogenase.

The most important enzymes in the aerobic ETC are NADH-dehydrogenases I and II, succinate dehydrogenase (SDH), cytochrome *bd*-I, *bd*-II and *bo* oxidases and F_OF_1-ATP synthase [41, 42]. The membrane-bound dehydrogenases extend into the cytoplasm *via* a number of metal cofactors, typically Fe-S clusters or heme groups, for shuttling electrons from the oxidation of an electron donor. NADH-dehydrogenase I has a H^+ pump with a stoichiometry of four H^+ translocated per NADH oxidised. This oxidation transfers two electrons to the flavin mononucleotide (FMN) binding site before passing them onto the Fe-S clusters. NADH-dehydrogenase II also oxidises NADH but lacks a H^+ pump and has a flavin adenine dinucleotide (FAD) binding site [42]. Succinate dehydrogenase (SDH) is the only enzyme to participate directly in the ETC and the TCA cycle. The enzyme lacks a H^+ pump and couples succinate oxidation to FAD reduction [43]. To regenerate FAD, $FADH_2$ oxidation couples to ubiquinone reduction *via* Fe-S clusters.

Cytochrome *bo* oxidase couples the two-electron oxidation of ubiquinol with the four-electron reduction of O_2 by a high-spin heme O_3 magnetically coupled to a copper atom (heme-copper binuclear center) [44]. Cytochrome *bo* oxidase has a relatively low affinity for O_2 and is most abundant when cells are grown in O_2 rich environments; it also has a H^+ pump with a net movement of four H^+ translocated per O_2 reduced. An example of the ETC between NADH-dehydrogenase I and cytochrome *bo* is shown in Figure 1.15. Cytochrome *bd*-I oxidase is like *bo* in redox chemistry; however it lacks a H^+ pump and copper atoms. This oxidase is expressed at low O_2 conditions as well as during other stressful growth conditions, such as iron deficiency [45]. Cytochrome *bd*-II oxidase has the highest affinity for O_2 out of the three oxidases making it the most effective oxidase at very low micro-aerobic conditions [46]. As the three oxidases all have different affinities for O_2, it allows *E. coli* to grow efficiently under a full range of O_2 tensions.

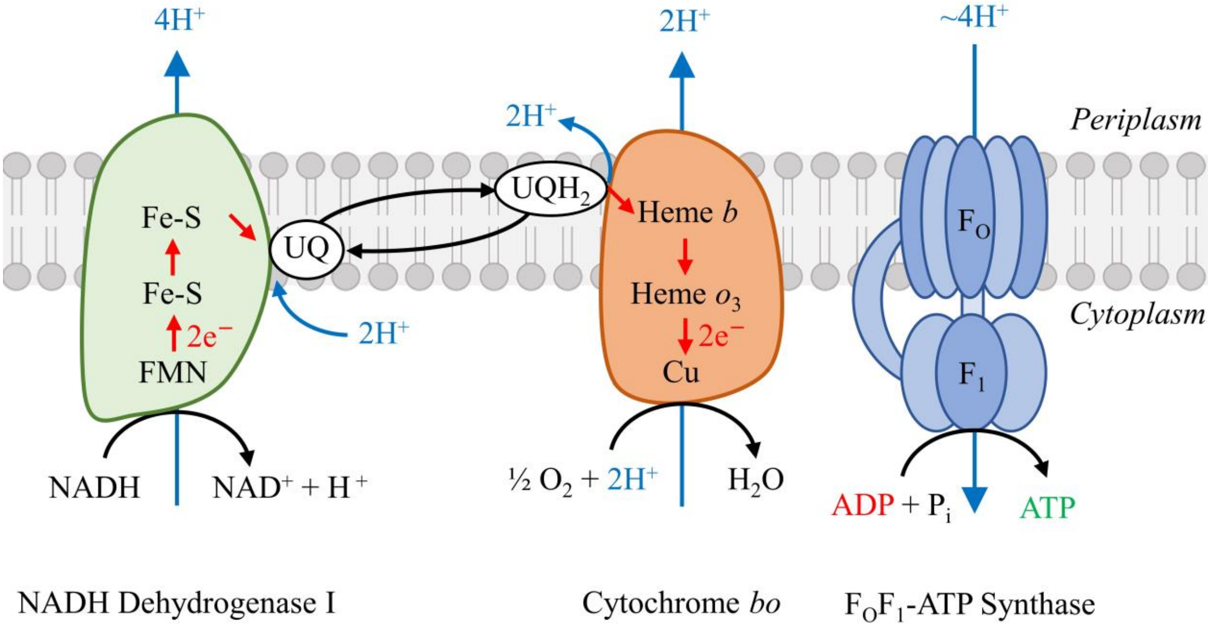

Figure 1.15 – The electron transport chain (ETC) between NADH dehydrogenase I and cytochrome *bo* during aerobic respiration. The resulting H^+ gradient drives oxidative phosphorylation of ADP to ATP by F_OF_1-ATP synthase.

ATP synthase is a rotary molecular nanomotor that couples the mechanical force of subunit rotation to the synthesis (or hydrolysis) of ATP [35]. It is organised into two distinct components, F_O and F_1, as shown in Figure 1.15. The F_O complex is a membrane-bound H^+ channel which allows the energetically favorable flow of H^+ down the gradient, from the periplasm to the cytoplasm. The flow of H^+ causes the F_O component to rotate and drives conformational changes of the hydrophilic F_1 complex where ATP synthesis occurs. The flow of roughly four H^+ is required for the synthesis of one ATP molecule.

Before the ETC, glycolysis of one glucose molecule produces two ATP and two NADH, followed by decarboxylation of two pyruvate molecules which produces two NADH and leads into two revolutions of the TCA cycle which produces two ATP, six NADH and two $FADH_2$. The reduction of ten NADH and two $FADH_2$ in the ETC produces twenty-four electrons that are transferred to the four-electron reduction of O_2, hence, six molecules of O_2 are consumed per molecule of glucose. The theoretical maximum yield of ATP is thirty-eight, with four produced by substrate-level phosphorylation and thirty-four by oxidative phosphorylation, assuming one NADH produces three ATP and one $FADH_2$ produces two. In reality, this theoretical ATP yield is not achieved due to losses including H^+ leaks across the membrane, competing metabolic pathways and ATP consumption by other cellular processes.

Under anaerobic conditions, *E. coli* can still express ETCs and undergo anaerobic oxidative phosphorylation if an alternate terminal electron acceptor is present, such as nitrate (NO_3^-), nitrite (NO_2^-), trimethylamine N-oxide (TMAO), dimethyl sulfoxide (DMSO) or fumarate [35]. The large difference in reduction potentials between NADH and O_2 (~1.14 V) ensures the highest yield of cellular energy production. These alternate electron acceptors have more positive reduction potentials than O_2 resulting in a lower ATP yield.

Expression of these alternative ETCs is tightly controlled by a number of regulatory proteins, such as ArcAB (aerobic respiration control) and FNR (fumarate and nitrate reduction), which prevent the expression of anaerobic enzymes in the presence of O_2 and stimulate their expression in its absence [47]. Aerobically, *E. coli* constitutively expresses a number of isoenzymes of the anaerobic reductases to take advantage of changes in environmental and nutritional changes, particularly for the transition to anaerobic conditions when O_2 is limited. However, these isoenzymes operate at much lower levels than their anaerobic counterparts. The quinone and quinol used also varies depending on the ETC, under micro-aerobic and anaerobic conditions menaquinone and demethylmenaquinone are used as electron carriers [47].

1.2.4 Anaerobic Fermentation

In the absence of terminal electron acceptors, *E. coli* adopts a mixed-acid fermentation due to insufficient oxidising power, as shown in Figure 1.16. Anaerobically, glucose is transported into the cell and catabolized to pyruvate the same way as in respiration. The metabolic modes then differ in how pyruvate is metabolised. In fermentation, NADH produced in glycolysis cannot be reoxidised by ETCs as in respiration and, furthermore, ATP cannot be synthesised by oxidative phosphorylation, but only by substrate-level phosphorylation. The major metabolic challenge for fermentative growth is the regeneration of NAD^+ to maintain redox balance by converting pyruvate to fermentation products, such as acetate, ethanol, formate, lactate and succinate, as well as CO_2 and H_2 gases, while also synthesising ATP [48].

Aerobically, the PDH complex produces acetyl-CoA, CO_2 and NAD^+, but anaerobically the complex is largely repressed in order to decrease NADH production and avoid the necessity of reoxidising it. Anaerobically, pyruvate is lysed to give acetyl-CoA and formate by pyruvate formate lyase (PFL). Alternatively, pyruvate metabolism can be bypassed by converting three-carbon PEP to four-carbon oxaloacetate by the incorporation of CO_2. Aerobically, the TCA cycle is the greatest source of NADH, but during fermentative growth the cycle becomes branched and incomplete. From oxaloacetate, a reducing branch runs to succinate while an oxidising branch runs to 2-oxoglutarate, which releases CO_2, in order to generate necessary precursor molecules for biosynthesis [48]. Around 10 % of the carbon source is assimilated during fermentative growth, hence, CO_2 release by isocitrate dehydrogenase is a relatively minor source of CO_2 when compared with FHL activity.

The metabolic reprogramming of the TCA cycle is achieved by repressing the 2-oxoglutarate dehydrogenase complex (containing sub-units SucA and SucD) and replacing succinate dehydrogenase (SDH) with fumarate reductase (Frd). Fumarate reduction couples to NADH-dehydrogenase I which can generate a H^+ gradient, as in fumarate respiration. However, despite offering some energy conservation, only minor amounts of succinate are produced by wild-type *E. coli* during fermentative growth on glucose [48, 49]. This is partly because of how the PEP to oxaloacetate step wastes a high-energy phosphate group which could be used to synthesise ATP if PEP is converted to pyruvate instead. Isocitrate can be converted to succinate and glyoxylate (which reacts with acetyl-CoA to form malate) *via* the glyoxylate shunt [48]. However, this pathway is repressed by sugars and only functions during aerobic growth on acetate or fatty acids that can only enter the TCA cycle by acetyl-CoA.

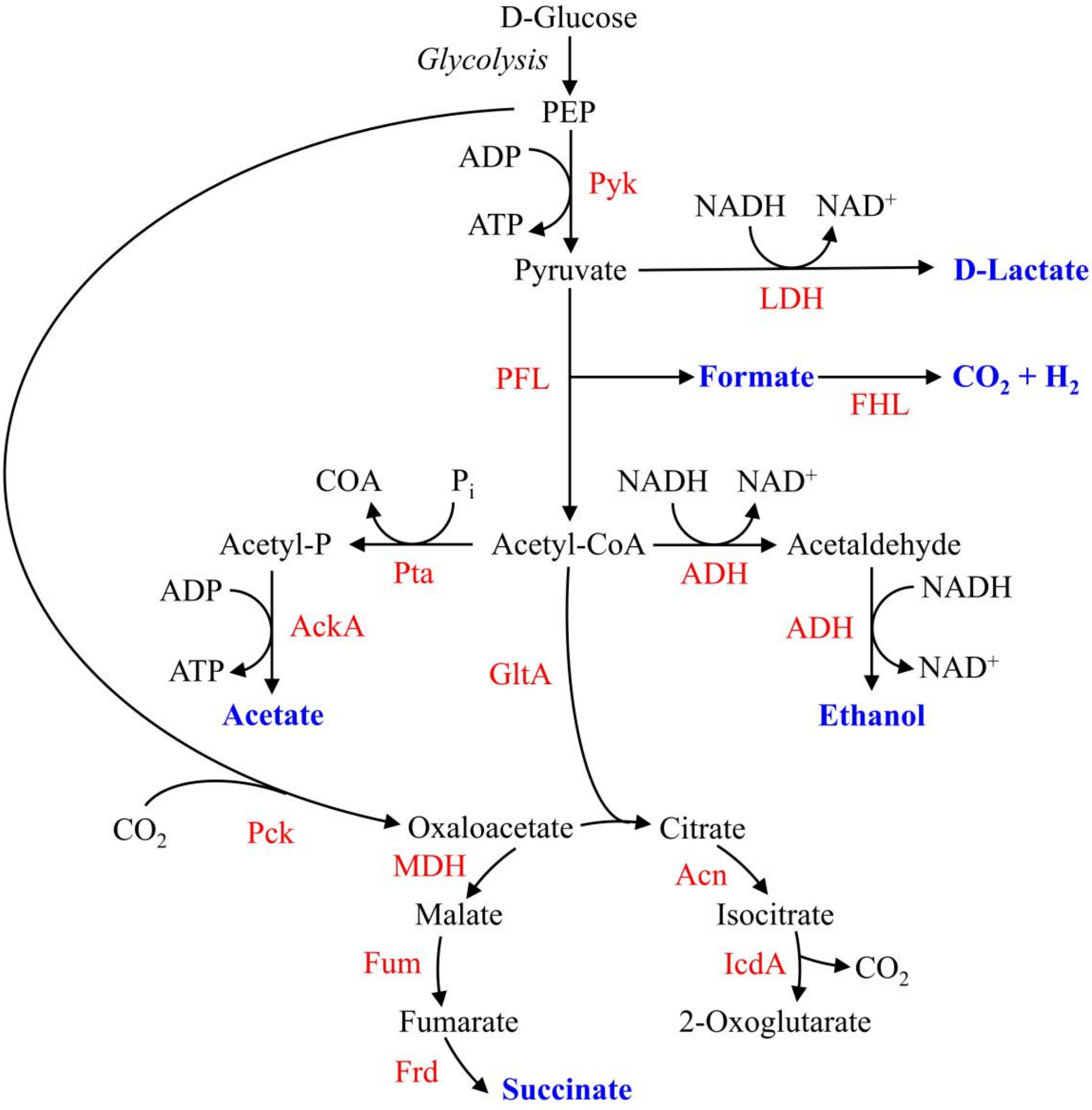

Figure 1.16 – Mixed-acid fermentation pathways with key products shown in blue. Enzymes: **AckA**, acetate kinase; **Acn**, aconitase; **ADH**, alcohol dehydrogenase; **FHL**, formate hydrogenlyase; **Frd**, fumarate reductase; **Fum**, fumarase; **GltA**, citrate synthase; **IcdA**, isocitrate dehydrogenase; **LDH**, lactate dehydrogenase; **MDH**, malate dehydrogenase; **Pck**, PEP carboxykinase; **PFL**, pyruvate formate lyase; **Pta**, phosphate acetyltransferase; **Pyk**, pyruvate kinase.

As well as entering the TCA cycle, acetyl-CoA can be either converted to acetate or ethanol in order to generate one ATP or two NAD^+, respectively, with the ratio of acetate to ethanol produced generally determined by the redox balance. During conditions of excess pyruvate accumulation or low pH, pyruvate may be converted to optically pure D-lactate while reoxidising NADH by lactate dehydrogenase (LDH). As the fermentation products are excreted to prevent cytoplasmic toxification, the pH drops over time which can lead to increased lactate production in the later stages of a closed batch fermentation. The net yield of ATP per glucose molecule for fermentative growth is two ATP from glycolysis and, on average, one additional ATP from the acetate producing pathway.

Formate is most-likely constantly excreted from the cell in the early stages of fermentation as the PFL enzyme is physically associated with the formate channel FocA at the cytoplasmic side of plasma membrane [50]. In a closed batch fermentation, the formate ($pK_a = 3.7$) will accumulate outside the cell and contribute to the pH becoming more acidic. At around pH 6.8, the FocA channel is thought to switch from a facilitator of excretion to a facilitator for import, and the previously externalised formate is then reimported to the cell. This triggers the transcription of a number of genes involved in formate and pH homeostasis, including those encoding the FHL complex [51, 52].

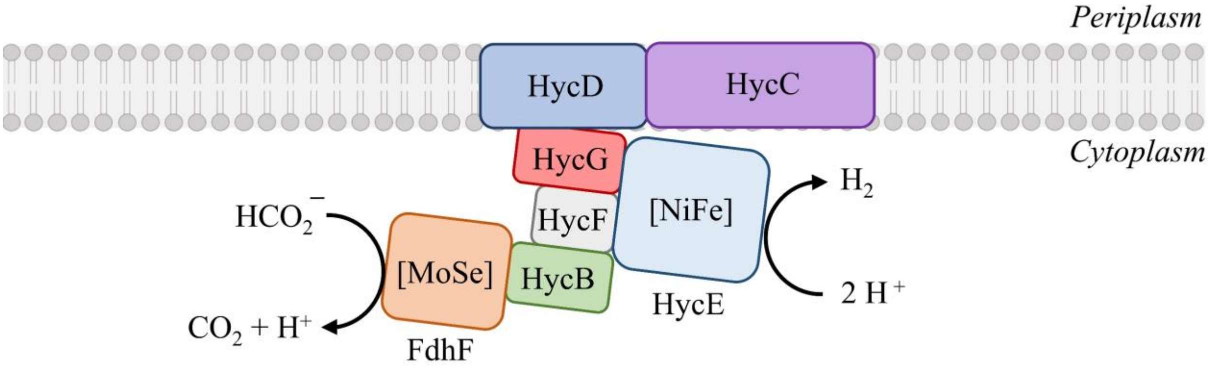

Figure 1.17 – Predicted structure of the *E. coli* formate hydrogenlyase (FHL) complex.

FHL is a membrane-bound enzyme made up of seven individual protein subunits [53]. It consists of a membrane arm, comprising two integral membrane proteins, and a peripheral (or catalytic) arm located at the cytoplasmic side of the membrane, comprising formate dehydrogenase-H (FDH-H) and hydrogenase-3 (Hyd-3), as shown in Figure 1.17. FDH-H is encoded by the *fdhF* gene and is a molybdenum- and selenium-dependent formate dehydrogenase [54]. Hyd-3 is a [NiFe] hydrogenase enzyme and is predicted to be the principal point of contact of the catalytic arm with the membrane arm [53, 55]. During fermentative growth, FHL works as a closed redox complex where FDH-H first oxidises formate to CO_2 and then passes two electrons directly, *via* [4Fe-4S] clusters, to the Hyd-3 active site where two H^+ are reduced to H_2 which can then diffuse away from the cell. Overall, therefore, FHL carries out the disproportionation of formate to H_2 and CO_2.

Under certain conditions, it is possible for both aerobic and anaerobic pathways to be active. Limited O_2 availability leads to micro-aerobic conditions, an intermediate range where both fermentative and respiratory enzymes are expressed in cell cultures. As O_2 is relatively insoluble, in a micro-aerobic environment it is consumed by the cells as fast as it is supplied by gas transfer and, thus, the dissolved O_2 concentration is close to zero [56]. If O_2 demand exceeds availability, the cells are subjected to stress by O_2 limitation leading to the activation of fermentative pathways. The accumulation of fermentation products results in less carbon available for biomass formation and inhibited cell growth by the acidification of the growth medium. Designing bioreactors for industrial-scale aerobic bioprocesses is a challenging engineering task with O_2 transfer typically being the rate-limiting step. Typically, air is sparged under high pressure from the bottom of a stirred tank bioreactor to maximise the yield of desired products and minimise acidic waste. Huge air compressors need to be deployed to meet O_2 requirements which have a high operating cost forming the major economic limitation of many industrial aerobic bioprocess, such as biological wastewater treatment [57].

Anaerobic pathways can be active even in aerobic environments. Overflow metabolism is a growth rate dependent phenomenon which occurs for aerobic and fast growing *E. coli* in concentrated glucose environments. The rapidly growing cells switch from exclusively using ATP-efficient aerobic respiration pathways to obtaining some energy by also using ATP-inefficient fermentative pathways to produce acetate. The Pta-AckA pathway is responsible for the majority of aerobic acetate production, as strains with this pathway deleted show up to an 80 % decrease in acetate excretion. Due to the diversity of experimental conditions and strains used in published studies, several mechanisms have been proposed to explain why *E. coli* shifts its metabolism to yield less ATP and produce this acidic waste product that is detrimental towards cell growth. As the Pta and AckA enzymes have a lower biosynthesis cost than to synthesise the ETC enzymes, some think that *E. coli* prefers this fermentation pathway during rapid growth to maintain the balance between the fluxes of glucose uptake, energy production and biosynthesis [58]. Other explanations hypothesise that the acetate pathway is needed during rapid growth due to the need to replenish CoA [59] or because of saturation of the enzymes in the ETC [60] and TCA cycle [61].

1.3 Overview of Bioreactor Sensors

1.3.1 Mass Spectrometry, Chromatography and Invasive Probes

The monitoring of bioreactors is essential for determining how bioprocesses develop and how to run the reactor most efficiently. Sensors can be used to directly measure metabolites (*e.g.* mixed-acid fermentation intermediates and end-products), detect changes in substrate (*e.g.* glucose) or measure metabolism indirectly through cellular respiration by monitoring changes in gas composition (*e.g.* O_2 and CO_2). Bioreactor automation is made possible when sensor measurements can trigger a response to when nutrients or other variables becoming growth-limiting. Broadly speaking, sensors are required to continuously measure three main types of variables in order to determine optimum feeding strategies, process conditions and scale-up procedures [62]:

- physical variables such as temperature, foam level, viscosity, pressure and stir speed.
- biological variables such as cell count, product concentration and cell morphology.
- chemical variables such as dissolved O_2 and CO_2, nutrient concentration and pH.

Sensors vary in application depending on how they are connected to the bioprocess. If a sensor is connected near to the bioreactor but requires manual or automated sampling, then it is an at-line sensor. If a sample is required to be removed from the system for laboratory analysis, after appropriate pre-treatments (*e.g.* dilution, filtration or digestion), then it is an off-line sensor. Finally, if a sensor provides continuous data analysis of a sensed variable in real-time or more frequently than it can change in the bioprocess, then it is an on-line sensor [62]. For on-line measurements, *in situ* configurations are the most common which require no sampling and, instead, a sensor is either directly inserted into the bioreactor (invasive) or separated from it by a glass wall (non-invasive) [63].

The gas composition is frequently monitored on-line in bioreactors, with O_2 and CO_2 being two key gases to consider [64]. O_2 availability is a key parameter for aerobic bioprocesses as well as anaerobic systems that are sensitive to distribution by O_2, such as biohydrogen production. CO_2 is a key byproduct of many metabolic modes and can be monitored to closely follow many bioprocesses. Mass spectrometry (MS) is readily applied for gas-phase sample analysis from bioreactor exhaust gas, including O_2 and CO_2 [65]. MS requires that the sample is introduced into a high vacuum (below 10^{-5} mbar) through a thermospray, electrospray or direct liquid inlet. The samples are consequently ionised through electron impact, chemical ionisation or desorption ionisation in order to measure the mass-to-charge ratio (m/z) of the ions produced. However, MS cannot always be used to examine a number of substances simultaneously without additional separation techniques such as gas chromatography (GC) or liquid chromatography (LC). This is because mass spectra can be complicated and examination of several compounds simultaneously can lead to significant overlap preventing quantitation of the individual species [66]. For instance, CO_2 is measured at m/z = 44 and can face interference from N_2O (formed by many denitrifiers) or from volatile fatty acids which may break down to CO_2 within the mass spectrometer [66]. Analysing dissolved gasses or volatile products, such as ethanol [67], can be achieved by membrane inlet mass spectrometry (MIMS) to analyse liquid-phase samples. MIMS allows analytes to be transferred from a complex aqueous sample to the ion source of a mass spectrometer *via* a semi-permeable membrane. Although MS is a powerful analytical tool given its high specificity, selectivity, sensitivity, dynamic range, resolution, mass accuracy and capable of on-line data analysis in specialised configurations [68], the technique is prohibitively expensive for routine use on single fermenters at the laboratory scale. Mass spectrometers are also highly power consuming, large, require users to have extensive training and are difficult to calibrate for quantitative analysis in practice.

The separation-based chromatographic techniques of GC and LC are well-established for analysing complex mixtures of substrates, intermediates and products. However, they normally require extended times for sample analysis as the analytes migrate out of the column and, therefore, do not enable real-time knowledge of the conditions affecting bioprocess performance [66]. The major challenge for on-line GC methods is the one or more sample preparation steps required. During anaerobic digestion, fermentative bacteria convert soluble organic compounds to intermediate short-chain volatile fatty acids (as well as ethanol) which are then further metabolised to biogas (CO_2 and CH_4) by syntrophic acetogens and methanogenic bacteria. However, toxic disturbances can lead to an imbalance in the acid production and consumption, preventing the bioprocess from running efficiently. Hence, concentrations of ethanol and the intermediate acids must be monitored, but GC analysis requires a time-consuming sample pre-treatment step with distillation, preventing on-line analysis [69]. A more rapid, on-line GC analysis can be achieved by using a direct injection method. However, the lack of pre-treatment can result in peak tailing and ghosting due to contamination of the GC column [70].

LC has been used to monitor countless bioprocesses, some examples include sugar consumption and organic acid production during bacterial fermentation [71], anaerobic degradation of wastewater from baker's yeast production [72] and the degradation of azo dyes from the wastewater of the textile industry [73]. Further analytical capabilities are unlocked by using a mass spectrometer as a detector for liquid chromatography (LC-MS). MS can distinguish between different isotopes (*e.g.* ^{12}C and ^{13}C) as they have different m/z. Isotopomers are versions of the same compound that differ in the distribution of isotopes of each element (*e.g.* $^{12}CO_2$ and $^{13}CO_2$). LC-MS can be used to quantify numerous bacterial metabolites and map metabolic pathways when a ^{13}C-labelled growth substrate is used (*e.g.* $^{13}C_6H_{12}O_6$) [74]. However, MS cannot distinguish between positional isotopomers (*e.g.* $^{14}N^{15}NO$ and $^{15}N^{14}NO$, as discussed in Section 4.3.1) as they have the same m/z. For this reason, nuclear magnetic resonance (NMR) spectroscopy has been used a complimentary biophysical technique with MS for studying metabolic pathways, as NMR is capable of distinguishing positional isotopomers [75].

Maintaining sterile working conditions is essential when continually sampling for techniques such as MS, GC and LC. Likewise, sterility must be considered when working with invasive probes that come into direct contact with the bioprocess inside the bioreactor, in order to give real-time data analysis. Invasive probes must be able to withstand steam sterilisation which can be an issue for probes with utilise biological components, such as enzymes or antibodies, as the proteins may not withstand the heat and pressure. Despite this, some autoclavable probes have been developed for glucose measurements using an immobilised glucose oxidase enzyme [76], as well as similar specific probes for fructose, glycerol and ethanol sensing [77]. Even though most enzyme probes do not withstand autoclavation, they benefit from their specificity enabling measurements from cell-containing samples.

Invasive probes are mainly based on electrical or optical measurement principles as these probes are autoclavable or can be sterilised by γ-radiation, as is common in the commercial construction of single-use bioreactors [78]. The standard electrochemical sensors routinely used in bioprocessing are pH and dissolved O_2 and CO_2 probes [62]. pH probes are typically classical potentiometric glass electrodes which are reliable and robust. For dissolved O_2, Clark electrodes are the standard which are amperometric in nature. However, Clark electrodes consume O_2 during the measurement which limits the utility of such probes in aerobic bioprocesses where O_2 must not be depleted, especially in smaller bioreactors. Optical probes for O_2 can also be employed based upon the principle of fluorescence quenching by O_2. Dissolved CO_2 can be measured electrochemically by using Severinghaus electrodes or optically based on the absorption of 4.26 μm light, a wavelength not prone to cross-correlations by other common gases or by water vapour. Invasive sensors often have a limited lifespan under bioreactor operating conditions as a result of poisoning. Furthermore, sensors have problems with long-term stability and can suffer inferences from other species.

Cheap optical probes are commonly used to measure the optical density (OD) of microbial cultures by analysing one wavelength (typically 600 – 650 nm), usually at 1 cm pathlength. OD measurements are logarithmic functions that rely on the principle that transmitted light is lost by scattering from cell culture *i.e.* $\log(I_0/I)$, hence, they are an indirect measure of cell density. Time-dependent OD measurements can also track changes in bacterial growth phases, such as lag, exponential, stationary or death phases. The major disadvantage of OD measurements is that they suffer from interferences as they cannot distinguish between living cells, dead cells, debris, precipitates, small air bubbles and culture colouration. However, as a low-cost estimate of cell density, OD measurements remain a useful parameter that can complement other analytical techniques, as will be demonstrated in this thesis.

1.3.2 Spectroscopic Sensors

Invasive and non-invasive spectroscopic sensors (*e.g*. UV-Vis, IR and Raman) are commonly used for bioreactor analysis. Non-invasive spectroscopic sensors are possible as electromagnetic radiation can interact with a bioprocess through a glass wall.

UV-Vis spectroscopy employs light in the range of 200 – 780 nm [62]. The absorbance of UV/Vis light, as described by the Beer-Lambert law, is restricted to molecular functional groups, known as chromophores, whose electrons are excited. Within this range, peptide bonds and a few amino acid residues are capable of photon absorption. However, high-energy molecules, such as saturated hydrocarbons and sugars, cannot be detected through UV-Vis spectroscopy. In the mid-UV (200 – 300 nm), differentiation and quantification of proteins is possible, but difficult and requires purification procedures [79]. However, this range offers an advantage in that there is low interference from water peaks. UV-Vis spectroscopy suffers from the fact that electronic transitions tend to be very broad and often featureless, this gives limited selectivity and makes multi-component analysis very difficult.

Also within the UV-Vis range, fluorescence spectroscopy can be used to monitor biological components with fluorescent properties such as amino acids, enzymes, cofactors and vitamins [80]. However, several secondary effects disturb fluorescence analyses such as inner filter effects that occur when non-fluorescent compounds absorb the exciting radiation, cascade effects that occur when the emission of a fluorophore excites another and quenching effects that cause a decrease in fluorescent intensity [80].

Typically, for bioreactor analysis, IR-based spectroscopic sensors will utilise either the mid-IR (MIR, 400 – 4000 cm^{-1}) or near-IR (NIR, 4000 – 12500 cm^{-1}) spectral regions. MIR is generally more sensitive when compared to NIR, however, NIR sensors are known to be more stable against interference and cheaper to implement [62]. Most excitations of fundamental molecular vibrations exist within the MIR range while vibration combinations and overtones exist within the NIR region. Fundamental transitions in the MIR are often characteristic and resolved, serving as a molecular fingerprint which is highly selective and very useful for multi-component analysis. Due to the higher energy of the NIR region when compared to the MIR, the spectra are less defined and spectrometers with high signal-to-noise ratios are required. In comparison, MIR spectroscopy has a higher absorption capacity and better-defined peaks. The greater resolution of MIR spectroscopy allows it to be employed for detecting components in aqueous solutions at low concentrations, such as glucose, acetate, lactate, ethanol and ammonium [81, 82]. As NIR spectra are much less defined, this region is used for more qualitative monitoring of variables such as glucose, lactate, ammonium and biomass [83]. Although MIR has a higher accuracy when quantifying single analytes, NIR has advantages when monitoring multiple analytes due to spectral bands typically having lower intensities and being more widely spaced, leading to less overlapping features and interferences. Furthermore, due to the low penetration depth in MIR spectroscopy, total cell concentration cannot be measured directly while NIR can employ light-scattering effects to measure cell density and cellular viability [62]. Due to the complexity of spectral data gathered through MIR and NIR spectroscopies, multivariate analyses are often employed [62]. For qualitative variance analysis, principle component analysis is sometimes employed. Alternatively, quantitative analysis requires a reference dataset to calibrate a model spectrum that can be used for determining analyte concentrations in recorded spectra. IR reference spectra can be found in databases such as HITRAN [8] or the Pacific Northwest National Laboratory (PNNL) [84].

Fourier-transform infrared (FTIR) spectroscopy is a non-dispersive technique widely used for its ability to record high-resolution spectral data over a wide spectral range, typically covering the MIR and extending into the NIR. FTIR techniques combined with attenuated total reflection (ATR) cells have been used for on-line monitoring of numerous components in aqueous solutions [81, 82]. FTIR spectrometers do not use a dispersive element (a grating or prism) which can only measure a narrow range of wavelengths at a time with a lower light throughput due to the inclusion of a slit. Instead, FTIR spectroscopy relies upon the constructive and destructive interference of IR radiation (provided by a globar blackbody source) inside a Michelson interferometer. The interferometer uses an IR-transparent salt beam splitter (*e.g*. KBr) and a pair of retroreflecting mirror cubes which are operated to split and then recombine the IR beam. The outgoing beam can then be used for IR measurements by passing it through a sample. During a measurement, one of the retroreflecting mirror cubes is moved backwards and forwards so that the pathlength difference travelled by the two split beams is varied over time. Depending on the mirror displacement, at the beam splitter certain wavelengths will constructively interfere while others will destructively interfere. Hence, only wavelengths which are in phase when recombined at the beam splitter will pass on through to the sample. The raw FTIR data is recorded as an interferogram which is a plot of intensity against mirror displacement. A Fourier transformation of the interferogram is used to recover a spectrum of intensity as a function of wavenumber. High wavenumber accuracy is achieved using a reference laser source that also passes through the interferometer with a well-defined emission wavelength, such as a 632.8 nm HeNe laser. The FTIR spectral resolution improves with increasing maximum mirror displacement. Effectively, the reciprocal of mirror displacement (cm) gives spectral resolution (cm^{-1}). An outline of a typical FTIR spectrometer is shown in Figure 1.18.

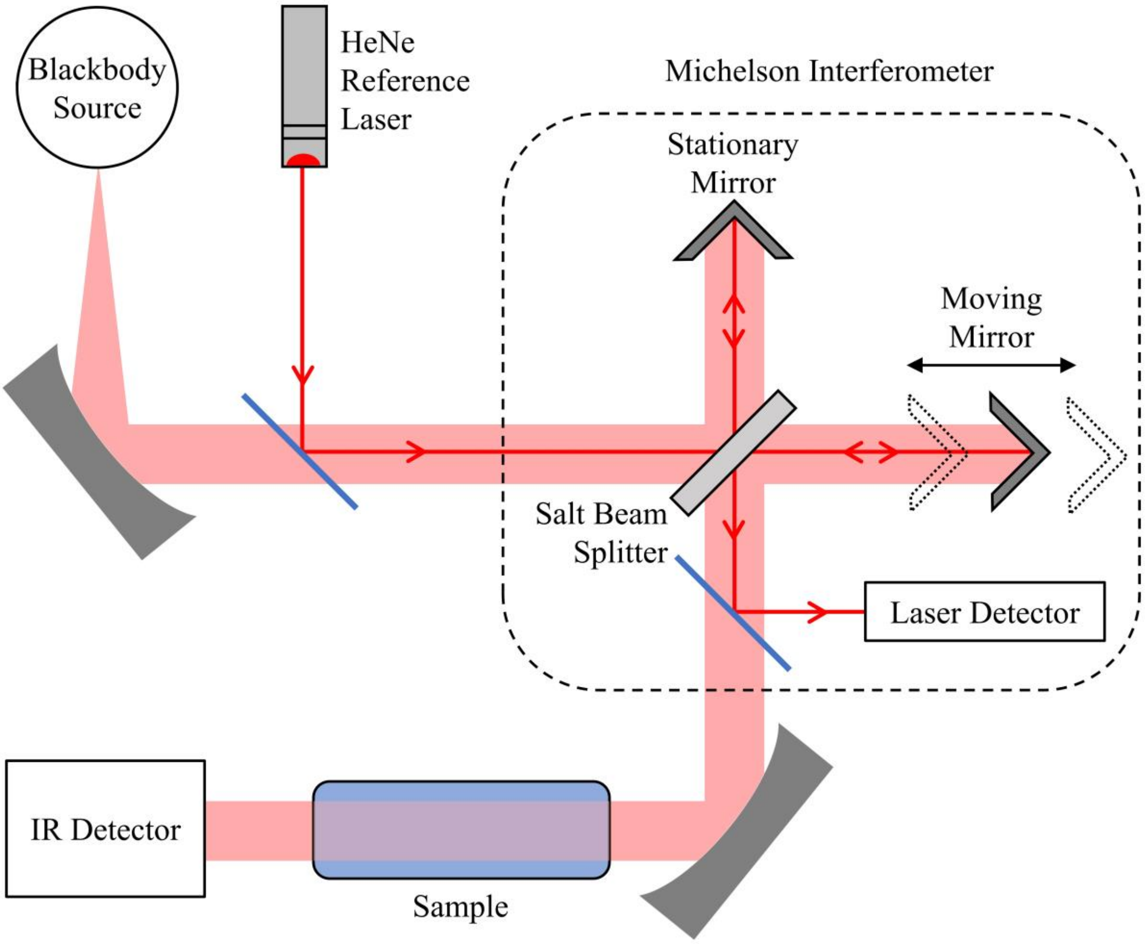

Figure 1.18 – A typical FTIR spectrometer.

On-line analysis of headspace gases by FTIR spectroscopy is an attractive alternative to the slower and more expensive techniques of GC and MS. A comparison of FTIR spectroscopy and GC-MS for analysing biogas found that FTIR was better suited for rapid determination of the composition of CO_2 and CH_4 [85]. However, GC-MS was better suited for trace analysis of the mixture of alcohols, carboxylic acids and esters also produced, as they were generated at concentrations below the 10 – 100 ppm detection limit of the FTIR spectrometer used. Also, as a rule, IR spectroscopy works best for small molecules with well defined, characteristic vibrations, whereas large molecules often have extended, overlapping vibrational bands that are difficult to analyse and quantify. The study concluded that the combination of the two techniques provided more information than any single of them would be able to. As FTIR spectroscopy follows the Beer-Lambert law as a direct absorption technique, one method for increasing the sensitivity of absorption measurements is to increase the sample pathlength. Maintaining as low a sample volume as possible is desired in order to avoid dilution effects, hence, multiple pass cells which use two or more mirrors to reflect the IR beam back and forth through the sample are the preferred means of improving sensitivity. The White cell is the most used multi-pass design in FTIR spectroscopy and is discussed in more detail in Chapter 3.

Due to being governed by different vibrational selection rules, Raman spectroscopy complements FTIR analysis. Unlike IR spectroscopy, Raman spectra are less sensitive to water which is a significant advantage for cell culture monitoring of variables such as glucose, glutamine, glutamate, lactate, ammonia and viable cell density [86]. Raman spectroscopy is highly flexible and can be applied to a wide variety of samples from solids, liquids and gases to any combination thereof (slurries, gels, etc) without sample preparation. However, one major disadvantage of Raman spectroscopy is the potential fluorescence of biological molecules that makes selection of an appropriate laser wavelength a critical parameter to consider [63]. Near-IR Raman spectroscopy has been widely used for qualitative analysis of lipids and carbohydrates because it has the advantage of overcoming significant interference from fluorescence [87]. Furthermore, Raman signals tend to be weak due to the relative infrequency of inelastic scattering, so enhancement techniques are often required. As Raman signals scale with laser power (see Equation 1.2), the use of high-power lasers to generate enough Raman scattered photons for detection is one option. However, high-power lasers have limitations such as increasing the complexity and cost of Raman instruments, greater laser safety considerations must be made, not all wavelengths are available and high laser power can destroy delicate or dark samples [63].

One alternative method of enhancement is resonance Raman spectroscopy which uses excitation light that is close or coincident with the electronic transition energy of a molecule resulting in intense Raman scattering. Resonance Raman spectroscopy is highly selective and has been used to study biological components that absorb deep-UV radiation (200 – 280 nm) such as nucleic and amino acids [88]. As well as resonance enhancement, deep-UV Raman spectroscopy, with excitation wavelengths below 250 nm, eliminates fluorescence interference. This provides better spectral separation between Raman and fluorescence emission bands, resulting in high signal-to-noise ratios and low detection limits. However, the deep-UV lasers available for UV Raman spectroscopy are expensive, have poor portability and require special optics as well as sample degradation, which makes them currently inadequate for bioreactor monitoring [63].

Another technique used to enhance Raman signals is surface enhanced Raman spectroscopy (SERS). SERS uses metallic nanoparticles (typically Au or Ag) which generate a localized surface plasmon upon laser excitation. If a Raman-active molecule is in close contact with that surface plasmon, then the Raman signal is enhanced from an electromagnetic interaction. SERS is capable of nanoscale analysis with numerous applications such as in cell-ligand binding, single-cell dynamics, hyper-localised structure or intracellular studies [63]. However, SERS is not suitable for on-line measurements as it requires sample adsorption onto the surface of the metal nanoparticles. A further limitation of SERS is translating the powerful enhancement into a reliable and quantifiable measurement due to very pronounced non-linearity and saturation effects, with efforts being made to use internal standards to improve intra-laboratory comparison of SERS results [89].

Fiber-enhanced Raman spectroscopy (FERS) is a recently introduced approach for enhancing the Raman signal of gases. FERS involves the enhancement of the laser intensity and interaction length using hollow-core photonic crystal fibers (HC-PCFs). HC-PCFs do not rely on total internal reflection but on the photonic bandgap, meaning it is possible to use the hollow core as the analyte gas chamber [90]. Light and the analyte gas are coupled into the fiber, and due to multiple reflections inside the fiber (which can be several metres of interaction length), the interaction length is enhanced compared to the free space trajectory. Furthermore, as HC-PCFs are only micrometres in diameter, the laser power is focussed inside the hollow core, therefore resulting in an electrical field magnification which results in an enhanced Raman signal. Hanf *et al.* have demonstrated with their FERS set-up detection limits in the ppm range, with CH_4 having a limit of 0.2 ppm [91]. FERS has great potential for gas-sensing applications such as breath analysis, where the ability to detect H_2 and CH_4 could allow painless point-of-care diagnosis of malabsorption disorders [92]. However, one limitation of FERS is that it requires the sample gas to be pushed by high pressure into the fiber. Previous gas samples are also difficult to remove completely afterwards due to adsorption to the internal fiber walls.

From an experimental perspective, Raman spectrometers can be categorised as dispersive or Fourier Transform (FT-Raman). Dispersive instruments use a grating spectrograph to disperse the Raman signal so that separate Raman bands can be detected across the width of a multi-channel detected, such as a charge coupled device (CCD). CCD detectors are very sensitive, have low noise and enable simultaneous measurement at several wavelengths of a particular spectral region. Furthermore, they can be extremely light sensitive, especially if the detector is cooled to limit electrical noise and dark currents. However, CCD detectors are designed to detect visible light so the excitation wavelength typically must be in visible region which can lead to obscured Raman signals by fluorescence [63]. FT-Raman spectroscopy, like FTIR, utilises an interferometer that enables detection of all wavelengths simultaneously, substantially reducing the time needed to record a Raman spectrum. The excitation laser provides NIR radiation typically at (780 or 1064 nm) which greatly reduces signal intensity (see Equation 1.2) but avoids a significant fluorescent background [93].

1.3.3 Cavity-Enhanced Raman Spectroscopy

The detection of homonuclear diatomic gases (*e.g.* H_2, N_2 and O_2) is a challenge for bioreactor monitoring, as well as in other fields such as energy (*e.g.* hydrogen energy storage) and medicine (*e.g.* breath analysis and disease detection). Conventional methods such as MS and invasive probes have limitations that prevent real-time, non-invasive monitoring. Raman spectroscopy can detect homonuclear diatomic gases but is limited by extremely low scattering cross sections and concentrations in the gas-phase. Instead of using high-power lasers or FERS, cavity-enhanced Raman spectroscopy (CERS) is a method of increasing optical power while using cost-effective low-power lasers. See ref. [94] for a recent review of gas-sensing by CERS.

One of the first published uses of CERS was done in 1967 by Weber *et al*. [95]. The Raman signal was enhanced by placing a multiple-pass Raman tube and analyte gas inside a He-Ne laser cavity. The term ‘cavity-enhanced Raman spectroscopy’ was first mentioned in an article from 1995 [96]. However, this form of CERS would become known as cavity-enhanced droplet spectroscopy as it involves the use of water droplets as microcavities to enhance the Raman signal for analysis of aqueous species in the droplets themselves. Based on a Google Scholar search, 368 results can be found for ‘cavity-enhanced Raman spectroscopy’ between 1995 – 2022. Of the 368 results, 128 contain the phrase ‘gas analysis’ but were published between 2012 – 2022, while the other results for CERS are related to droplet and other spectroscopies. Gas-phase analysis by CERS became a growing topic of research in part due to the introduction of CERS using a Fabry-Pérot cavity and optical feedback cw diode lasers by the Hippler group in 2012 [97]. In 2015, Hippler applied his CERS set-up to the detection of natural gas mixtures, including species such as H_2, H_2S, N_2, CO_2 and alkanes [98]. Then, in

2017, CERS was applied by the Hippler group to monitoring the anaerobic fermentation of glucose and glycerol by batch cultures of *E. coli* [99]. Other groups have also used CERS over the last decade in a wide variety of gas-sensing applications such as the evolution of greenhouse gases from peat bog [100] the kinetics of photosynthetic $^{13}CO_2$ uptake and O_2 production by cuttings of *Populus trichocarpa* (black cottonwood tree) [101], the gas composition of soil samples [102] and biogas production [103].

Many different cavity-enhanced technologies have been developed for gas analysis including multiple-pass cavities, Fabry-Pérot cavities, laser cavities and microcavities. Non-resonant, multiple-pass cavities reflect the laser beam many times between cavity mirrors to give laser power enhancement by constructive interference. However, around 100 passes is the most reported for such arrangements [104]. The number of reflections can be significantly increased by using a Fabry-Pérot cavity which consists of two high-reflectivity but slightly transmissible mirrors (at least one is concave) placed in parallel [6]. This arrangement acts as a power build-up cavity due to both a longer interaction length from thousands of reflections as well as the optical resonator effect.

When low-power laser radiation is coupled inside an optical cavity, the light reflecting between the cavity mirrors will constructively and destructively interfere with itself, leading to the formation of standing waves (longitudinal modes) with a discrete set of wavelengths λ which must satisfy

$$n\,\frac{\lambda}{2} = L \tag{1.20}$$

where n is an integer and L is the cavity length. Only an integer number of half-wavelengths fit into the cavity and are reinforced by constructive interference [6]. All other wavelengths are supressed by destructive interference with themselves. The frequency of longitudinal modes $v = nc/2L$, as found by substituting the wave equation $\lambda v = c$ into Equation 1.20 and rearranging. Hence, longitudinal modes are equally spaced by $c/2L$.

Resonator modes may also be transverse which differ in both wavelength and the intensity pattern of the light from each other. In the simplest case of a two-mirror cavity containing only parabolic mirrors and optically homogeneous media, transverse resonator modes are Hermite-Gaussian modes [6]. At the minimum beam radius (the beam waist), the electric field distribution can be written as a product of two Gaussian functions and two Hermite polynomials with non-negative integers n and m corresponding to the x and y

directions. These modes are notated as TEM_{nm} and have n nodes in the horizontal direction and m nodes in the vertical direction. TEM_{00} represents fundamental modes which have a Gaussian beam profile, and all other modes are higher-order modes, as shown in Figure 1.19.

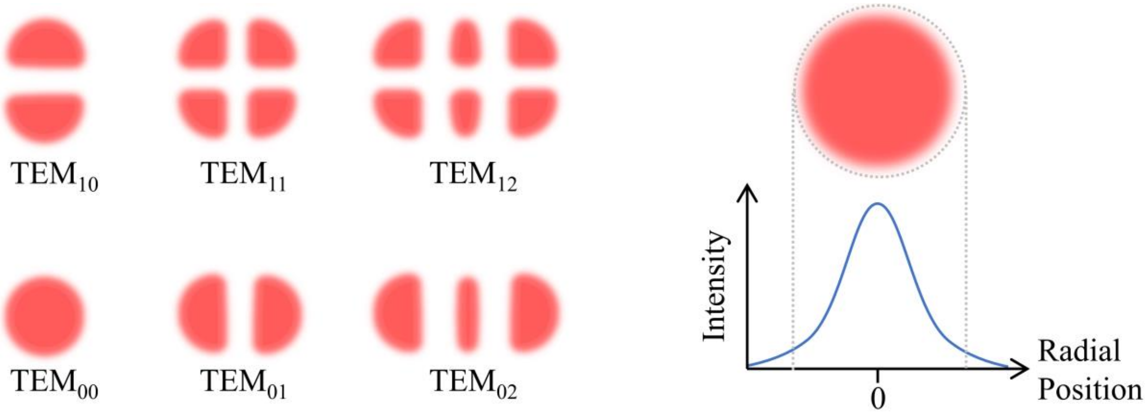

Figure 1.19 – Left, intensity distributions of TEM_{nm} modes. Right, the Gaussian intensity distribution of the fundamental TEM_{00} mode.

Only certain ranges of values for the cavity length L and the radii of curvature for the mirrors $r_{\mathrm{c},1}$ and $r_{\mathrm{c},2}$ will produce stable two-mirror resonators. A stability parameter g is defined for each mirror

$$g_1 = 1 - \frac{L}{r_{\mathrm{c},1}} \qquad g_2 = 1 - \frac{L}{r_{\mathrm{c},2}} \tag{1.21}$$

with the stability condition being $0 \leq g_1 g_2 \leq 1$, as displayed graphically by plotting g_2 against g_1 in Figure 1.20 with some common cavity arrangements shown [6]. The blue shaded area represents stable cavity configurations with cavities on the boundary $g_1 g_2 = 1$ being marginally stable, but small variations in L can cause the resonator to become unstable. Thus, resonators on the stability threshold *e.g.* concentric and plane-parallel, are operated just inside the stability line. The confocal cavity ($r_{\mathrm{c},1} = r_{\mathrm{c},2} = L$) is a favourable set-up as any small changes in L do force the cavity outside the stable region.

One variable to describe on optical cavity is the finesse $F = \Delta\lambda \,/\, \delta\lambda$ where $\Delta\lambda$ is the distance between two spectral maxima (longitudinal modes) and $\delta\lambda$ is the FWHM of a single maximum spectral line [6]. For high-reflectivities of the cavity mirrors and a small damping, the finesse can also be described through the reflectivity R by $F = \pi\sqrt{R}/1 - R$. The finesse itself is a quality indicator for an optical resonator: the higher the finesse, the higher the power build-up inside the resonator [6]. The enhancement factor β is calculated with the reflectivity by $\beta = 1 / 1 - R$. For instance, in 2010, the Hippler group measured the reflectivity of their optical cavity mirrors (Newport, Irvine, CA, $R \geq 99.99$ %, 1 m radius of curvature, 1 inch diameter) to be 99.988 %, close to the manufacturer's specification [105]. This gives an enhancement factor $\beta = 8333$ meaning that 1 mW of laser input power can give an 8.3 W optical power build-up inside the cavity. However, this value may not be reached in a real environment for reasons such as diffraction losses, mirror absorption losses and imperfect mode-matching.

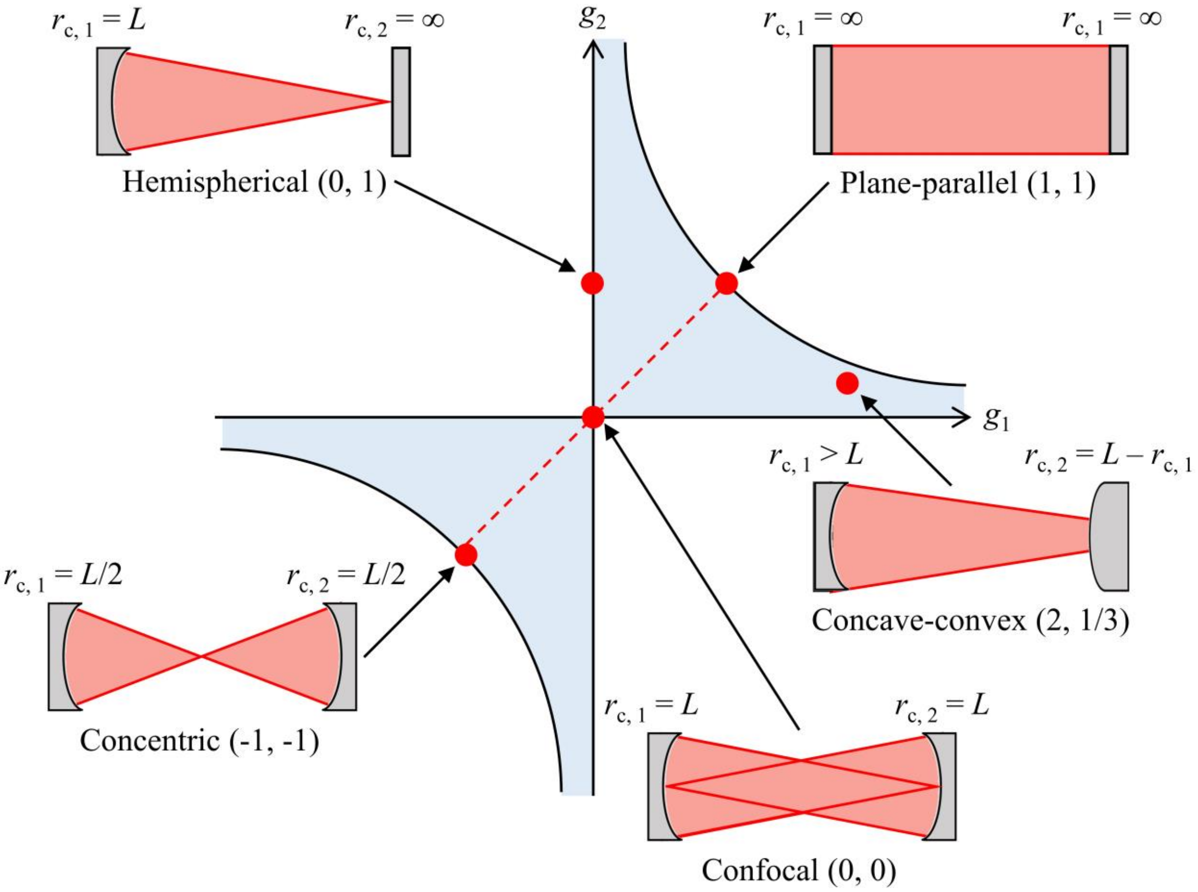

Figure 1.20 – Stability diagram for two-mirror optical resonators where the blue shaded area corresponds to stable configurations. Some commonly used cavity arrangements are shown.

The resonance condition for an optical cavity is challenging to maintain due to slight variations in the cavity length over time (*e.g.* by mechanical vibrations or temperature shifts). Accordingly, an appropriate frequency-locking method that maintains the resonance is necessary, such as Pound-Drever-Hall frequency-locking (PDHFL) or optical feedback frequency-locking (OFFL). Briefly, PDHFL involves the difference in frequency between the Raman excitation laser and the optical cavity being measured in real-time so that the laser frequency can be adjusted accordingly to any fluctuations in the resonance frequency [106]. However, the PDHFL method is expensive, requiring costly electronics. OFFL is a cheaper alternative as by making a slight compromise on performance, cheap, low-power diode lasers can be used as the light source. In brief, the principle of optical injection locking involves a single-mode master laser source (the Rayleigh scattered light leaving the optical cavity) that provides laser radiation and injects into another slave laser source (the Raman excitation laser) so that the frequency and phase characteristics of the master laser will be copied to the slave laser. In OFFL, the excitation laser, which can have a broader output spectrum, is coupled into an optical cavity. This cavity works as both a frequency standard, as well as a master laser, giving rise to a specific frequency. The output of the cavity is then coupled back to the excitation laser, which is forced to lase at the same wavelength, essentially locking the excitation laser to the optical cavity. There must not be a direct reflection from the first cavity mirror to the laser source, as this would disable OFFL by cavity light. This can be prevented using optical isolators, such as a Faraday isolator assembly, which are commonly used to prevent back-scattering into lasers. A summary of the OFFL method, as first demonstrated by the Hippler group [97], is shown in Figure 1.21.

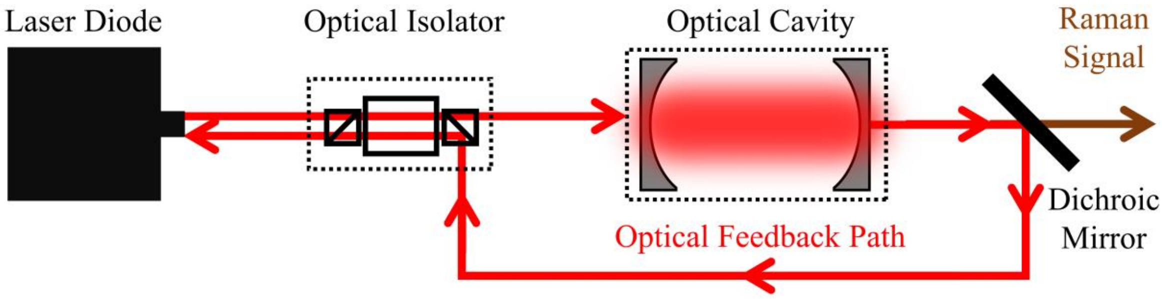

Figure 1.21 – Optical feedback frequency-locking. The emitted light out of the cavity is injected back into the excitation laser to enforce a resonant frequency.

Other techniques for gas-sensing that use resonant cavities include cavity ring-down spectroscopy (CRDS) and cavity-enhanced absorption spectroscopy (CEAS). CRDS was discovered serendipitously in 1980 by Herbelin *et al*. when testing how long a pulse of light could be stored within an optical cavity [107]. They found that the lifetime of the stored light varied depending on the concentrations of absorbing pollutants within the cavity. In 1988, the first spectroscopic measurements by CRDS were published involving the detection of an extremely weak magnetic dipole transition of O_2 [108]. CEAS is a more conventional approach of spectroscopic gas analysis as the intensity of light transmitted through the cavity during resonance is measured as a function of wavelength, as opposed to the decay time measured in CRDS [109].

1.4 Aims and Thesis Structure

Innovative new methods for analysing bioreactors are needed to provide further insight into how bioprocesses develop by monitoring variables not easily determined by more conventional techniques. The aim of the work described in this thesis is to develop and employ new and existing analytical gas- and liquid-phase spectroscopic techniques for use in analysing different metabolic processes using the model organism *E. coli*. The spectroscopic techniques used include cavity-enhanced Raman (CERS), photoacoustic detection in a differential Helmholtz resonator (DHR), White cell FTIR and liquid-phase Raman.

Chapter 2 compares the CERS and DHR techniques for monitoring glucose-lactose diauxie. As both gas-phase analytical techniques can distinguish $^{12}CO_2$ and $^{13}CO_2$, supplementing the bacterial growth medium with ^{13}C-glucose and unlabelled lactose allows a contactless, *in situ* approach for visualising the diauxic shift from glucose to lactose metabolism by the sequential production of the CO_2 isotopomers.

Chapter 3 introduces liquid-phase Raman and White cell FTIR spectroscopies for analysing anaerobic fermentation. Liquid-phase Raman monitors acetate, formate, glucose, HPO_4^{2-} and $H_2PO_4^-$ while gas-phase FTIR detects acetaldehyde, ethanol and CO_2. Spectral analysis and quantitative fitting procedures are discussed for all species, as well as the *in situ* pH determination of the bacterial culture *via* a modified Henderson-Hasselbalch equation using the phosphate buffer anion concentrations.

Chapter 4 combines the techniques of CERS, liquid-phase Raman and White cell FTIR for a ^{15}N-isotopic labelling study of nitrate and nitrite reduction by *E. coli* to the major and minor end-products of ammonium and nitrous oxide, respectively. Mechanistic insights are obtained through interpretation of the different $^{14}N/^{15}N$-isotopomers of nitrous oxide produced.

Chapter 5 revisits the fermentative pathways of *E. coli* in the absence and presence of O_2. Using the same experimental set-up as described in Chapter 4, new insights into the formate and H_2 physiology of *E. coli* are obtained. Evidence is found that formate hydrogenlyase (FHL) is part of a formic acid detoxification system involved in pH homeostasis as well as there being at least two separate routes, or mechanisms, for formic acid influx and efflux. Finally, there is evidence that FHL can be assembled and functional under micro-aerobic conditions, which could remove some barriers to biotechnological applications such as biohydrogen generation.

Chapter 2

A New Approach for a Classical *E. coli* Experiment: $^{13}CO_2$ Distinction of Glucose-Lactose Diauxie by Raman and Photoacoustic Spectroscopies

Abstract

Two powerful new techniques for headspace gas analysis above *E. coli* batch cultures by spectroscopy are introduced and compared: cavity-enhanced Raman Spectroscopy (CERS) and photoacoustic detection in a differential Helmholtz resonator (DHR). Both techniques are able to monitor O_2 and the $^{12}C/^{13}C$ isotopomers of CO_2 with excellent sensitivity and time-resolution in order to characterise distinct bacterial growth phases and metabolic activity. *In Situ* optical density (OD) measurements are recorded alongside CERS in order to complement and validate the growth phase distinction from the gas-phase data analysis.

The aerobic respiration of *E. coli* grown on glucose is measured in both LB and M9 media in order to compare respiratory quotients (RQs) between complex and minimal media, as well as to serve as a baseline for mixed sugar experiments. With the addition of fully substituted ^{13}C-labelled glucose ($^{13}C_6H_{12}O_6$) and unlabelled lactose to the growth medium, gas-phase analysis of CO_2 isotopomers by both spectroscopic techniques enables the distinction of glucose-lactose diauxie in real-time. Interestingly, under the growth conditions described in this chapter, the traditional Monod-style diauxic shift is not observed. Instead of a diauxic lag phase between $^{13}CO_2$ production from ^{13}C-glucose and $^{12}CO_2$ production from unlabelled lactose, there is a slight overlap between the two sugar metabolisms, albeit starting when $^{13}CO_2$ production is nearly finished.

CERS and DHR are shown to be cost-effective and highly selective analytical tools in the biosciences and in biotechnology, complementing and superseding existing conventional techniques. They also provide new capabilities for mechanistic investigations and show a great deal of promise for use in stable isotope bioassays.

The work presented in this chapter covers a scientific publication (ref. [110]);

Cavity-Enhanced Raman and Helmholtz Resonator Photoacoustic Spectroscopy to Monitor the Mixed Sugar Metabolism of E. coli
George D. Metcalfe, Saeed Alahmari, Thomas W. Smith and Michael Hippler (2019).
Analytical Chemistry. **91**, 13096-13104.
https://doi.org/10.1021/acs.analchem.9b03284

Author Statements

G. D. Metcalfe designed experiments, conducted the research, analysed data, prepared figures for publication and wrote the paper. S. Alahmari conducted the research, analysed data and wrote the paper. T. W. Smith conceived the project, designed experiments and wrote the paper. M. Hippler assembled the research team, designed the research, supervised the research, analysed data, prepared figures for publication and wrote the paper.

2.1 Introduction

Analysing metabolites is an essential task in microbiology; for example it allows the study of metabolic pathways, microbial activity, enzyme reaction mechanisms, interactions between organisms and is essential to the optimization of industrial processes in biotechnology. Cell growth and survival is determined by the availability of growth substrates and energy sources which can fluctuate greatly in nature, for instance in the soil and aquatic environments where *E. coli* can be found as well as in mammalian intestines [111]. Microorganisms adapt to environmental changes by tight regulation of their metabolic phenotypes by sensing the availability of certain nutrients, synthesising the necessary enzymes for their catabolism and repressing them after those metabolites are depleted [112].

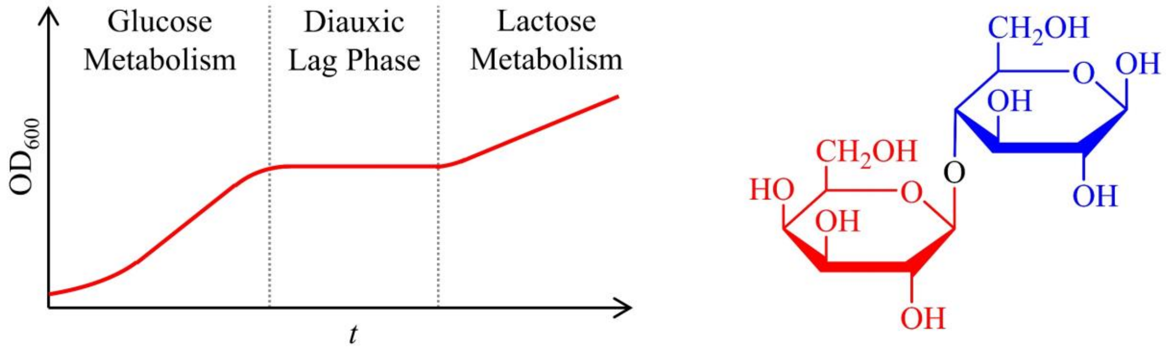

Figure 2.1 – Left, a typical bacterial growth curve for glucose-lactose diauxie. Right, the disaccharide lactose: glucose (blue) and galactose (red) joined by a glycosidic linkage.

A spectrum of different metabolic adaption strategies can be observed when growing bacterial cells in a mixture of growth substates including diauxic growth, simultaneous consumption and bistable growth [113]. Over eighty years ago, the classic example of diauxic growth was first described by Jacques Monod after presenting *E. coli* with a mixture of glucose and lactose [114]. Monod observed the biphasic exponential growth of *E. coli*, intermittent with a lag phase of minimal growth (which will be referred to as the ‘diauxic lag phase’), due to the sequential consumption of glucose followed by lactose, as shown in Figure 2.1. Glucose is the preferred carbon source for *E. coli* and many other organisms [115]. These microbes will typically feed on other sugars only when glucose is absent.

The regulatory mechanism by which the expression of genes required for the utilization of secondary carbon sources is prevented in the presence of a preferred substrate is known as carbon catabolite repression (CCR). CCR enables microbes to increase their fitness by optimizing growth rates in natural environments that provide complex mixtures of nutrients. On the other hand, in industrial processes such as biofuel production, CCR is one of the barriers to the increased yield of fermentation products [116]. During *E. coli* glucose-lactose diauxie, the presence of glucose represses the *lac* operon, a set of genes coding for *lac* permease and β-galactosidase which are required for lactose uptake and lactose hydrolysis to catabolizable glucose and galactose subunits, respectively.

Optical density (OD) measurements over time are convenient for monitoring diauxic growth and diauxic lag phases [114, 117]. However, the metabolism of mixed growth substrates does not always mirror the classical example of glucose-lactose diauxie in *E. coli*. The diauxic lag phase may be very brief, for instance some strains of budding yeast have little change in growth rates between sequential sugar consumption of glucose and galactose [118]. Furthermore, although glucose sits at the top of the sugar hierarchy for *E. coli* and is frequently consumed first, mixed non-glucose sugars may exhibit simultaneous metabolism instead of sequential [115]. OD measurements alone cannot provide sufficient information for mixed sugar metabolism; hence, the time-dependent concentrations of growth substrates and metabolites must be monitored. High-performance liquid chromatography is a commonly used method to determine changes in mixed sugar concentrations during microbial metabolism [119-121]. However, such analytical methods that require sampling are not ideal as they consume the analyte and require extra considerations to prevent contamination of the system.

The gas composition is another process parameter frequently monitored on-line in bioreactors. O_2 and CO_2 are two key gases to consider. O_2 availability is a key parameter for aerobic bioprocesses as well as anaerobic systems that are sensitive to distribution by O_2, such as the production of biohydrogen. CO_2 is a key byproduct of both aerobic respiration and fermentation and can be monitored to closely follow these processes. Dissolved gases can be monitored by gas-sensitive electrode-based sensors, some of which have the advantage of not consuming the analyte. However, most sensors are invasive because they must be submerged in the microbial culture and often have a limited lifespan under the operating conditions of the bioreactor as a result of poisoning. On-line, solution-based sensors create challenges such as the requirement for including an additional port on the bioreactor, an increased risk of contamination, and the challenges associated with sterilization and needing to frequently calibrate the sensor, which is often impossible without process contamination. Disadvantages also include interference with other components, aging, temperature dependence, long time stability, poisoning and long response and settlement times. The measurement of partial pressures in the effluent headspace gases can give a good approximation of dissolved gases *via* Henry's law and eliminates the need to use invasive devices. Gas chromatography (GC) and mass spectrometry (MS) are two common methods of gas-phase analysis. However, both techniques require sampling, are expensive, require frequent calibration, and have limitations, including difficulties detecting certain components. Also, chromatographic techniques rely upon the spatial separation of the compounds that are being quantified and so are only of use on a non-continual basis.

As an alternative to invasive sensors and sampling for GC-MS analysis, spectroscopic methods for gas-phase analysis offer numerous benefits including high precision and accuracy, no sampling necessary, and the ability to perform non-invasive real-time measurements. Detection in the near-IR has the advantage of low-cost light sources and detectors; the sensitivity, however, suffers from low absorption cross sections. In addition, relevant homonuclear molecules including O_2 cannot be observed by IR absorption because of unfavourable selection rules. Molecular O_2 has two main absorption bands in its UV-Vis spectrum: one deep in the UV at 145 nm and the other at 760 nm. O_2 detection at 145 nm faces interference by water vapor and CO_2, and the weak absorption lines at 760 nm typically provide detection limits that are of little practical use. Raman spectroscopy, in contrast, can detect homonuclear molecules, but it has very low sensitivity. Both near-IR absorption and Raman spectroscopy need special enhancement techniques to be useful in gas-phase analysis.

Recently, two new techniques were introduced for sensitive and selective trace gas detection: near-IR absorption enhanced by photoacoustic detection in a differential Helmholtz resonator (DHR) [122-125] and cavity-enhanced Raman spectroscopy (CERS) [97-99, 101, 126]. In this chapter, these techniques are used to study bacterial metabolism in order to compare their performance and suitability for applications in the biosciences and biotechnology. It will be demonstrated that both spectroscopic techniques can clearly and unambiguously distinguish all of the main phases of bacterial growth, can monitor the consumption of a mixed organic feedstock using ^{13}C-isotopic labelling of sugars, and can be employed to establish whether the various components are sequentially or simultaneously metabolized.

2.2 Experimental

2.2.1 Bacterial Growth Conditions

E. coli K-12 MG1655 was transferred from – 80 °C glycerol stocks, struck on LB-agar plates and incubated overnight at 37 °C. Starter cultures were prepared by inoculating 50 mL of LB medium (lysogeny broth; 10 g L^{-1} tryptone, 5 g L^{-1} yeast extract and 5 g L^{-1} NaCl) with a single colony from the plate and incubating for 5 h (37 °C, 200 rpm) in a sponge-capped tube. After 5 h, starter cultures would reach a typical OD$_{600}$ of 1.0 (optical density at 600 nm in a 1 cm cuvette). If allowed to grow overnight, starter cultures would peak at an OD$_{600}$ of 2.0; however, 5 h growth was selected as the lower bacterial density was desired to give a more pronounced lag phase after transferring to fresh medium. Ultimately, 1 mL of the starter culture was centrifuged, and the bacterial pellet resuspended into 20 mL of fresh LB or M9 media to be added to a further 230 mL when starting experiments. Depending on the experiment, the culture was supplemented with D-glucose and/or D-lactose. For isotope-labelling experiments, fully ^{13}C-substituted D-glucose was used ($^{13}C_6H_{12}O_6$, 99 %, Ck isotopes). M9 is a minimal growth medium with our formulation containing:

48 mM Na_2HPO_4
22 mM KH_2PO_4
18 mM NH_4Cl
8.5 mM NaCl
1 mM $MgSO_4$
1 mM thiamine
300 µM $CaCl_2$
135 µM Na_4EDTA
57 µM H_3BO_3
31 µM $FeCl_3$
6.2 µM $ZnCl_2$
4 µM biotin
2.7 µM $CoCl_2$
1.3 µM $MnCl_2$
0.2 µM $CuSO_4$

2.2.2 The Two Experimental Set-ups

Before starting each experiment, 230 mL of LB or M9 media was prepared in a 500 mL custom round-bottom flask with a side-arm. The flask was submerged and heated in a 37 °C water bath under rapid stirring for efficient gas transfer. The 20 mL of media containing *E. coli* from the starter culture was added before sealing the flask and analysing the gases in the closed system by either Raman (CERS) or laser diode photoacoustic (DHR) spectroscopy. Schemes of the two experimental set-ups are shown in Figure 2.2. In both set-ups, the neck of the flask was sealed by a stopper with two glass feedthroughs for cycling the headspace between the flask and the spectroscopic measurement cell using a peristaltic pump (**PP-G**, 4.5 L h^{-1}). The total headspace gas volume was 720 mL in the CERS set-up and 510 mL in the DHR set-up. In the DHR experiments, lower concentrations of glucose and lactose were used (10 mM instead of 20 mM as in the CERS experiments) due to the lower headspace volume of the DHR set-up.

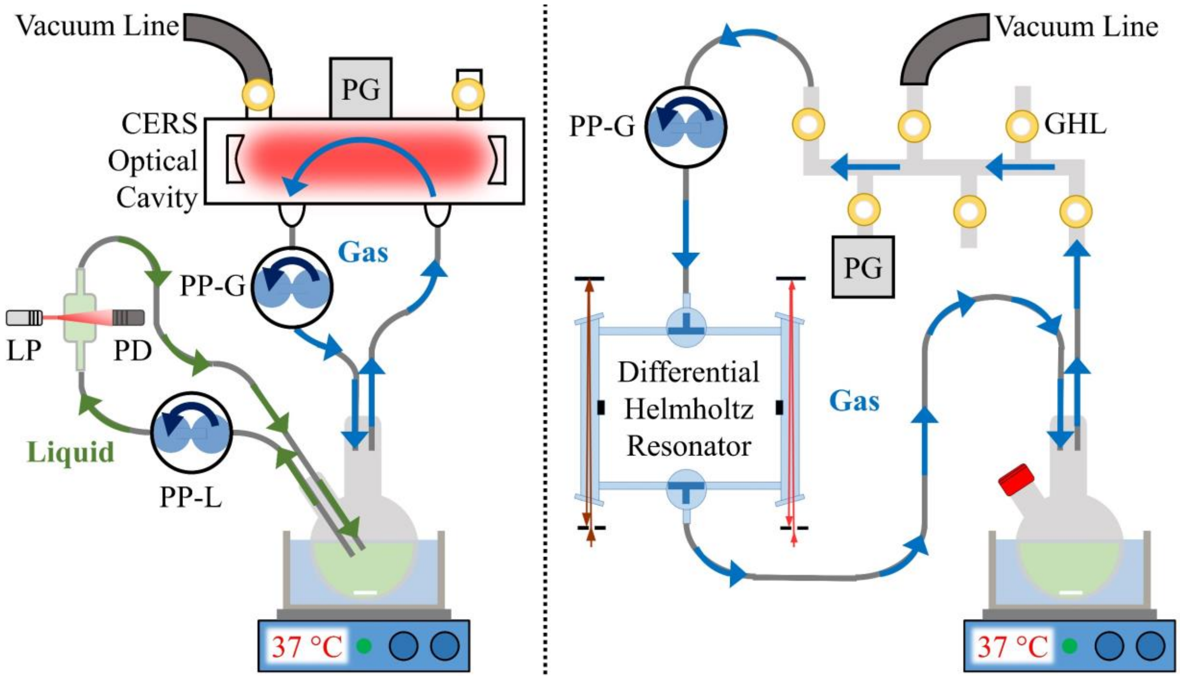

Figure 2.2 – The two experimental set-ups. CERS with *in situ* OD_{600} (left) and DHR (right). **GHL**, gas handling line; **LP**, laser pointer; **PD**, photodiode; **PG**, pressure gauge; **PP-G,** gas-phase peristaltic pump; **PP-L**, liquid-phase peristaltic pump.

The spectroscopic measurement cells and the gas transfer tubes were warmed to *ca.* 50 °C by heating wire to prevent water condensation on the internal optics. The appearance time of gases from the flask to either spectroscopic measurement cell was less than 5 min. Both set-ups included a 1000 mbar diaphragm pressure gauge (**PG**, Edwards model D35735000) for recording the total pressure inside each closed system. In the CERS set-up, the pressure gauge was attached to the custom glass enclosure of the CERS optical cavity. The enclosure also included two ports with Young valves, one was connected to a vacuum line while the other was used as an air inlet. Both ports were closed during experiments. The compact DHR had no extra ports so the headspace in this set-up was also cycled through a gas handling line (**GHL**) which served as an air inlet as well as for attaching the pressure gauge and vacuum line.

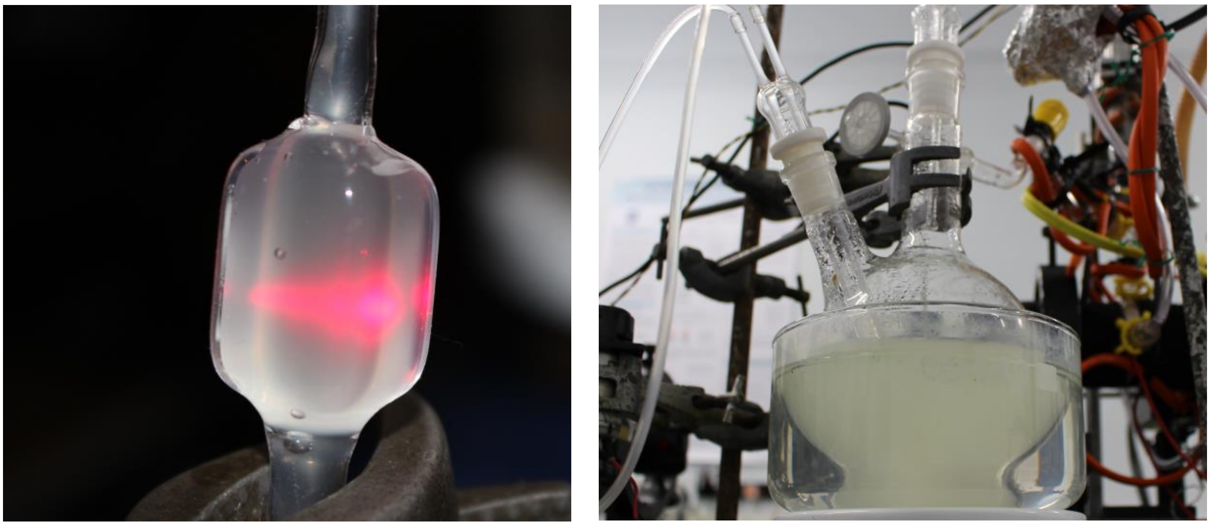

Figure 2.3 – Photographs of OD_{600} light scattering by the bacterial culture (left) and the custom round-bottom flask containing the bacterial culture (right).

The major difference between the two experimental set-ups, apart from the spectroscopic measurement cell employed, was that *in situ* OD_{600} measurements of the bacterial culture were recorded in the CERS set-up. The side-arm of the round-bottom flask was sealed by a custom glass stopper with two glass feedthroughs that reached into the bacterial culture. Using a second peristaltic pump (**PP-L**, 4.5 L h^{-1}) the bacterial culture was cycled between the flask and a sealed 1 cm glass cuvette. *In Situ* OD_{600} measurements were recorded from the scattering of red laser pointer light (**LP**, 1 mW, 650 nm) through the cuvette using a photodiode (**PD**). Photographs of the scattering of red light in the cuvette and the round-bottom flask in the CERS set-up are shown in Figure 2.3. The transmitted intensity was converted to OD_{600} by calibration using a UV-Vis spectrometer. As the bacterial culture was not cycled in the DHR set-up, the side-arm of the flask was sealed by a rubber septum.

At the start of experiments, the closed systems contained roughly 210 mbar O_2 (21 %) and 800 mbar N_2 (79 %) from lab air. Experiments lasted until either O_2 or the sugars were depleted resulting in no further O_2 consumption or CO_2 production being observed. Endpoint measurements of the pH and dry biomass were recorded for each experiment. The bacterial suspension was centrifuged at the end of each experiment and the pH of the supernatant was recorded using a Mettler Toledo SevenMulti pH meter (glass electrode with internal Ag/AgCl reference). Fresh LB and M9 media both had a pH around 6.8 – 7.0, while the endpoint value was between 4.5 – 5.0 due to organic acid excretion during bacterial growth. The dry biomass was typically around 60 mg and was measured by weighing the centrifuged cellular material after decanting off the supernatant and allowing the pellet to dry in a 37 °C oven.

2.2.3 Cavity-Enhanced Raman Spectroscopy

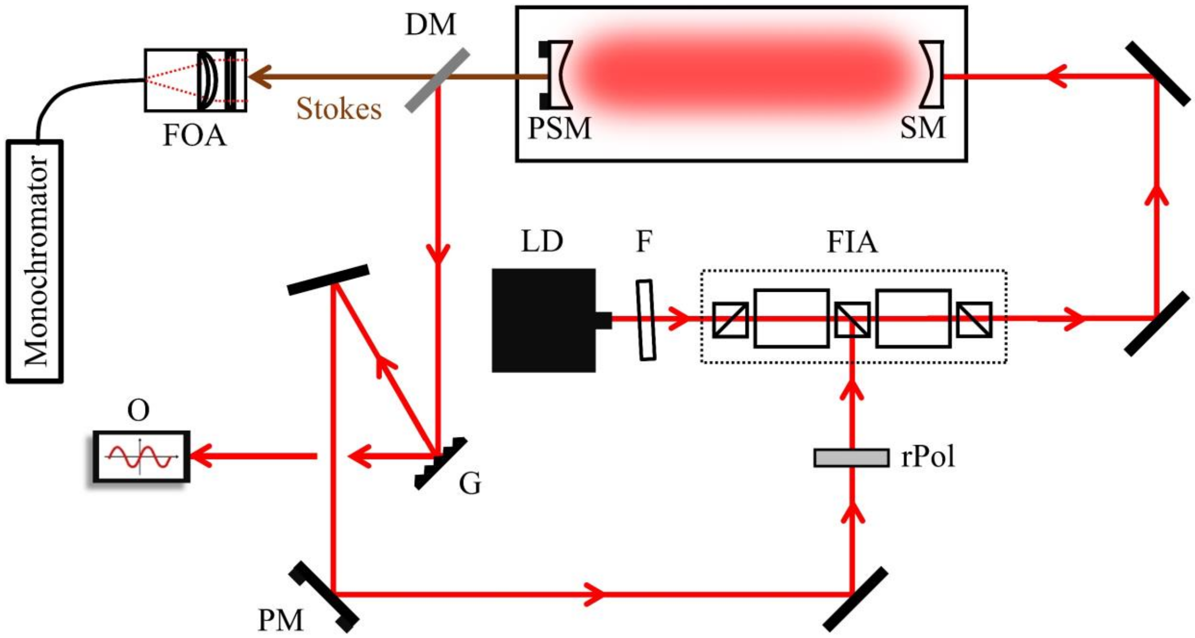

Figure 2.4 – CERS optical components. **DM**, dichroic mirror; **F**, filter; **FIA**, Faraday isolator assembly; **FOA**, fibre optical assembly; **G**, grating; **LD**, laser diode; **O**, oscilloscope; **PM**, mirror on a piezomount; **PSM**, supermirror on a piezomount; **rPol**, rotating polarizer; **SM**, supermirror.

The optical components used for headspace gas analysis by CERS are depicted in Figure 2.4. A single-mode continuous wave (cw) laser diode (**LD**, Opnext HL63133DG) was mounted on a temperature-stabilised thermoelectric cooler (Thorlabs TCLDM9) regulated by an OEM diode current and temperature controller (Thorlabs ITC102). The diode lased at 636.7 nm and at full driving current could provide up to 170 mW power; however, it was operated at a reduced power of 40 mW to facilitate single-mode operation. The laser output was coupled *via* a short-pass filter (**F**, angled slightly to avoid direct back reflections off its surface) and a Faraday isolator assembly (**FIA**) into an optical cavity composed of two highly reflective, concave supermirrors (**SM**, Newport, Irvine, CA, $R \geq 99.99\,\%$, 1 m radius of curvature, 1 inch diameter) in a custom glass enclosure. To ensure efficient coupling into the cavity, previous iterations of CERS used an anamorphic prism pair to circularise the laser emission and a mode-matching lens to focus it [97-99]. These optics were removed as the focusing into the cavity was achieved by optimising the distance of the collimating lens of the laser diode. The cavity supermirrors were held on an optical cage system (Thorlabs) and separated by 35 cm inside the glass enclosure. One supermirror was mounted on a piezoelectric actuator (**PSM**, Physik Instrumente, S-314.10, Karlsruhe, Germany) which allowed fine adjusting of the cavity length to the laser wavelength. An optical power build-up occurred inside the cavity when multiples of the laser wavelength matched this cavity length. In 2010, the power enhancement from these supermirrors has been measured to be around 8000 times in magnitude [105]. Figure 2.5 is a photograph of the enhancement.

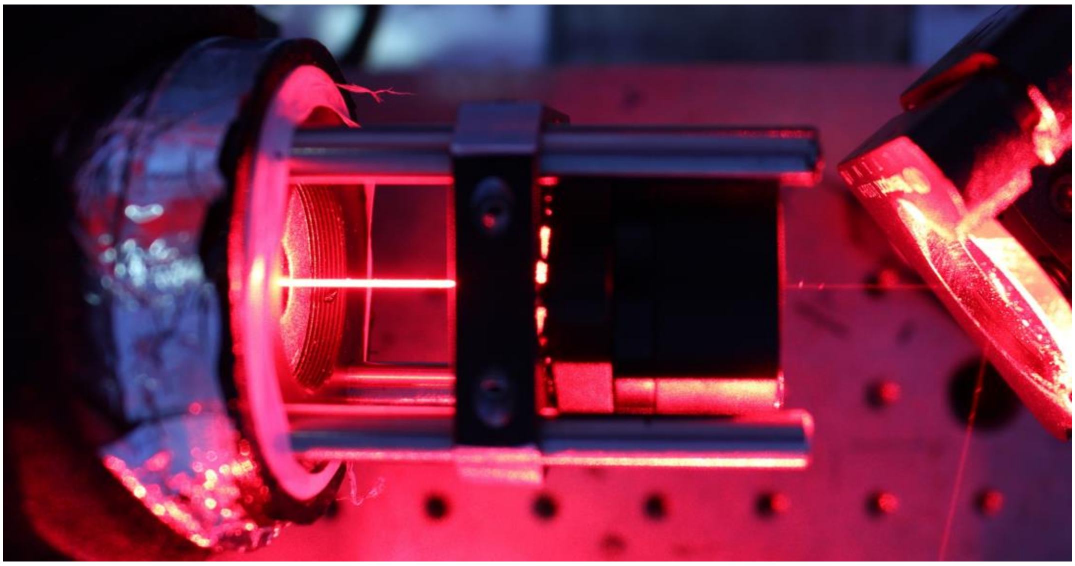

Figure 2.5 – Photograph taken inside the optical cavity while open for cleaning.

The linear design of the cavity required the ingoing beam to strike normal to the rear face of the first supermirror which resulted in a direct back reflection along the incoming beam path. The Faraday isolator assembly prevented the back reflection from reaching the laser diode and potentially damaging it. The assembly consisted of two Faraday isolators arranged in series (OFR, IO-3D-633-PBS, 30 – 36 dB isolation each at 633 nm). Figure 2.6 shows how the assembly was made up of two Faraday rotators (**FR**) and three polarizing beam splitters (**PBS**). The laser diode was physically rotated to an angle of + 45° so that the linearly polarized laser emission matched polarizer 1 and this component could pass through. Faraday rotator 1 then rotated the polarization plane by – 45° so that the light was horizontally polarized with respect to the bench (0°) and could pass through polarizer 2. Faraday rotator 2 rotated the polarization plane a second time by – 45° resulting in the beam exiting the assembly through polarizer 3 being polarized at an angle of – 45°. The beam was then directed to the cavity where the back reflection from the rear face of the first supermirror returned back to the assembly. The back reflection passed through polarizer 3 as it was still linearly polarized at an angle of – 45°. Faraday rotator 2 then rotated the polarization plane by – 45° so that the back reflection was vertically polarized with respect to the bench (90°). Polarizer 2 allowed horizontally polarized light to pass through, but vertically polarized light would be diverted. Thus, the back reflection was diverted by polarizer 2, preventing it from returning to the laser diode.

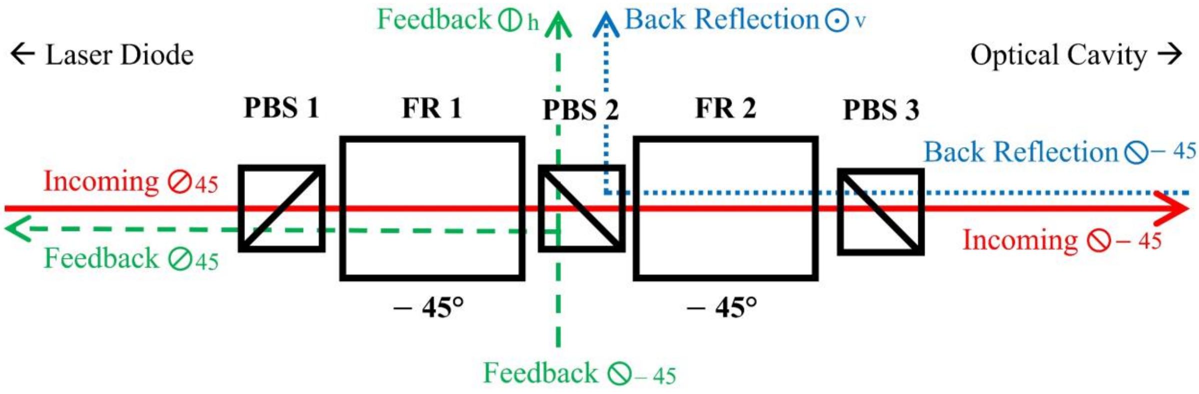

Figure 2.6 – Faraday isolator assembly consisting of two Faraday rotators (**FR**) and three polarizing beam splitters (**PBM**). The angles of the linearly polarized incoming beam from the laser diode, back reflection from the optical cavity and optical feedback are given upon entry and exiting of the assembly.

Both elastically scattered Rayleigh light (636.7 nm) and inelastically scattered Raman light exited the cavity from the rear faces of the supermirrors. Raman scattered light was collected in the 0° linear scattering geometry from the piezoelectric transducer mounted supermirror. A sharp cut-off dichroic mirror (**DM**, Semrock RazorEdge LPD01-633RS-25) was used to separate the red-shifted Raman (Stokes) light from Rayleigh and leftover excitation light. The excitation light was rerouted to and dispersed by a diffraction grating (**G**). The zero-order mode was diverted to a photodiode connected to an oscilloscope (**O**) for monitoring the intensity of the excitation light; this was useful for finding the optimum cavity alignment.

The first-order mode was diverted back to the laser diode for stabilising optical feedback *via* a mirror mounted on a piezoelectric transducer (**PM**), a linear glass polarizer on a rotating mount (**rPol**) and the Faraday isolator assembly. The piezo-mirror was used to match the phase of the feedback light to the diode laser by adjusting the feedback loop length to the laser wavelength. The feedback loop had to be a multiple of the laser wavelength in order that constructive interference within the diode led to efficient feedback. The rotating polarizer could adjust the intensity of the feedback light to prevent damage or overdriving the laser.

The feedback light was mainly linearly polarized at an angle of + 45° and entered the Faraday isolator assembly by polarizing beam splitter 2, as shown in Figure 2.6. Light polarized at an angle of + 45° can be considered as a superposition of 50 % horizontally (0°) and 50 % vertically (90°) polarized light. The horizontally polarized component of the feedback passed through polarizer 2 while the vertically polarized component was diverted and passed through Faraday rotator 1. The polarization plane was then rotated to an angle of + 45° so that the feedback could pass through polarizer 1 and reach the laser diode. The diode injection current was modulated around one cavity mode; in each cycle, the wavelength changed until it was self-locked by optical feedback to a longitudinal cavity mode. In a simplification to the set-up, no attempts were made to actively stabilise the laser by electronic mode tracking because the optical self-locking was strong enough to keep accidental resonances at duty cycles between 50 and 80 %.

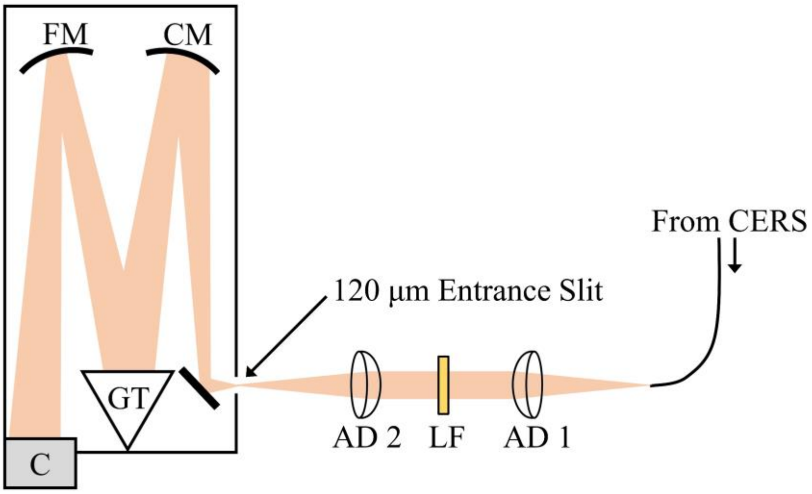

Figure 2.7 – Czerny-Turner spectrograph. **AD**, achromatic doublet; **C**, CCD camera; **CM**, collimating mirror; **FM**, focusing mirror; **GT**, grating turret; **LF**, long-pass filter.

Raman light passing through the dichroic mirror was coupled by a fibre optic assembly (**FOA**, convex 1 inch diameter, *f* = 25.4 mm lens) into a round-to-linear glass fibre bundle

(7 x Ø105 µm). The fibre output was transmitted to the monochromator *via* two achromatic doublets (**AD**) and a long-pass filter (**LF**), as shown in Figure 2.7. The achromatic doublets were needed to match the fibre output to the 120 µm slit of the spectrograph. The long-pass filter was used to block any remaining excitation and Rayleigh scattered light transmitted by the fibre from overwhelming the sensitive camera. The monochromator was a Czerny-Turner spectrograph (Shamrock SR-750-A, *f* = 750 mm) equipped with a CCD camera (**C**, Andor iVac DR32400, cooled at −60 °C) and a rotating grating turret (**GT**). The turret contained three gratings of different resolutions: low (150 lines mm^{-1}, blazed at 750 nm), medium (600 lines mm^{-1}, blazed at 500 nm) and high (1200 lines mm^{-1}, blazed at 750 nm). Andor Solis imaging and spectrograph software controlled the monochromator and camera. The kinetics acquisition mode was used to record spectra every 200 s with 30 s integration time. To prolong the lifespan of the laser diode, an in-house programmed Arduino board controlled the turning on and off of the diode during the 170 s intermissions between the acquisitions of spectra. The Arduino board was also connected to the pressure gauge and OD_{600} photodiode to record the total pressure inside the closed system and the intensity of scattered light every 200 s.

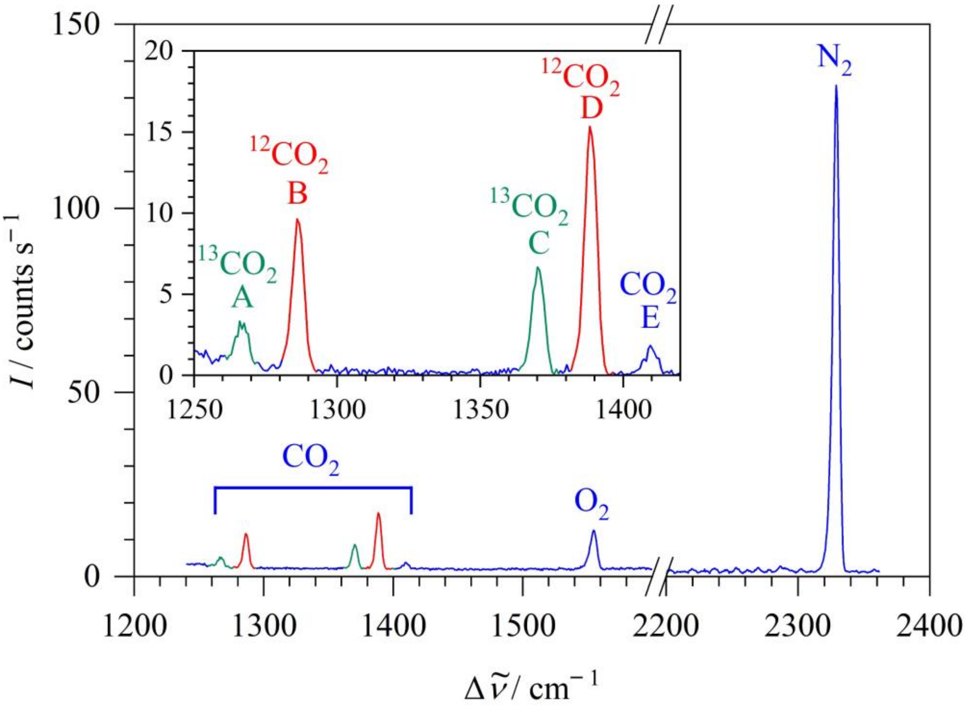

Figure 2.8 – CERS spectrum of 31 mbar $^{13}CO_2$ (green), 73 mbar $^{12}CO_2$ (red), 65 mbar O_2 and 800 mbar N_2 recorded using the medium 600 lines mm^{-1} (medium resolution) grating at 13 h during *E. coli* growth in M9 medium supplemented with 3 mM ^{13}C-glucose and 20 mM ^{12}C-lactose (see Section 2.3.2 for more detail).

The majority of measurements described in this chapter used the medium resolution grating which provided a 1127 cm^{-1} spectral range at 5 cm^{-1} resolution covering Raman shifts between 1240 – 2367 cm^{-1}. The medium resolution grating was used for obtaining spectra containing O_2, N_2, $^{13}CO_2$ and $^{12}CO_2$ peaks, as shown in Figure 2.8. The O_2 and N_2 peaks are both Q-branches belonging to the single vibrational mode of each diatomic molecule with ν_0 = 1556 and 2329 cm^{-1}, respectively. Five CO_2 peaks are observed, labelled from A – E. Peaks A and C are the Q-branches of $\nu_1/2\nu_2{}^0$ Fermi resonance pair for $^{13}CO_2$, B and D are the pair for $^{12}CO_2$ and E is a CO_2 vibrational hot band. For $^{13}CO_2$, A and C have ν_0 = 1265 and 1370 cm^{-1}, respectively. For $^{12}CO_2$, B and D have ν_0 = 1285 and 1388 cm^{-1}, respectively. Cavity resonances varied over time resulting in fluctuating Raman signals which affected all bands equally so that signals required normalisation through the use of a suitable internal standard. The signals were normalised using the N_2 Q-branch by assuming that N_2 was inert to *E. coli* K-12 and stayed constant inside the closed system at 800 mbar. Partial pressures p were calculated by

$$p_x = \frac{A_x}{A_{N_2}} \times \frac{A_{N_2}{}^{1\text{ bar}}}{A_x{}^{1\text{ bar}}} \times p_{N_2} \tag{2.1}$$

where A is integrated peak area and $A^{1\text{ bar}}$ is the standard integrated peak area for 1 bar of gas. The subscript x denotes the analyte gas, in this case either O_2 or CO_2. Integrated peak areas were obtained by a Gaussian fitting procedure. Standard peak areas for CERS, determined experimentally in 2015, are displayed in Table 2.1 [98]. The standard peak area for $^{13}CO_2$ was assumed to be the same as for $^{12}CO_2$.

Noise-equivalent (1 σ) detection limits of 1.0 mbar N_2 and 1.4 mbar O_2 for 30 s integration time were reported in 2015 [98]. These limits were determined from the CERS baseline noise level (standard deviation) of 0.08 counts s^{-1} at 30 s and the peak heights of N_2 and O_2 in air. Note that detection limits may also be quoted as the limit of detection (3 σ) or limit of quantification (5 σ). Signal-to-noise and consequently detection limits improve linearly with the square route of integration time. Detection limits also improve by integrating peak areas instead of using peak heights. Time-dependent CERS data displayed in the Results and Discussion average every nine data-points equivalent to 270 s integration time. Using a Gaussian fitting procedure and the high-resolution grating, noise-equivalent (1 σ) detection limits of 195 ppmv N_2, 265 ppmv O_2 and 240 ppmv CO_2 were obtained for 270 s integration time. Note that 1 ppmv is equal to 1 μbar at 1 bar total pressure.

Gas	Spectral Feature	Peak Position / cm^{-1}	Peak Height / counts s^{-1}	Integrated Area / counts s^{-1} cm^{-1}
$^{14}N_2$	*Q*-branch	2329.0	85	263
$^{16}O_2$	*Q*-branch	1555.5	57	210
$^{12}CO_2$	$v_1/2v_2{}^0$ *Q*-branch component	1285.1	78	134
$^{12}CO_2$	$v_1/2v_2{}^0$ *Q*-branch component	1387.7	129	212

Table 2.1 – CERS Raman characteristics of key compounds taken from [98]. Peak heights and areas correspond to 1 bar partial pressure.

2.2.4 Photoacoustic Spectroscopy in a Differential Helmholtz Resonator

The DHR in the present experiment is described in greater detail in a previous publication from 2019 [125]. Former PhD student Saeed Alahmari and previous MChem student Xiu-Wen Kang constructed the DHR set-up. The DHR followed a design first published in 2003 [123]. As shown in Figure 2.9, it had two identical cylindrical compartments A and B made of glass, 10 cm long with 1 cm inner diameter. The compartments were connected by two capillary glass tubes, 10 cm long with 0.2 cm inner diameter. In the middle of each compartment, an electret microphone (Knowles, EK-23024) was mounted on the side. The compartments had glass windows at their ends to allow laser light to pass through. The windows were slightly tilted to avoid back reflections into the laser. The thin connecting tubes each had a three-way valve in the middle that could be used to isolate the DHR for static measurements or to have a symmetrical gas flow through both compartments (as was required in this study).

Unlike an organ pipe acoustic resonator, which requires the laser beam to be focussed into the middle of the resonator to enhance the longitudinal acoustic mode, focussing is not required for this DHR design as the acoustic mode extends over the entire compartment. This had the advantage that a simple mirror was enough to double the interaction pathlength by passing diode laser light through each compartment and then reflecting it back at a slight angle. Two irises acted as the backstops for the reflected beams.

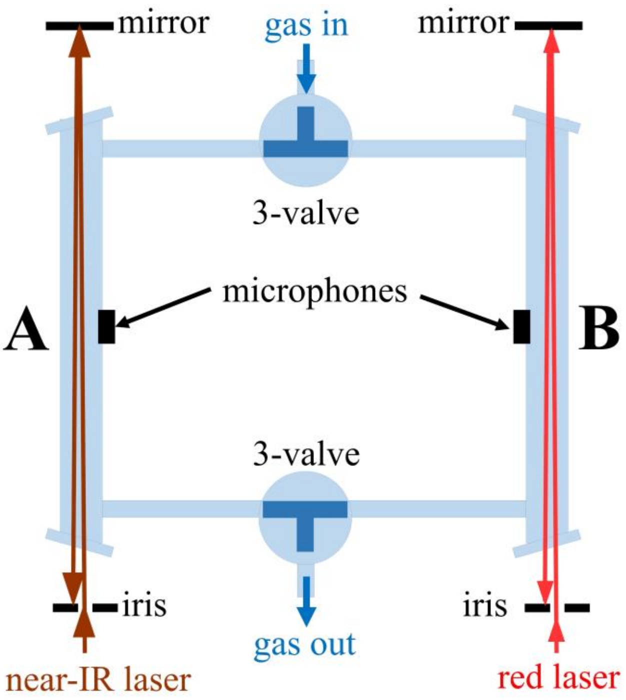

Figure 2.9 – The differential Helmholtz resonator with two compartments A and B.

When laser light was absorbed by molecules inside one compartment, collisional deactivation led to a temperature jump and pressure expansion (the photoacoustic effect). The pressure build-up would then travel from one compartment to the other *via* the connecting capillaries, leaving a pressure depression in the initial compartment. For instance, if laser light was absorbed in compartment A, the pressure build-up would travel from A to B and leave a pressure depression behind in A. If the laser was turned off, the pressure build-up would return to A and leave a pressure depression behind in B. By pulsing the laser light, the pressure build-up and pressure depression alternated between the two compartments. Periodic pressure waves (sound) were created in A and B by modulating the laser periodically. The sound waves would have the same frequency but opposing phases between compartments. By matching the laser modulation to a resonance frequency of the cell, a standing wave developed with maximum amplitude (resonant photoacoustics).

Key features that make DHR an attractive choice for trace gas detection applications are its signal enhancement and noise cancellation by differential amplification of microphone signals A – B. Absorption signals inside the cell were out-of-phase between microphones A and B; differential amplification of A – B thus doubled the signal, as shown in Figure 2.10. External and flow noises affected the two symmetrical compartments in nearly the same way, which created noise signals in both A and B that were in-phase. As well as signal enhancement, differential amplification of A – B led to effective cancellation of noise, as also shown in

Figure 2.10. The differential signals were processed in lock-in amplifiers which further greatly reduced noise.

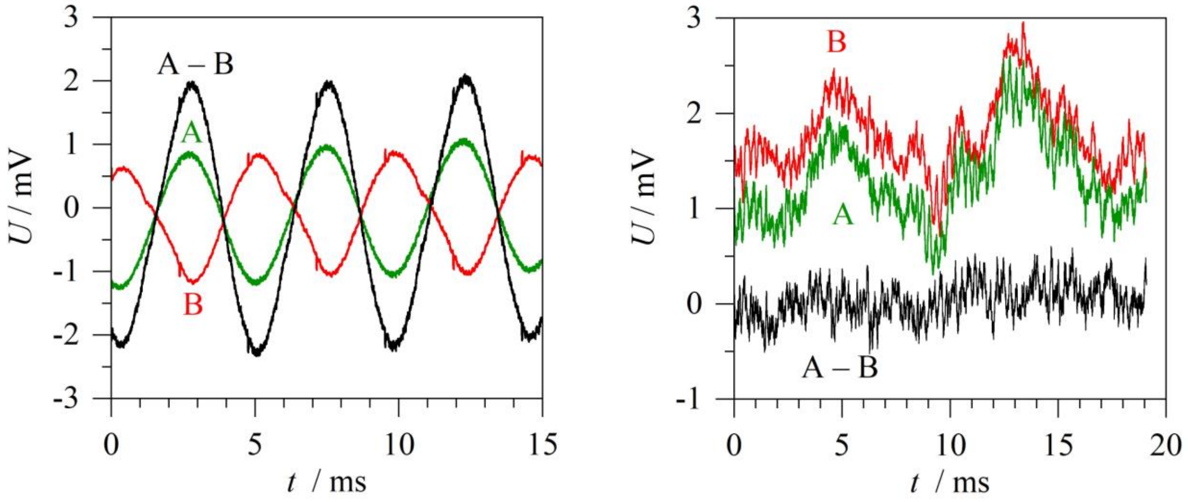

Figure 2.10 – Oscilloscope traces of the signal from microphone A (green), microphone B (red) and the differential signal A – B (black). Signal enhancement of the CO_2 absorption near 1.57 µm (left) and noise cancellation (right).

The DHR set-up used two distributed feedback laser (DFB) lasers. A near-IR laser for detecting CO_2 near 1.57 µm passed through compartment A and a red laser near 764 nm for detecting O_2 passed through compartment B. The near-IR laser has also been used in a previous study for detecting H_2S alongside CO_2 [125]. Both lasers were modulated by their injection current at the acoustic resonance frequency with a square wave giving a 50 % duty cycle. The near-IR single-mode DFB diode (Mitsubishi, FU-650SDF, 4 mW) was amplified in a booster optical amplifier (Thorlabs, S9FC1004P) to a peak power of 30 mW. This laser was temperature tuneable between 20 and 60 °C providing a mode-hop-free tuning range from 6357 to 6378 cm^{-1} (1.568 to 1.573 µm). The red laser (Eagleyard, EYP-DFB-0764, 35 mW) was temperature tuneable between 18 to 40 °C giving a 13067 – 13089 cm^{-1} (764.0 – 765.3 nm) mode-hop-free tuning range.

For $^{13}CO_2$ and $^{12}CO_2$ analysis, the temperature of the near-IR laser was increased from 29.5 to 34 °C at a rate of 0.02 °C s^{-1} to give good spectral resolution. This temperature tuning range corresponded to a spectral range of 6371.0 – 6373.4 cm^{-1}, with each CO_2 spectrum taking 225 s to acquire. For O_2 analysis, the temperature of the red laser was increased from 33.6 to 36 °C, also at a rate of 0.02 °C s^{-1}, corresponding to a spectral range of 13082.6 – 13085.0 cm^{-1}, with each O_2 spectrum taking 120 s to acquire.

The time sequence for the continuous monitoring of bacterial cultures was first to switch on the near-IR laser in compartment A, wait 10 s and then record the CO_2 photoacoustic spectrum for 225 s. Next, the near-IR laser would be switched off and the red laser switched on in compartment B, wait 10 s and then record the O_2 photoacoustic spectrum for 120 s. CO_2 and O_2 spectra were recorded every 15 min during experiments so there was a 535 s intermission between the switching off of the red laser and the switching on again of the near-IR laser. The gas-phase peristaltic pump was switched off during CO_2 and O_2 scans as its noise interfered with the microphone. The pump was switched on during the 535 s intermissions between scans. An Arduino microprocessor board controlled the switching on and off of the peristaltic pump and the DFB lasers in time with the measurements as well as recording the total pressure inside the closed system.

Within the tuning range of the near-IR DFB laser are $^{13}CO_2$ and $^{12}CO_2$ features. From 6000 – 6600 cm^{-1}, $^{12}CO_2$ has four moderately strong bands from the [$3v_1 + v_3$, $2v_1 + 2v_2^0 + v_3$, $v_1 + 4v_2^0 + v_3$, $6v_2^0 + v_3$] Fermi resonance tetrad (four interacting bands), as shown in the HITRAN absorption cross sections displayed in Figure 2.11. In the vibrational notation introduced by McClatchey *et al.* [127] and used in the HITRAN database [8], the four bands are denoted as 30014 ← 00001 (v_0 = 6075.9 cm^{-1}), 30013 ← 00001 (v_0 = 6227.9 cm^{-1}), 30012 ← 00001 (v_0 = 6347.8 cm^{-1}) and 30011 ← 00001 (v_0 = 6503.0 cm^{-1}). For $^{13}CO_2$, these values shift to lower wavenumbers of 5951.6, 6119.6, 6119.6 and 6363.6 cm^{-1}, respectively. The vibrational notation uses five digits for each state, in order, $v_1\ v_2\ \ell_2\ v_3\ r$. Quantum numbers v_1, v_2 and v_3 are for the symmetric, bending and asymmetric vibrations of CO_2, respectively. ℓ_2 is the angular momentum quantum number assigned to the bending mode v_2. The fifth digit, r, is a ranking index with the highest energy vibrational level of a Fermi resonance group being assigned as unity. The value of r increases with the decreasing energy of the Fermi resonance bands. The strongest feature was the $R(18)$ line of the 30012 ← 00001 band at 6361.25 cm^{-1}, which can be used to distinguish CO_2 at natural abundance in lab air (410 ppmv) [125].

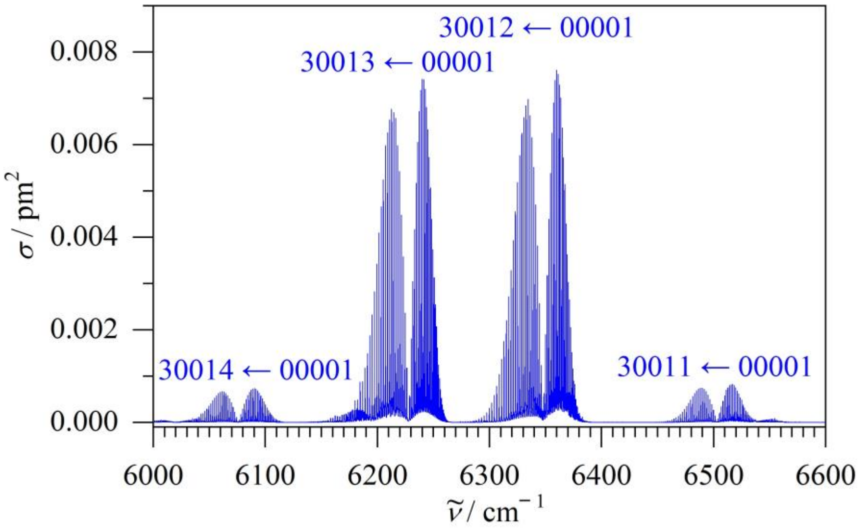

Figure 2.11 – HITRAN absorption cross sections (1 bar pressure broadening) of the ($3\nu_1 + \nu_3$) Fermi resonance tetrad of $^{12}CO_2$.

Calibrated CO_2 gas mixtures in 1 bar N_2 were prepared and the amplitude of the $R(18)$ line was measured for calibration, as shown in Figure 2.12. The CO_2 calibration plot showed good linearity, but a slightly better fit was obtained by a non-linear fit to $y = a\,x^b$ with $b = 1.04$. The deviation from linearity was likely due to the change in gas composition from trace to higher levels. The resonance frequency of the cell is given by the cell dimensions and also depends linearly on the speed of sound c, which for an ideal gas is given by

$$c = \sqrt{\frac{\gamma R T}{M}} \tag{2.2}$$

where R is the gas constant, T is the temperature and γ and M are the heat capacity ratio and the molar mass of the medium inside the resonator, respectively. As the resonance frequency changes with temperature and medium, a calibration is strictly only valid for a given temperature and gas composition. At 1 s integration time, the standard deviation of the baseline was 0.98 mV with the laser still on and this level is marked by the horizontal dashed line in Figure 2.12. The $^{12}CO_2$ noise-equivalent (1 σ) detection limit was 0.16 mbar (160 ppmv) at 1 s integration time given by the point the non-linear red fit line meets the noise floor.

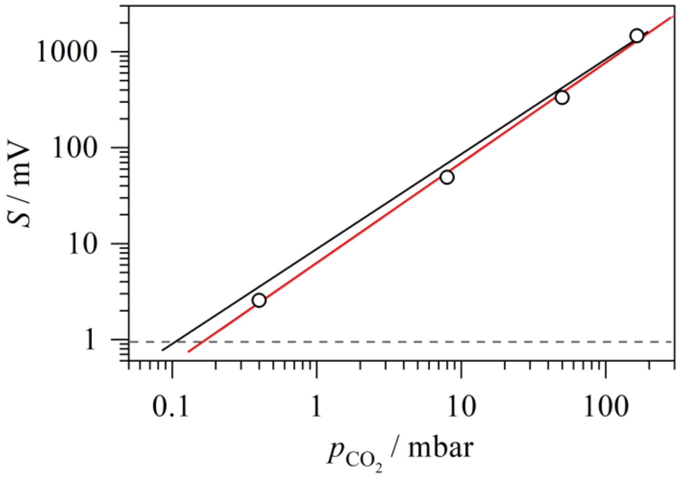

Figure 2.12 – Calibration plot using the amplitude of the $R(18)$ line of the 30012 ← 00001 band of $^{12}CO_2$ in 1 bar N_2 mixtures. The black line is a linear fit through the origin ($y = m\,x$) and the red line is a non-linear fit ($y = a\,x^b$). The horizontal dashed line indicates the noise floor at 1 s integration time.

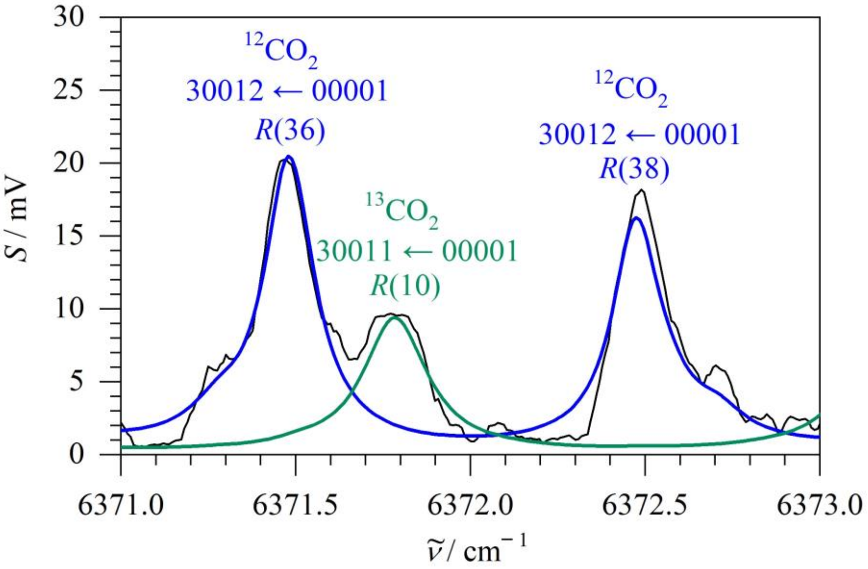

Figure 2.13 – Photoacoustic absorption spectrum of 5.0 mbar $^{13}CO_2$ and 56.5 mbar $^{12}CO_2$ in black. In green and blue are HITRAN data for $^{13}CO_2$ and $^{12}CO_2$, respectively.

For $^{13}CO_2$ and $^{12}CO_2$ analysis, the $R(10)$ line of the $^{13}CO_2$ 30011 ← 00001 band at 6371.78 cm^{-1} and the $R(36)$ line of the $^{12}CO_2$ 30012 ← 00001 band at 6371.48 cm^{-1} were used, as shown in Figure 2.13. Compared to the $R(18)$ line of the 30012 ← 00001 band, these $^{13}CO_2$ and $^{12}CO_2$ lines are about 22 and 35 % as intense, respectively, based on HITRAN cross section peak heights. Despite this, within the 6357 to 6378 cm^{-1} tuning range of the near-IR laser, these lines were the only two $^{13}CO_2$ and $^{12}CO_2$ features next to each other with similar intensities, so as to not compromise the sensitivity of one CO_2 isotopomer for the other. The ${}^{13}CO_2$ and ${}^{12}CO_2$ lines were both analysed by a Gaussian fitting routine and the returned peak areas were converted to partial pressures according to the calibration plot for the $R(18)$ line of the ${}^{12}CO_2$ 30012 ← 00001 band, albeit corrected for the lower absorption cross sections.

O_2 does not have an IR-active vibration, but it does have four absorption bands in the visible region which are electronic transitions between the triplet ground state $X\,{}^3\Sigma_g^-$ and the second excited singlet state in its lowest vibration state $b\,{}^1\Sigma_g^+$. These four bands, denoted A, B, γ and δ, correspond to the vibrational transitions $(v' \leftarrow v'') = (0 \leftarrow 0)$, $(1 \leftarrow 0)$, $(2 \leftarrow 0)$ and $(3 \leftarrow 0)$, respectively. These O_2 bands are weak, spin-forbidden magnetic-dipole transitions. Despite this, the A and B bands are prominent in atmospheric spectra due to the large amount of O_2 in the atmosphere and the long absorption pathlengths. The A band is located near 760 nm, which is a relatively empty portion of the atmospheric spectrum, making it useful for atmospheric remote sensing. The A band consists of lots of individual transitions involving different rotational quantum states, as shown in the HITRAN absorption cross sections displayed in Figure 2.14 (top panel). The absorption cross sections for the Fermi resonance tetrad of CO_2 and the A band of O_2 are of the same order of magnitude. The rotational energy levels of the O_2 electronic states are denoted by the quantum numbers N and J for the rotational and total angular momentum, respectively. The individual lines of the A band are indicated by ${}^{\Delta N}\Delta J(N'', J'')$ forming two r-form branches, ${}^{r}R(N'', J'' = N'')$ and ${}^{r}Q(N'', J'' = N'' + 1)$, and two p-form branches, ${}^{p}P(N'', J'' = N'')$ and ${}^{p}Q(N'', J'' = N'' - 1)$, composed of pairs of lines separated by approximately 2 cm^{-1} up until $N'' \approx 30$ [128]. The strongest line in the A band was used for DHR detection of O_2, which was the ${}^{p}P(11, 11)$ line at 13084 cm^{-1} or 764.28 nm (vacuum), as shown in Figure 2.14 (bottom panel). At an abundance of 210 mbar O_2 in 1 bar air, the peak photoacoustic signal of the ${}^{p}P(11, 11)$ line was 310 mV and this was used for calibration by assuming linearity. The standard deviation of the baseline (σ), 0.88 mV at 1 s integration time, served as an estimate of the noise level to obtain a noise-equivalent (1 σ) detection limit of 0.60 mbar (600 ppmv) for O_2 at 1 s integration time [125].

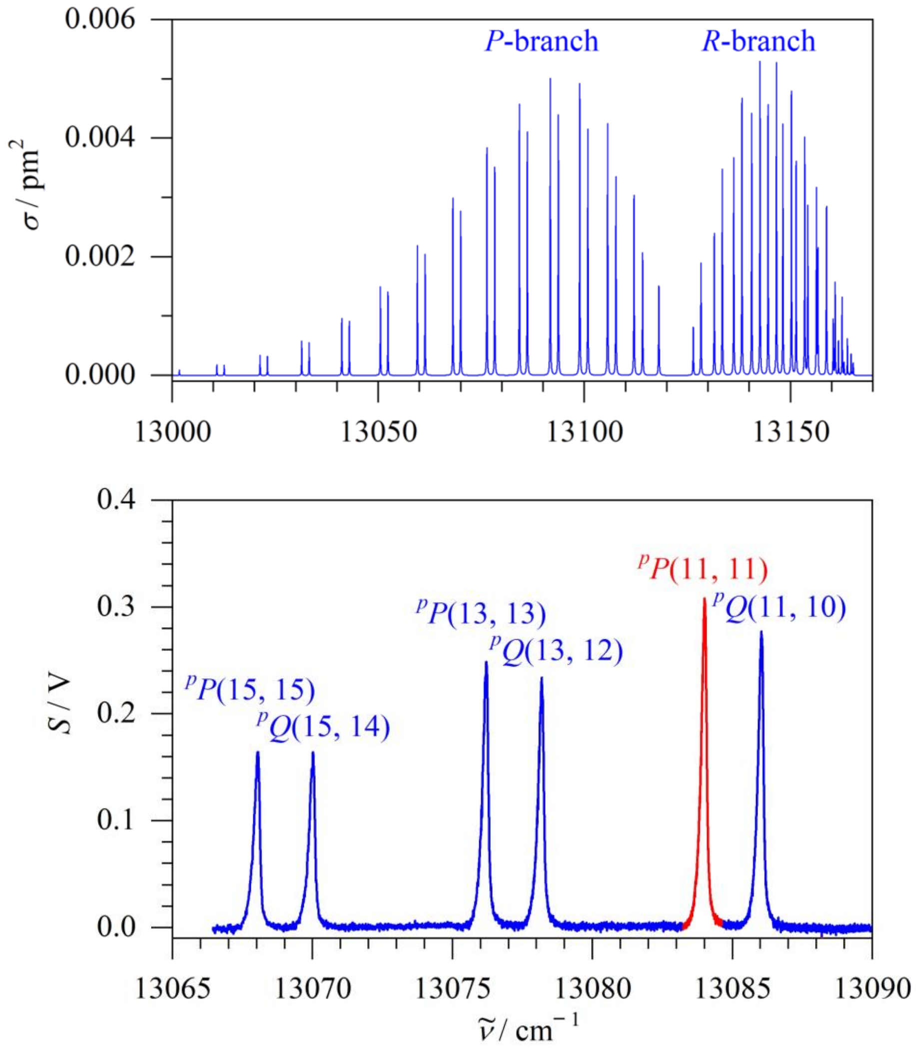

Figure 2.14 – Top panel: HITRAN $^{16}O_2$ *A* band absorption cross sections (1 bar pressure broadening). Bottom panel: photoacoustic absorption spectrum of 210 mbar O_2 (air) in the DHR, obtained by temperature tuning the red DFB laser from 24 to 38 °C. The six peaks belong to the *A* band of O_2. The red $^PP(11, 11)$ line was used for O_2 detection.

2.3 Results and Discussion

2.3.1 Characterising Aerobic Growth in LB and M9 Media

Initial experiments studied the O_2 limited growth of *E. coli* in LB and M9 media supplemented with a single sugar, either glucose or lactose, to characterise the analytical techniques and bacterial growth behaviour before conducting diauxic growth experiments. For a fair comparison of growth media, due to the different headspace volumes between CERS and DHR, only CERS measurements are displayed in this Section 2.3.1.

Figure 2.15 is a typical example of the time-dependent number of moles (n / mmol) and equivalent partial pressures (p / mbar) for O_2 and CO_2 during aerobic growth of *E. coli* in LB medium supplemented with 20 mM glucose. Partial pressures were converted to moles using the ideal gas law ($V(\text{CERS}) = 7.2 \times 10^{-4}$ m^3, $T = 310$ K) with n and p of CO_2 corrected for the approximately 18 % of dissolved CO_2 according to Henry's law. A small proportion of the dissolved CO_2 will react with water to form carbonic acid which will be at equilibrium with bicarbonate and carbonate ions, depending on the pH. Under our conditions, less than 1% of dissolved CO_2 is expected to be lost to carbonic acid and carbonates. Also included in the figure (middle panel **b**) is the respiratory quotient (RQ), the ratio of Henry's law corrected CO_2 produced to O_2 consumed, and the total pressure $p_{\text{total}} = p(O_2) + p(CO_2) + p(N_2)$. Finally, the figure also includes (bottom panel **c**) the bacterial growth curve (OD_{600}) which distinguishes the lag phase **A** (0 – 1 h), exponential phase **B** (1 – 5 h) and stationary phase **C** (> 5 h). All biological experiments were repeated in triplicate, and all repeats showed essentially the same behaviour. All time-dependent data displayed is for a single representative experiment selected from the repeats. For clarity, all data was averaged so that each datapoint displayed in the figures are spaced at 30 min intervals.

Although OD_{600} measurements are convenient for indicating the bacterial growth phase and estimating cell density, a more complete characterization of bacterial growth requires a complementary method such as CERS. As shown in the gas-phase data, a brief lag phase **A** of around 1 h occurs for *E. coli* growth in LB medium. After the lag phase, significant O_2 consumption and CO_2 production begins indicating the onset of exponential phase **B**, with an increase in OD_{600} up to a peak value of about 1.5 at 5 h. The OD_{600} plateaus between 5 and 24 h, indicating equal rates for cell division and cell death. The stationary culture is still metabolically active as aerobic respiration continues until O_2 is exhausted at 24 h. Ignoring the lag phase **A**, the O_2 uptake rate is constant over the 24 h, as can be shown by an exponential decay fit $n = n_0 + A \exp(-kt)$ with a rate constant of $k = 0.153\ \mathrm{h}^{-1}$ or a half-life of $t_{1/2} = 4.5$ h. These results are confirmed in the repeated experiments which show the lag phase **A** varies in length between 1 and 2 h, the onset of the stationary phase between 5 and 6 h, and an O_2 uptake rate within 0.15 – 0.19 h^{-1}.

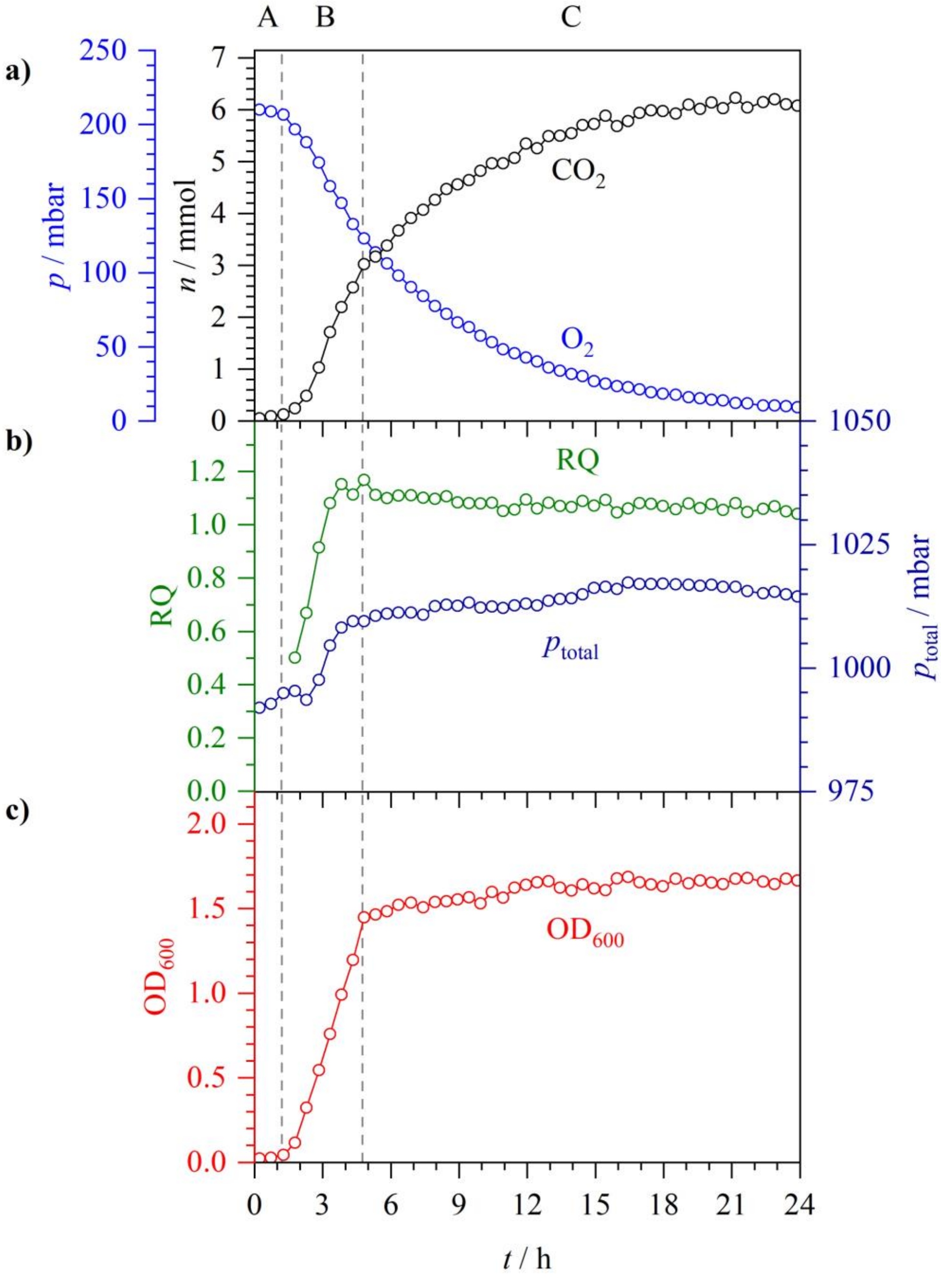

Figure 2.15 – CERS measurement of aerobic *E. coli* growth in LB medium supplemented with 20 mM glucose. A to C denotes three distinct bacterial growth phases: lag (A), exponential (B) and stationary (C) phases. **a)** Time-dependent number of moles (n) of O_2 and CO_2 (corrected for dissolved CO_2) with equivalent partial pressures (p). **b)** Respiratory quotient (RQ) and total pressure (p_{total}). **c)** Optical density (OD_{600}).

As described by Equation 1.18, during aerobic respiration one glucose molecule is completely oxidised to six CO_2 molecules with six O_2 molecules also consumed. Hence, for carbohydrates, the RQ is typically about 1.0 for aerobic growth. Like the OD_{600} measurements, the RQ can be used to distinguish between exponential phase **B** and stationary phase **C** where a constant RQ of about 1.0 is reached during stationary growth. The 1:1 ratio between O_2 consumed and CO_2 produced can also be observed in the near constant p_{total} during stationary phase **C**. A typical *E. coli* cell contains approximately 48 % carbon by dry mass [129]. In LB medium, sugars are available to be fully oxidised to CO_2 as tryptone and yeast extract are primarily used as carbon sources for biosynthesis [130]. *E. coli* has several oligopeptide permeases and peptidases enabling it to recover free catabolizable amino acids from tryptone and yeast extract [131]. The 210 mbar of O_2 in the 720 mL headspace of the CERS experiment corresponds to 6 mmol, and the 20 mM glucose in the 250 mL suspension corresponds to 5 mmol. Hence, based on the stoichiometry of the equation for aerobic respiration, there is an excess of glucose and the bacteria are limited by the O_2 available.

When O_2 is depleted by 24 h, despite oxidisable carbon sources still remaining in the form of glucose and the LB components, no further CO_2 is produced by fermentative pathways. During aerobic growth, acidic byproducts are excreted, most likely acetate from overflow metabolism, causing the pH to decrease from 6.8 at the start to between 4.5 – 5.0 by 24 h. The acidic pH will cause stress for the *E. coli* culture which may prevent the transition to the fermentation pathways that produce acetate, ethanol, formate and CO_2 (see Figure 1.16) that would further decrease the pH. The CO_2 levels were monitored for up to three days (not displayed in Figure 2.15) to confirm that CO_2 did not increase after O_2 depletion, but rather it gradually decreased from 6.0 mmol to around 4.1 mmol (145 mbar). This decrease in CO_2 was not due to a leak because no increase in O_2 was observed. One possible explanation might be provided by the slow conversion of dissolved CO_2 to carbonic acid. Alternatively, CO_2 uptake is required to convert phosphoenolpyruvate (PEP) to oxaloacetate for the anaerobic TCA cycle. This pathway or other CO_2 fixation routes [132] may become significant as a starvation response to O_2 depletion.

To make sure that in the isotopically labelled glucose-lactose diauxie experiments (Section 2.3.2) that all CO_2 observed was coming from the sugars and not from other media components (such as tryptone or yeast extract in LB), aerobic respiration experiments were also conducted in M9 minimal medium. Figure 2.16 is a typical example of the aerobic growth of *E. coli* in M9 medium supplemented with 20 mM glucose (the only carbon source).

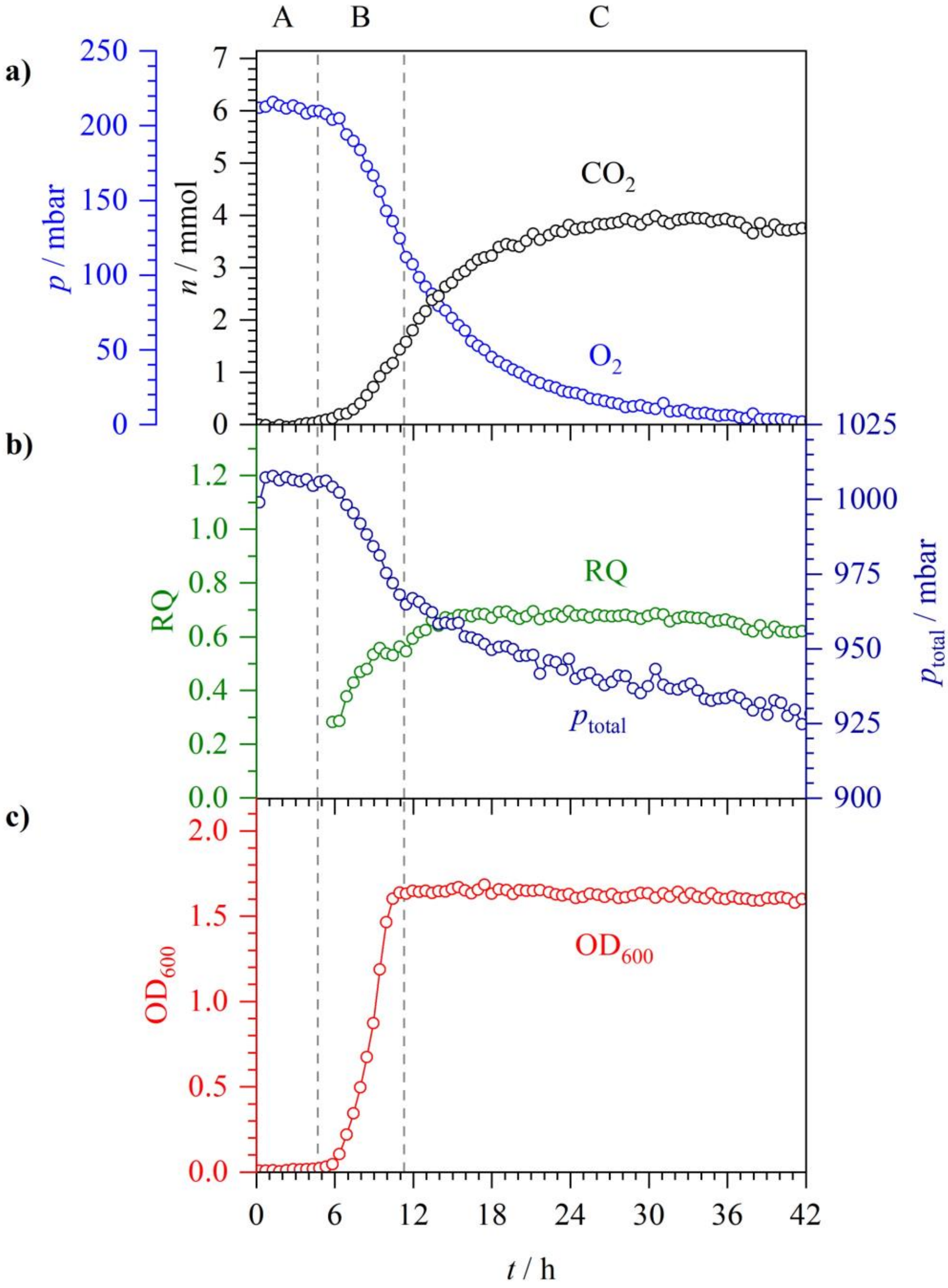

Figure 2.16 – CERS measurement of aerobic *E. coli* growth in M9 medium supplemented with 20 mM glucose. A to C denotes three distinct bacterial growth phases: lag (A), exponential (B) and stationary (C) phases. **a)** n and p of O_2 and CO_2. **b)** RQ and p_{total}. **c)** OD_{600}.

As before, the lag phase **A** (0 – 5 h), exponential phase **B** (5 – 11 h) and stationary phase **C** (> 11 h) can be distingished by the gas-phase analysis as well as by the OD_{600}. In M9 medium, the lag phase **A** and exponential phase **B** last around 5 and 6 h, respectively, which are both longer when compared to growth in LB medium. After the lag phase **A**, the O_2 uptake rate is constant as can be shown by an exponential decay fit with $k = 0.137\ h^{-1}$ or $t_{1/2} = 5.1$ h. Similar results were found in the repeat experiments which showed a lag phase **A** of between

4 and 7 h, the onset of stationary phase **B** between 10 and 13 h, and O_2 uptake rates of between 0.13 and 0.15 h^{-1}. The O_2 uptake rates are roughly the same between the two growth media which suggests that the rate-limiting step for O_2 uptake is the same in both cases. This is likely due to the rate of O_2 diffusion into the liquid culture being slower than the rate of O_2 consumption by *E. coli*. Due to the low solubility of O_2, its diffusion into liquid culture is often rate-limiting for O_2 consumption. This can also lead to micro-aerobic conditions in the bulk liquid which can cause fermentative pathways operating alongside aerobic respiration. It is unknown which acids were excreted to cause the pH of both growth media to decrease during aerobic respiration, however, later chapters include the use of liquid-phase Raman spectroscopy alongside CERS to also detect organic acids which is a major addition to the experimental CERS set-up discussed in this chapter.

A very distinct behaviour is exhibited in terms of the total yield of CO_2. In M9 medium, there is no 1:1 relationship between O_2 consumed and CO_2 produced, but rather a peak RQ of around 0.7 is observed indicating that 30 % of carbon from glucose that could have been fully oxidised to CO_2 was not. This is even clearer in the plot of p_{total} which decreases overtime during growth in M9 medium by around 70 mbar to give a slight under-pressure inside the closed system. The RQ of 0.7 is not caused by leaching of some dissolved CO_2 *via* carbonic acid into bicarbonate and carbonate ions, as determined in a test experiment in which acidifying by injecting HCl into the bacterial culture at the end did not release any extra CO_2 over an extended period of time.

The imbalance between O_2 consumption and CO_2 production in M9 medium is due to some glucose not being fully oxidised to CO_2 because it is the only catabolizable carbon source available for biomass synthesis. Tryptone and yeast extract provide amino acids for growth in LB medium, but in the minimal medium, *E. coli* must synthesise amino acids, nucleobases and other biomolecules from glucose. In minimal media, *E. coli* has been found to accumulate a large amount of enzymes, which are virtually absent when grown in LB medium, that catalyse the formation of amino acids from the glucose, ammonium and sulphate components of M9 medium [133]. Some formulations of minimal media incorporate casamino acids for biomass synthesis so that sugars are not utilized as building blocks. We did not incorporate casamino acids into the M9 medium to be certain that the only available carbon sources for CO_2 production were the supplemented sugars. The need to synthesize essential precursor molecules in M9 medium also contributes to the longer lag phase and slower growth rate. It can be seen from the plot of the total pressure that the rate of decrease is much higher during exponential phase **B** than during stationary phase **C**. This is consistent with a more significant imbalance between CO_2 and O_2 and a higher requirement for carbon for growth during the exponential phase. About 80 mbar of CO_2 is missing at the end of the experiment, which corresponds to approximately 2.5 mmol of carbon atoms. The dry weight of bacteria at the end is about 60 mg. Assuming that about 48 % of this is carbon, the bacteria contain about 2.5 mmol of carbon atoms in total, in agreement with the missing CO_2.

Experiments were repeated in M9 supplemented with lactose, instead of glucose. Figure 2.17 is a typical example of the aerobic growth of *E. coli* in M9 medium supplemented with 20 mM lactose. The results are very similar to M9 supplemented with glucose with a similar lag phase. The exponential decay of O_2 has an uptake rate of $k = 0.152\ h^{-1}$ with a range of $0.15 – 0.17\ h^{-1}$ in the repeats. At complete oxidation of lactose to CO_2 *via* sugar hydrolysis to give glucose and galactose, there is again a 1:1 relationship between O_2 consumed and CO_2 produced. However, again as this is a minimal growth medium, the RQ is less than unity and peaks around 0.8 in the stationary phase **C**. The slightly higher RQ for lactose supplemented M9 media over glucose supplementation is likely due to the 20 mM lactose providing 40 mM of monosaccharide growth substrates (glucose and galactose) which is double the 20 mM glucose, hence, more carbon sources are available for biosynthesis.

A noticeable difference between glucose and lactose supplemented M9 media concerns the behaviour of the bacterial growth curve. As before, the lag phase **A** (0 – 6 h) and exponential phase **B** (6 – 12 h) can be easily seen in the OD_{600} curve. In the stationary phase **C** (> 12 h), however, the OD_{600} does not remain constant but first declines a little before increasing again around the point where O_2 is depleted, continuing to rise outside the range displayed in Figure 2.17. The reason for this behaviour is unclear at present; it might be related to dead cells breaking up, possibly releasing slightly coloured compounds which absorb red light, in addition to scattering losses. In any case, it shows that OD_{600} measurements are a rather indirect determination of cell density and therefore can suffer from interferences not directly related to the density of living cells.

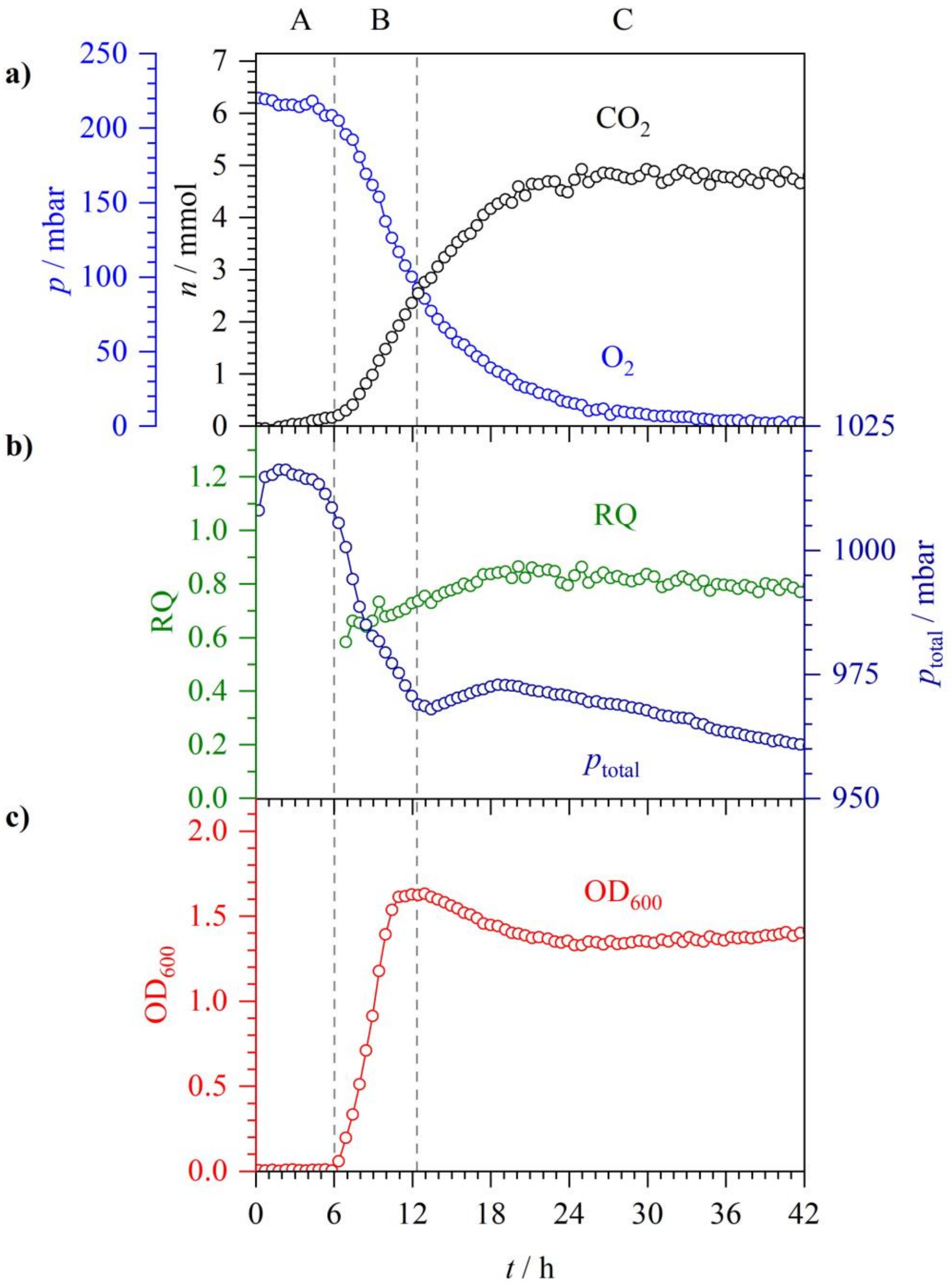

Figure 2.17 – CERS measurement of aerobic *E. coli* growth in M9 medium supplemented with 20 mM lactose. A to C denotes three distinct bacterial growth phases: lag (A), exponential (B) and stationary (C) phases. **a)** n and p of O_2 and CO_2. **b)** RQ and p_{total}. **c)** OD_{600}.

2.3.2 Glucose-Lactose Diauxie

Diauxic growth is typically studied with the concentration of one sugar being up to one order of magnitude greater than the other. In glucose-lactose diauxie, larger concentrations of lactose are typically used in order to show the clear preference for glucose metabolism, despite the lower glucose concentration. Experiments were also conducted using the DHR set-up (which lacked *in situ* OD_{600} measurements) to characterise the aerobic growth of *E. coli*. The glucose-limited growth of *E. coli* was also studied before conducting mixed sugar experiments. Figure 2.18 is a typical example of the aerobic growth of *E. coli* in M9 medium supplemented with 2.5 mM glucose as measured by the DHR set-up. After the lag phase **A** (0 – 6 h), exponential phase **B** (6 – 11 h) beings with around 1.0 mmol (50 mbar) O_2 consumed and 0.7 mmol (35 mbar) CO_2 produced for a RQ of around 0.7. At 11 h, glucose is depleted and no further aerobic respiration is possible. Hence, phase **C** in this figure is referred to as glucose depletion.

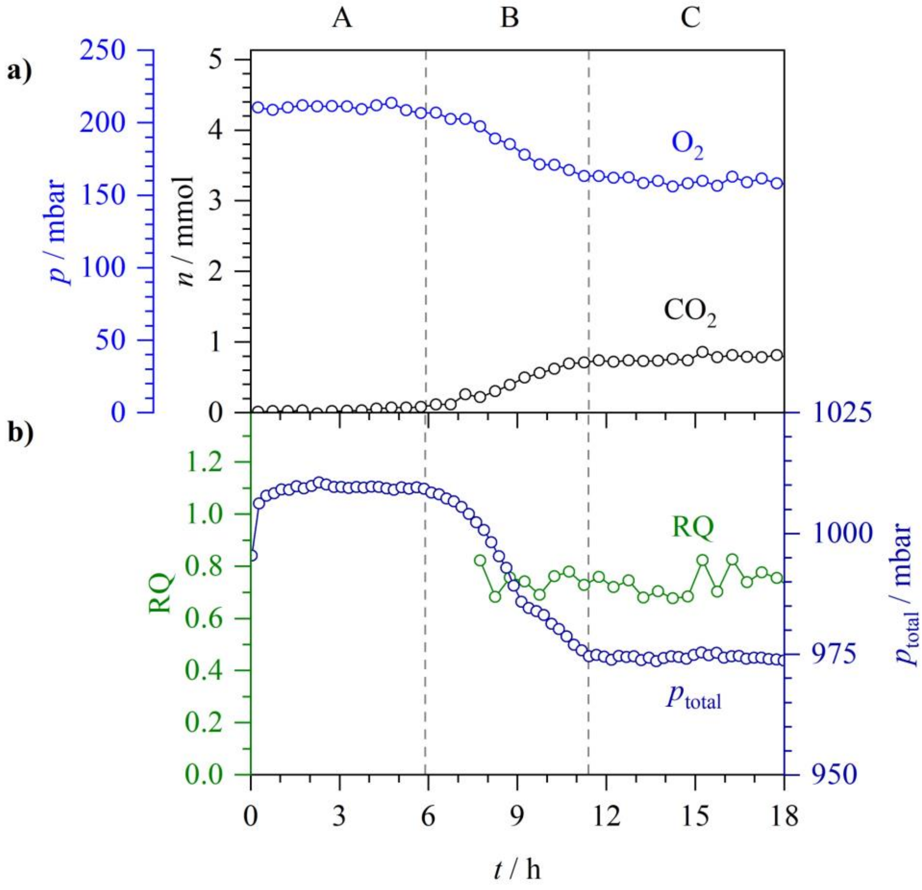

Figure 2.18 – DHR measurement of aerobic *E. coli* growth in M9 medium supplemented with 2.5 mM glucose. A to C denotes three distinct phases: lag (A), exponential (B) and glucose depletion (C) phases. **a)** n and p of O_2 and CO_2. **b)** RQ and p_{total}.

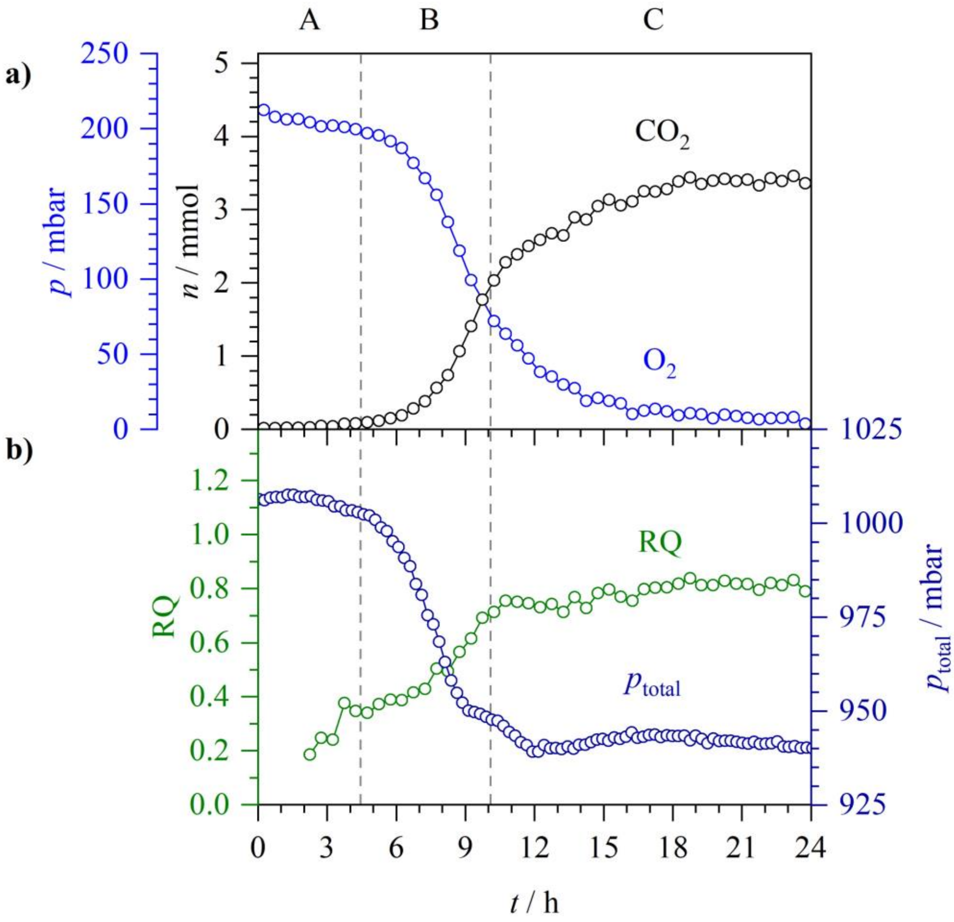

Figure 2.19 – DHR measurement of aerobic *E. coli* growth in M9 medium supplemented with 2.5 mM glucose and 10 mM lactose. A to C denotes three distinct phases: lag (A), exponential (B) and stationary (C) phases. **a)** n and p of O_2 and CO_2. **b)** RQ and p_{total}.

Figure 2.19 is a typical example of the aerobic growth of *E. coli* in M9 medium supplemented with 2.5 mM glucose and 10 mM lactose as measured by the DHR set-up. Even without OD_{600} measurements by the DHR set-up, the gas-phase measurements allow the distinction of the lag phase **A** (0 – 4.5 h), exponential phase **B** (4.5 – 10 h) and stationary phase **C** (> 10 h). However, the point of glucose depletion and transition to lactose metabolism is not apparent as O_2 consumption and CO_2 production both occur continuously until O_2 depletion. A Monod-style diauxic lag phase is not apparent and based on this data it would be inconclusive whether glucose or lactose are metabolised first or both simultaneously. The power of spectroscopic detection, however, is the possibility to distinguish isotopes such as $^{13}CO_2$ and $^{12}CO_2$ in the headspace. Fully substituted ^{13}C labelled glucose ($^{13}C_6H_{12}O_6$) can be used to produce $^{13}CO_2$ exclusively, distinct from $^{12}CO_2$ produced from unlabelled lactose.

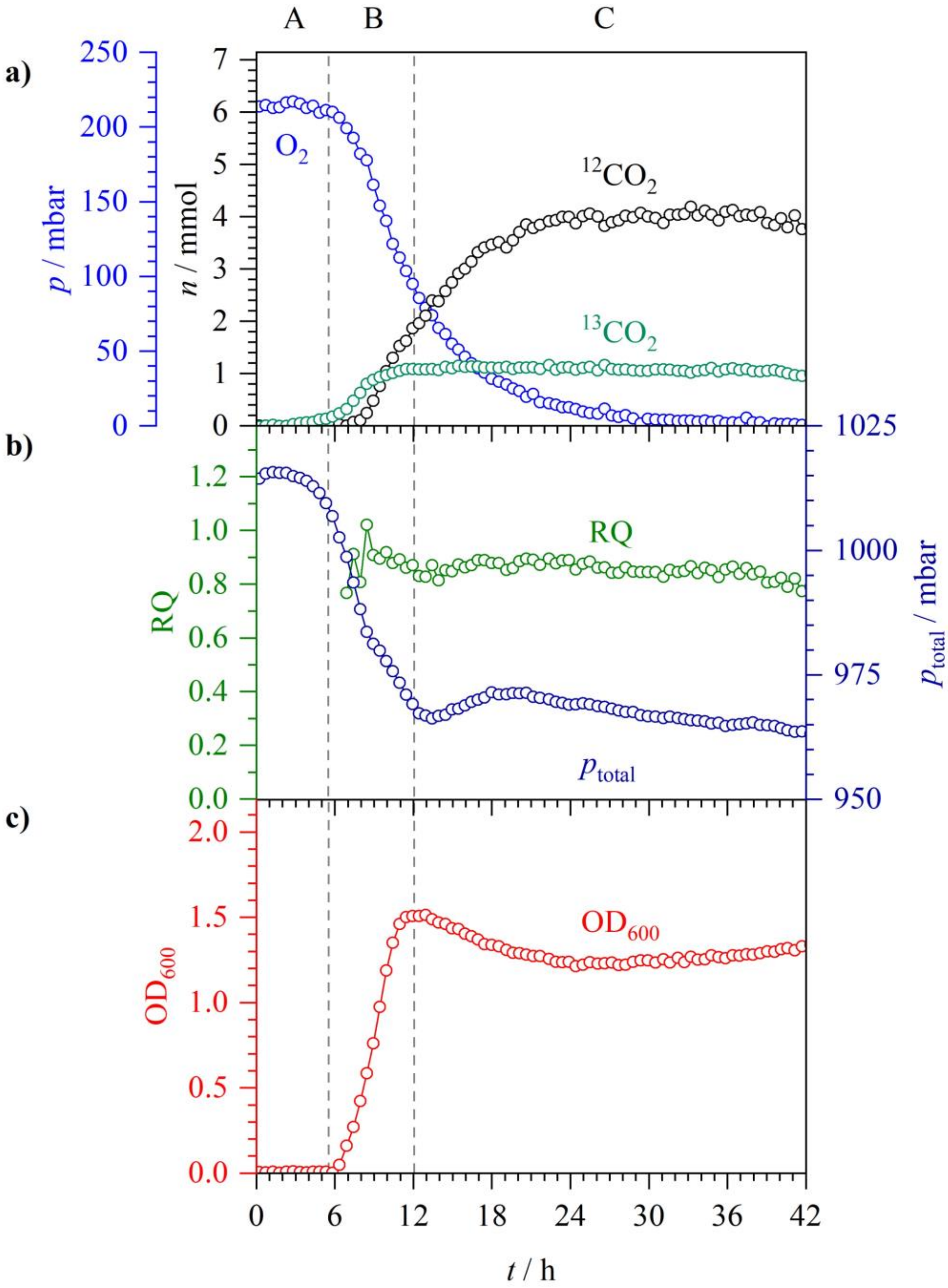

Figure 2.20 – CERS measurement of aerobic *E. coli* growth in M9 medium supplemented with 3 mM ^{13}C-glucose and 20 mM ^{12}C-lactose. A to C denotes three distinct phases: lag (A), exponential (B) and stationary (C) phases. **a)** n and p of O$_2$, ^{13}CO$_2$ and ^{12}CO$_2$. **b)** RQ and p_{total}. **c)** OD$_{600}$.

Figure 2.20 is a typical example of the aerobic growth of *E. coli* in M9 medium supplemented with 3 mM ^{13}C-glucose and 20 mM ^{12}C-lactose as measured by the CERS set-up. The DHR set-up is also capable of distinguishing ^{13}CO$_2$ and ^{12}CO$_2$ but for simplicity a typical CERS experiment is presented for the inclusion of the *in situ* OD$_{600}$ measurements; the DHR results and all repeats have essentially the same qualitative and quantitative behaviour.

As before, there is a lag phase **A** (0 – 6 h), exponential phase **B** (6 – 12 h) and stationary phase **C** (> 12 h). At 12 h, the OD_{600} peaks around 1.8 before declining and then rising again in stationary phase **C**; this behaviour seems to be typical for lactose metabolism under these experimental conditions, as discussed prior. As before, the RQ is less than unity, which is attributed to incomplete oxidation of the sugars to CO_2 as M9 medium does not contain any alternative catabolizable carbon sources for biosynthesis.

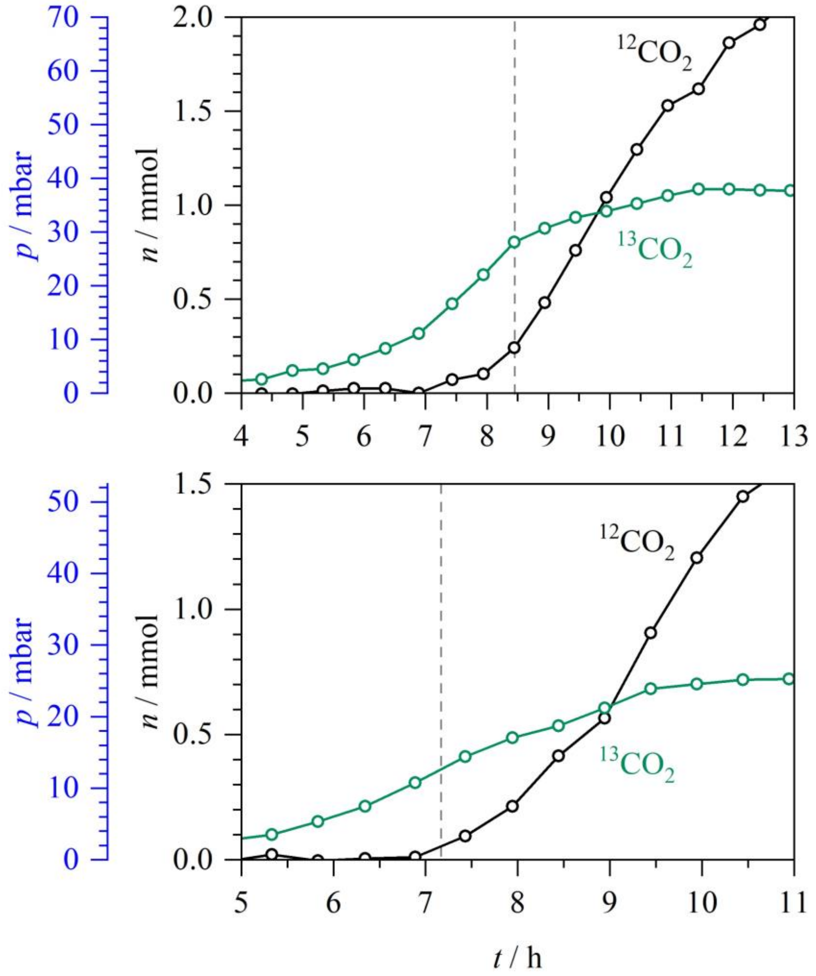

Figure 2.21 – *n* and *p* of $^{13}CO_2$ and $^{12}CO_2$ produced during *E. coli* glucose-lactose diauxie. CERS measurement of 3 mM ^{13}C-glucose and 20 mM ^{12}C-lactose (top) and DHR measurement of 2.5 mM ^{13}C-glucose and 20 mM ^{12}C-lactose (bottom). The dashed line indicates the time at which $^{12}CO_2$ is first observed.

In Figure 2.20, there was no apparent diauxic lag phase in the OD_{600} measurements. Instead, the glucose-lactose diauxie under our experimental conditions can only be distinguished by the use of the $^{13}CO_2$ and $^{12}CO_2$ isotopomers. Figure 2.21 are two typical examples of glucose-lactose diauxie, one recorded by CERS and the other by DHR. The CERS example (top panel) is a zoom-in of the data displayed in Figure 2.20. In both examples, during the exponential growth phase **B**, there is a clear shift from glucose metabolism to lactose metabolism, as indicated by the dashed lines in Figure 2.21. When glucose is nearly exhausted, lactose metabolism begins, without any apparent diauxic lag phase. In addition there is possibly some overlap between glucose and lactose metabolism. Similar observations were made by Wang *et al.* in which *Saccharomyces cerevisiae* natural isolates growing in mixtures of glucose and galactose would switch to metabolizing both sugars before all of the supplemented glucose was exhausted [134]. They stated that classic diauxic growth with a distinct diauxic lag phase is one extreme on a continuum of growth strategies determined by a cost–benefit trade-off.

In the literature, under conditions similar to those in our experiment, diauxic lag phases typically of up to 1 h have been reported for the diauxic shift from glucose to lactose in *E. coli*, often including OD measurements which showed an increase during glucose metabolism and then a lag phase (stationary OD), followed by a further increase attributed to lactose metabolism [114, 135]. In the experiments presented in this chapter, no prolonged diauxic lag phase is apparent in the O_2 consumption, CO_2 isotopomer production or in the OD_{600} measurements. Instead, a smooth transition with some overlap from glucose to lactose metabolism is observed. Diauxic growth is not always made apparent by a prolonged diauxic lag phase. Chu and Barnes proposed a hypothesis that the length of the diauxic lag phase depends on the characteristics of the environment [136]. Bacteria growing in rapidly changing environments need to be able to rapidly adapt between two sugars. Our environment is distinct from the majority of previous work studying diauxic shifts because it is O_2-limited, and the effects of rapidly depleted O_2 levels on the glucose–lactose diauxic growth of *E. coli* are as of yet unknown. Hence, without the spectroscopic detection of the $^{13}CO_2$ and $^{12}CO_2$ isotopomers, the glucose-lactose diauxie under our experimental conditions would not be apparent.

2.4 Conclusion

Measuring the headspace above bacterial suspensions by spectroscopy to characterise bacterial growth and metabolism has many advantages compared to more conventional techniques. It is non-invasive, it does not require sampling and, thus, can be applied to closed systems easily and it is very sensitive and highly selective because of the spectroscopic fingerprint of headspace gases. The high selectivity allows isotopic distinction, which enables isotopic labelling studies. This chapter has introduced two powerful new techniques for headspace monitoring: cavity-enhanced Raman spectroscopy (CERS) and photoacoustic detection in a differential Helmholtz resonator (DHR). Both techniques have been shown to be able to monitor O_2 and CO_2 and its isotopomers with excellent sensitivity and time resolution. Compared to DHR, CERS has the advantage of easier calibration due to the availability of internal standards (N_2). Without further modifications, the CERS method can also detect other important gases in the metabolism of bacteria, such as H_2, H_2S, or N_2. DHR has the advantage of a much simpler setup and being even more cost-effective. The technique can measure O_2, CO_2, and H_2S with high sensitivity and selectivity; extension to the detection of other molecules would require different diode laser sources, however.

OD measurements are a standard, widely used technique to characterise bacterial growth, albeit indirectly. They suffer from interferences, and they cannot distinguish living cells from dead cells and debris. OD measurements can therefore not provide sufficient information once the OD becomes constant during the stationary phase of bacterial growth. They also cannot distinguish diauxic growth without a diauxic lag phase present. The spectroscopic measurements, however, can clearly and unambiguously distinguish the different stages of bacterial growth characterising the growth phases in the different media studied, LB and M9, without OD measurements. This chapter demonstrates how ^{13}C-isotopic labelling of sugars in the spectroscopic detection allows the study of glucose-lactose diauxie which, for *E. coli* under O_2 limited conditions, has been characterised without a classic Monod-style diauxic lag phase

CERS and DHR have been proven to be cost-effective, highly specific analytical tools in the biosciences and in biotechnology, complementing and, in some cases, superseding existing conventional techniques. They also provide new capabilities for mechanistic investigations, in particular due to the possibility to use isotopic labelling easily.

Chapter 3

On-line Analysis and *in situ* pH Monitoring of *E. coli* Mixed-Acid Fermentation by FTIR and Raman Spectroscopies

Abstract

Mixed-acid fermentation of glucose by *E. coli* is monitored by FTIR headspace gas detection of CO_2, acetaldehyde and ethanol and liquid-phase Raman spectroscopy of acetate, formate, glucose and phosphate buffer anions. The best spectral features for detection are discussed with how to obtain the partial pressures and concentrations of compounds by integrations and least-squares fitting procedures of the features.

Liquid-phase Raman detection affords noise-equivalent (1 σ) detection limits of 0.8 mM acetate, 0.4 mM formate, 0.5 mM glucose, 0.5 mM HPO_4^{2-} and 0.6 mM $H_2PO_4^{-}$ at 1 h integration time. The measurement of the phosphate buffer anions allows the spectroscopic, *in situ* pH determination of the bacterial culture *via* a modified Henderson-Hasselbalch equation which uses activities instead of concentrations to extend the useful range of the equation to moderately strong electrolytes ($I < 0.5$). Without this correction, the calculated pH of a typical phosphate buffer is too high by up to 0.4. The 4 m White cell FTIR measurements provides noise-equivalent (1 σ) detection limits of 0.21 µbar acetaldehyde and 0.26 µbar ethanol in the gas-phase, corresponding to 3.2 µM acetaldehyde and 22 µM ethanol in solution, using Henry’s law. The analytical dynamic range exceeds 0.5 mbar ethanol, corresponding to 41 mM in solution. The bacterial culture is also sampled for conventional gas chromatographic analysis of acetate and ethanol showing good agreement with the spectroscopic methods.

The mixed-acid fermentation of glucose by *E. coli* is studied with the changes in pH and the production of CO_2, acetate, formate, acetaldehyde and ethanol discussed in the context of the fermentative pathways. Acetate and formate are excreted from the cell causing the extracellular pH to decrease. When the pH becomes too acidic, acetate excretion stops and formate is reimported to be disproportionated to H_2 and CO_2 by formate hydrogenlyase.

The work presented in this chapter covers two scientific publications (refs. [137, 138]);

Using Activities to Correct the Henderson-Hasselbalch Equation
Michael Hippler and George D. Metcalfe (2020).
Bunsen-Magazin. **22**, 102-105.
https://doi.org/10.26125/y7p7-an56

Author Statements

M. Hippler conceived the project, assembled the research team, designed the research, supervised the research, analysed data, prepared figures for publication and wrote the paper. G. D. Metcalfe conducted the research, analysed data and wrote the paper.

On-line Analysis and in situ pH Monitoring of Mixed Acid Fermentation by Escherichia coli Using Combined FTIR and Raman Techniques
George D. Metcalfe, Thomas W. Smith and Michael Hippler (2020).
Analytical and Bioanalytical Chemistry. **412**, 7307-7319.
https://doi.org/10.1007/s00216-020-02865-5

Author Statements

G. D. Metcalfe designed all experiments, conducted the research, analysed data, prepared figures for publication and wrote the paper. T. W. Smith analysed data and wrote the paper. M. Hippler conceived the project, assembled the research team, designed the research, supervised the research, analysed data and wrote the paper.

3.1 Introduction

Microbial fermentation is a fascinating and important process with broad relevance to the fields of biotechnology, environmental science, and medicine. In the absence of terminal electron acceptors, such as O_2, various forms of fermentation are carried out by many facultative and obligate anaerobes in order to obtain energy to sustain growth and cellular functions [48]. The production of organic compounds characterises all microbial fermentations; in some cases, these products can be valuable chemical intermediates or commodities such as with acetone-butanol-ethanol (ABE) fermentations [139] or the brewing process carried out by *Saccharomyces cerevisiae* [140].

E. coli utilises a mixed-acid fermentation when grown anaerobically with glucose (see Figure 1.16) with up to one-third of carbon derived from glucose converted to formate [48]. Above an extracellular pH of 7, the major fermentation products are acetate, ethanol, and formate [141]. Acidic products are excreted to prevent cytoplasmic acidification. When the extracellular pH decreases below 6.8, formate is reimported back into the cell to be disproportionated to H_2 and CO_2 by the formate hydrogenlyase (FHL) complex [53]. Two additional hydrogenases are also expressed, which can then reoxidise H_2 [51, 99]. As an additional strategy during later fermentation stages, *E. coli* switches to lactate production instead of acetate and formate to minimise further acidification [141, 142]. Given its wide range of fermentation products, *E. coli* has been investigated as a potential platform for biologically produced biohydrogen, bioethanol, succinic acid and biopolymers such as polylactic acid (PLA) [143, 144]. As FHL activity to produce H_2 is dependent on the pH, it is a critical control parameter in the conversion of organic feedstock to biohydrogen.

Spectroscopic techniques are powerful analytical tools which allow for rapid, selective, and on-line measurements. The non-invasive nature of using light to probe a bacterial culture in a closed system also enables greater confidence in preventing contamination. FTIR and other techniques using mid-IR wavelengths are sensitive as they rely on strong fundamental vibrational transitions. While they do find some application, their usefulness is limited in solution to some extent by the broad absorption profile of water over almost the entire region. In a couple of previous studies, liquid-phase FTIR has been applied to monitor bioprocesses, usually employing an attenuated total reflection (ATR) probe immersed in the suspension. Examples include monitoring glucose and lactic acid in *Lactobacillus casei* fermentation [145], glucose and acetate in *E. coli* fermentation [146] or the fermentation of phenoxyacetic acid to penicillin V by *Penicillium chrysogenum* [147]. Compounds can be detected at millimolar levels, but the probes require sterilisation before use which introduces issues with disassembling the equipment and maintaining optical performance. In contrast, in the vapour phase, the lack of complex hydrogen-bonded networks of water molecules leads to narrower and better defined absorption bands, with windows which are relatively free of water vapour, enabling sensitive detection of volatile organics and oxygen-containing compounds without interference from water.

For direct analysis of the liquid-phase, near-IR (NIR) spectroscopy is much more widely applied in bioprocess and fermentation monitoring [148-151] due to the much weaker absorption profile of water in this region. However, the spectral features observed in NIR spectroscopy are overtone or combination transitions that are also weaker, typically by at least an order of magnitude compared with the corresponding fundamental transitions, reducing the inherent sensitivity. Also, such overtone bands are broad and typically less characteristic with significant overlap of spectral features from different compounds, leading to the use of complex mathematical models which are not easily transferable between different systems or media types. In a recent comparison of NIR with ATR-FTIR monitoring of fermentation processes, NIR has been found to have high prediction errors due to light scattering and the lack of distinctive and sharp spectral features [145].

Raman spectroscopy is a complementary technique to absorption-based techniques; like NIR spectroscopy, Raman spectroscopy is comparatively insensitive towards water although bands are typically far more characteristic of the compounds being measured. Raman spectroscopy has seen extensive applications in biotechnology [152-154] including in lignocellulosic fermentation for bioethanol production [155]. In most applications, a Raman probe is inserted into the suspension which introduces problems maintaining sterile conditions, optical performance and disassembling the reactor for sterilisation before use. As an example, in a previous Raman application to monitor glucose, acetate, formate, lactate, and phenylalanine in the aerobic metabolism of *E. coli*, changes in optical characteristics of the probe and its sapphire window after steam sterilisation have been reported [152]. Although theoretical detection limits of the order of 0.1 mM at 300 s integration have been predicted to be possible, sensitivity is ultimately limited and compromised due to systematic errors caused by spectral shifts between reference and sample spectra [152]. Severe interferences are possible in Raman spectroscopy due to fluorescence, in particular, if growth media like lysogeny broth (LB) are used that are coloured and have visible absorption bands [156]. This limitation requires careful design and selection of excitation wavelength. Raman spectroscopy itself is not a very sensitive technique due to low scattering cross sections. One technique to overcome sensitivity issues is to apply resonance Raman spectroscopy; this requires analytes having absorption bands close to the excitation wavelength, but not overpowering Raman signals by fluorescence. This condition, however, is only achieved in special cases, like carotenoid detection at micromolar levels in yeast fermentation at 785 nm Raman excitation [157]. In addition to applications in process monitoring, vibrational spectroscopies are powerful emerging tools for *in situ* bacterial species identification [158].

This chapter describes and characterises the performance of a combined non-invasive FTIR and Raman approach in the gas-phase and in solution, respectively, for monitoring and controlling microbial fermentation, with the mixed-acid fermentation of *E. coli* serving as a particularly relevant example. By using Raman monitoring of the two major phosphate species of the phosphate buffer present in M9 minimal medium, it is possible to spectroscopically determine the pH of the growth medium. The pH is an important parameter in fermentation processes, and the theoretical basis of this analysis is derived. Critical issues associated with electrochemical probes, including contamination and long-term drift, are avoided by being able to measure the pH *in situ*, accurately and on-line. Combined with continuous optical density (OD) measurements, a conventional measure of bacterial growth and cell density, interesting insights into the metabolism of the cell and the production of acids, ethanol, and formate disproportionation are obtained.

3.2 Experimental

3.2.1 Bacterial Growth Conditions

E. coli K-12 MG1655 was transferred from – 80 °C glycerol stocks, struck on LB-agar plates and incubated overnight at 37 °C. Starter cultures were prepared by inoculating 50 mL of LB medium with a single colony from the plate and incubating overnight (37 °C, 200 rpm) in a sealed 50 mL centrifuge tube for anaerobic growth conditions. Overnight, the anaerobic starter cultures grew to a typical OD_{600} of 1.2. Ultimately, 1 mL of the starter culture was centrifuged and the bacterial pellet resuspended into 1 mL of fresh M9 medium to be added to a further 60 mL when starting experiments. The M9 medium was supplemented with 30 mM glucose, as in Section 2.2.1, but with added anaerobic trace elements of 9 µM $NiCl_2$, 4 µM Na_2SeO_3 and 3.2 µM Na_2MoO_4. The entire M9 minimal medium formulation contained:

48 mM Na_2HPO_4
30 mM glucose
22 mM KH_2PO_4
18 mM NH_4Cl
8.5 mM NaCl
1 mM $MgSO_4$
1 mM thiamine
300 µM $CaCl_2$
135 µM Na_4EDTA
57 µM H_3BO_3
31 µM $FeCl_3$
9 µM $NiCl_2$
6.2 µM $ZnCl_2$
4 µM biotin
4 µM Na_2SeO_3
3.2 µM Na_2MoO_4
2.7 µM $CoCl_2$
1.3 µM $MnCl_2$
0.2 µM $CuSO_4$

3.2.2 The Experimental Set-up

Before starting each experiment, 60 mL of M9 medium was prepared in a 100 mL custom five-neck flask and submerged in a 37 °C water bath under rapid stirring for efficient gas transfer. The flask was sealed after adding the 1 mL of media containing *E. coli* from the starter culture. A scheme of the experimental set-up is shown in Figure 3.1 and a photograph of the set-up is shown in Figure 3.2. From the left-neck, the bacterial culture was cycled by a peristaltic pump (**PP-L**, 4.5 L h^{-1}) for *in situ* OD_{600} and liquid-phase Raman measurements. The OD_{600} measurements were obtained as outlined in Section 2.2.2, using a laser pointer (**LP**), 1 cm sealed glass cuvette and photodiode (**PD**). From the right-neck, the headspace gases were cycled by a peristaltic pump (**PP-G**, 4.5 L h^{-1}) for gas-phase FTIR measurements in a long-path White cell (**WC**). The White cell and the gas transfer tubes were warmed to *ca.* 50 °C by heating wire to prevent water condensation on the internal optics. The total headspace gas volume was 525 mL. The middle-neck was equipped with a Suba-Seal rubber septum to allow sampling of the culture for gas chromatography analysis. Not shown in Figure 3.1 are the two other necks, one leading to a vacuum pump and the other connecting to a N_2 cylinder. Before starting experiments, alternating between these vacuum and N_2 lines several times enabled purging of O_2 from the closed system to give anaerobic growth conditions.

Bacterial cultures were monitored until no further CO_2 production was observed due to the depletion of oxidisable carbon sources. Endpoint measurements of the pH and dry biomass were recorded for each experiment. The bacterial suspension was centrifuged at the end of each experiment and the pH of the supernatant was recorded using a Mettler Toledo SevenMulti pH meter (glass electrode with internal Ag/AgCl reference). The dry biomass was typically around 30 mg in total and was measured by weighing the centrifuged cellular material after decanting off the supernatant and allowing the pellet to dry in a 37 °C oven.

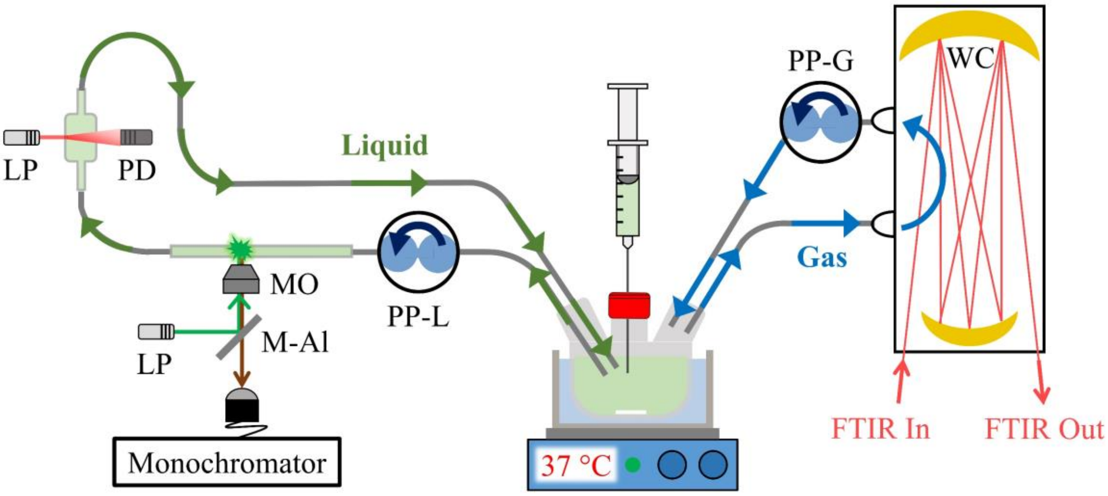

Figure 3.1 – The experimental set-up. Headspace analysis by White cell FTIR spectroscopy and liquid-phase analysis by Raman spectroscopy and OD_{600}. **LP**, laser pointer; **M-Al**, mirror (glass slide with 2 mm × 3 mm Al spot); **MO**, microscope objective; **PD**, photodiode; **PP-G,** gas-phase peristaltic pump; **PP-L**, liquid-phase peristaltic pump; **WC**, White cell.

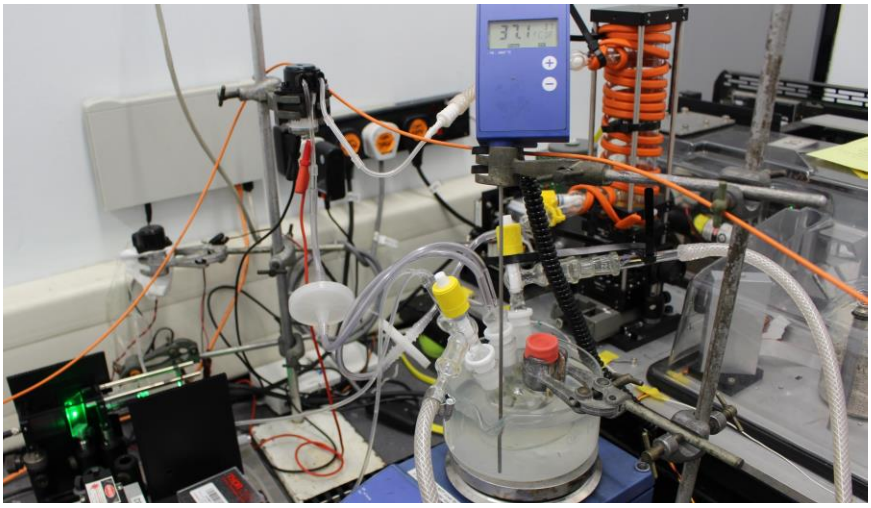

Figure 3.2 – Photograph of the experimental set-up.

3.2.3 Liquid-Phase Raman Spectroscopy

The home-built liquid-phase Raman spectrometer in the present experiment was first described in a publication from 2010 [159]; however, several modifications have been implemented since then. A schematic of the Raman spectrometer is shown in Figure 3.3. The optical components are mounted on a 250 mm × 250 mm × 10 mm aluminium plate. A frequency doubled Nd:YAG laser (**LP**, Lasos, GL3dT) emitted 20 mW of linearly polarized 532.2 nm radiation. The green light was turned 90° by a mirror (**M-Al**) and coupled into a microscope objective (**MO**). The mirror needed to be as small as possible so that it did not take away too much of the backscattered Raman light so a 2 mm × 3 mm oval aluminium film deposited on a glass slide was used. The microscope objective was a 20 ×, 0.50 NA achromatic objective (OptoSigma, 028-0220) with a large clear aperture (8.2 mm). The objective focussed the laser light very tightly at 2 mm distance from the objective front into the sample tube (**ST**) through which the bacterial culture was circulated. The sample tube was simply a borosilicate glass NMR tube with the bottom removed to give two openings. The sample volume was essentially the focus volume with an estimated spatial resolution below 100 μm.

Raman backscattered light (180° detection geometry) was collimated by the same microscope objective. The oval aluminium film blocked some of the Raman light but the majority passed through the glass slide. To stop unwanted Rayleigh light from reaching the detector, the Raman light passed through a filter (**F**, SCHOTT, OG-550, orange colour) and was then focused with an *f* = 25.4 mm lens (**L**) into a glass fiber (**GF**, 100 μm core SMA fiber patch cable) and transmitted to the monochromator, which was the Czerny-Turner spectrograph (Shamrock SR-750-A, f = 750 mm) equipped with a CCD camera (Andor iVac DR32400, cooled at −60 °C) previously described in Section 2.2.3. The high resolution grating (1200 lines mm^{-1}, blazed at 750 nm) provided an 880 cm^{-1} spectral range from 830 to 1710 cm^{-1} at about 0.8 cm^{-1} resolution. After wavenumber calibration, Raman peak position accuracy was estimated to be ± 3 cm^{-1}. Spectra were recorded every 5 min in ten accumulations of 30 s. The spectral range covered characteristic acetate, formate, glucose, phosphate (HPO_4^{2-} and $H_2PO_4^-$) and water peaks, as discussed further in Section 3.3.1. A photograph of the liquid-phase Raman spectrometer is shown in Figure 3.4.

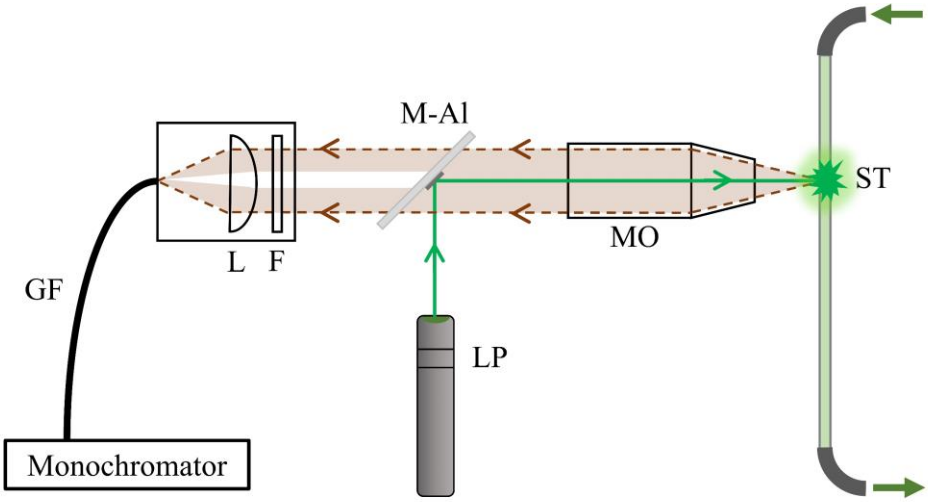

Figure 3.3 – The liquid-phase Raman spectrometer. **F**, filter; **GF**, glass fiber; **L**, lens; **LP**, laser pointer; **M-Al**, mirror (glass slide with 2 mm × 3 mm Al spot); **MO**, microscope objective; **ST**, sample tube.

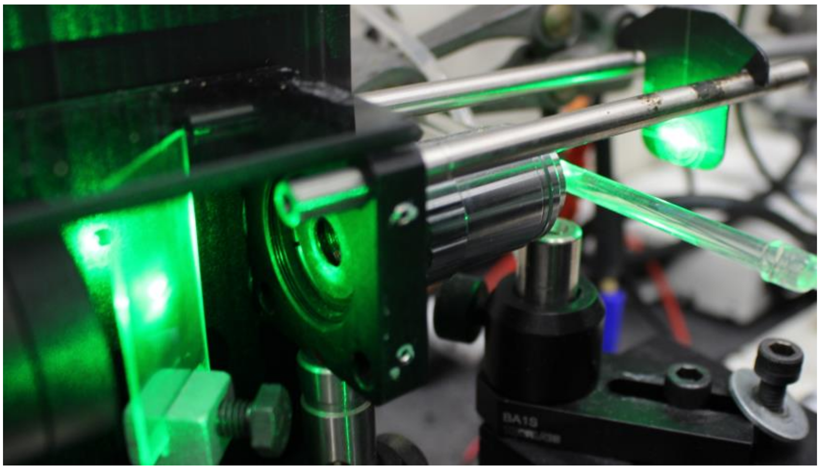

Figure 3.4 – Photograph of the home-built Raman spectrometer, showing a closeup of the oval aluminum film deposited on a glass slide, microscope objective and sample tube.

3.2.4 White Cell FTIR Spectroscopy

The home-built multiple-pass absorption White cell was constructed by a previous PhD student, Thomas W. Smith [160]. The classical White cell design is based around three concave mirrors arranged in a V-shaped configuration, as shown in Figure 3.5. Note that for simplicity the White cell design in Figure 3.5 shows eight passes while the home-built White cell is capable of up to forty passes. Steering mirrors are used to divert the IR beam into and out of the sealed measurement cell. The IR beam is reflected back and forth between two upper mirrors (A and C) and the lower field mirror (B). All three mirrors have the same focal length and are separated at twice the focal length (the radius of curvature). The total number of passes is dictated by how the upper mirrors A and C are angled relative to the incoming and outgoing beam. The number of passes supported by a White cell must be a multiple of four and is equal to $2(N + 1)$ where N is the number of spots on the field mirror. Each cycle of four consists of the IR beam passing from the field mirror (or the IR window for the first cycle) to one of the upper mirrors, then being reflected back to the field mirror, next to the second upper mirror and finally returning to the field mirror (or the IR window for the final cycle).

The home-built White cell was constructed after the silver mirrors in a commercial White cell corroded over time due to hydrogen sulfide measurements. The home-built White cell used two gold coated mirrors (Thorlabs, $f = 100$ mm, 2 inch diameter) as gold has good chemical resistance towards hydrogen sulfide and thiols. Although gold has poor reflectivity for visible light, due to the surface plasmon resonance bands, its reflectivity in the MIR range is excellent which covers 98 % of the fundamental region of FTIR spectra. One of the gold coated mirrors was cut along the diameter to give the two upper, refocusing mirrors (A and C). Two wedges were cut from the field mirror (B) to make it T-shaped. Apart from reflection loses, the maximum number of passes is usually limited by the total number of reflections that can fit along the field mirror diameter. A T-shaped mirror allows the incoming beam to enter the White cell slightly away from the field mirror to generate two rows of reflections, as shown in Figure 3.6. This design made more efficient use of the mirror surface by allowing a larger number of passes to be accommodated without increasing the mirror diameter. The White cell mirrors were aligned using a 636 nm HeNe laser collinear with the IR beam during construction, this allowed up to nineteen reflections to be visualised on the field mirror. Nineteen spots was the maximum number possible corresponding to forty passes and a folded pathlength of 8 m, based on the 20 cm base length. The White cell was aligned for twenty passes or a 4 m folded pathlength for the data presented in this chapter. In later chapters, the White cell was realigned for thirty passes or a 6 m folded pathlength.

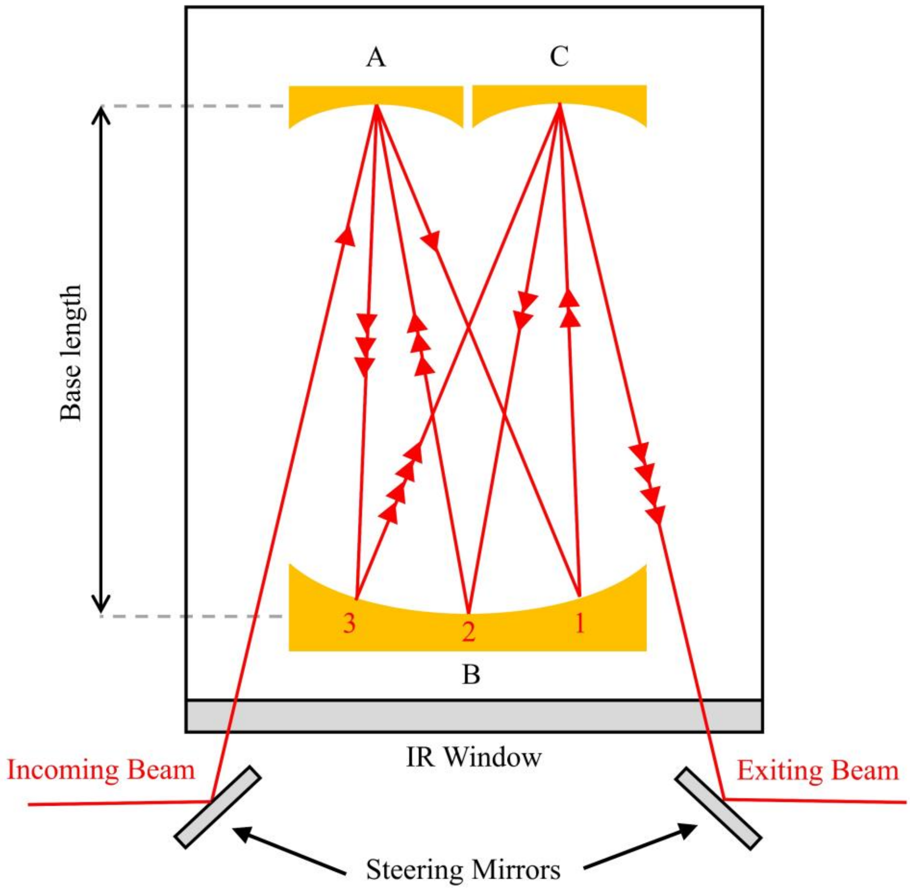

Figure 3.5 – The basic design of an eight-pass White cell. Mirrors A and C are the refocusing mirrors while mirror B is the field mirror. The three concave mirrors have the same focal length.

The gold coated mirrors were placed inside a custom glass cylindrical enclosure, 250 mm long with 55 mm diameter, containing two ports that could be isolated by Young valves for static measurements or left open for continuous gas flow. Calcium fluoride was selected for the IR window (Crystran Ltd., 55 mm diameter, 3 mm thickness) as it offered a good compromise between moisture resistance and good transmission over most of the IR and visible region. Despite calcium fluoride cutting off wavenumbers below 1000 cm^{-1}, meaning that low energy vibrational modes could not be observed, most small molecules have their fundamental absorption bands at relatively high wavenumbers, with stretching modes typically above 1500 cm^{-1}. Salt optics such as sodium chloride or potassium bromide cut off at much lower wavenumbers, but they are very hydroscopic making them unsuitable for the analysis of bacterial cultures. Calcium fluoride is insoluble in water making it ideal for analysing liquid samples which produce excess water vapour inside the closed system. The sealed glass cell was mounted inside a 60 mm optical cage system (Thorlabs) to provide maximum rigidity and equipped with two plane diverting mirrors (Thorlabs, protected gold, 24.5 mm) for steering the IR beam. A photograph of the White cell and the FTIR instrument is shown in Figure 3.7. The spectral range of the FTIR instrument (Matteson Research Series FTIR, no apodisation, 128 scans, 0.4 cm^{-1} resolution, MCT detector) was from 1000 to 7000 cm^{-1}, limited at higher wavenumbers by the globar light source. The MCT detector was cooled by liquid N_2 and required refilling every 12 h. Spectra were recorded every 5 min and analysed for CO_2, acetaldehyde and ethanol partial pressures, as discussed in Section 3.3.3.

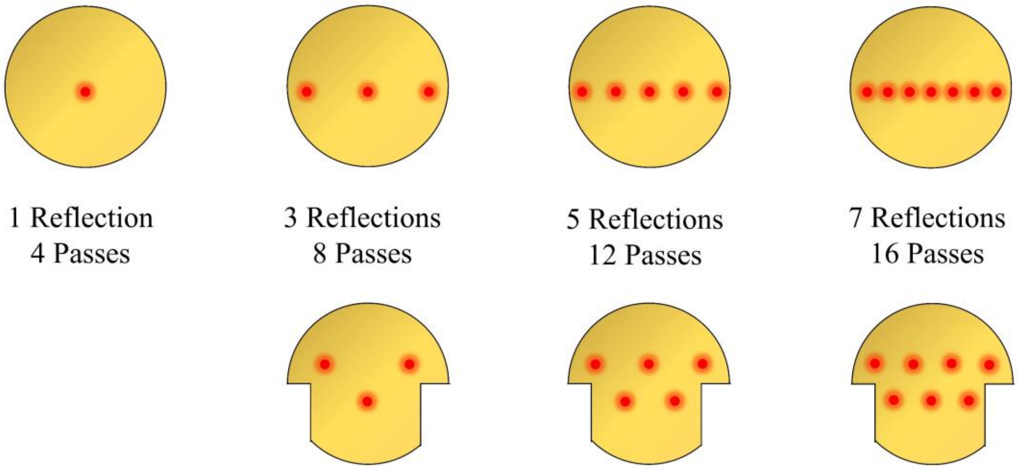

Figure 3.6 – The arrangement of reflections on the field mirror of a single row (top) and two row (bottom) White cell. The field mirror of a two row White cell is cut to be T-shaped.

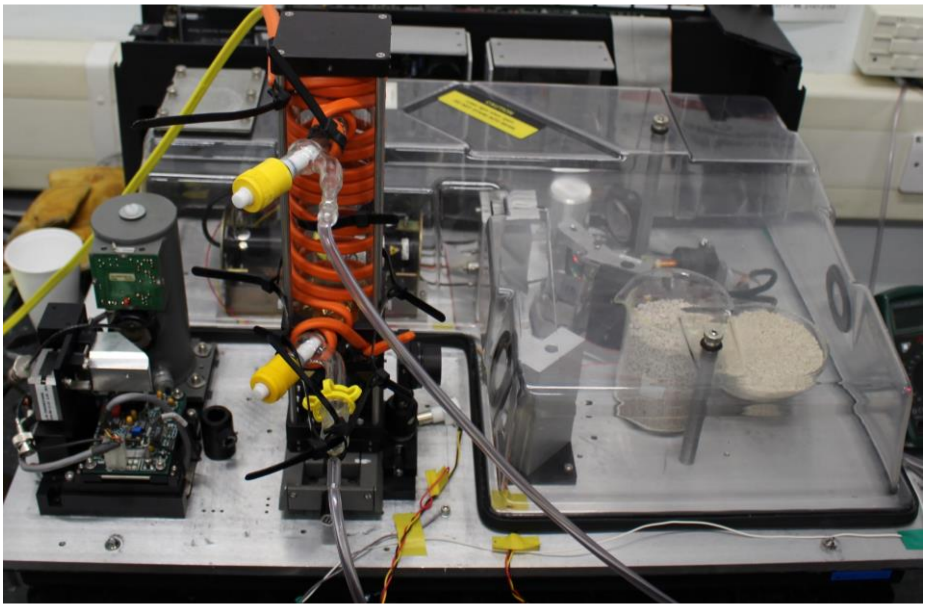

Figure 3.7 – Photograph of the White cell and FTIR spectrometer.

3.2.5 Gas Chromatography

The bacterial culture was sampled several times during experiments for gas chromatographic analysis of acetate and ethanol to compare with and to validate the liquid-phase Raman and gas-phase FTIR methods, respectively. The samples were centrifuged and 0.2 mL of the supernatant was dissolved in 0.8 mL acetone, then 0.3 μL of this solution was injected into the gas chromatograph (temperature programmed Agilent DB-WAX UI, with 1.4 mL min^{-1} H_2 carrier gas and flame ionisation detector). Retention times for ethanol and acetate were 4.5 and 11 min, respectively. From the gas chromatogram peak integrals, the concentrations of acetate and ethanol in the sample were determined by a calibration. The calibration plots are shown in Figure 3.8.

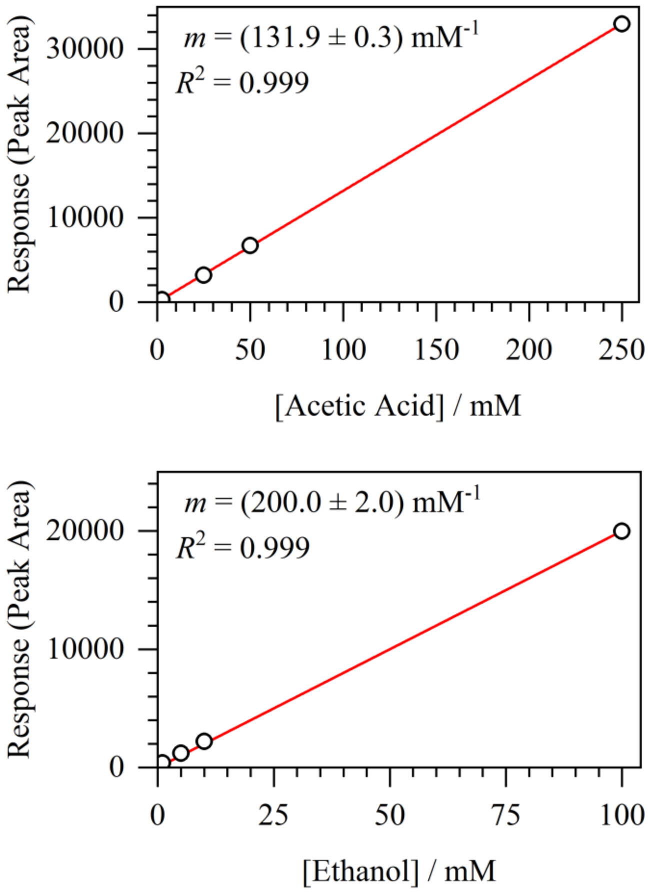

Figure 3.8 – Gas chromatography calibration plots for acetic acid and ethanol.

3.3 Results and Discussion

3.3.1 Analysing Liquid-Phase Raman Spectra

Raman spectra of mixtures in aqueous solution are generally complex with numerous overlapping features that may be very broad or relatively narrow and intense. Lower frequency peaks between 500 to 1100 cm^{-1} generally belong to the main vibrational modes of anions present in the solution [161]. At higher frequencies, Raman spectra exhibit wide bands corresponding to the vibrations of water: the OH bending (ν_2) and OH stretching bands, as shown in Figure 3.9. This experimental water Raman spectrum was acquired using the low resolution grating (150 lines mm^{-1}) for the greater spectral range. There is no generally accepted view on the nature of the OH stretching Raman peak and it has been proposed to be made up of several sub-bands (symmetric stretching, antisymmetric stretching, Fermi resonance with water bending overtone), as well as being sensitive to variations in hydrogen bonding between water molecules [162].

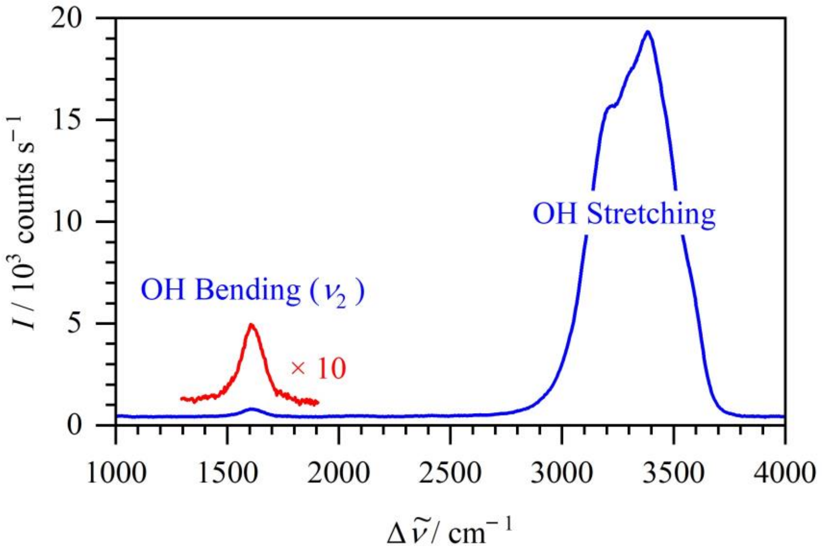

Figure 3.9 – Experimental liquid-phase Raman spectrum of water acquired using the low-resolution grating (150 lines mm^{-1}).

With the high-resolution grating (1200 lines mm^{-1}), liquid-phase Raman spectra were obtained within 830 – 1710 cm^{-1} which covered characteristic acetate, formate, glucose, monohydrogen phosphate (HPO_4^{2-}), dihydrogen phosphate ($H_2PO_4^{-}$) and water peaks. Note that the high resolution grating was necessary to distinguish these relatively sharp overlapping peaks. Intracellular acids and other metabolites may also have contributed to the experimental spectra. However, as the sum volume of the bacterial cells is significantly less than the volume of the growth medium, it can be assumed that the experimental spectra correspond mainly to the extracellular species in solution. For comparison and calibration, Raman reference spectra were obtained in borosilicate sample tubes. Raman spectra of the empty sample tube, water and fresh M9 medium are shown in Figure 3.10. The borosilicate sample tube spectrum had a broad silicate peak with $\nu_0 = 1040\ \mathrm{cm}^{-1}$ and FWHM = $110\ \mathrm{cm}^{-1}$. This silicate peak was present in all recorded spectra, for instance it can be seen in the water spectrum, but this artifact could be easily removed by subtracting the sample tube spectrum. The water bending vibration had $\nu_0 = 1630\ \mathrm{cm}^{-1}$ and a FWHM of $96\ \mathrm{cm}^{-1}$. This water peak was used to normalise spectra which was particularly relevant for the bacterial cultures which became more turbid with time resulting in weaker Raman signals. In the normalisation, the water peak was fitted with a Gaussian contour and it was assumed that the Gaussian area should be the same for all Raman spectra due to the large concentration of water (55.5 M for pure water) compared to the millimolar concentrations of species in solution. In addition to the silicate and water peaks, the fresh M9 medium spectrum contained overlapping features from the 30 mM glucose, 47 mM HPO_4^{2-} and 22 mM $H_2PO_4^{-}$.

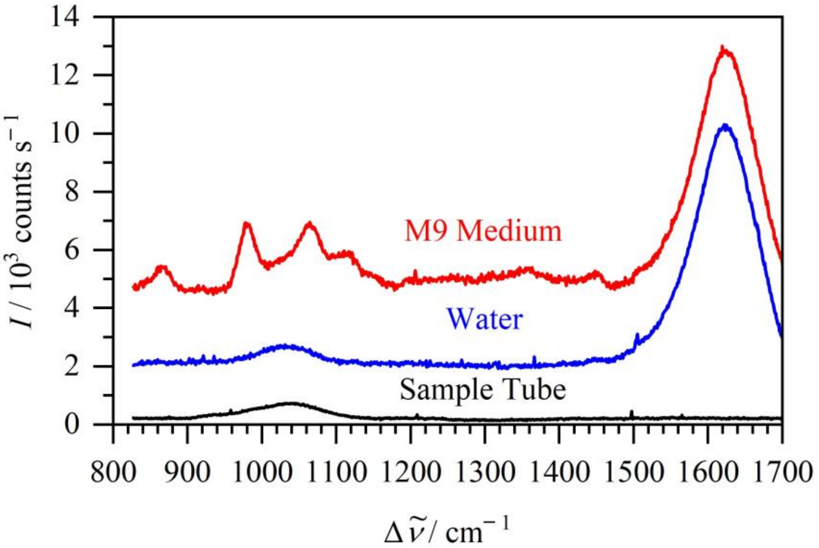

Figure 3.10 – Experimental Raman spectra of the empty borosilicate sample tube (black), water (blue) and fresh M9 medium supplemented with 30 mM glucose (red). Note that the offset in the baselines of the water and M9 spectra are artificially added for clarity.

Reference spectra of 100 mM each of glucose, HPO_4^{2-} and $H_2PO_4^{-}$ were recorded, normalised with the water peak and divided by one hundred to create model spectra corresponding to 1 mM of each species. An in-house written computer programme implemented a least-squares fit of each experimental Raman spectrum to the sum of the model spectra and a linear baseline. The result of one such fit for fresh M9 medium is shown in Figure 3.11. The HPO_4^{2-} peak at 989 cm^{-1} was due to the symmetric stretching of the PO_3 group while the two $H_2PO_4^-$ peaks at 867 and 1076 cm^{-1} originate from the symmetric stretching of the $P(OH)_2$ and the PO_2 groups, respectively [163].

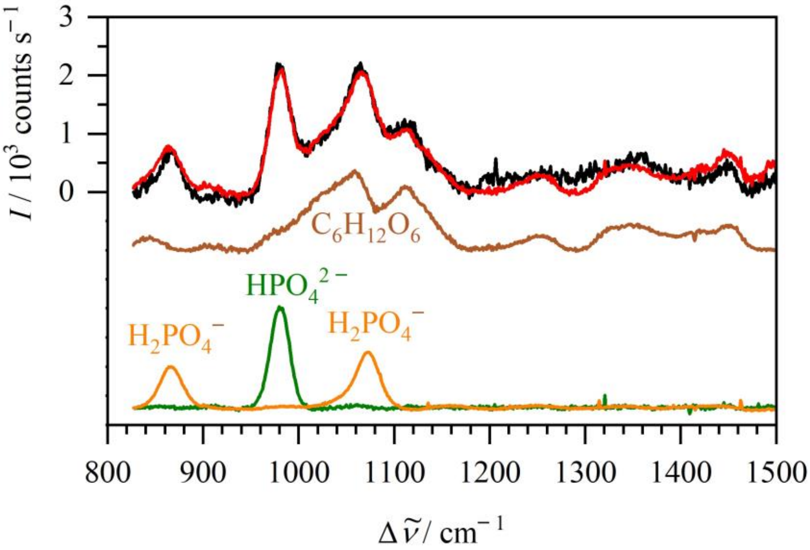

Figure 3.11 – In black, an experimental Raman spectrum of fresh M9 medium. In red, the sum of the 30 mM glucose, 47 mM monohydrogen phosphate and 22 mM dihydrogen phosphate models shown in brown, green and orange, respectively.

Glucose has numerous features in its Raman spectrum, for instance the out-of-plane ring deformations between 350 to 600 cm^{-1} and the C–H and O–H stretching bands above 2800 cm^{-1} [164]. Glucose has two distinct spectral regions in the range displayed in Figure 3.11. From 1000 to 1250 cm^{-1} are bands corresponding primarily to coupled heavy atom stretching motions involving both the ring and the hydroxyl groups. From 1200 to 1500 cm^{-1} are bands corresponding primarily to the coupled deformations of various H-containing functional groups, such as hydroxyl (–OH), methylene ($-CH_2-$) and methine (>CH–). Acetic and formic acids excreted during mixed-acid fermentation by *E. coli* will dissociate at neutral pH to the acetate and formate anions, releasing acidic protons. The phosphate buffer prevented severe acidification of the external medium by converting HPO_4^{2-} to $H_2PO_4^-$. The result of a least-squares fit of model spectra for an experimental Raman spectrum taken around 12 h into a fermentation experiment is shown in Figure 3.12. Glucose was depleted while almost the entirety of HPO_4^{2-} had been converted to $H_2PO_4^-$ due to the excretion of 30 mM acetate and 10 mM formate. The model spectra of acetate and formate were also produced from 100 mM reference spectra. Within our spectral range, acetate had three distinct peaks at 928, 1346 and 1414 cm^{-1} belonging to the C–C stretching, CH_3 deformation and C–O stretching vibrations, respectively [165]. The lone formate peak observed at 1349 cm^{-1} belonged to the C–O stretching vibration. Although the formate peak overlapped with the 1346 cm^{-1} acetate peak, the fitting routine could successfully distinguish the two species, as shown in Figure 3.13.

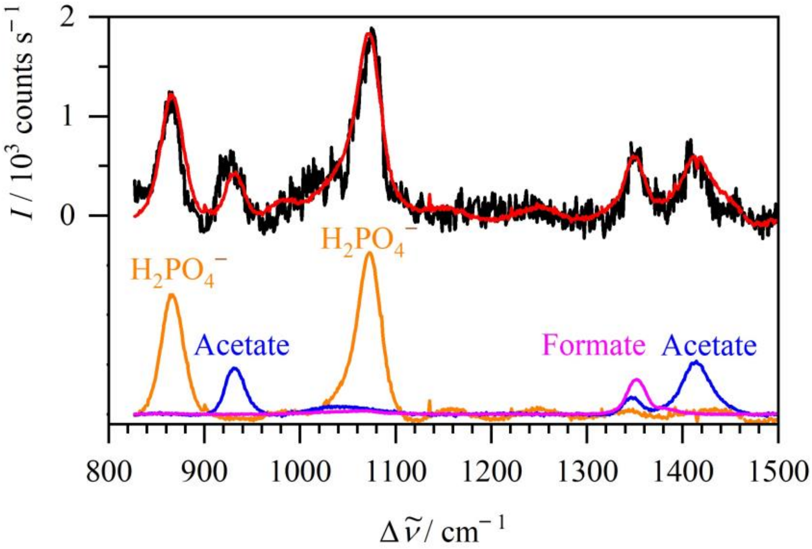

Figure 3.12 – In black, an experimental Raman spectrum of M9 medium during mixed-acid fermentation by *E. coli*. In red, the sum of the 30 mM acetate, 10 mM formate and 67 mM dihydrogen phosphate models shown in blue, pink and orange, respectively.

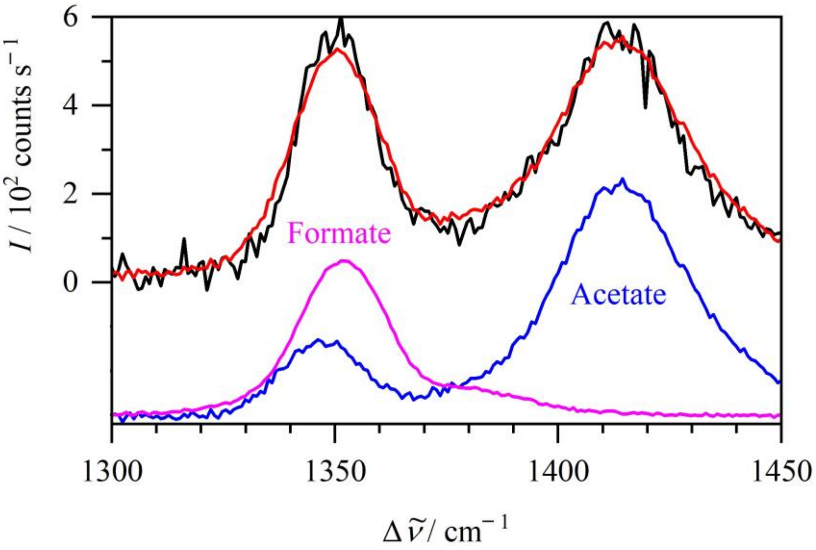

Figure 3.13 – A zoom into the overlapping acetate and formate peaks from the spectrum displayed in Figure 3.12.

The least-squares fit of an experimental Raman spectrum to the sum of the model spectra and a linear baseline returned multipliers for each model spectrum. A Gaussian contour was also fitted to the water bending peak in the experimental Raman spectrum for normalisation. The model spectra multipliers *x* were normalised by dividing by the water bending peak area to give *x*'. The normalised *x*' was converted to concentration *via* calibration plots, as shown in Figure 3.14. Excellent linearity (as shown by the R^2 value) and a good dynamic range were observed for all compounds. Note that error bars, as represented by the standard deviation of repeat measurements, were approximately the size of the data point symbols and were therefore not displayed in the calibration plots.

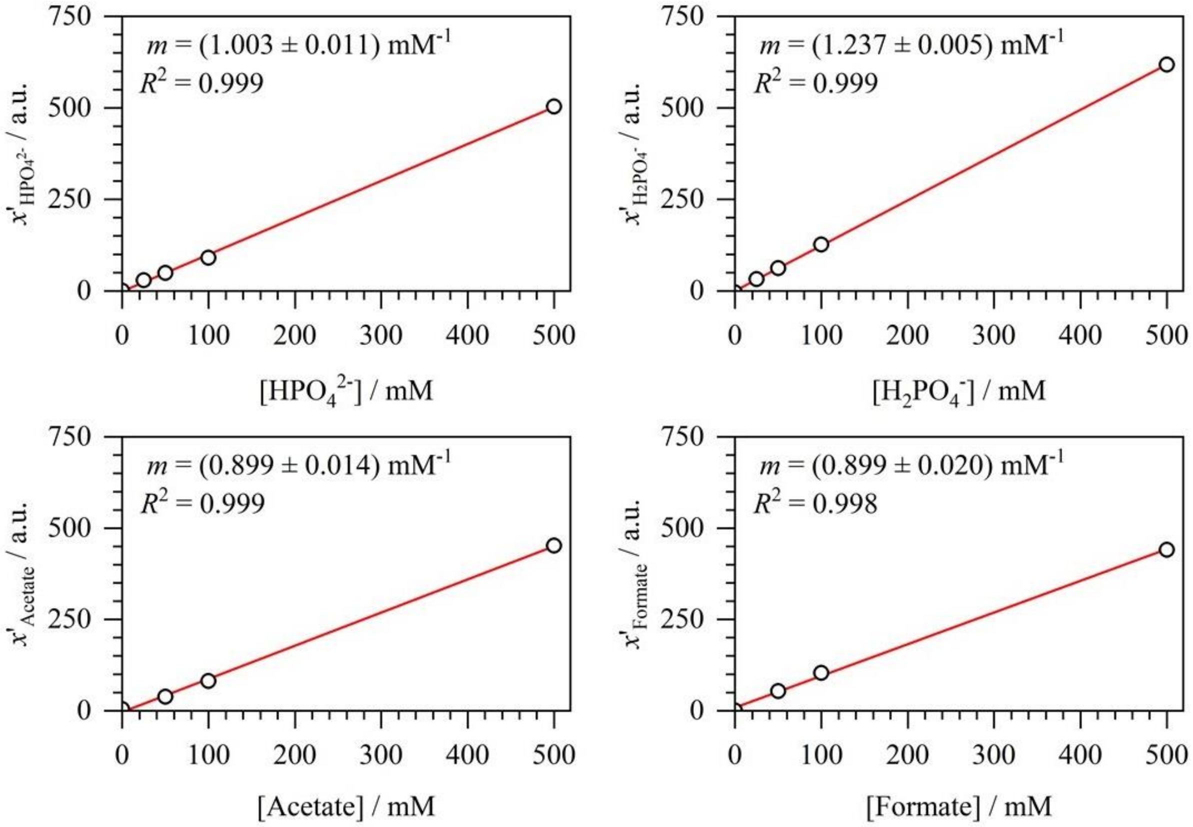

Figure 3.14 – Calibration plots of normalized Raman model spectrum multipliers *x*' against analyte concentrations in solution, including linear fit lines with gradients *m* and R^2 values.

By recording a series of Raman spectra and analysing the noise level (standard deviation) of the baseline (essentially a blank M9 sample), estimates of the noise-equivalent (1 σ) detection limits of each species were determined. With a standard signal integration time of 5 min (ten accumulations of 30 s), the detection limits were 2.6 mM acetate, 1.5 mM formate, 1.9 mM glucose, 1.9 mM HPO_4^{2-} and 2.0 mM $H_2PO_4^{-}$. With additional averaging of twelve spectra to an integration time of 1 h (as was done with the data displayed in Sections 3.3.2 and 3.3.4), the limits improved to 0.8 mM acetate, 0.4 mM formate, 0.5 mM glucose, 0.5 mM HPO_4^{2-} and 0.6 mM $H_2PO_4^-$. Note that these improved limits were calculated by assuming that the signal-to-noise ratio was proportional to the square root of the integration time.

Two main factors limit the analytical performance of liquid-phase Raman spectroscopy in bacterial culture analysis. First, with increasing cell density, the solution becomes progressively turbid and reduces Raman signal intensity. Increased turbidity seriously affects sensitivity and, more importantly, calibration. The calibration can be maintained using OD measurements or, as discussed prior, the water bending peak area. The second factor that frequently plagues Raman spectroscopy is interference by fluorescence which can mask Raman signals. Fluorescence was not a significant issue in M9 medium which is colourless and non-fluorescent. It has been shown before, however, that fluorescence can become limiting if coloured growth media such as LB are used [156]. Fluorescence can often be alleviated by moving to a longer wavelength Raman excitation, towards the red or near-IR.

3.3.2 *In Situ* pH Measurements

This section covers the publication '*Using Activities to Correct the Henderson-Hasselbalch Equation*' [137]. To prevent significant changes in pH, buffer solutions utilise the equilibrium between a weak Brønsted-Lowry acid (HA) and its conjugate base (A^-),

$$\mathrm{HA_{(aq)}} = \mathrm{H^+{}_{(aq)}} + \mathrm{A^-{}_{(aq)}} \tag{3.1}$$

and the pH of a buffer solution can be estimated by the Henderson-Hasselbalch equation,

$$\mathrm{pH} = \mathrm{p}K_\mathrm{a} + \log_{10}\left\{\frac{c(\mathrm{A^-})}{c(\mathrm{HA})}\right\} \tag{3.2}$$

where c denotes the concentrations of the acid-base pair and K_a is the thermodynamic equilibrium constant of the acid ionisation,

$$K_\mathrm{a} = \frac{a(\mathrm{H^+})\, a(\mathrm{A^-})}{a(\mathrm{HA})} \tag{3.3}$$

where $a(\mathrm{H}^+)$, for example, is the (dimensionless) activity of a hydrated proton H^+. The activity a of an ion is the concentration c divided by the standard concentration c^{o} ($1\ \mathrm{mol\ L}^{-1}$) multiplied by the activity coefficient γ which depends on the charge z of the ion and the composition of the solution, in particular on the ionic strength I,

$$I = \frac{1}{2}\sum_{\mathrm{i}=1}^{\mathrm{n}} c_i\ z_i^2 \tag{3.4}$$

Equation 3.5 is obtained by taking the $\log_{10}$ of both sides of Equation 3.3, identifying that $\mathrm{p}K_\mathrm{a} = -\log K_\mathrm{a}$ and $\mathrm{pH} = -\log a(\mathrm{H}^+)$ and finally rearranging,

$$\begin{aligned}\mathrm{pH} &= \mathrm{p}K_\mathrm{a} + \log_{10}\left\{\frac{a(\mathrm{A}^-)}{a(\mathrm{HA})}\right\} \\ &= \mathrm{p}K_\mathrm{a} + \log_{10}\left\{\frac{c(\mathrm{A}^-)}{c(\mathrm{HA})}\right\} + \log_{10}\left\{\frac{\gamma(\mathrm{A}^-)}{\gamma(\mathrm{HA})}\right\}\end{aligned} \tag{3.5}$$

The Henderson-Hasselbalch equation is essentially Equation 3.5 but approximating activities with concentrations by assuming that $\gamma(\mathrm{A}^-) = \gamma(\mathrm{HA})$. More complicated expressions are derived for polyprotic acids, but if the different ionisation constants are sufficiently separated, the reactions can be approximated by step-wise single ionisation reactions. This applies to phosphoric acid (H_3PO_4) with $\mathrm{p}K_{\mathrm{a},1} = 2.14$, $\mathrm{p}K_{\mathrm{a},2} = 7.20$ and $\mathrm{p}K_{\mathrm{a},3} = 12.34$ at 25 °C. For a phosphate buffer around pH = 7, the relevant ionisation reaction is

$$\mathrm{H_2PO_4}^-{}_{(\mathrm{aq})} = \mathrm{H}^+{}_{(\mathrm{aq})} + \mathrm{HPO_4}^{2-}{}_{(\mathrm{aq})} \tag{3.6}$$

By measuring the concentrations of $\mathrm{HPO_4}^{2-}$ and $\mathrm{H_2PO_4}^-$ using liquid-phase Raman spectroscopy, the pH of phosphate-buffered M9 medium could be estimated by the Henderson-Hasselbalch equation. However, this estimated pH was around the order of 0.4 greater than the pH recorded using calibrated pH electrodes. A more accurate estimation by the Henderson-Hasselbalch equation required the conversion of concentrations to activities.

Activities are defined thermodynamically by the change of the chemical potential with concentration. Debye-Hückel derived approximate expressions for highly diluted electrolytes ($I << 0.1$ M), based on ions interacting by electrostatic forces with surrounding ions (‘ion atmosphere'), depending on the concentration of ions *via* I and their distance of closest approach α (also called ion size parameter, in Å units),

$$\log_{10} \gamma_i = \frac{-0.51\, z_i^2 \sqrt{I}}{(1 + 0.33\, \alpha_i \sqrt{I}\,)} \tag{3.7}$$

where 0.51 and 0.33 are constants for water as solvent at 25 °C [166, 167]. Davies modified and extended this expression semi-empirically to higher I (up to ≈ 0.5 M) [167, 168],

$$\log_{10} \gamma_i = -\,0.51\, z_i^2 \left\{ \frac{\sqrt{I}}{(1 + \sqrt{I}\,)} - 0.3\, I \right\} \tag{3.8}$$

Both Equations 3.7 and 3.8 and related expressions are of the form

$$\log_{10} \gamma_i = -\,A(I)\, z_i^2 \tag{3.9}$$

where the factor A depends on the ionic strength and on the ion and water properties. Combining Equations 3.5 and 3.9 gives a modified Henderson-Hasselbalch equation that corrects concentrations to activities,

$$\mathrm{pH} = \mathrm{p}K_a + \log_{10}\left\{ \frac{c(\mathrm{A}^-)}{c(\mathrm{HA})} \right\} - A(I)\, \{ z^2(\mathrm{A}^-) - z^2(\mathrm{HA}) \} \tag{3.10}$$

For a monoprotic acid where A^- is singly charged and HA is neutral, the last correction term is just $-\,A(I)$. But, when applying Equation 3.10 to a phosphate buffer around pH 7 the last correction term becomes $-\,3\,A(I)$ as $z^2(\mathrm{HPO_4}^{2-}) = 4$ and $z^2(\mathrm{H_2PO_4}^-) = 1$, hence,

$$\begin{aligned} \mathrm{pH} &= 7.20 + \log_{10}\left\{ \frac{c(\mathrm{HPO_4}^{2-})}{c(\mathrm{H_2PO_4}^-)} \right\} - 3\, A(I) \\ &= 7.20 + \log_{10}\left\{ \frac{c(\mathrm{HPO_4}^{2-})}{c(\mathrm{H_2PO_4}^-)} \right\} - 1.53 \left\{ \frac{\sqrt{I}}{(1 + \sqrt{I}\,)} - 0.3\, I \right\} \end{aligned} \tag{3.11}$$

The $-3\,A(I)$ term can become quite considerable as it mainly depends on the ionic strength of the solution. At 25 °C, the $-3\,A(I)$ correction factor for a phosphate buffer around pH 7 rises dramatically as I increases from 0 to 0.1 M and asymptotically approaches -0.41 for $I > 0.15$ M, as shown in Figure 3.15.

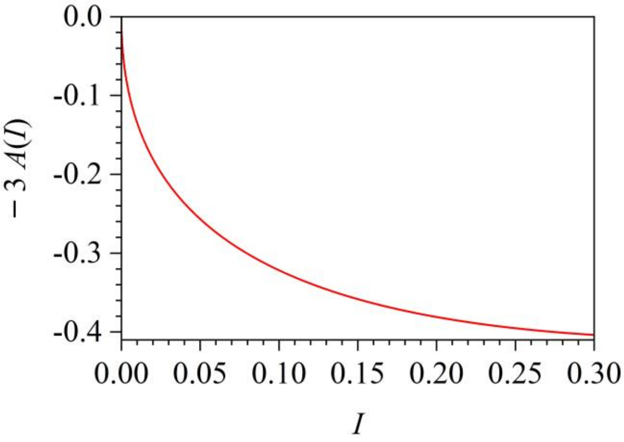

Figure 3.15 – Davies' $-3\,A(I)$ correction to the pH of a phosphate buffer around pH 7 for different ionic strengths I.

Buffer solutions of 50 mM monobasic and 50 mM dibasic anhydrous potassium phosphate salts were prepared to show how the Henderson-Hasselbalch equation could be easily corrected, as in Equation 3.11. Known amounts of HCl or NaOH were added as necessary with the independent variable $[\mathrm{H}^+]_{\mathrm{index}}$ defining the concentrations of acid or base added. The concentrations of $\mathrm{HPO_4}^{2-}$ and $\mathrm{H_2PO_4}^{-}$ equilibrated depending on the $[\mathrm{H}^+]_{\mathrm{index}}$. If x mM HCl was added, the $[\mathrm{H}^+]_{\mathrm{index}}$ was positive and x mM $\mathrm{HPO_4}^{2-}$ was converted to $\mathrm{H_2PO_4}^{-}$. The opposite was true if y mM NaOH was added, the $[\mathrm{H}^+]_{\mathrm{index}}$ was negative and y mM $\mathrm{H_2PO_4}^{-}$ was converted to $\mathrm{HPO_4}^{2-}$. Due to the logarithm in the Henderson-Hasselbalch equation, the pH of the solution did not change drastically when interconverting between $\mathrm{HPO_4}^{2-}$ and $\mathrm{H_2PO_4}^{-}$, hence the buffering effect. As shown in Figure 3.16, pH measurements of the phosphate solutions were made using a Mettler Toledo SevenMulti pH meter and compared with the pH calculated by the Henderson-Hasselbalch equation and the $-3\,A(I)$ corrected equation. Without the correction, the pH is consistently around 0.4 too high. Note that the ionic strength of the solution must consider the concentrations and charges of all ions in solution, as according to Equation 3.4. For instance, for $[\mathrm{H}^+]_{\mathrm{index}} = 40$ mM, the ions in solution were

90 mM HPO_4^{2-}, 10 mM $H_2PO_4^-$, 150 mM K^+ (from the phosphate salts) and 40 mM Cl^- (from the added HCl) giving $I = 0.28$ M.

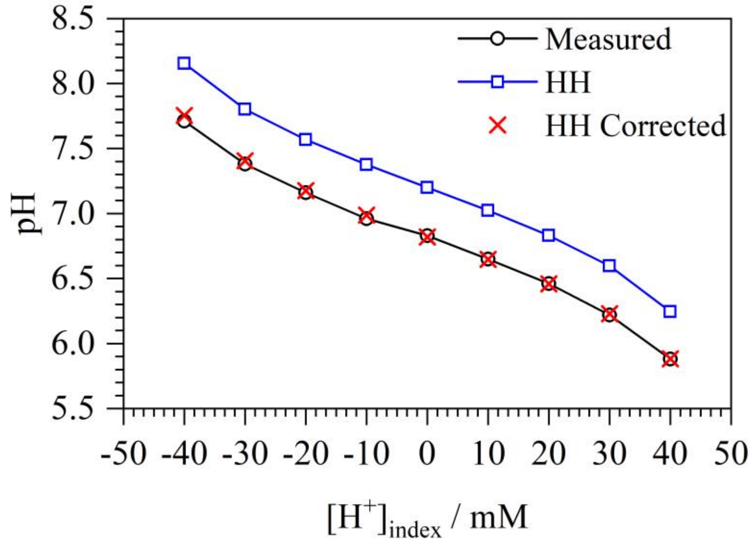

Figure 3.16 – pH of phosphate buffer solutions containing 50 mM HPO_4^{2-} and 50 mM $H_2PO_4^-$ with HCl (+ $[H^+]_{index}$) or NaOH (– $[H^+]_{index}$) added. **pH Measured**: recorded with a pH meter. **pH HH**: calculated by the Henderson-Hasselbalch equation using concentrations (Equation 3.2). **pH HH Corrected**: pH HH – 3 $A(I)$ (Equation 3.11).

During mixed-acid fermentation by *E. coli*, HPO_4^{2-} would convert to $H_2PO_4^-$ in response to acid excretion, as shown as an example of an actual biological measurement in Figure 3.17. Note that each data-point originates from averaging twelve liquid-phase Raman spectra at 300 s integration time. Initially, the buffer contained 47 mM HPO_4^{2-} and 22 mM $H_2PO_4^-$. At around 12 h, almost the entirety of HPO_4^{2-} was converted to $H_2PO_4^-$. If acids continued to be excreted from this time the phosphate buffer would have been overwhelmed and the pH would have decreased drastically. Fortunately, from 12 – 36 h, around 10 mM $H_2PO_4^-$ was converted back to HPO_4^{2-}. This was due to the reimport of excreted formate, as discussed in more detail in Section 3.3.4. The pH calculated with the – 3 $A(I)$ corrected Henderson-Hasselbalch equation showed excellent agreement with the pH measured externally by a pH meter at $t = 0$ and 60 h. The ionic strength was calculated including all millimolar concentration ions in solution but the trace elements at micromolar levels were ignored. Included in the I calculation were the time-dependent values of HPO_4^{2-}, $H_2PO_4^-$, acetate and formate, as well as the 103 mM Na^+, 27 mM Cl^-, 22 mM K^+, 18 mM NH_4^+ and 1 mM $MgSO_4$ from the M9 medium components that were assumed to stay constant. At $t = 0$ h, $I = 0.19$ M and – 3 $A(I)$ = – 0.38. Mainly due to the decrease in HPO_4^{2-} by t = 60 h, I decreased to 0.14 M but – 3 $A(I)$ hardly changed at a value of – 0.36. In conclusion, spectroscopic measurement of phosphate anion concentrations affords the contactless calculation of the pH of a bacterial culture, if the corrected version of the Henderson-Hasselbalch equation is applied.

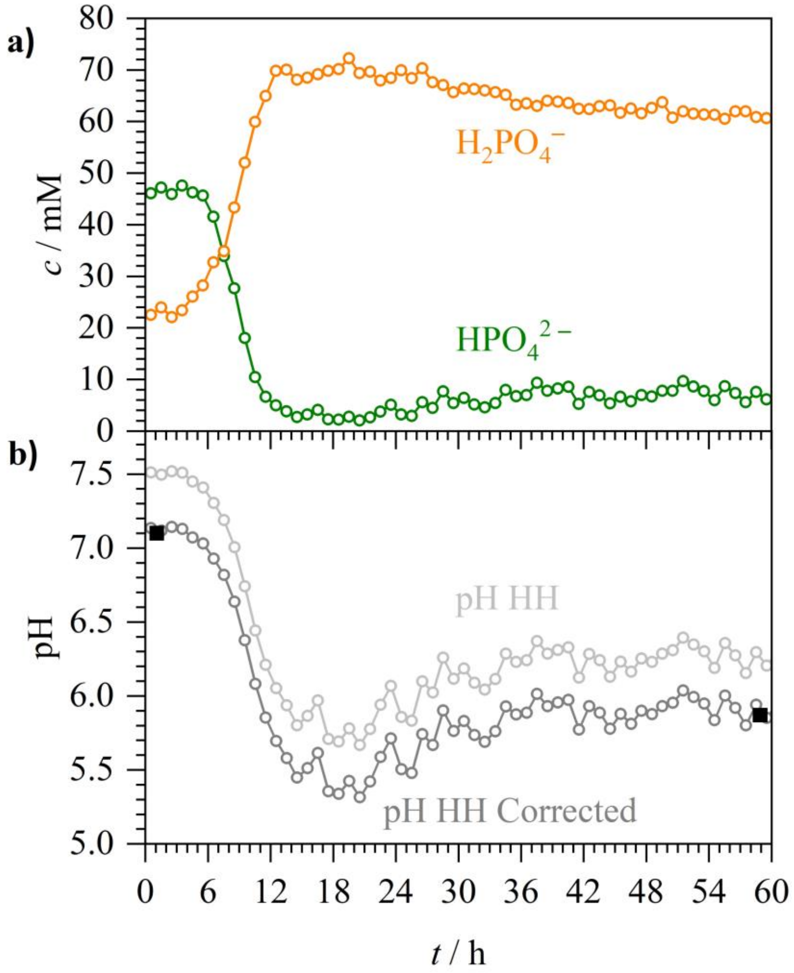

Figure 3.17 – Anaerobic fermentation by *E. coli* during growth in M9 medium supplemented with 30 mM glucose. **a)** Concentrations c of HPO_4^{2-} and $H_2PO_4^-$. **b)** pH calculated by the Henderson-Hasselbalch equation (open circles) and recorded with a pH meter (solid squares).

3.3.3 Analysing Gas-Phase FTIR Spectra

FTIR spectra were recorded using the 4.0 m White cell from 1000 to 7000 cm^{-1} at 0.4 cm^{-1} spectral resolution, as shown in Figure 3.18 for an ambient air sample, to detect gas-phase species in the headspace produced from the mixed-acid fermentation of *E. coli*. Note that throughout this entire thesis all absorbances A in FTIR spectra are defined as $\ln(I_0/I)$. The spectra contain numerous rovibrationally resolved water lines between 1000 – 2000 cm^{-1} from the OH bending fundamental, between 3000 – 4000 cm^{-1} from the OH stretching fundamental and between 5100 – 5500 cm^{-1} from the combination bands of the OH stretching and bending modes.

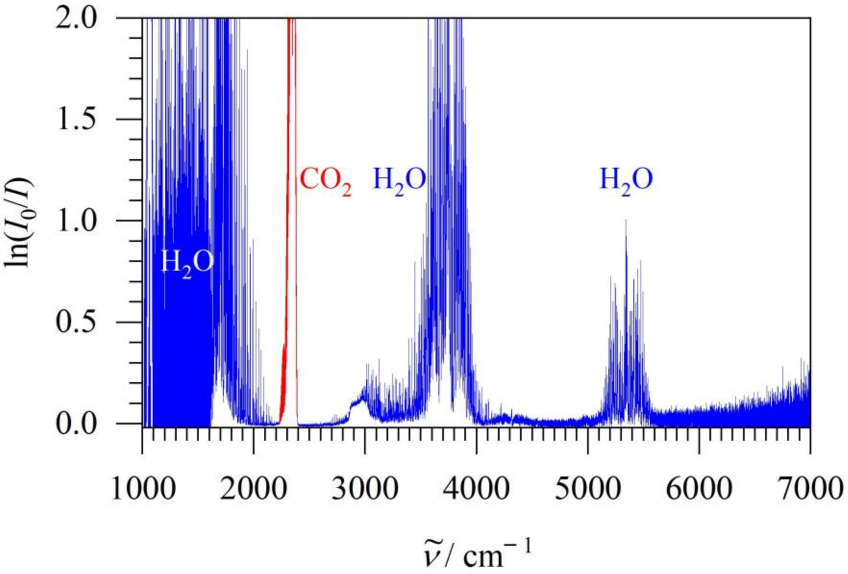

Figure 3.18 – Experimental FTIR spectrum of 1 bar air dominated by CO_2 and water lines.

CO_2 is perhaps the most indicative gas of bacterial metabolism and activity. For its quantification by FTIR spectroscopy, the main CO_2 absorption bands, such as the asymmetric stretching (ν_3) fundamental between 2200 – 2400 cm^{-1}, cannot be used due to saturation even under ambient levels. From 4800 – 5150 cm^{-1}, $^{12}CO_2$ has three characteristic bands that do not suffer any noticeable interferences. They are the $[2\nu_1 + \nu_3, \nu_1 + 2\nu_2^0 + \nu_3, 4\nu_2^0 + \nu_3]$ Fermi resonance triad, as shown in Figure 3.19. An in-house written computer programme performed a linear baseline correction of experimental FTIR spectra and integrated the 20012 ← 00001 (ν_0 = 4977.8 cm^{-1}) band from 4920 – 5015 cm^{-1}, as it was the most intense component of the triad. Comparison with the integral from a reference gas-phase spectrum for 1 ppmv CO_2 from the PNNL database [84] provided the conversion to partial pressure of headspace CO_2. Note that PNNL reference spectra corresponded to 1 ppmv-meter with $A = \log_{10}(I_0/I)$ and so were scaled to a pathlength of 4 m and multiplied by ln(10) to be comparable with our spectra.

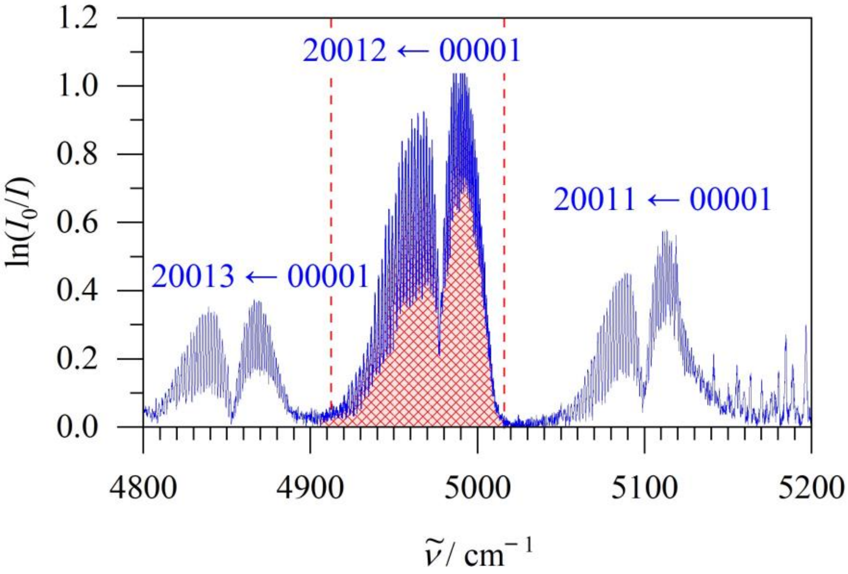

Figure 3.19 – Experimental FTIR spectrum of the $(2\nu_1 + \nu_3)$ Fermi resonance triad of $^{12}CO_2$. The CO_2 partial pressure was 100 mbar, as calculated from the integral of the red shaded band.

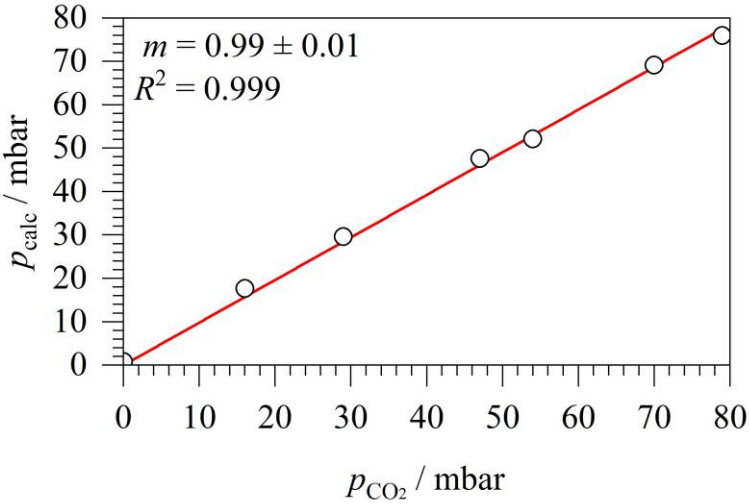

Figure 3.20 – Calibration plot showing calculated CO_2 partial pressure as a function of CO_2 partial pressure, assuming a folded pathlength of 4 m.

Excellent linearity was observed between the calculated partial pressures of CO_2 and known partial pressures of CO_2 in 1 bar air (defined mixtures prepared on a gas handling line), as shown in Figure 3.20. This also confirmed the 4 m folded pathlength of the White cell. Non-linearity was observed at CO_2 partial pressures greater than 100 mbar due to the 20012 ← 00001 band exceeding a peak absorbance of 1.0. Note that this was a limitation of our FTIR spectrometer as its useful absorbance range extended up to *ca.* 1.0. Non-linearity was not an issue for the data displayed in Section 3.3.4 as the CO_2 partial pressure produced did not exceed 100 mbar, under our conditions. To quantify above 100 mbar CO_2, one of the weaker ($2\nu_1 + \nu_3$) Fermi resonance triad bands could be used.

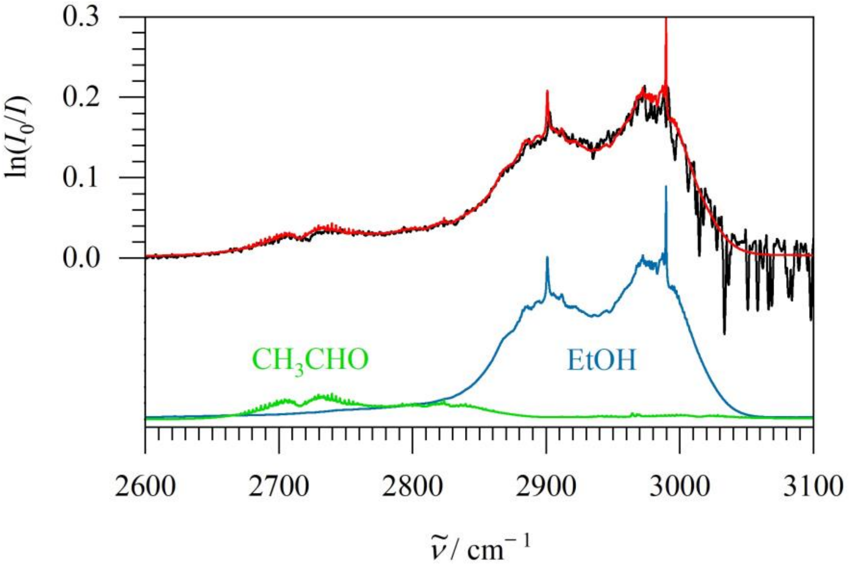

Figure 3.21 – In black, experimental FTIR spectrum of overlapping bands of acetaldehyde and ethanol corresponding to 18 and 105 ppm, respectively. In red, the sum of the acetaldehyde and ethanol models shown in green and blue, respectively.

Acetaldehyde and ethanol could also be detected by FTIR spectroscopy in the headspace above the bacterial culture. Ethanol is a very relevant end-product of fermentation in bioprocesses and acetaldehyde is its precursor. Their spectral signatures are apparent in the C-H stretching region of 2575 – 3100 cm^{-1}, as shown in Figure 3.21. Unlike CO_2, a simple integration of acetaldehyde and ethanol spectral features would not work since both species are overlapping and ethanol is affected by water interferences at the higher wavenumber end of its band. Similar to the liquid-phase Raman spectral analysis described in Section 3.2.1, the 2575 – 3100 cm^{-1} region was fitted to the sum of 1 ppmv each of acetaldehyde and ethanol PNNL model spectra and a linear baseline using an in-house written computer programme to implement a least-squares fit. The returned multipliers of the model spectra were equal to the partial pressures of the respective species (at 1 bar total pressure, 1 µbar = 1 ppmv).

Using Henry's law, the molarity of a dissolved gas can be calculated from its partial pressure. This allowed the estimation of molar concentrations of dissolved CO_2, acetaldehyde and ethanol from the FTIR measurements in the headspace. Henry's law constants for aqueous solutions at 37 °C are calculated as 0.026 mM $mbar^{-1}$ for CO_2, 6.3 mM $mbar^{-1}$ for acetaldehyde and 82 mM $mbar^{-1}$ for ethanol using constants from ref. [169]. By using the ideal gas law, it is estimated that 7.0 % CO_2, 94.9 % acetaldehyde and 99.6 % ethanol were held in solution. Under the experimental conditions, less than 1 % CO_2 was estimated to be lost to carbonic acid and carbonates.

Each FTIR measurement used 128 accumulations taking 2 min to acquire. An analysis of the baseline for an empty sample by the model fitting routine provided a standard deviation (noise floor) of 0.21 µbar for acetaldehyde and 0.26 µbar for ethanol, which may serve as estimates for the noise-equivalent (1 σ) detection limits. Using Henry's law, these detection limits correspond to 3.2 µM acetaldehyde and 22 µM ethanol. The analytical range exceeds 0.5 mbar ethanol in the gas phase corresponding to 41 mM in solution; for quantifying higher concentrations, shorter pathlengths and/or other spectroscopic bands are available.

3.3.4 Spectroscopic Analysis of Fermentation by *E. coli*

In an applied example of spectroscopic analysis by gas-phase FTIR and liquid-phase Raman spectroscopy, the mixed-acid fermentation of *E. coli* was studied. This application is particularly relevant because fermentative processes have a pronounced pH dependence and are essential in biotechnology to produce biohydrogen and other high value chemicals. On-line spectroscopic analysis of metabolites and pH enables process control and optimisation.

Figure 3.22 is a typical example of the time-dependent number of moles (n / mmol) of several metabolites, pH and OD_{600} measurements recorded during anaerobic fermentation by *E. coli* in M9 medium supplemented with 20 mM glucose. Partial pressures (p) of CO_2, acetaldehyde and ethanol were converted to n using the ideal gas law ($V = 5.25 \times 10^{-4}$ m^3, $T = 310$ K) and corrected by Henry's law for the dissolved percentage of each species (7.0 % CO_2, 94.9 % acetaldehyde and 99.6 % ethanol). CO_2 is slightly soluble in water; once it has dissolved, a small proportion of the CO_2 reacts with water to form carbonic acid which will be at equilibrium with bicarbonate and carbonate ions, depending on the pH. Under our conditions, less than 1% of dissolved CO_2 will be lost to carbonic acid and carbonates as estimated using equilibrium constants. Figure 3.22 contains the n and p of CO_2 in the upper panel **a**, the n of acetaldehyde (scaled up by × 50), formate and glucose in panel **b**, the n of acetate and ethanol (as measured both spectroscopically and by GC) in panel **c** and the pH and OD_{600} in lower panel **d**. Experiments were repeated in triplicate, and all repeats showed essentially the same qualitative and quantitative behaviour.

As discussed in Chapter 2, OD_{600} measurements are convenient for distinguishing bacterial growth phases and estimating bacterial density but are best suited for supplementing more sophisticated analytical techniques. In Figure 3.22, the OD_{600} began quite low (around 0.03) and did not increase noticeably for about 3 h which characterises the lag phase of bacterial growth, where the microbes prime themselves for cell division. From about 3 to 12 h, the OD_{600} rises to its peak value of 1.4, indicative of the exponential growth phase. For simplicity, phase **A** (0 – 12 h) is referred to as the exponential growth phase.

At 12 h, glucose is depleted at almost the same time as the stationary phase is reached. Despite glucose depletion, CO_2 production continues until around 40 h when formate is depleted. Hence, stationary phase growth is divided into phases **B** (12 – 40 h) and **C** (> 40 h) which are referred to as the glucose depletion and formate depletion phases, respectively. The OD_{600} measurements alone are neither very specific nor conclusive in phases **B** and **C**, as the OD_{600} was observed to first fall to 0.9 from 12 to 30 h, followed by a steady, slow rise. Based on the OD_{600} alone, it is unclear what is happening; these changes could be caused by changes in cellular morphology, the build-up of metabolites or cell death and the accumulation of cell debris. As in Chapter 2, this demonstrates the limitations of monitoring bioprocesses by the OD_{600} without additional supporting measurements.

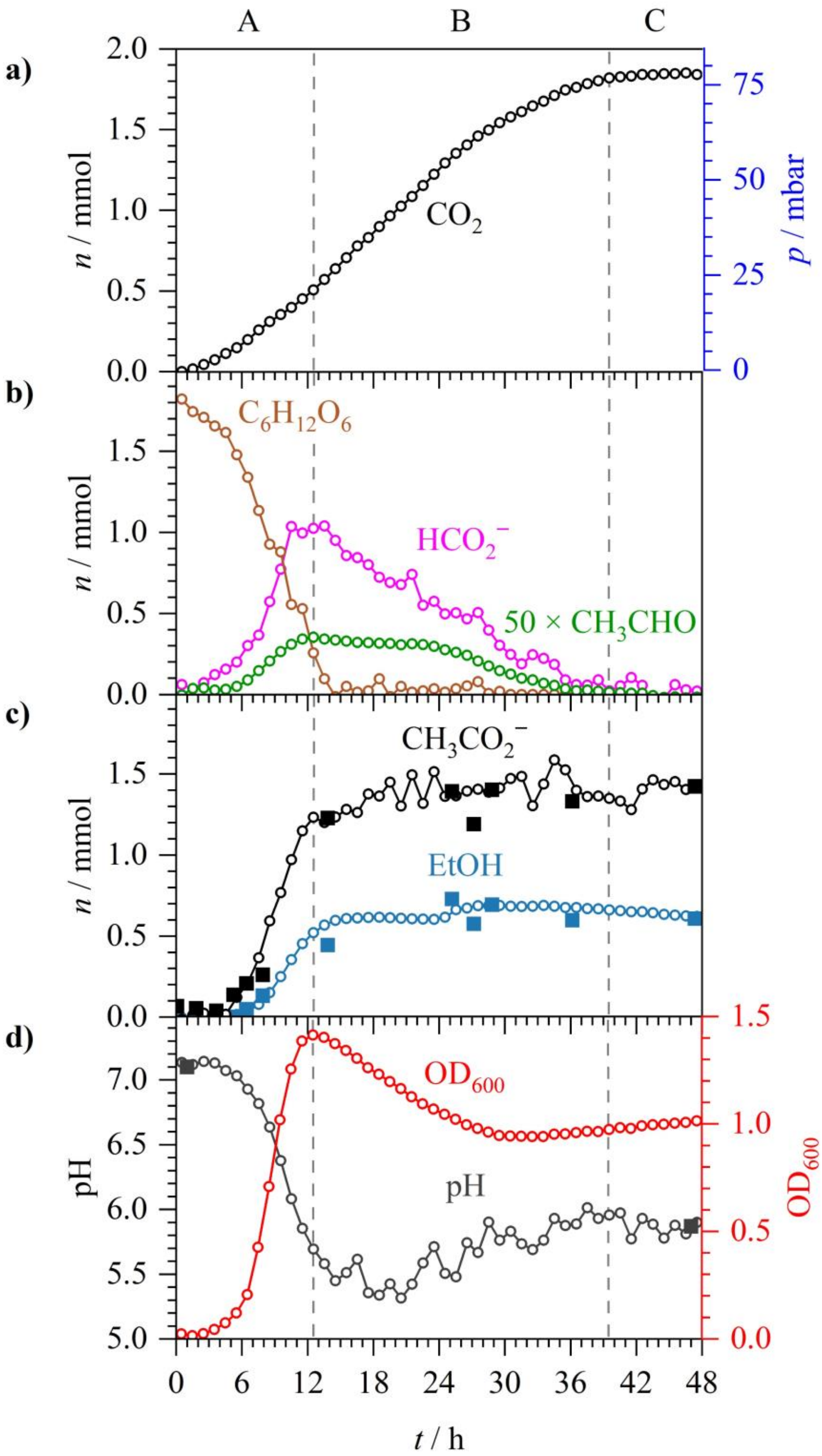

Figure 3.22 – Anaerobic fermentation of 30 mM glucose by *E. coli* in M9 medium. A to C denotes three distinct phases: exponential growth (A), glucose depletion (B) and formate depletion (C). **a)** n and p of CO_2. **b)** n of acetaldehyde (× 50), formate and glucose. **c)** n of acetate and formate. Open circles are from Raman measurements and solid squares from GC. **d**) Spectroscopic pH (open circles), externally measured pH (solid squares) and OD_{600}.

CO_2 production is a more direct measure of metabolism. During the mixed-acid fermentation of *E. coli*, CO_2 and H_2 evolve from the disproportionation of formate by FHL activity. While the OD_{600}, pH and n of other metabolites remain virtually constant during the lag phase (0 – 3 h), glucose decreases and CO_2 rises immediately due to metabolic activities occurring as the cells prime themselves for exponential growth. Although there is no apparent cell division occurring during the lag phase, the inoculated cells will adapt from the shock of the transfer to a new medium as they synthesise the necessary enzymes required for metabolism in the new environment. M9 medium lacks essential amino acids and peptides found in more complex media (such as LB) and requires new enzymes to synthesise these biomass precursor molecules from oxaloacetate, malate, and glycolytic intermediates [133]. At 3 h, when exponential bacterial growth begins, the CO_2 evolution rate increases and then continues into phase **B** in an S-shape curve. CO_2 peaks and then plateaus at 1.9 mmol (78 mbar) at 40 h, indicating the end of fermentative activity.

The FTIR measurements for acetaldehyde (panel **b**) and ethanol (panel **c**) show their production begins at around 5 h, as the lag phase ends. As it is an intermediate to ethanol, acetaldehyde accumulates at low values with a peak of 7 μmol (18 ppmv in the gas-phase) at 12 h. During phase **B**, as glucose is depleted, appreciable acetaldehyde cannot be formed and the remaining amounts are converted to ethanol, hence, acetaldehyde levels decrease and are depleted by 36 h. Ethanol rises rapidly to 0.55 mmol (105 ppmv in the gas-phase) in phase **A** and is then relatively constant after glucose depletion. The increase in both volatiles during the exponential phase **A** appears to follow first-order kinetics with a rise time of $t_{1/2}$ = 2.5 h. The disappearance of acetaldehyde in phase **B** at first has a slower decay with $t_{1/2}$ = 30 h between 15 and 29 h, followed by a faster decay with $t_{1/2}$ = 5.3 h. In control measurements, the bacterial culture was sampled at different stages and measured for the ethanol content by GC (solid squares). Excellent agreement was found between FTIR and GC measurements corroborating the spectroscopic measurement procedure but note that the recorded GC data is much more scattered.

Alongside CO_2, acetaldehyde and ethanol monitoring by gas-phase FTIR analysis, acetate and formate production were monitored on-line by liquid-phase Raman spectroscopy. The validity of the Raman measurements was confirmed with acetate GC measurements of samples of the bacterial culture. The agreement between the different methods is satisfactory with both methods having a similar degree of scatter, however, Raman spectroscopy has the superior time resolution due to convenience of on-line *in situ* measurements over sampling methods. Production of both acids began at 4 h with 1.2 mmol acetate and 1.1 mmol formate produced by 12 h. As CO_2 production is observed alongside formate excretion in phase **A**, this suggests that both excretion by FocA and disproportionation by FHL of formate must be occurring. This is corroborated by the 1.8 mmol total of 1.2 mmol acetate and 0.55 mmol ethanol produced by 12 h showing good agreement with the 1.7 mmol total of 0.6 mmol CO_2 produced and 1.1 mmol formate excreted. Formate is cleaved from pyruvate by pyruvate formate lyase (PFL) to form acetyl-CoA which will be ultimately converted to acetate or ethanol or enter the anaerobic TCA cycle. Hence, ignoring other pathways, the total of acetate and ethanol should be roughly equal to the total of CO_2 and formate.

In phase **B**, formate is then consumed almost linearly, indicating zeroth-order kinetics with a rate constant of 0.04 mmol h^{-1}. As glucose is depleted in phase **B** and new formate cannot be produced and excreted, the CO_2 produced is due to the reimport and disproportionation of the excreted formate from phase **A**. Hence, the reimport of 1.1 mmol formate causes the CO_2 to increase by a similar value of 1.2 mmol from 0.6 to 1.8 mmol. The pH began at 7.15 and rapidly decreased to 5.5 at 12 h, due to the excretion of the 1.2 mmol acetate and 1.1 mmol formate. Notably, a pH of 5.5 has been reported as significant for increasing H_2 production compared with neutral pH, due to increased expression of the *hyc* operon (encoding hydrogenase-3 in the FHL complex) [170]. During phase **B**, the pH recovers to a less acidic pH of 5.9 at 40 h and then remains constant during phase **C**. The end-point pH has been confirmed by a sample measured externally to have pH 5.9. The reimport of excreted formate appears to be responsible for the recovery in pH, as will be discussed in greater detail in Chapter 5.

3.4 Conclusion

This chapter has introduced an experimental set-up for continuous monitoring of bacterial fermentation processes by simultaneous OD measurements, long-path FTIR gas monitoring and liquid-phase Raman analysis with spectroscopic pH determination. Analysis of FTIR spectra provides partial pressures of CO_2, ethanol, and acetaldehyde which can be converted to concentration in the bacterial suspension *via* Henry's law. Liquid-phase Raman spectroscopy provides concentrations of aqueous species, including glucose, acetate and formate anions and the anions of the phosphate buffer. Using a modified Henderson-Hasselbalch equation, this allows the spectroscopic, *in situ* determination of the pH of the suspension. These spectroscopic techniques are non-invasive, provide concentrations in real-time, and do not require sampling, in contrast to standard analytical methods such as GC or MS. This allows measurements in closed systems or, for example, the measurement of the outgoing stream of a bioreactor for process control.

The liquid-phase Raman set-up is truly contactless, just shining and collecting light through the glass capillary where the suspension is flowing. This is in contrast to commercial Raman probes which have to be immersed in the solution, which have issues with maintaining optical performance and sterile conditions. Further advantages of liquid-phase Raman spectroscopy are that it can be easily adapted to monitor additional components, its high selectivity due to unique spectroscopic signatures, the distinction of isotopomers, which is essential for isotope labelling, and the ability to measure pH contactless. Spectroscopy is also a very cost efficient alternative to more expensive instruments such as GC and MS.

These techniques have been applied to studying the mixed-acid fermentation of *E. coli*. Different phases of bacterial growth have been observed and characterised and the consumption of glucose and resulting production of CO_2, acetate, formate, acetaldehyde and ethanol have been discussed in context of fermentative pathways and pH changes. A shortcoming of the spectroscopic techniques introduced in this chapter is that they cannot detect H_2 (a major product of anaerobic fermentation) due to unfavourable selection rules. In the following chapters, these spectroscopic techniques will be used in combination with CERS which can detect H_2 in addition to O_2 and N_2 (see Chapter 2) to enable a more complete characterisation of microbial metabolism, as well as to perform isotope labelling studies to elucidate reaction mechanisms.

Chapter 4

^{15}N-Isotopic Labelling Study of Nitrate and Nitrite Reduction to Ammonia and Nitrous Oxide by *E. coli*

Abstract

Nitrate and nitrite reduction to ammonia and nitrous oxide by anaerobic *E. coli* batch cultures is investigated by analytical spectroscopic techniques with ^{15}N-isotopic labelling. Non-invasive, *in situ* analysis of the headspace gases is achieved using White cell FTIR and cavity-enhanced Raman (CERS) spectroscopies alongside liquid-phase Raman spectroscopy.

For gas-phase analysis, White cell FTIR measures CO_2, ethanol and N_2O while CERS allows H_2, N_2 and O_2 monitoring. The 6 m pathlength White cell affords trace gas detection of N_2O with a noise equivalent detection limit (1 σ) of 60 nbar or 60 ppbv in 1 atm. Quantitative analysis is discussed for all four ^{14}N/^{15}N-isotopomers of N_2O. Liquid-phase Raman spectroscopy obtains NO_3^- concentrations with a noise-equivalent (1 σ) detection limit of 0.6 mM at 300 s integration time. NO_2^- concentrations are determined by sampling of the bacterial culture for colorimetric analysis and NH_4^+ by basifying samples to release ^{14}N/^{15}N-isotopomers of NH_3 for measurement in a second FTIR White cell.

The reductions of $^{15}NO_3^-$, $^{15}NO_2^-$ and mixed $^{15}NO_3^-$ and $^{14}NO_2^-$ by anaerobic *E. coli* batch cultures is discussed. In a major pathway, NO_3^- is reduced to NH_4^+ *via* NO_2^-, with the bulk of NO_2^- reduction occurring after NO_3^- depletion. Using isotopically labelled $^{15}NO_3^-$, $^{15}NH_4^+$ is distinguished from background $^{14}NH_4^+$ in the M9 growth medium. In a minor pathway, NO_2^- is reduced to N_2O *via* the toxic radical NO. With its excellent detection sensitivities, N_2O serves as a monitor for trace NO_2^- reduction, even when the cells are predominantly reducing NO_3^-. The analysis of N_2O isotopomers reveals that for cultures supplemented with mixed $^{15}NO_3^-$ and $^{14}NO_2^-$ some enzymatic activity to reduce $^{14}NO_2^-$ occurs immediately, even before $^{15}NO_3^-$ reduction begins. Optical density and spectroscopic pH measurements are discussed in the context of acetate, formate and CO_2 production. The production of H_2 is repressed by NO_3^-; but, in experiments supplemented with NO_2^- only, CERS detects H_2 produced by formate disproportionation after NO_2^- depletion.

The work presented in this chapter covers a scientific publication (ref. [171]);

Advanced Spectroscopic Analysis and ^{15}N-Isotopic Labelling Study of Nitrate and Nitrite Reduction to Ammonia and Nitrous Oxide by E. coli
George D. Metcalfe, Thomas W. Smith and Michael Hippler (2021).
Analyst. **146**, 7021-7033.
https://doi.org/10.1039/D1AN01261D

Author Statements

G. D. Metcalfe designed experiments, conducted the research, analysed data, prepared figures for publication and wrote the paper. T. W. Smith conceived the project, analysed data and wrote the paper. M. Hippler assembled the research team, designed the research, supervised the research, analysed data and wrote the paper.

4.1 Introduction

In the absence of O_2, *E. coli* can utilise alternative terminal electron acceptors for anaerobic growth, such as NO_3^- and NO_2^-. The sequence of reductions from NO_3^- to NO_2^- to NH_3 (NH_4^+ at physiological pH) is generally referred to as dissimilatory nitrate reduction to ammonia (DNRA) [172]. The coupling of these reductions to the oxidation of organic substrates, such as formate, enables the generation of a proton gradient across the cytoplasmic membrane. DNRA is considerably more efficient for obtaining energy than the mixed-acid fermentation pathways utilised when electron acceptors are unavailable. The expression of the respiratory NO_3^- and NO_2^- reductases is tightly controlled by FNR, an O_2 sensitive transcription factor, [173] and NarXL/NarQP, both of which are two-component NO_3^-/ NO_2^- sensitive regulatory systems [174].

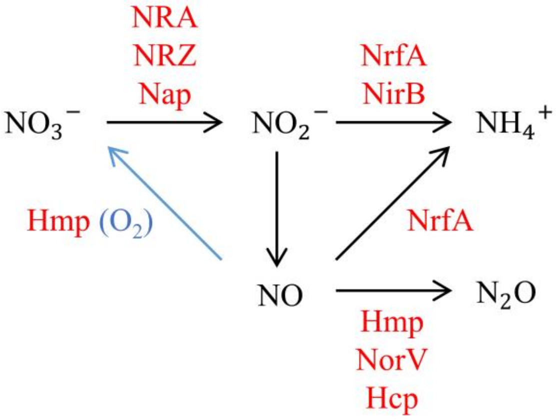

Figure 4.1 – DNRA with NO generation and detoxification by *E. coli*. Enzymes are displayed in red: **Hcp**, hybrid cluster protein; **Hmp**, flavohemoglobin; **Nap**, periplasmic nitrate reductase, **NirB**, NADH-dependent nitrite reductase; **NorV**, flavorubredoxin; **NRA**, nitrate reductase A; **NrfA**, periplasmic nitrite reductase; **NRZ**, nitrate reductase Z.

Although DNRA is the major NO_3^- reduction pathway in *E. coli*, the bacterium also generates minor amounts of the toxic radical nitric oxide (NO) from NO_2^- reduction. The low level of NO production by *E. coli* may be due to disproportionation of NO_2^- under acidic conditions or non-specific reduction by metalloproteins. The NADH-dependent cytoplasmic NO_2^- reductase (NirB) [175], the membrane-bounds periplasmic NO_2^- reductase (NrfA) [176] and the major anaerobic NO_3^- reductase (NRA) [177, 178] have all been proposed to be significant sources of NO formation as a byproduct of their roles in the DNRA pathway. Aerobically, flavohemoglobin (Hmp) detoxifies NO by oxidation back to NO_3^-; while anaerobically, NO is reduced further to nitrous oxide (N_2O) reportedly by Hmp [179], flavorubredoxin (NorV) [180] and hybrid cluster protein (Hcp) [181]. N_2O is comparatively less toxic than NO and can rapidly diffuse out of the cell. *E. coli* is not a true denitrifier but N_2O production by NO_3^- respiring *E. coli* cultures does share similarities with the denitrification pathway of NO_3^- to N_2 *via* NO_2^-, NO and N_2O. As *E. coli* K-12 does not possess any known N_2O reductases, reduction to N_2 is not expected to occur. However, there is some evidence that N_2 might be produced under certain conditions by a yet unknown mechanism [182]. A summary of DNRA with NO generation and detoxification is shown in Figure 4.1.

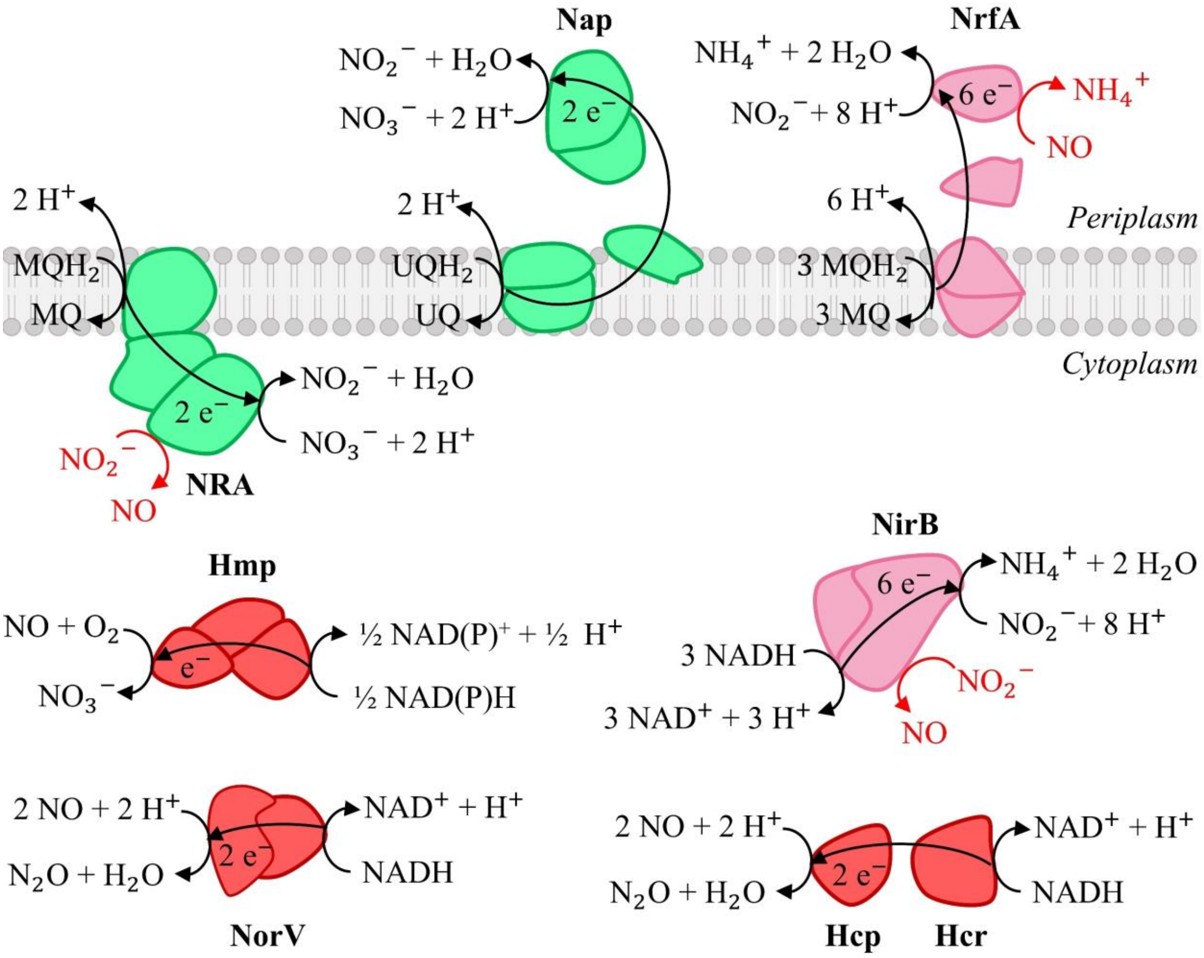

Figure 4.2 – The cellular locations of key enzymes during NO_3^- and NO_2^- reduction by *E. coli*, with the proposed generation or detoxification of NO by NO_3^- and NO_2^- reductases shown in red. The enzymes displayed include **Hcp**, hybrid cluster protein; **Hcr**, NADH-dependent Hcp reductase; **Hmp**, flavohemoglobin; **NirB**, NADH-dependent NO_2^- reductase; **NorV**, flavorubredoxin; **Nap**, periplasmic NO_3^- reductase; **NRA**, NO_3^- reductase A; **NrfA**, periplasmic NO_2^- reductase.

The cellular locations of key enzymes involved during NO_3^- and NO_2^- reduction by *E. coli* are shown in Figure 4.2. *E. coli* expresses three NO_3^- reductases [183-185]: the respiratory NO_3^- reductases A and Z (NRA and NRZ) and the periplasmic NO_3^- reductase (Nap). NRA is the major anaerobic NO_3^- reductase active at high NO_3^- levels (> 2 mM) while Nap is induced by low NO_3^- levels [186]. NRZ is expressed at low levels constitutively and may function under stress-associated conditions or in an adaptive role in the transition from aerobiosis to anaerobic NO_3^- respiration [187, 188]. Formate is a physiological source of electrons for NO_3^- reduction. Formate is oxidised to CO_2 by the NO_3^- inducible formate dehydrogenase (FDH-N) which transfers electrons to the quinone pool of the membrane [184]. Other physiological electron donors include NADH, lactate and glycerol [183]. The NADH-dependent cytoplasmic NO_2^- reductase (NirB) and the membrane-bound periplasmic NO_2^- reductase (NrfA) both formally catalyse the six-electron reduction of NO_2^- to NH_3, as well as the one-electron reduction of NO_2^- to NO [189]. Both $NO_2^-$and NO are cytotoxic species and careful control of their intracellular concentration is required, either through detoxification to less reactive species such as N_2O or by export from the cell.

DNRA has been studied extensively in *E. coli*, however, comparatively less is known about the minor pathway leading to N_2O and how its generation differs between NO_3^- and NO_2^- respiring cultures. To gain a better mechanistic understanding, monitoring the key compounds and parameters of these processes is essential. Accurate and reliable analytical techniques are crucial for understanding cell biochemistry and pathway elucidation. This represents a challenge for analytical chemistry, requiring a combination of advanced analytical techniques. Spectroscopic techniques can be readily applied for monitoring bioprocesses *in situ* and on-line, with no sampling. Good sensitivities are observed in the condensed phase, but measuring headspace gases often suffers from low sensitivity thus special enhancement techniques are required, such as CERS (see Chapter 2) or long-path absorption White cells in FTIR spectroscopy (see Chapter 3). Quantum Cascade Laser (QCL) absorption spectroscopy has been applied to detect N_2O and other trace gases [190-192]; while sensitive, the limited tuning range of QCLs over a single IR absorption band limits the dynamic range due to band saturation effects. Vibrational spectroscopic tools have been previously applied to monitoring NO_3^- metabolism in bacteria; CERS has been used to follow N_2O and N_2 production in denitrifying organisms, with the use of $^{15}NO_3^-$ to produce $^{15}N_2$ distinguishable from background $^{14}N_2$ [193, 194]. A robust CERS instrument has also been designed for field application to study the gas composition of soil samples [102].

This chapter introduces a combined approach for characterising DNRA and N_2O production in anaerobic *E. coli* batch cultures using mostly non-invasive spectroscopic techniques. Sampling of the bacterial culture was only done for NO_2^- colorimetry and FTIR detection of $^{14}NH_3$ and $^{15}NH_3$ isotopomers. Headspace gas analysis was provided by the complementary techniques of FTIR and CERS. FTIR allowed detection of CO_2, ethanol and N_2O while CERS enabled monitoring of the homonuclear diatomic molecules N_2, O_2 and H_2. As introduced in Chapter 3, the capability of liquid-phase culture analysis by Raman spectroscopy to monitor acidic products (acetate and formate), glucose consumption and the resulting *in situ* pH from phosphate signatures using a modified Henderson–Hasselbalch equation is here applied to NO_3^- and NO_2^- respiration. Liquid-phase Raman spectroscopy also allows quantification of NO_3^-. With the use of ^{15}N-isotopic labelling, mechanistic insights into NO_3^- and NO_2^- reduction to NH_4^+ and N_2O are obtained through interpretation of the different $^{14}N/^{15}N$-isotopomers produced. The aims of this chapter are to introduce and characterise a unique combination of advanced spectroscopic techniques with great potential for bioanalytical applications with an interesting biochemical application: a ^{15}N-isotope labelling study of N_2O production during DNRA by *E. coli*, with a focus on the differences observed between NO_3^- and NO_2^- respiration.

4.2 Experimental

4.2.1 Bacterial Growth Conditions

E. coli K-12 MG1655 was transferred from – 80 °C glycerol stocks, struck on LB-agar plates and incubated overnight at 37 °C. Starter cultures were prepared by inoculating 50 mL of LB medium with a single colony from the plate and incubating overnight (37 °C, 200 rpm) in a sealed 50 mL centrifuge tube for anaerobic growth conditions. Overnight, the anaerobic starter cultures grew to a typical OD_{600} of 1.2. Ultimately, 20 mL of the starter culture was centrifuged, and the bacterial pellet resuspended into 20 mL of fresh M9 medium to be added to a further 230 mL when starting experiments. The M9 medium was supplemented with 10 mM $K^{15}NO_3$ (10 mM, 98 % ^{15}N, Sigma Aldrich) and/or 5 mM KNO_2 (^{14}N or ^{15}N). The entire M9 minimal medium formulation contained:

48 mM Na_2HPO_4
30 mM glucose
22 mM KH_2PO_4
18 mM NH_4Cl
8.5 mM NaCl
1 mM $MgSO_4$
1 mM thiamine
300 µM $CaCl_2$
135 µM Na_4EDTA
57 µM H_3BO_3
31 µM $FeCl_3$
9 µM $NiCl_2$
6.2 µM $ZnCl_2$
4 µM biotin
4 µM Na_2SeO_3
3.2 µM Na_2MoO_4
2.7 µM $CoCl_2$
1.3 µM $MnCl_2$
0.2 µM $CuSO_4$

4.2.2 The Experimental Set-up

Before starting each experiment, 230 mL of M9 medium was prepared in a 500 mL custom round-bottom flask with two side-arms and submerged in a 37 °C water bath under rapid stirring for efficient gas transfer. The flask was sealed after adding the 20 mL of media containing *E. coli* from the starter culture. A scheme of the experimental set-up is shown in Figure 4.3 and a photograph of the set-up is shown in Figure 4.4. From one side-arm, the bacterial culture was cycled by a peristaltic pump (**PP-L**, 4.5 L h^{-1}) for *in situ* OD_{600} and liquid-phase Raman measurements. The OD_{600} measurements were obtained as outlined in Section 2.2.2, using a laser pointer (**LP**), 1 cm sealed glass cuvette and photodiode (**PD**). From the main-neck of the flask, the headspace gases were cycled by a peristaltic pump (**PP-G**, 4.5 L h^{-1}) for gas-phase CERS and White cell (**WC**) FTIR measurements. The CERS cavity, White cell and the gas transfer tubes were warmed to *ca.* 50 °C by heating wire to prevent water condensation on the internal optics. The total headspace gas volume was 1425 mL. The second side-arm was equipped with a Suba-Seal rubber septum to allow sampling of the culture for NO_2^- and NH_3 analysis. The CERS enclosure also included two ports with Young valves, one was connected to a vacuum line while the other was connected to a N_2 cylinder. Before starting experiments, alternating between these vacuum and N_2 lines several times enabled purging of O_2 from the closed system to give anaerobic growth conditions, as confirmed by CERS measurements that showed 1 atm N_2 and no detectable O_2 at the start.

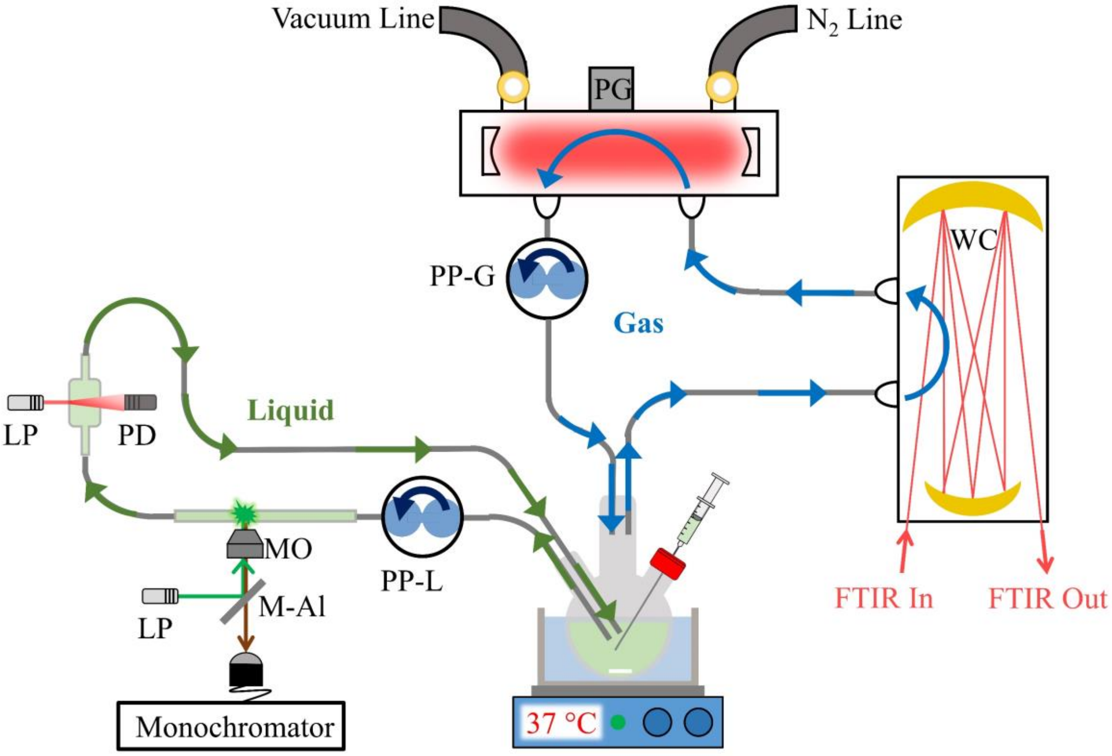

Figure 4.3 – The experimental set-up. Headspace analysis by CERS and White cell FTIR spectroscopy and liquid-phase analysis by Raman spectroscopy and OD_{600}. **LP**, laser pointer; **M-Al**, mirror (glass slide with 2 mm × 3 mm Al spot); **MO**, microscope objective; **PD**, photodiode; **PG**, pressure gauge; **PP-G,** gas-phase peristaltic pump; **PP-L**, liquid-phase peristaltic pump; **WC**, White cell.

During experiments, 1 mL of the bacterial culture was sampled every 40 min and centrifuged. The supernatant was then analysed for NO_2^- and NH_4^+ content. Bacterial cultures were monitored until no further CO_2 production was observed due to the depletion of oxidisable carbon sources. Endpoint measurements of the pH and dry biomass were recorded for each experiment. The bacterial suspension was centrifuged at the end of each experiment and the pH of the supernatant was recorded using a Mettler Toledo SevenMulti pH meter (glass electrode with internal Ag/AgCl reference). The M9 medium began with a typical pH of 6.9 and ended between 5.0–5.5 due to organic acid excretion. The dry biomass was typically around 200 mg and was measured by weighing the centrifuged cellular material after decanting off the supernatant and allowing the pellet to dry in a 37 °C oven.

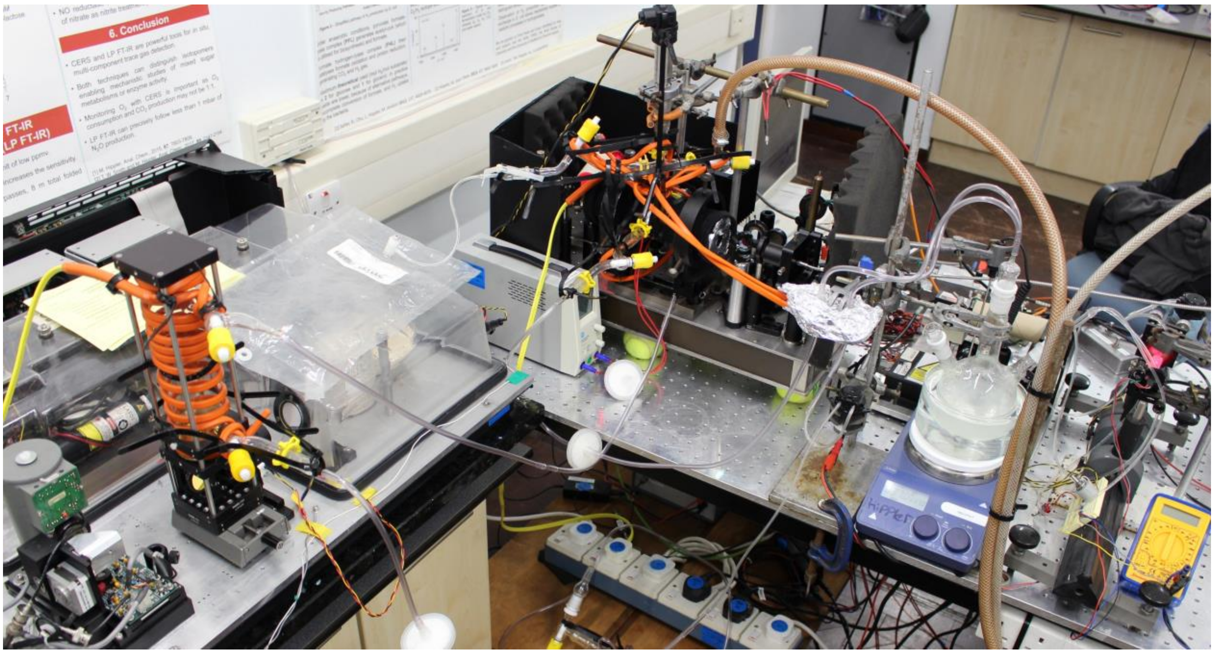

Figure 4.4 – Photograph of the experimental set-up.

Liquid-phase Raman spectroscopy was conducted as described in Section 3.2.3. Within the Raman spectral range was a characteristic peak for the symmetric stretching vibration of NO_3^- ($\Delta\tilde{\nu}_0 = 1049\ cm^{-1}$). Using a least-squares fitting routine, Raman spectra of the bacterial suspension between 830 – 1200 cm^{-1} were fitted to NO_3^-, glucose, $H_2PO_4^-$ and HPO_4^{2-} reference spectra, as well as a linear baseline, as shown in Figure 4.5. The returned multipliers of the reference spectra were then converted into concentrations *via* calibration plots. Noise analysis of background sample measurements (pure water) provided noise-equivalent (1 σ) detection limits of 0.6 mM NO_3^- at 300 s integration time. With additional averaging to an integration time of 0.5 h (as was done with all time-dependent data displayed in this study), this limit improves to 0.25 mM NO_3^-. Although NO_2^- has a N-O stretching peak at 1326 cm^{-1}, this feature was too weak to be used in this study with a noise-equivalent (1 σ) detection limit of 5.0 mM NO_2^- at 300 s integration time. Hence, sampling the bacterial culture for NO_2^- colorimetry was necessary (see Section 4.2.4).

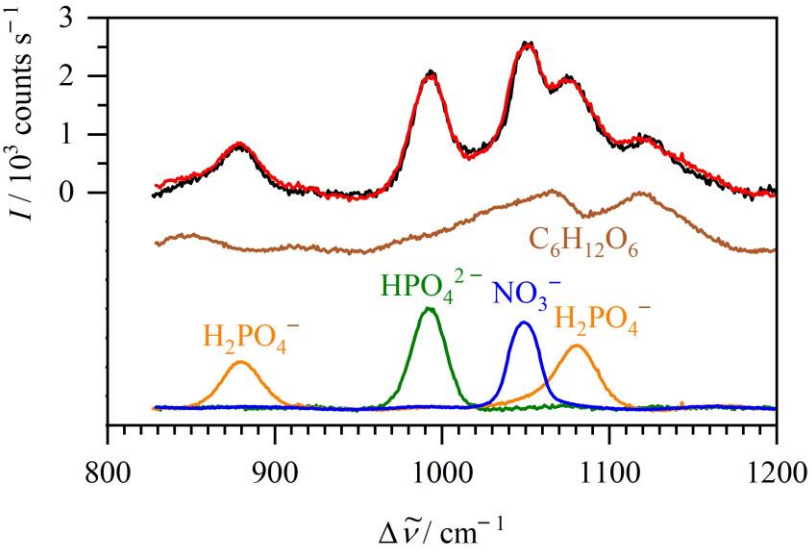

Figure 4.5 – In black, an experimental Raman spectrum of fresh M9 medium for NO_3^- respiration. In red, the sum of the 10 mM NO_3^-, 30 mM glucose, 47 mM HPO_4^{2-} and 22 mM $H_2PO_4^-$ models shown in blue, brown, green and orange, respectively.

Liquid-phase Raman analysis of NH_3 (or NH_4^+) was not possible as there were no usable features within our Raman spectral range, hence, the sampling for NH_4^+ analysis was necessary. To release NH_3 gas from solution (held as NH_4^+ due to the pH), samples of the bacterial culture were centrifuged and the supernatant was basified. $^{14}N/^{15}N$-isotopomers of NH_3 were then measured in a second FTIR White cell, as explained further in Section 4.2.5.

White cell FTIR spectroscopy was conducted as described in Section 3.2.4; however, the White cell was realigned for thirty passes or a 6 m folded pathlength. Furthermore, in addition to CO_2 and ethanol analysis, the $^{14}N/^{15}N$-isotopomers of N_2O were also quantified, as outlined in Section 4.3.1 of the Results and Discussion.

4.2.3 Cavity-Enhanced Raman Spectroscopy

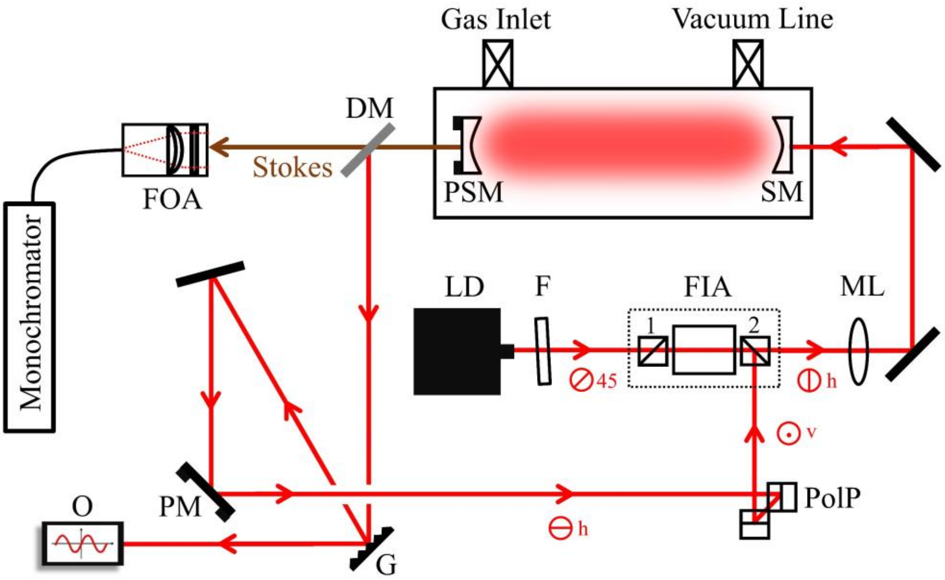

Figure 4.6 – CERS optical components. **DM**, dichroic mirror; **F**, filter; **FIA**, Faraday isolator assembly; **FOA**, fibre optical assembly; **G**, grating; **LD**, laser diode; **ML**, mode-matching lens; **O**, oscilloscope; **PM**, mirror on a piezomount; **PolP**, polarization plane turning prism pair; **PSM**, supermirror on a piezomount; **SM**, supermirror.

The CERS set-up was previously described in Section 2.2.3, however, some modifications were made for the iteration of CERS employed for these experiments. The optical components used for headspace gas analysis by CERS are depicted in Figure 4.6. A 40 mW 636 nm single-mode cw-diode laser (**LD**, HL63133DG) was coupled *via* a short-pass filter (**F**), a single Faraday isolator (**FIA**) and a mode-matching lens (**ML**) into a linear optical cavity composed of two highly reflective supermirrors. If the laser wavelength matched the cavity length, then an optical resonance built up optical power inside the cavity by up to 8000 times in magnitude which enhanced the Raman signals [105]. In the present simplified set-up, no active mode-matching was attempted; the diode laser current was rather modulated periodically to allow periodic mode-matching which is then re-enforced by optical feedback. After the cavity, a dichroic mirror separated leftover excitation light from Raman signals which were coupled into a round-to-linear glass fibre bundle (7 × Ø105 μm) and transferred to the monochromator. Remaining excitation light was fed back to the diode for frequency stabilisation to match the laser wavelength to the cavity. In the feedback loop there was a grating (**G**), a piezo-mounted mirror (**PM**) and a set of two prisms (**PolP**) to change the polarisation from horizontally to vertically polarised. The grating was in 1st order reflection to select just one wavelength of the possible cavity modes, to encourage single mode operation by feedback. The piezo-mirror was used to adjust the feedback loop length to the laser wavelength (‘phase matching’). In a simplification, no active phase matching was used but an applied periodic change which locked the laser periodically to a resonance. In the simplified set-up, only one Faraday isolator was used, unlike the two used as described in Section 2.2.3. The original 45° polarised diode laser light was horizontally polarised (0°) after the isolator. To allow feeding light back to the diode *via* the rejection port of the Faraday isolator, it had to be vertically polarised (90°) which was achieved by the prism pair rotating the polarisation by 90°.

The Czerny-Turner spectrograph equipped with a CCD camera (as described in Section 2.2.3) was needed for high-resolution liquid-phase Raman measurements, hence, a different monochromator was used for this CERS set-up (Andor Shamrock SR163, 1200 lines mm^{-1} grating, DV420A-OE CCD). The 400 – 2500 cm^{-1} spectral range at 6 cm^{-1} resolution encompassed the rotational *S*-branch lines of H_2, the $\nu_1/2\nu_2^0$ Fermi resonance pair of CO_2 and the vibrational fundamentals of O_2 and N_2. To normalize Raman signals, the N_2 peak was used as an internal standard since N_2 was not expected to change during the metabolic activities of *E. coli*. CO_2 analysis by CERS was used to corroborate the FTIR analysis; however, CERS CO_2 data was not displayed in this study due to FTIR CO_2 detection being more sensitive.

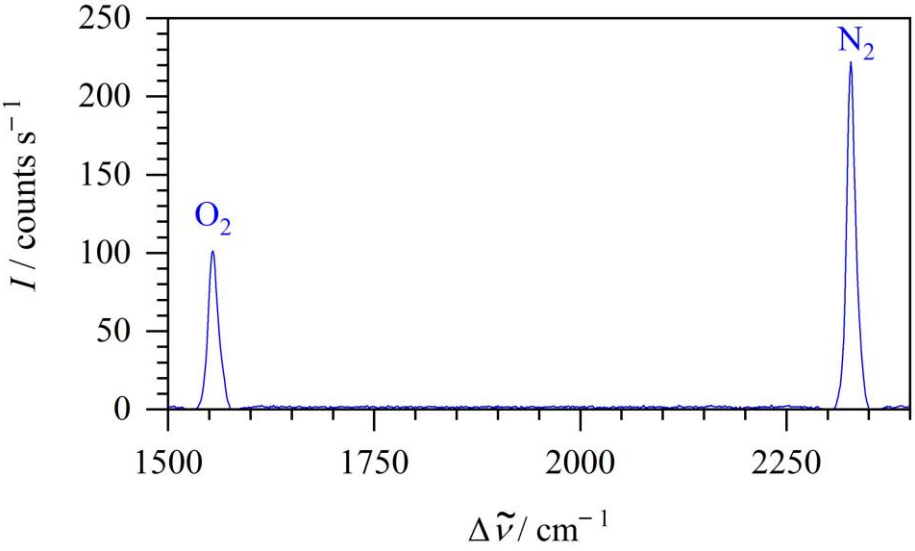

Figure 4.7 – CERS spectrum of 1 atm air (210 mbar O_2 and 790 mbar N_2).

Figure 4.7 shows a CERS spectrum of 1 atm lab air, with the *Q*-branches of the O_2 and N_2 vibrational fundamentals visible. Figure 4.8 shows a CERS spectrum of 140 mbar each of H_2 and CO_2, taken during an anaerobic fermentation experiment (see Chapter 5). The area of the *S*(1) rotational peak of H_2 was divided by the area of the *Q*-branch of N_2 (equal to 1 atm in anaerobic conditions) in order to obtain H_2 partial pressures after a calibration. Using known partial gas pressures, a calibration was made for H_2 showing excellent linearity. A similar procedure was applied to CO_2, with both calibration plots shown in Figure 4.9.

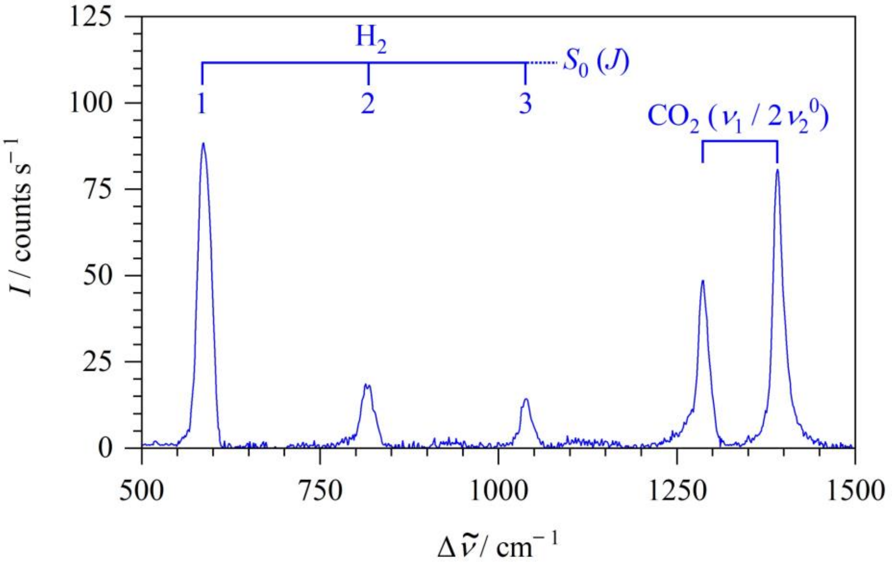

Figure 4.8 – CERS spectrum of 140 mbar each of H_2 (rotational lines) and CO_2.

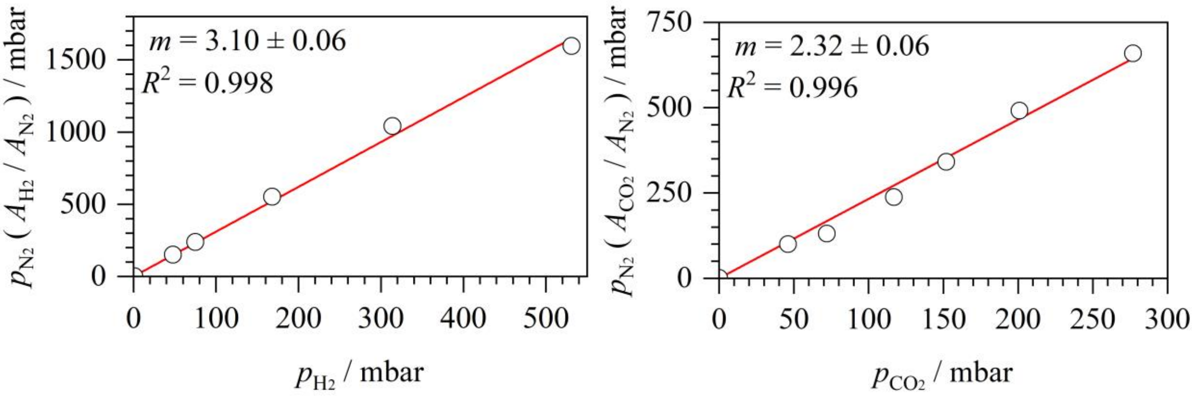

Figure 4.9 – CERS H_2 and CO_2 calibration plots showing excellent linearity.

Figure 4.10 shows the CERS spectrum of 1 atm H_2 recorded using the high-resolution monochromator (which was used for liquid-phase Raman measurements). The region near 4155 cm^{-1} has strong Raman transitions due to rotationally resolved Q-branch transitions to its fundamental vibration, with characteristic 1:3 intensity variation between even and odd J-values due to nuclear spin statistics (see Section 1.1.2). At room temperature, the strongest transition is the $Q(1)$ line at 4155.3 cm^{-1} which gives a noise-equivalent (1 σ) detection limit of 30 ppmv at 300 s integration time. Note that for all time-dependent H_2 measurements displayed in this thesis, the $S_0(1)$ line at 587 cm^{-1} was analysed.

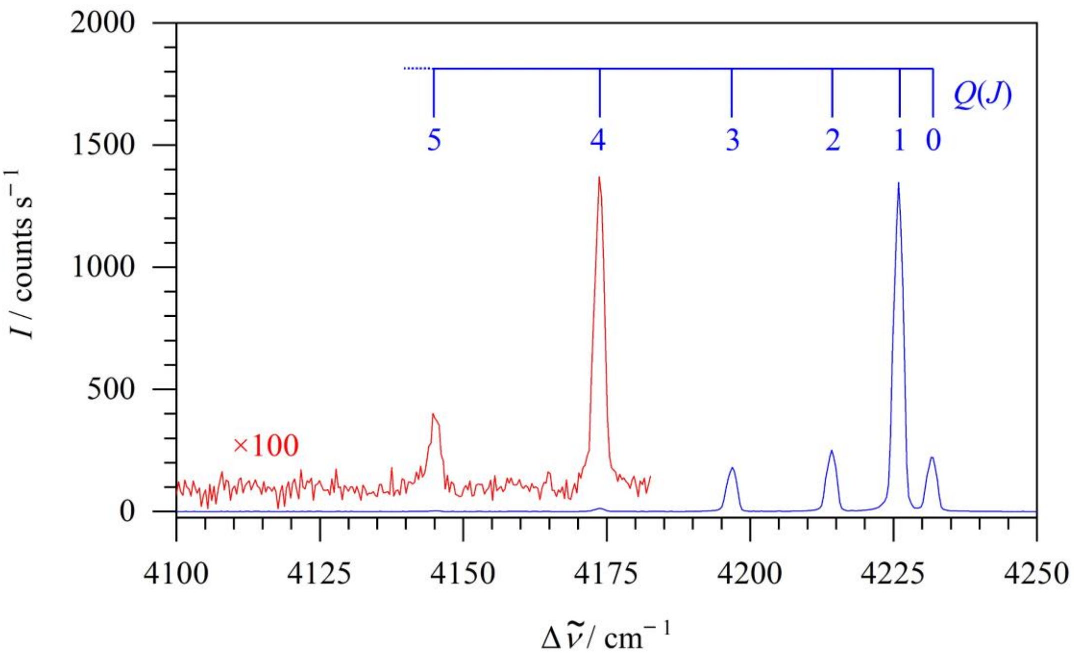

Figure 4.10 – CERS spectrum of 1 atm H_2 with rotationally resolved Q-branch transitions to its fundamental vibrational.

4.2.4 Nitrite Colorimetry

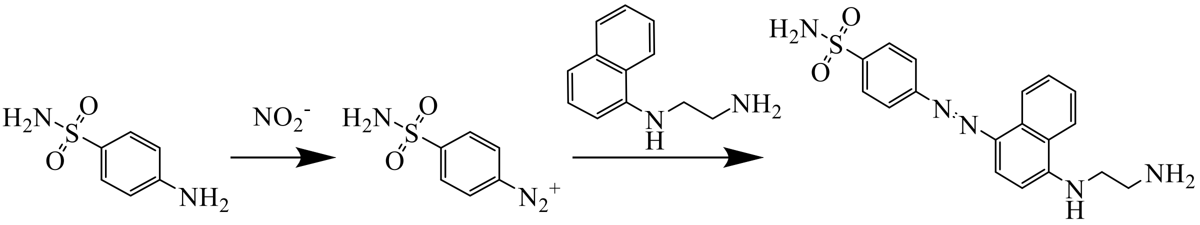

Scheme 4.1 – The two subsequent reactions of the Griess test.

Bacterial culture samples were centrifuged and the NO_2^- content of the supernatant was determined by the Griess test [195]. The Griess reagent was made up of 50 mL L^{-1} phosphoric acid, 5 g L^{-1} sulphanilamide and 0.25 g L^{-1} N-(1-naphthyl)ethylenediamine dihydrochloride. As shown in Scheme 4.1, the Griess test involves two subsequent reactions. First, NO_2^- reacts with sulphanilamide to form a diazonium salt in the Griess diazotization reaction. Then, in an azo coupling reaction, N-(1-naphthyl)ethylenediamine reacts with the diazonium salt to form a pink-red azo dye. The dye colour is shown in Figure 4.11. NO_2^- could be quantitatively determined by measuring the absorbance at 520 nm with a UV/Vis spectrometer, as shown by the calibration plot in Figure 4.11. Note that 14.007 mg L^{-1} (N) is equal to 1 mM NO_2^-. The calibration was linear up to 3 mg L^{-1} (N) or 210 μM NO_2^- so samples were diluted accordingly to be within the analytical range (typically a fifty fold dilution). The noise-equivalent (1 σ) detection limit of NO_2^- was 17 μg L^{-1} (N) or 1.2 μM.

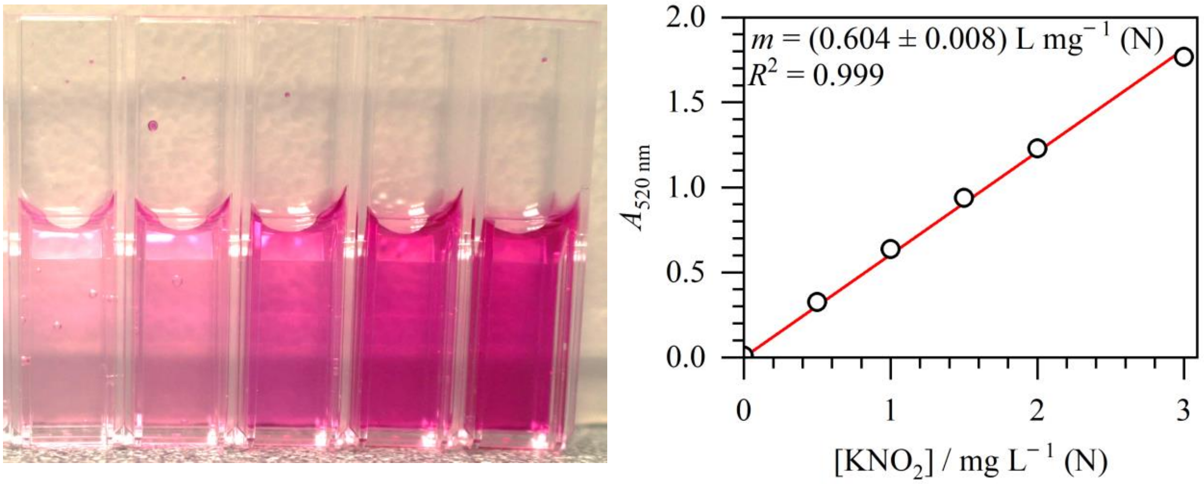

Figure 4.11 – Photograph of the pink-red azo dye formed by the Griess test (left) and nitrite colorimetry calibration plot (right).

4.2.5 ^{14}N/^{15}N-Ammonium Analysis

Fresh M9 medium began with a typical pH of 6.9 and became more acidic during bacterial growth, ending between 5.0 – 5.5 due to organic acid excretion. With a pK_a of 9.25, NH_3 exists almost entirely as NH_4^+ at acidic pHs which excludes direct FTIR detection of NH_3 gas in the headspace. For $^{14}NH_4^+$ and $^{15}NH_4^+$ analysis, 0.6 mL of sample was withdrawn from the batch culture using a syringe through the side-arm fitted with a rubber septum. Then, 2 mL 1 M NaOH was added to 0.6 mL of sample to release NH_3 gas in a flask connected to a second FTIR set-up (Bruker Alpha FTIR, 0.8 cm^{-1} spectral resolution, 350 – 7000 cm^{-1} range) also with a home-built multiple-pass absorption White cell (2.8 m folded pathlength). A photograph of the FTIR set-up is shown in Figure 4.12. Spectra were recorded every 5 minutes with around 30 minutes needed before NH_3 concentration peaked in the headspace. The basified solution was rapidly stirred and the 2 L headspace in the closed system was cycled between the sample flask and White cell using a peristaltic pump (4.5 L h^{-1}).

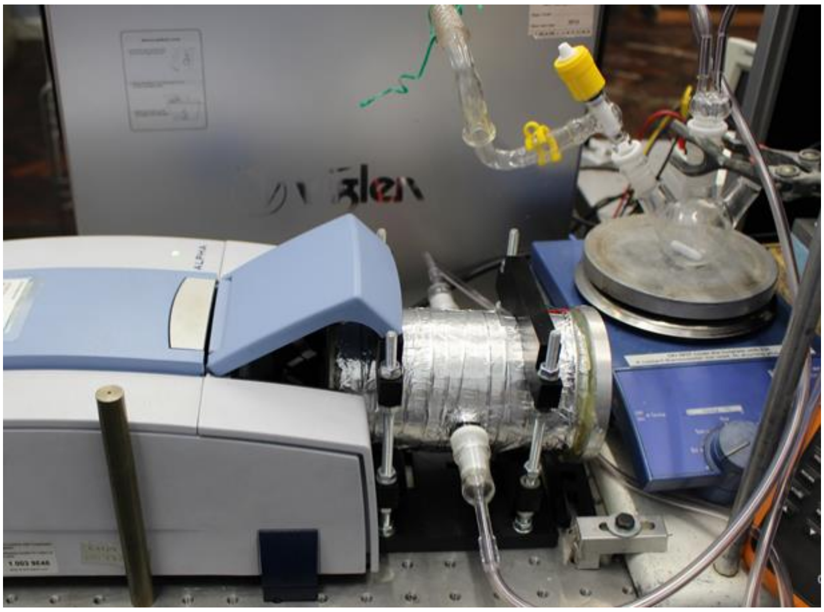

Figure 4.12 – Photograph of the 2.8 m White cell FTIR and flask set-up for analysing $^{14}NH_3$ and $^{15}NH_3$ gas released from basified bacterial culture samples.

Figure 4.13 shows typical experimental FTIR spectra of $^{14}NH_3$ (cyan) and $^{15}NH_3$ (dark blue) gases released, both corresponding to 20 mM NH_4^+ in solution. The two Q-branches of the ν_2 N-H wagging (umbrella) fundamental are visible; it is centred around 950 cm^{-1} for $^{14}NH_3$. Two Q-branches are observed due to the inversion doubling phenomenon exhibited by trigonal pyramidal molecules. The ν_2 *P*- and *R*-branches extend over 700 – 1200 cm^{-1}, outside the range displayed in Figure 4.13. The ν_2 band is the strongest in the IR spectrum of NH_3 and is free from interferences from CO_2 and water lines making it commonly used for FTIR analysis of $^{14}NH_4^+$ and $^{15}NH_4^+$ [196]. A self-written computer programme implemented a least-squares fit of the 955 – 970 cm^{-1} region of experimental FTIR spectra to the sum of scaled $^{14}NH_4^+$ and $^{15}NH_4^+$ model spectra and a linear baseline, as shown in Figure 4.14.

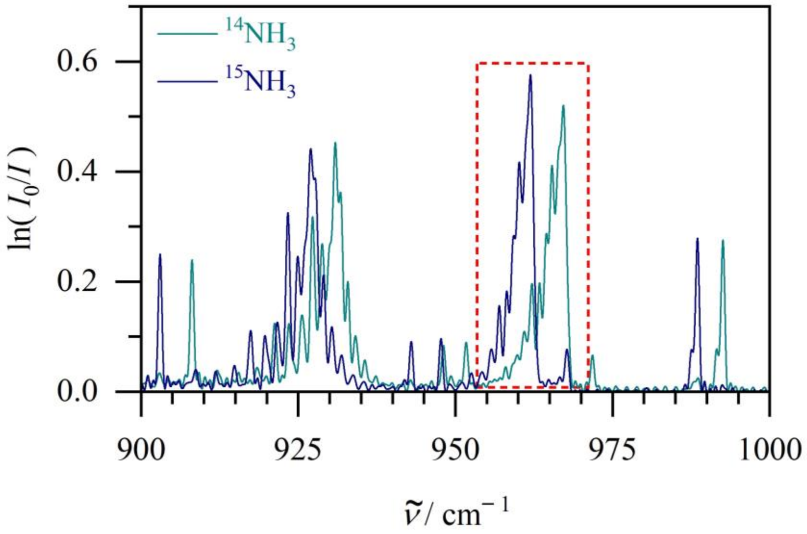

Figure 4.13 – Experimental White cell FTIR spectra of $^{14}NH_3$ (cyan) and $^{15}NH_3$ (dark blue) gases, each corresponding to 20 mM NH_4^+ in solution. The red dashed box indicates the ν_2 *Q*-branch fitted for NH_3 analysis.

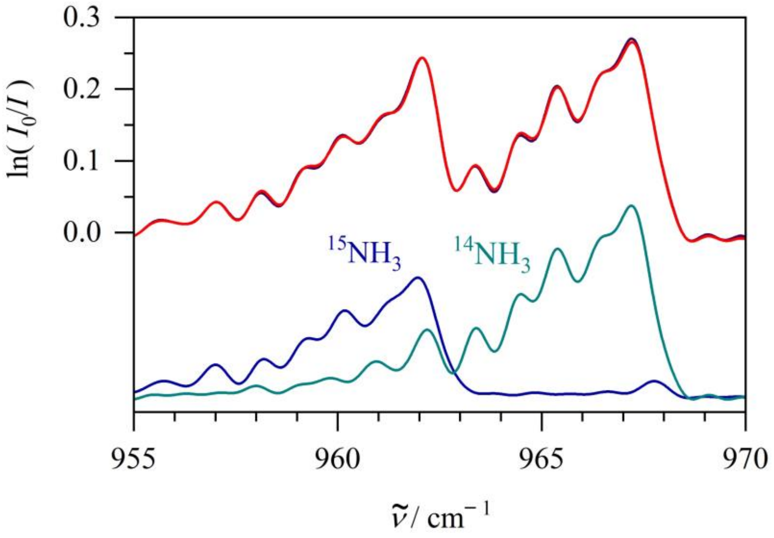

Figure 4.14 – In black, an experimental White cell FTIR spectrum of released $^{14}NH_3$ and $^{15}NH_3$ gases corresponding to 12.5 mM $^{14}NH_4^+$ and 8.25 mM $^{15}NH_4^+$ in solution. In red, the sum of the fitted $^{14}NH_3$ and $^{15}NH_3$ models shown in cyan and dark blue, respectively.

Figure 4.15 shows calibration plots for $^{14}NH_4^+$ and $^{15}NH_4^+$ that were constructed to convert the multipliers *x* of the model spectra returned from the least-squares fitting procedure into concentrations in solution. Under these conditions, a dynamic range up to 22.5 mM and noise-equivalent (1 σ) detection limits of 0.13 mM are obtained for both $^{14}NH_4^+$ and $^{15}NH_4^+$. This was suitable for analysing samples of the bacterial culture which contained 18 mM $^{14}NH_4^+$ and up to 10 mM $^{15}NO_3^-$ at the start. Isotopic labelling was necessary to distinguish supplemented $^{14}NH_4^+$ from $^{15}NH_4^+$ produced from DNRA. $^{14}NH_4^+$ concentrations could only decrease due to cellular biosynthesis while $^{15}NH_4^+$ concentrations produced could not exceed that of the $^{15}NO_3^-$ (or $^{15}NO_2^-$) supplied.

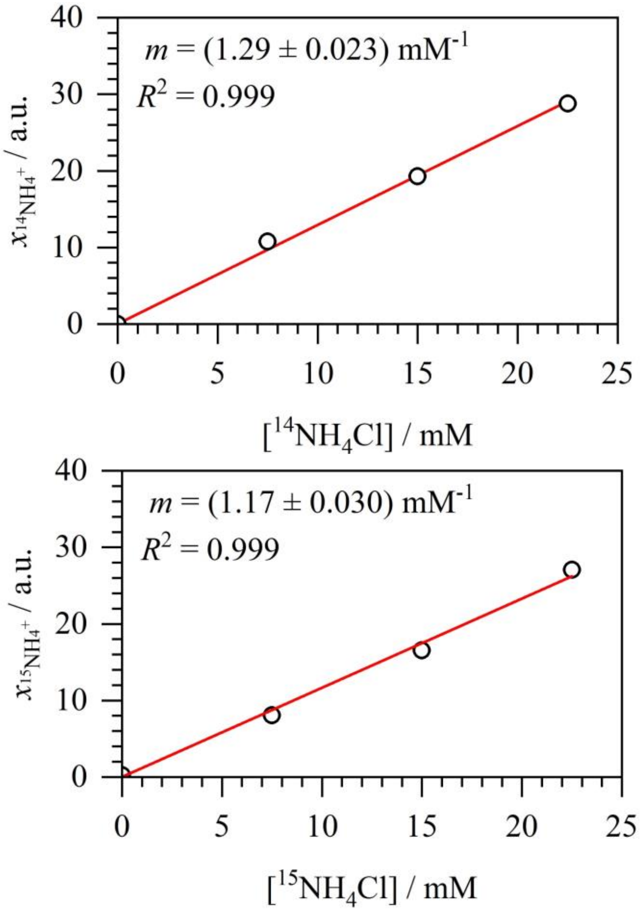

Figure 4.15 – Calibration plots for $^{14}NH_3$ and $^{15}NH_3$.

4.3 Results and Discussion

4.3.1 FTIR Spectroscopy of N_2O and its $^{14}N/^{15}N$-Isotopomers

The linear, triatomic molecule N_2O has four vibrational modes; these vibrations are symmetric stretching (ν_1) at 1285 cm^{-1}, doubly degenerate bending (ν_2) at 598 cm^{-1} and asymmetric stretching (ν_3) at 2224 cm^{-1}. It has four $^{14}N/^{15}N$-isotopomers, *i.e.* $^{14}N_2O$, $^{15}N_2O$ and the structural isomers $^{14}N^{15}NO$ and $^{15}N^{14}NO$. N_2O is amenable to ^{15}N-isotope labelling studies due to the low natural abundance of the ^{15}N-isotope (0.37 %). In the 2000 – 3000 cm^{-1} spectral range, characteristic partially rotationally resolved bands of the N_2O isotopomers are available for FTIR analysis. Apart from 2250 – 2400 cm^{-1}, which is saturated by the CO_2 asymmetric stretching fundamental, this region is free from significant spectral interferences, such as water vapour. The HITRAN molecular database contains line lists for the three most abundant $^{14}N/^{15}N$-isotopomers, excluding $^{15}N_2O$ [8]. A reference spectrum of $^{15}N_2O$ was obtained in the present study. A survey of HITRAN and the experimental spectra showed that the following four vibrational bands were available for quantitative analysis, including band positions of $^{14}N_2O$, integrated absorption cross-sections G and peak absorbances A_{peak} under our experimental conditions for 1 μbar at 6 m folded pathlength:

- the ν_3 fundamental band near 2224 cm^{-1} with $G = 5.55 \times 10^{-17}$ cm and $A_{\text{peak}} \approx 0.023$ for rotational lines in the *P*- and *R*-branches.
- the $\nu_1 + 2\nu_2$ combination band near 2461 cm^{-1} with $G = 3.02 \times 10^{-19}$ cm and $A_{\text{peak}} \approx 1.5 \times 10^{-4}$ for rotational features in the *P*- and *R*-branches.
- the $2\nu_1$ overtone band near 2563 cm^{-1} with $G = 1.33 \times 10^{-18}$ cm and $A_{\text{peak}} \approx 6.0 \times 10^{-4}$ for rotational features in the *P*- and *R*-branches.
- the $\nu_2 + \nu_3$ combination band near 2798 cm^{-1} with $G = 9.00 \times 10^{-20}$ cm and $A_{\text{peak}} \approx 2.6 \times 10^{-4}$ for its *Q*-branch.

Characteristic spectral shifts allowed distinction of the isotopomers, while their G and A_{peak} values remained essentially the same. For accurate quantitative results, A_{peak} should not exceed unity. The dynamic range of the ν_3 fundamental thus extended from trace levels up to *ca*. 45 µbar N_2O, the $\nu_1 + 2\nu_2$ combination up to 6.8 mbar, the $2\nu_1$ overtone up to 1.7 mbar and the $\nu_2 + \nu_3$ combination up to 3.8 mbar. This range could be extended by reducing the absorption pathlength of the White cell from 6 to 4 m; however, this was not necessary for the present study. Using Henry's law, N_2O partial pressures could be converted into concentrations in solution with 7 % of the total estimated to be dissolved.

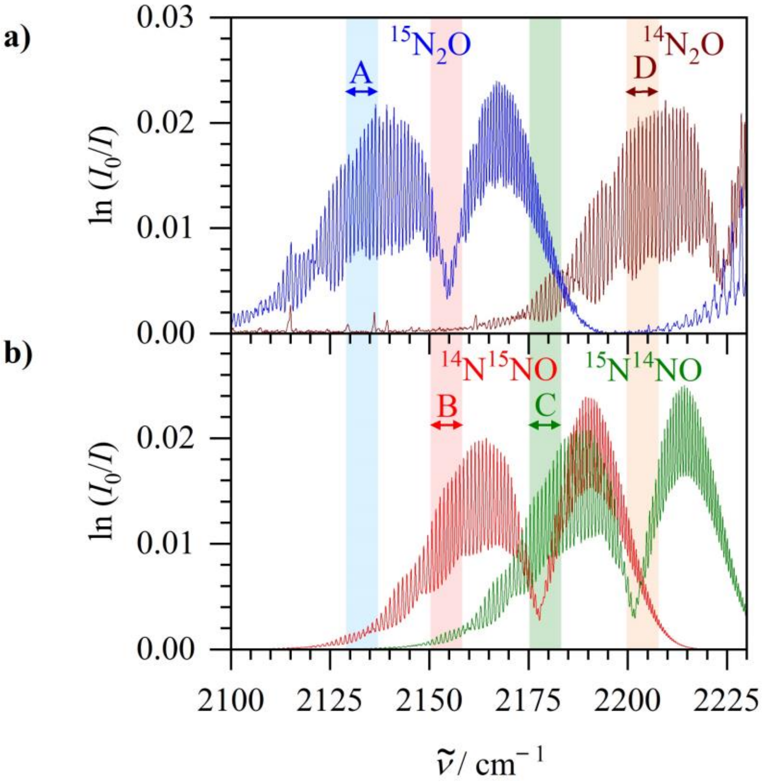

Figure 4.16 – ν_3 fundamental bands of N_2O isotopomers with partially resolved rotational *P*- and *R*-branches. Absorbances are scaled to correspond to 1 µbar (1 ppmv) at 6 m pathlength. **a)** Experimental FTIR spectra of $^{15}N_2O$ (blue) and $^{14}N_2O$ (brown). **b)** Isotopomers (structural isomers) $^{14}N^{15}NO$ (red) and $^{15}N^{14}NO$ (green) calculated from the HITRAN database. **A** to **D** denotes spectral ranges used in the fit.

Figure 4.16 shows the ν_3 fundamental bands of the four N_2O isotopomers, with distinct *P*- and *R*-branch features. $^{14}N_2O$ has its origin near 2224 cm^{-1} and in a spectrum containing only this isotopomer, a least-squares fit to the reference spectrum in the region denoted 'D' returns a multiplier which corresponds to N_2O partial pressure. A simple integration over the ν_3 band was not suitable because, at higher wavenumbers, part of the *R*-branch was buried in $^{13}CO_2$ absorptions at natural abundance. The region ‘D’ was selected because it had some of the strongest absorption features, it has very characteristic partially resolved lines and it was the least affected by $^{13}CO_2$. With this fitting routine, noise analysis of blank samples provided a noise-equivalent (1 σ) detection limit of 60 nbar (60 ppbv at 1 bar total pressure) at 6 m pathlength and 128 accumulations which required 2 min to acquire. Detection limits could be improved by more averaging or increasing the pathlength to 8 m. Note that this limit should be sufficient to detect the 330 ppbv ambient levels of N_2O for environmental analytical applications. The ν_3 fundamental band shifted to lower wavenumbers for the heavier isotopomers at 2201 cm^{-1} for $^{15}N^{14}NO$, 2178 cm^{-1} for $^{14}N^{15}NO$ and 2155 cm^{-1} for $^{15}N_2O$. As the ν_3 bands were overlapping, only a simultaneous fit to all four model spectra could yield individual partial pressures. However, a fit over the entire 2100 – 2200 cm^{-1} region had serious problems with cross-correlations. After careful analysis, a simultaneous fit only including the regions ‘A’ to ‘D’ was devised, as shown in Figure 4.16. Each region was chosen so than an individual isotopomer had a maximum weight while the other isotopomers had as little weight as possible. The fit returned multipliers which were not noticeably affected by cross-correlations and yielded reliable isotopic partial pressures up to a dynamic range of about 45 μbar per isotopomer.

Figure 4.17 shows the weaker absorption bands that were more suitable for N_2O analysis at partial pressures above 45 μbar. In isotopically pure samples, the $2\nu_1$ overtone band near 2563 cm^{-1} could be integrated from 2505 – 2613 cm^{-1} to obtain $^{14}N_2O$ partial pressures after comparison with a PNNL reference spectrum. For $^{15}N_2O$, the $2\nu_1$ band shifted near 2523 cm^{-1} and could be integrated from 2460 – 2580 cm^{-1}. Fitting the $2\nu_1$ band provided a dynamic range up to 1.7 mbar. To obtain $^{14}N_2O$ partial pressures up to 6.8 mbar, the $\nu_1 + 2\nu_2$ combination band near 2461 cm^{-1} could be integrated from 2420 – 2500 cm^{-1}. A similar fit for $^{15}N_2O$ would require a different fitting routine, such as integrating only the *R*-branch instead of the entire $\nu_1 + 2\nu_2$ band. This is due to the combination band shifting near 2407 cm^{-1} and requiring integration from 2370 – 2450 cm^{-1}; however, from 2200 – 2400 cm^{-1} the spectrum was saturated by the asymmetric stretching fundamental of CO_2 so that the *P*-branch could not be integrated. Note that Figure 4.17 cuts off below 2400 cm^{-1} due to the saturation by CO_2.

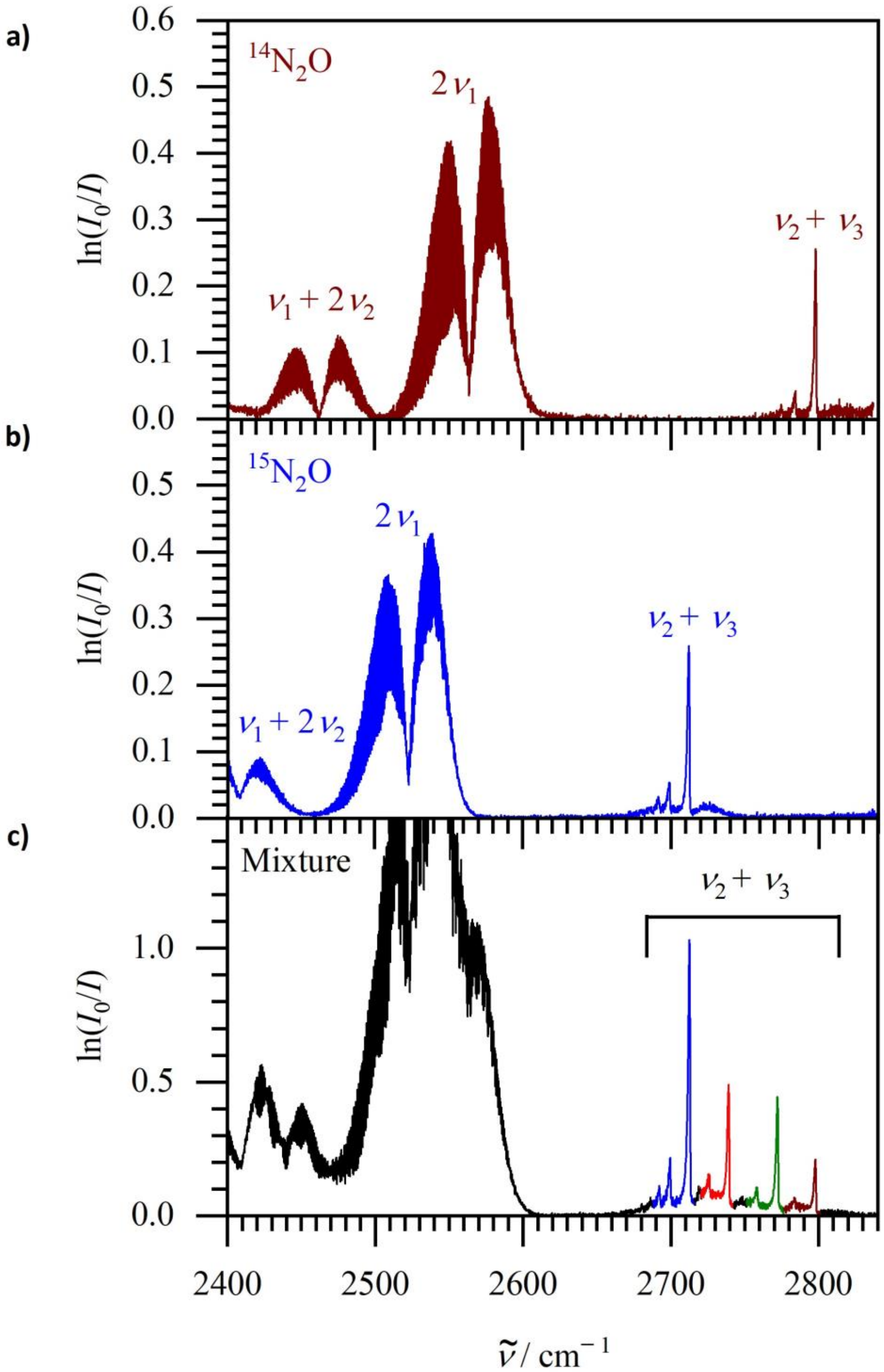

Figure 4.17 – Experimental FTIR spectra of N_2O overtone and combination bands for **a)** $^{14}N_2O$, **b)** $^{15}N_2O$ and **c)** a mixture of the four $^{14}N/^{15}N$-isotopomers, see Figure 4.18 for more detail.

Also shown in Figure 4.17 is a mixture of the four $^{14}N/^{15}N$-isotopomers. The $2\nu_1$ and $\nu_1 + 2\nu_2$ bands overlapped and would require a more sophisticated simultaneous fit, like the routine for the ν_3 fundamental shown in Figure 4.16. Fortunately, this was not required as the $\nu_2 + \nu_3$ combination band near 2798 cm^{-1} for $^{14}N_2O$ had a sharp, characteristic *Q*-branch which remained well resolved and separated in isotopic mixtures. After comparison with reference spectra, simple integrations over the separate *Q*-branch peaks yielded isotopic partial pressures in a mixture up to a dynamic range of about 3.8 mbar. The $\nu_2 + \nu_3$ combination bands of the isotopomer mixture are shown in more detail in Figure 4.18. The mixture contained 2.8 mbar $^{15}N_2O$ (49 %), 1.1 mbar $^{14}N^{15}NO$ (20 %), 1.2 mbar $^{15}N^{14}NO$ (22 %) and 0.5 mbar $^{14}N_2O$ (9 %). The spectrum was recorded at 30 h during the anaerobic respiration of *E. coli* supplemented with 10 mM $^{15}NO_3^-$ and 5 mM $^{14}NO_3^-$, as discussed further in Section 4.3.4.

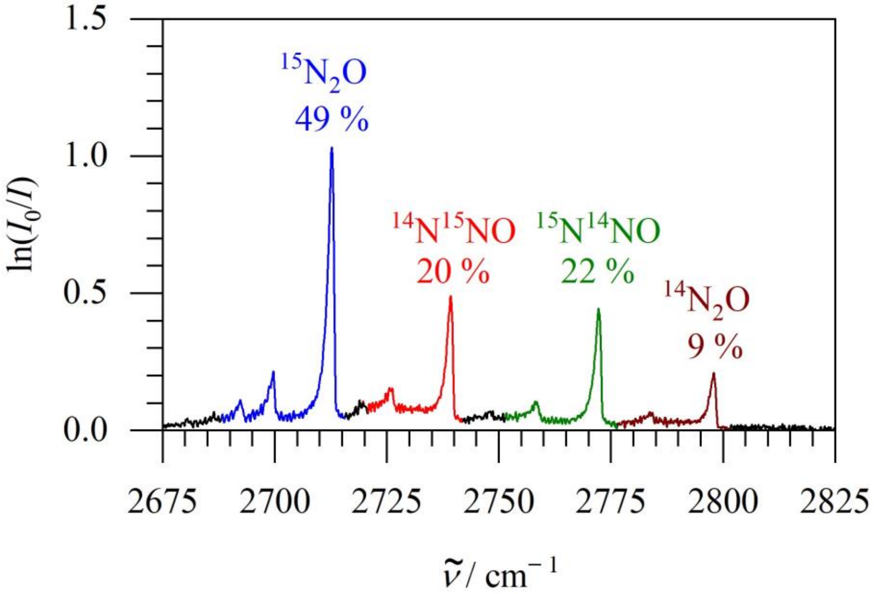

Figure 4.18 – Experimental FTIR spectrum of the $\nu_2 + \nu_3$ bands of 2.8 mbar $^{15}N_2O$ (49 %), 1.1 mbar $^{14}N^{15}NO$ (20 %), 1.2 mbar $^{15}N^{14}NO$ (22 %) and 0.5 mbar $^{14}N_2O$ (9 %). The isotopomer mixture was recorded at 30 h during the anaerobic respiration of *E. coli* supplemented with 10 mM $^{15}NO_3^-$ and 5 mM $^{14}NO_3^-$ (see Section 4.3.4). Note that this figure is a zoom-in of the spectrum displayed in Figure 4.17 Panel c.

4.3.2 Nitrate Reduction by *E. coli*

Figure 4.19 is a typical example of pH, OD_{600} and number of moles (n) of electron acceptors and other metabolites measured during the reduction of 10 mM $^{15}NO_3^-$ by anaerobic *E. coli* batch cultures. Concentrations (mM) in solution were converted to n (mmol) by multiplying by the culture volume (0.25 L), as were partial pressures using the ideal gas law ($V = 1.425 \times 10^{-3}$ m^3, $T = 310$ K) and correcting for the dissolved percentage calculated *via* Henry's law (10 % CO_2, 7 % N_2O and 99.7 % ethanol). All biological experiments were repeated in triplicate, and all repeats showed essentially the same behaviour. The time-dependent data displayed is for a single representative experiment selected from the repeats. Phase **A** (0 – 6.5 h) lasted until all NO_3^- was reduced to NO_2^-. Phase **B** (6.5 – 10 h) lasted until all NO_2^- was reduced to NH_4^+ and N_2O. Phase **C** (> 10 h) had no electron acceptors remaining so the bacteria utilised fermentative pathways solely. The ^{15}N-label transferred to $^{15}NH_4^+$ and $^{15}N_2O$ with no other trace of N_2O isotopomers formed. This was consistent with other studies that have found that the N-atoms in N_2O both originate from NO_3^-/ NO_2^- and not from any other N-containing species, such as N_2 or NH_4^+ [193, 194, 197]. The externally measured start and end-point pH values showed good agreement with the time-dependent spectroscopically determined pH.

After a brief lag phase, exponential growth began at 3 h with a rapid increase in the OD_{600} observed. NO_3^- reduction to NO_2^- mirrored the growth curve with most of the NO_2^- excreted in order to prevent cytoplasmic toxification [198]. NO_2^- peaked at 2.2 mmol at 6.5 h, which is less than the initial 2.5 mmol NO_3^- supplied due to some NO_2^- being reduced alongside NO_3^- in phase **A**. The production of 0.3 mmol $^{15}NH_4^+$ and 1.6 µmol $^{15}N_2O$ from NO_2^- reduction during phase **A** accounts for the total N-balance. Only 1 % of the NO_2^- reduced during phase **A** was converted to N_2O instead of NH_4^+. The NADH-dependent cytoplasmic NO_2^- reductase (NirB) likely produced NH_4^+ during phase **A** as it is active when NO_3^- is readily available, unlike the membrane-bound periplasmic NO_2^- reductase (NrfA) which is not [189].

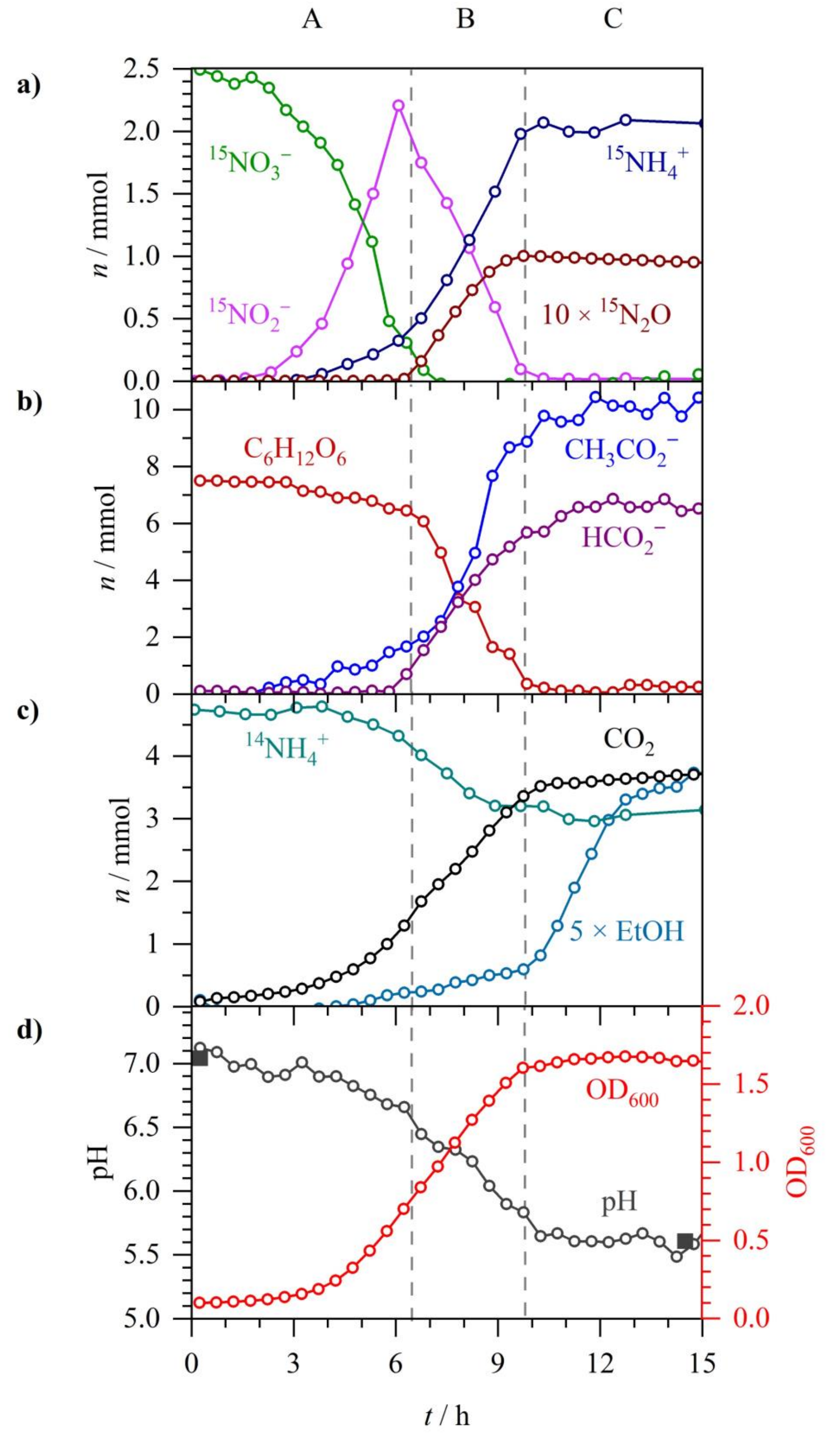

Figure 4.19 – Anaerobic *E. coli* growth in M9 medium supplemented with 10 mM $^{15}NO_3^-$. A to C denotes three distinct phases: NO_3^- reduction (A), NO_2^- reduction (B) and NO_2^- depletion (C). **a)** *n* of $^{15}NO_3^-$, $^{15}NO_2^-$, $^{15}NH_4^+$ and $^{15}N_2O$ (× 10). **b)** *n* of acetate, formate and glucose. **c)** *n* of CO_2, ethanol (× 5) and $^{14}NH_4^+$. **d)** Spectroscopic pH (open circles), externally measured pH (solid squares) and OD_{600}.

As *E. coli* does not possess any known native N_2O reductases, further reduction to N_2 was not expected to occur. However, there is some evidence in literature that N_2 can be generated from high amounts of N_2O by a yet unknown mechanism [182]. To investigate whether under our experimental conditions N_2 was produced, the 10 mM $^{15}NO_3^-$ reduction experiment was repeated, but under an argon atmosphere instead of N_2. No trace of N_2 production was observed in the CERS spectra within the noise-equivalent (1 σ) detection limit of *ca*. 0.2 mbar or 12 µmol N_2.

Formate oxidation to CO_2 by the NO_3^- inducible formate dehydrogenase (FDH-N) is a key physiological electron source for NO_3^- reduction [184]. 1.7 of the 2.5 mmol NO_3^- reduced was coupled to FDH-N activity as CO_2 increased by such in phase **A**. The remaining 0.8 mmol NO_3^- was likely coupled to NADH oxidation [199]. As no significant formate was excreted during phase **A**, the majority of all formate produced by pyruvate formate lyase (PFL) activity must have been oxidised to CO_2. For each formate produced by PFL, one acetyl-CoA is formed which can be either directed into the anaerobic TCA cycle or converted to acetate (to produce ATP) or ethanol (to remove reducing equivalents). During phase **A**, 1.7 mmol acetate and 0.05 mmol ethanol were excreted corresponding to 1.75 mmol formate, in good agreement with the 1.7 mmol CO_2 produced. Acetate was excreted to prevent cytoplasmic acidification which caused the extracellular pH to decrease from 7.1 to 6.7 during phase **A**. The minor amount of ethanol detected was likely due to reducing equivalents being coupled directly into the reduction of NO_3^- instead of ethanol production. Previous studies have found a similar repression of substrate-level NADH consuming pathways when electron acceptors are available [200]. Finally, pertaining to the discussion of phase **A**, glucose decreased by 1.1 mmol owing to the production of CO_2, acetate, ethanol and biomass synthesis.

During phase **B**, the 2.2 mmol $^{15}NO_2^-$ excreting in phase **A** was reimported into the cell and reduced to 2.0 mmol $^{15}NH_4^+$ and 0.1 mmol $^{15}N_2O$. 91 % NO_2^- was reduced to NH_4^+ and 9 % to N_2O, which is a higher partitioning to N_2O than observed in phase **A** (1 %). A higher partitioning to N_2O after NO_3^- was depleted is consistent with several studies of *E. coli* and *Salmonella enterica* that have implicated nitrate reductase A (NRA) as the enzyme that produces the majority of NO when NO_2^- is abundant and NO_3^- absent [177, 178, 201, 202]. NrfA, which is induced by NO_2^- but repressed by NO_3^-, may have also contributed towards the higher partitioning to N_2O in phase **B** as it has been proposed as a source of NO [176, 203]. The radical NO has a distinct line-resolved absorption band centred at 1904 cm^{-1} (for ^{14}NO) and a favourable partitioning into the headspace [204]. However, no intermediate ^{15}NO gas was observed by FTIR spectroscopy to accumulate, owing to its rapid detoxification to $^{15}N_2O$. The concentration of NO that accumulates in the cytoplasm of anaerobic bacteria is unknown, but indirect evidence indicates that it is in the low picomolar to low nanomolar range [205].

During phase **B**, a further 1.9 mmol CO_2 was produced and the pH decreased from 6.7 to 5.7 due to the excretion of 5.7 mmol formate and a further 7.5 mmol acetate. Due to the 3:1 stoichiometry of two-electron formate oxidation to CO_2 to six-electron NO_2^- reduction to NH_4^+, 0.6 mmol NO_2^- reduced by NrfA was likely coupled to 1.9 mmol formate oxidised to CO_2 [206]. The 5.7 mmol formate excreted during phase **B** would be plentiful for coupling its oxidation to the remainder 1.4 mmol NO_2^- left to reduce. However, NrfA is most active at low NO_2^- levels, while NirB is most active at high levels for detoxification of excess NO_2^- [189, 198]. Hence, the other 1.4 mmol NO_2^- was likely reduced by NirB.

Phase **C** started with exponential growth ending as the OD_{600} peaked at 1.7, due to the depletion of glucose and NO_2^-. With no significant electron acceptors available, the cells funnelled reducing equivalents into ethanol as a further 0.7 mmol was produced over the first 5 h of phase **C**. The remaining 5.7 mmol formate was slowly oxidised to CO_2 at a rate of 0.03 mmol h^{-1}. Under anaerobic conditions, the presence of formate induces formate hydrogenlyase (FHL) activity that disproportionates formate to H_2 and CO_2 [207]. O_2 and NO_3^- repress FHL expression and instead induce the aerobic and formate-NO_3^- respiratory chains. High formate concentrations can partially reverse the repression by NO_3^-, but not by O_2 [208, 209]. However, CERS measurements detected no H_2 production during 10 mM $^{15}NO_3^-$ reduction experiments. During phase **C**, there was a slight decline in N_2O observed, but this was an artefact due to the gas adsorbing to the tubing and glass surfaces inside the closed system.

These experiments were terminated after 2 days with around 5 mmol formate still remaining. The dry biomass was typically around 200 mg. As *E. coli* can be approximated to be 48 % carbon and 14 % nitrogen by mass [129], *ca*. 8 mmol C and 2 mmol N in the biomass originated from the 7.5 mmol glucose (45 mmol C) and NH_4^+, respectively. 44 out of the 45 mmol C from glucose can be accounted for in the biomass, 5 mmol CO_2, 5 mmol formate, 12 mmol acetate (24 mmol C) and 1 mmol ethanol (2 mmol C). During exponential growth over phases **A** and **B**, $^{14}NH_4^+$ decreased from 4.5 to 3.0 mmol accounting for 1.5 out of the 2 mmol N in the biomass. The remaining 0.5 mmol N likely was taken from reimporting the excreted $^{15}NH_4^+$. The 2.5 mmol ^{15}N-label can be accounted for in the 2.0 $^{15}NH_4^+$, 0.1 mmol $^{15}N_2O$ (0.2 mmol ^{15}N) and ~ 0.5 mmol $^{15}NH_4^+$ used for biosynthesis.

4.3.3 Nitrite Reduction by *E. coli*

To study the response to NO_2^- reduction alone, anaerobic *E. coli* cultures were supplemented with 5 mM $^{15}NO_2^-$, as shown in Figure 4.20. Phase **A'** (0 – 9 h) corresponded to the reduction of NO_2^- to NH_4^+ with concurrent N_2O production *via* NO. Phase **B'** (9 – 15 h) was when the bacteria utilised fermentative pathways only, due to the depletion of NO_2^-. During phase **A'**, 1.25 mmol $^{15}NO_2^-$ was reduced almost exponentially to 1.15 mmol $^{15}NH_4^+$ (90 %) and 0.06 mmol $^{15}N_2O$ (10 %), mirroring the bacterial growth curve which increased to an OD_{600} of 0.7. The 10 % partitioning to N_2O here was consistent with the 9 % observed during the NO_2^- reduction phase **B** in Figure 4.19. During phase **A'**, 1.9 mmol CO_2, 3.7 mmol acetate, 2.0 mmol formate and 0.3 mmol ethanol were produced as glucose decreased from 7.5 to 5.2 mmol. Excretion of acetate and formate caused the pH to decrease from 6.9 to 6.3. The sum of acetate and ethanol (4.0 mmol) showed good agreement with the sum of CO_2 and ethanol (3.9 mmol). Due to the 3:1 stoichiometry of formate oxidation to NO_2^- reduction and 1.9 mmol CO_2 being produced, 0.63 out of the initial 1.15 mmol NO_2^- reduced to NH_4^+ was coupled to formate oxidation to CO_2. The remaining 0.52 mmol NO_2^- was likely reduced *via* coupling to NADH oxidation by NirB.

Phase **B'** began at 9 h when $^{15}NO_2^-$ was depleted. *E. coli* can only utilise fermentative pathways in the absence of electron acceptors such as NO_3^- and NO_2^-. The most notable difference between 10 mM $^{15}NO_3^-$ reduction (discussed in Section 4.3.2) and 5 mM $^{15}NO_2^-$ reduction was that H_2 production occurred after NO_2^- depletion in Figure 4.20. No H_2 production was observed during phase **A'** as formate-dependent NO_2^- reduction likely made the intracellular formate unavailable for FHL induction. The presence of formate is required for FHL expression but it can be made unavailable by coupling to the reduction of electron acceptors. This inhibiting effect has been observed for NO_3^- and trimethyl amine N-oxide (TMAO) respiring *E. coli* cultures and in both cases the effect could be partially relieved by adding exogenous formate [209, 210]. When NO_2^- was depleted, 5.2 mmol glucose was still present meaning further formate could be produced in phase **B'** which may have triggered the induction of FHL. From 9 – 15 h, 6.0 mmol H_2 and a further 6.0 mmol CO_2 were produced from the disproportionation of formate. At 10 h, there was a peak value of 2.1 mmol excreted.

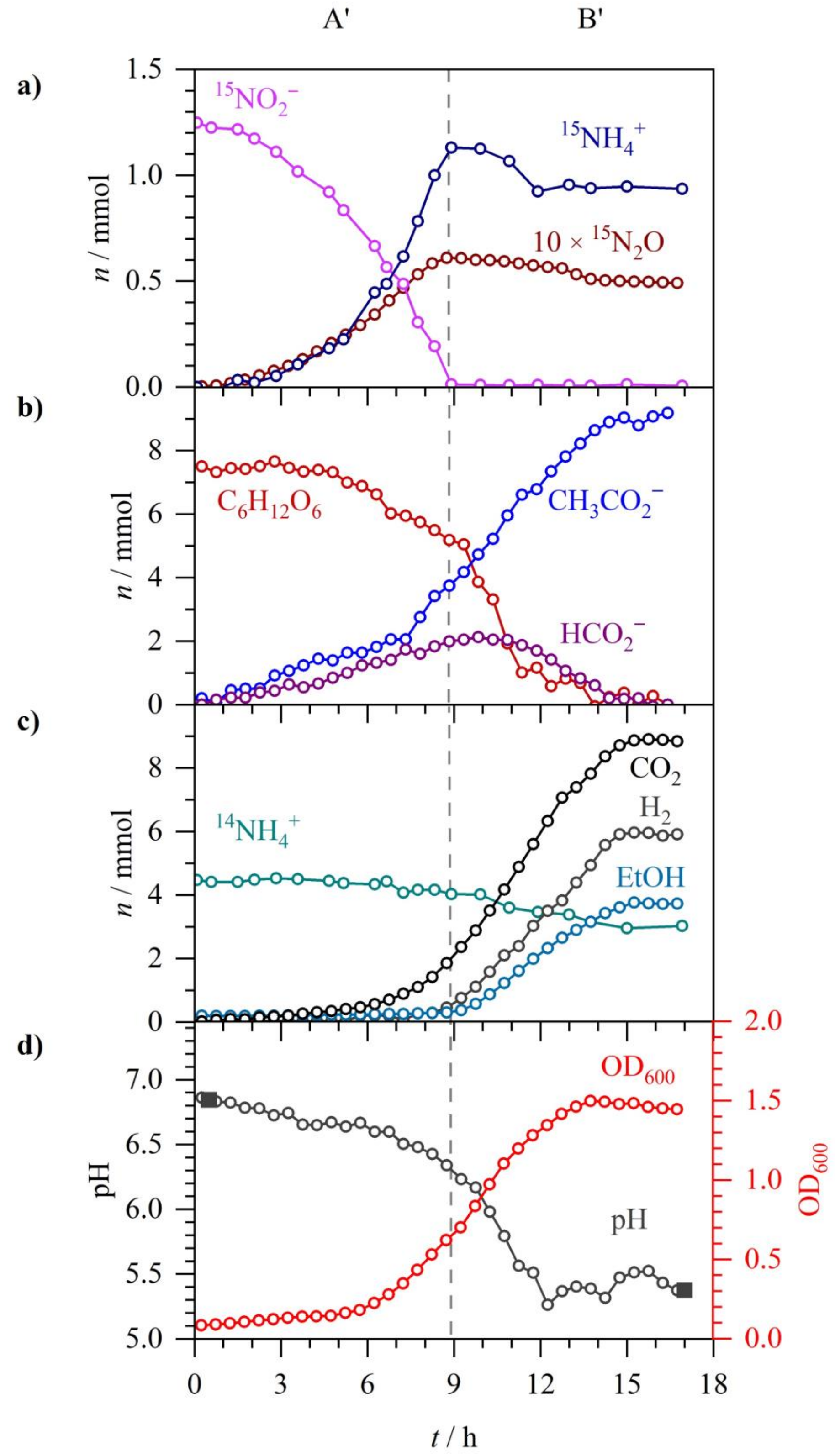

Figure 4.20 – Anaerobic *E. coli* growth in M9 medium supplemented with 5 mM $^{15}NO_2^-$. A' and B' denote two distinct phases: NO_2^- reduction (A') and NO_2^- depletion (B'). **a)** *n* of $^{15}NO_2^-$, $^{15}NH_4^+$ and $^{15}N_2O$ (× 10). **b)** *n* of acetate, formate and glucose. **c)** *n* of CO_2, H_2 ethanol and $^{14}NH_4^+$. **d)** Spectroscopic pH (open circles), externally measured pH (solid squares) and OD_{600}.

During phase **B’**, a further 5.3 mmol acetate and 3.5 mmol ethanol were produced. By 12 h, the pH dropped to 5.4 and then remained stable as 1.6 mmol acetate was excreted and balanced by the reimport and disproportionation of 1.5 mmol formate. By 14 h, the OD_{600} peaked at 1.5, just before the end of observable metabolic activity due to the depletion of glucose and formate. 42.8 out of the 45 mmol C from glucose could be accounted for in the biomass (~ 8 mmol C), 8.9 mmol CO_2, 9 mmol acetate (18 mmol C) and 3.8 mmol ethanol (7.6 mmol C). During exponential growth, $^{14}NH_4^+$ decreased from 4.5 to 2.9 mmol as did $^{15}NH_4^+$ from a peak value of 1.15 to 0.9 mmol accounting for 1.85 mmol out of the ~ 2 mmol N in the biomass.

4.3.4 Simultaneous Nitrate and Nitrite Reduction

In Section 4.3.2, when *E. coli* was supplemented with 10 mM $^{15}NO_2^-$, there was a distinct hierarchy of metabolic pathways between phases **A**, **B** and **C**. NO_3^- reduction dominated in phase **A**, followed by NO_2^- reimport and reduction in phase **B** and finally fermentative pathways solely occurred in phase **C**. However, in phase **A** it was observed that some NO_2^- was simultaneously reduced to NH_4^+ and N_2O alongside NO_3^- reduction. To further investigate the overlap between the reductions of NO_3^- and NO_2^- in phase **A**, anaerobic *E. coli* cultures were supplemented with 10 mM $^{15}NO_3^-$ and 5 mM $^{14}NO_2^-$, as shown in Figures 4.21 and 4.22.

Phase **A** (0 – 9 h) lasted until all $^{15}NO_3^-$ was reduced to $^{15}NO_2^-$. Phase **B** (9 – 30 h) corresponded to the reduction of NO_2^- to NH_4^+ with concurrent N_2O production *via* NO. At 15.5 h, the OD_{600} peaked and exponential growth of *E. coli* ended; thus, phase **B1** (9 – 15.5 h) was NO_2^- reduction with glucose still present and phase **B2** (15.5 – 30 h) was NO_2^- reduction during glucose depletion. Figure 4.21 displays *n* of $^{15}NO_3^-$, NO_2^-, $^{14}NH_4^+$, $^{15}NH_4^+$ (× 10) and N_2O isotopomers during phase **A**. The complete characterisation of bacterial growth is given in Figure 4.22.

In phase **A**, 2.5 mmol $^{15}NO_3^-$ was reduced and *ca.* 2.25 mmol $^{15}NO_2^-$ was excreted. NO_2^- colorimetry cannot distinguish between $^{14}NO_2^-$ and $^{15}NO_2^-$, so the total NO_2^- was observed to increase from 1.25 to 3.5 mmol. During phase **A**, as in Section 4.3.2, some NO_2^- was reduced alongside $^{15}NO_3^-$ to 0.2 mmol $^{15}NH_4^+$ and N_2O isotopomers. $^{14}NO_2^-$ reduction to $^{14}N_2O$ occurred immediately with 2.2 µmol $^{14}N_2O$ produced almost-linearly by 9 h. This indicated that even before significant $^{15}NO_3^-$ reduction began, some enzymatic activity to reduce small quantities of NO_2^- to N_2O was immediately active. For the first 3 h, $^{15}NO_3^-$ and NO_2^- measurements were virtually constant suggesting a lag in the expression of NRA. This lag was best indicated by the highly-sensitive positional isomers $^{14}N^{15}NO$ and $^{15}N^{14}NO$ which were not detected until $^{15}NO_2^-$ was made available by $^{15}NO_3^-$ reduction starting from 3 h. $^{15}N_2O$ production also began at 3 h, but much slower than the production of $^{14}N_2O$ and the positional isomers, due to $^{14}NO_2^-$ initially being more available than $^{15}NO_2^-$.

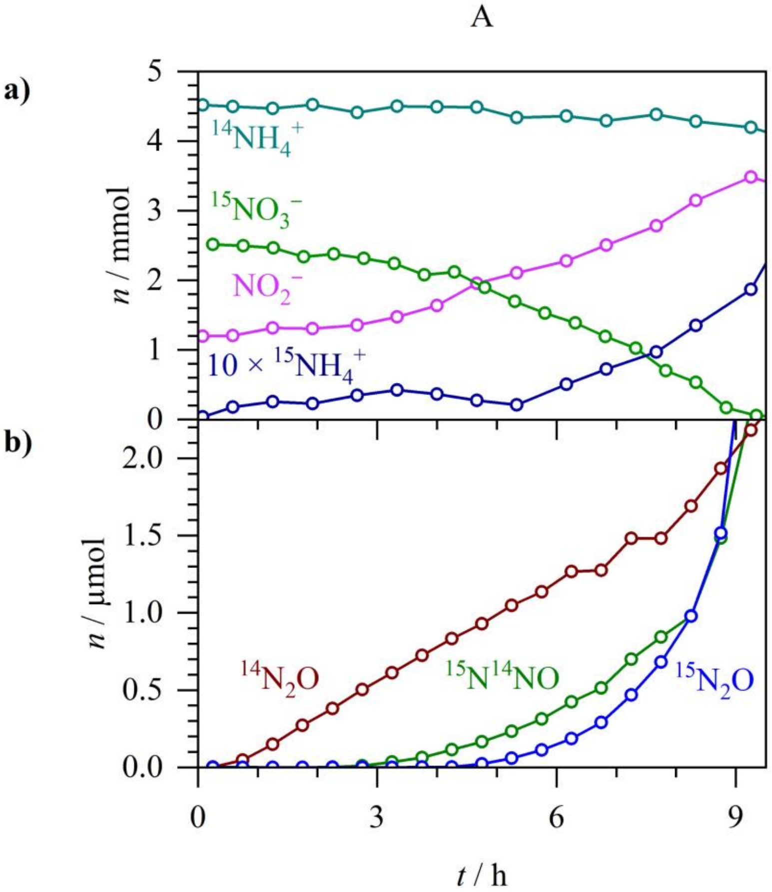

Figure 4.21 – N_2O isotopomers produced in the NO_3^- reduction phase **A** of anaerobic *E. coli* growth in M9 medium supplemented with 10 mM $^{15}NO_3^-$ and 5 mM $^{14}NO_2^-$. **a)** *n* of $^{15}NO_3^-$, NO_2^- (both ^{14}N and ^{15}N), $^{14}NH_4^+$ and $^{15}NH_4^+$ (× 10). **b)** *n* of N_2O isotopomers produced. $^{14}N^{15}NO$ is omitted due to essentially having the same behaviour as $^{15}N^{14}NO$.

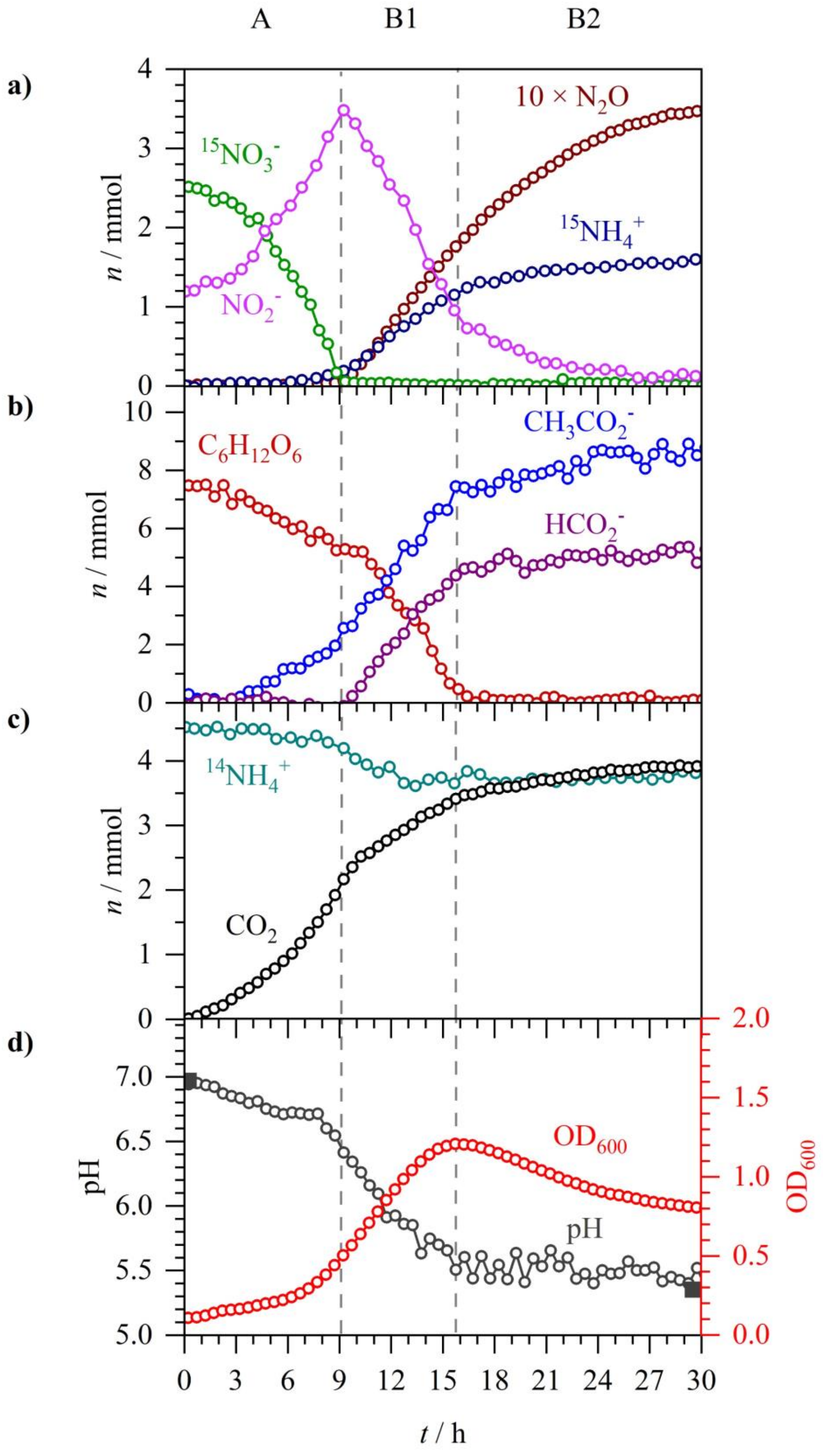

Figure 4.22 – Anaerobic *E. coli* growth in M9 medium supplemented with 10 mM $^{15}NO_3^-$ and 5 mM $^{14}NO_2^-$. A, B1 and B2 denotes three distinct phases: NO_3^- reduction (A), NO_2^- reduction with glucose present (B1) and NO_2^- reduction with glucose depleted (B2). **a)** n of $^{15}NO_3^-$, NO_2^-, $^{15}NH_4^+$ and sum of all N_2O isotopomers (× 10). **b)** n of acetate, formate and glucose. **c)** n of CO_2, H_2, ethanol and $^{14}NH_4^+$. **d)** Spectroscopic pH (open circles), externally measured pH (solid squares) and OD_{600}.

By the end of phase **A**, 1.5 µmol each of $^{14}N^{15}NO$, $^{15}N^{14}NO$ and $^{15}N_2O$ were produced alongside the 2.2 µmol $^{14}N_2O$, totalling 6.7 µmol N_2O. It is unknown if $^{14}NO_2^-$ was also immediately reduced to $^{14}NH_4^+$ due to the large background of 4.5 mmol $^{14}NH_4^+$ in the M9 growth medium. It can be assumed that *ca.* 0.25 mmol $NO_2^-$was reduced during phase **A** based on the NO_2^- colorimetry measurements giving a partitioning of 5 % NO_2^- reduced to N_2O, instead of to NH_4^+. This was a higher value than the 1 % partitioning observed during phase **A** in Section 4.3.2, indicating that the added 5 mM $^{14}NO_2^-$ led to more NO generation and detoxification to N_2O. During phase **A**, glucose decreased from 7.5 to 5.6 mmol due to the production of 2.1 mmol CO_2, 2.0 mmol acetate and biosynthetic pathways. The OD_{600} began increasing indicating exponential bacterial growth while acetate excretion caused the pH to decrease from 7.0 to 6.5. No formate was excreted during phase **A**, as the *n* of CO_2 and acetate suggested all formate was oxidised to CO_2. No ethanol was detected during the entire 30 h experiment, likely due to the abundance of electron acceptors to couple the reducing equivalents to.

Phase **B1** began with $^{15}NO_3^-$ depletion and ended at 15.5 h when glucose was depleted, coinciding with the OD_{600} peaking at 1.2. The pH dropped further to 5.6 due to the excretion of 5.0 mmol formate and a further 6.0 mmol acetate. The sum of formate excreted and the further 1.3 mmol CO_2 produced was in good agreement with the amount of acetate excreted.

Phase **B2** lasted until NO_2^- depletion at 30 h. From NO_2^- reduction, 1.6 mmol $^{15}NH_4^+$ and 0.35 mmol N_2O (sum of all isotopomers) were produced overall. The final composition of N_2O isotopomers was previously introduced in Figure 4.18. As the majority of N_2O production occurred in phase **B** when the NO_2^- composition was *ca.* 33 % $^{14}NO_2^-$ and 66 % $^{15}NO_2^-$, a near statistical mixture of N_2O isotopomers was formed of 0.17 mmol $^{15}N_2O$ (49 %), 0.08 mmol $^{15}N^{14}NO$ (22 %), 0.07 mmol $^{14}N^{15}NO$ (20 %) and 0.3 mmol $^{14}N_2O$ (9 %). For comparison, a perfect statistical mixture would have produced 44.4 % $^{15}N_2O$, 22.2 % $^{15}N^{14}NO$, 22.2 % $^{14}N^{15}NO$ and 11.1 % $^{14}N_2O$. It is unknown whether the slight preference for $^{15}N^{14}NO$ over $^{14}N^{15}NO$ is significant or due to experimental uncertainty. The partitioning of the 3.5 mmol NO_2^- to N_2O in phase **B** was 20 %, a much higher value than the 10 % observed in Section 4.3.2. This is consistent with previous studies that found that between 5 – 36 % of NO_3^- is converted to N_2O by *E. coli*, depending on growth conditions [198].

During phase **B2**, CO_2 increased by a further 0.5 mmol while the pH remained constant at 5.6 due to no significant change in extracellular acetate and formate concentrations. 33 out of the 45 mmol C from glucose can be accounted for in the biomass (~ 8 mmol C), 4 mmol CO_2, 8 mmol acetate (16 mmol C) and 5 mmol formate. The higher NO_2^- content may have had cytotoxic effects in *E. coli* resulting in other products that have not been accounted for in the C balance. During phase **B2**, the OD_{600} decreased from 1.2 to 0.8 suggesting cell death or changes in cellular size and morphology, possibly due to the cytotoxicity of NO_2^- and NO. The 2.5 mmol ^{15}N label was accounted for in the 1.6 mmol $^{15}NH_4^+$, 0.17 mmol $^{15}N_2O$ (0.34 mmol ^{15}N), 0.08 mmol $^{15}N^{14}NO$, 0.07 mmol $^{14}N^{15}NO$ and *ca.* 0.5 mmol $^{15}NH_4^+$ assumed to have been used for biosynthesis. As *ca.* 2.0 mmol NH_4^+ was needed for biosynthesis, it was assumed that *ca.* 1.5 mmol was taken from $^{14}NH_4^+$, which decreased overall from 4.5 to 4.0 mmol suggesting that *ca.* 1.0 mmol $^{14}NH_4^+$ was produced from the reduction of the 1.25 mmol $^{14}NO_2^-$. This was in good agreement with the 0.26 mmol $^{14}NO_2^-$ reduced to N_2O isotopomers with 0.03 mmol $^{14}N_2O$ (0.06 mmol ^{14}N), 0.08 mmol $^{15}N^{14}NO$ and 0.07 mmol $^{14}N^{15}NO$.

4.4 Conclusion

This chapter has covered a study on NO_3^- and NO_2^- reduction during DNRA by anaerobic *E. coli* batch cultures using a combination of advanced spectroscopic analytical techniques in conjunction with ^{15}N-isotopic labelling. The spectroscopy of N_2O and its $^{14}N/^{15}N$-isotopomers have been discussed in detail, including which spectral features are most useful for quantitative analysis and the fitting routines employed. Notably, even the positional isomers $^{14}N^{15}NO$ and $^{15}N^{14}NO$ can be distinguished, a unique capability not available to other analytical techniques. *In Situ* analysis of the headspace was achieved using CERS and FTIR spectroscopies alongside liquid-phase Raman spectroscopy for NO_3^-, acetate, formate, glucose and pH analysis. Gas-phase CERS allowed CO_2, H_2, N_2 and O_2 monitoring while White cell FTIR measured CO_2, ethanol and N_2O. The 6 m folded pathlength White cell afforded trace gas detection of N_2O with a noise-equivalent (1 σ) detection limit of 60 nbar or 60 ppbv in 1 atm at 120 s acquisition time. This extremely high sensitivity could be used for situations where N_2O concentrations cannot be allowed to build-up, such as in certain continuous culture studies. NO_2^- and NH_4^+ analysis was achieved by sampling the bacterial culture for colorimetric and FTIR analysis, respectively. These spectroscopic techniques can detect key species in the nitrogen cycle and with the ability to distinguish N_2O isotopomers they may be of great interest for better understanding global N_2O budgets.

^{15}N-isotopic-labelling of NO_3^- and NO_2^- identified the sources of N-atoms in the products and provided insights into the mechanism of N_2O production. The reductions of $^{15}NO_3^-$, $^{15}NO_2^-$ and mixed $^{15}NO_3^-$ and $^{14}NO_2^-$ to NH_4^+ and N_2O have been discussed. In a major pathway, NO_3^- is reduced to NH_4^+ *via* NO_2^-, with the bulk of NO_2^- reduction occurring after NO_3^- depletion. By isotopically labelling $^{15}NO_3^-$, $^{15}NH_4^+$ production is distinguished from $^{14}NH_4^+$ in the growth medium. In a minor pathway, NO_2^- is reduced to N_2O *via* the toxic radical NO. With excellent detection sensitivities, N_2O monitors trace NO_2^- reduction, even when cells are predominantly reducing NO_3^-. The N_2O isotopomers revealed that some enzymatic NO_2^- reduction activity occurred immediately for cultures supplemented with mixed $^{15}NO_3^-$ and $^{14}NO_2^-$. OD_{600} and pH measurements were discussed in the context of acetate, formate and CO_2 production. H_2 production was repressed by NO_3^-, but NO_2^- respiring cultures produced H_2 after NO_2^- depletion.

Chapter 5

Hydrogen Production in the Presence of Oxygen by *E. coli* K-12

Abstract

E. coli is a facultative anaerobe that can grow in a variety of environmental conditions. In the complete absence of O_2, *E. coli* can perform a mixed-acid fermentation that contains within it an elaborate metabolism of formic acid. In this chapter, cavity-enhanced Raman spectroscopy (CERS), FTIR, liquid-phase Raman spectroscopy, isotopic labelling and molecular genetics are used to make advances in the understanding of bacterial formate and H_2 metabolism. It is shown that, under anaerobic conditions, formic acid is generated endogenously, excreted briefly from the cell and then taken up again to be disproportionated to H_2 and CO_2 by formate hydrogenlyase (FHL-1). However, exogenously added D-labelled formate behaves quite differently from the endogenous formate and is taken up immediately, independently and possibly by a different mechanism, by the cell and converted to H_2 and CO_2. The data supports an anion-proton symport model for formic acid transport. In addition, when *E. coli* was grown in a micro-aerobic environment, it was possible to analyse aspects of formate and O_2 respiration occurring alongside anaerobic metabolism. While cells growing under micro-aerobic conditions generated endogenous formic acid, no H_2 was produced. However, addition of exogenous formate at the outset of cell growth did induce FHL-1 biosynthesis and resulted in formate-dependent H_2 production in the presence of O_2.

The work presented in this chapter covers a scientific publication (ref. [211]);

Hydrogen Production in the Presence of Oxygen by Escherichia coli K-12
George D. Metcalfe, Frank Sargent and Michael Hippler (2022).
Microbiology. **168**, 3.
https://doi.org/10.1099/mic.0.001167

Author Statements

G. D. Metcalfe designed all experiments, conducted the research, analysed data, prepared figures for publication and wrote the paper. F. Sargent analysed data and wrote the paper. M. Hippler conceived the project, assembled the research team, designed the research, conducted the research, supervised the research, analysed data and wrote the paper.

5.1 Introduction

E. coli is a **γ**-proteobacterium and facultative anaerobe [25]. The bacterium is commonly found as a gut commensal in many animals (an anaerobic environment) [19], but is also found in estuaries (where micro-aerobic environments can be identified) [20] and, in addition, is associated with plant tissues and other aerobic environments [21]. As a result, *E. coli* can adapt, primarily through regulating gene expression, to changing environmental conditions [22].

The preferred mode of energy metabolism for *E. coli* is aerobic respiration. Aerobically, *E. coli* assembles short, quinone-dependent, respiratory electron transport chains [212]. The bacterium has no cytochrome bc_1 oxidase or cytochrome *c* oxidase, but instead calls upon three quinol oxidases to carry out aerobic respiration: cytochrome bo_3 oxidase, cytochrome *bd* oxidase I and cytochrome *bd* oxidase II. Each of these enzymes has a different affinity for O_2, with cytochrome bo_3 oxidase having the lowest affinity for O_2 and cytochrome *bd* oxidase II having the highest, thus allowing the bacterium to compete under a full range of different O_2 tensions [213].

A prominent electron donor in aerobic respiration is NADH, however, other possible respiratory electron donors in play under this condition are formate, glycerol-3-phosphate, pyruvate and succinate [212]. In order to use formate ($HCOO^-$) as a respiratory electron donor, *E. coli* produces two respiratory formate dehydrogenases: FDH-N and FDH-O [51]. These enzymes oxidise formate at the periplasmic side of the cytoplasmic membrane and pass electrons to the quinone pool thus generating a transmembrane proton gradient by a redox loop mechanism [214]. The FDH-N isoenzyme is encoded by the *fdnGHI* operon and is maximally expressed anaerobically in the presence of exogenous nitrate, while the FDH-O enzyme shares sequence identity with FDH-N, but the genes encoding this isoenzyme are constitutively expressed [51]. Under aerobic conditions, FDH-O is thought to couple formate oxidation to the reduction of O_2 to water by cytochrome *bd* oxidase I [215].

Under anaerobic conditions, and in the absence of any other exogenous respiratory electron acceptors, *E. coli* will carry out a mixed-acid fermentation of glucose [52]. Here, *E. coli* will generate ATP by substrate-level phosphorylation and excrete ethanol, together with a number of different organic acids, as waste products. These include acetic acid, lactic acid and formic acid. Under fermentative conditions, the *E. coli* TCA cycle is no longer a cycle. Instead, the reactions are split into a reductive arm, terminating with a low level of endogenous fumarate reductase activity, and an oxidative arm, terminating with isocitrate dehydrogenase. Acetyl-CoA is fed into the oxidative arm of the TCA cycle *via* the action of the anaerobic pyruvate formate lyase (PFL) enzyme, which is fully activated in the absence of O_2. PFL combines pyruvate with coenzyme A to generate acetyl-CoA and a formate anion [216]. Interestingly, the PFL enzyme is physically associated with the formate channel FocA at the cytoplasmic face of the plasma membrane [50]. This means that the formate so-generated is most-likely constantly excreted from the cell *via* FocA in the early stages of fermentation. In a closed batch fermentation environment, the formate ($pK_a = 3.7$) will accumulate outside the cell together with acetic acid and other products of mixed-acid fermentation, where the pH is thought to tend towards acidic as a result. At around pH 6.8, the FocA channel switches from a facilitator of excretion to a facilitator for import, and the previously externalised formate is then readmitted to the cell. This triggers the transcription of a number of genes involved in formate and pH homeostasis, including those encoding the enzyme formate hydrogenlyase (FHL-1) [51, 52].

FHL-1 is a membrane-bound enzyme made up of seven individual protein subunits [53]. It consists of a membrane arm, comprising two integral membrane proteins, and a peripheral (or catalytic) arm located at the cytoplasmic side of the membrane, comprising formate dehydrogenase-H (FDH-H) and hydrogenase-3 (Hyd-3). FDH-H is encoded by the *fdhF* gene and is a molybdenum and selenium-dependent formate dehydrogenase [54]. Hyd-3 is a [NiFe] hydrogenase enzyme [55, 217] and is predicted to be the principal point of contact of the catalytic arm with the membrane arm [53, 55]. Under mixed-acid fermentation conditions, the two enzyme activities work together as a closed redox complex directly to the Hyd-3 active site where two protons are reduced to H_2, which can then diffuse away from the cell. Overall, therefore, FHL-1 carries out the disproportionation of formate to H_2 and CO_2.

In this chapter, the physiology of H_2 and formate metabolism in living intact cells has been revisited using powerful analytical spectroscopic technique and isotopic labelling, which can monitor formation and consumption of compounds over time without invasive sampling of the batch culture. Surprisingly, under anaerobic fermentative conditions, isotopic labelling experiments revealed that exogenously-added formate behaved quite differently from endogenously-produced formate, being taken up and immediately disproportionated to H_2 and CO_2 while excretion of endogenous formate continued as normal. In addition, when *E. coli* was grown in our system in the presence of O_2, it was possible to identify aspects of anaerobic metabolism (for instance formate and ethanol production) occurring at the same time as O_2

uptake, indicative of the establishment of a micro-aerobic environment. Interestingly, under this micro-aerobic growth regimen, despite formate production and consumption being observed, no H_2 gas production was detected unless exogenous formate was added to the culture, in which case H_2 gas production proceeded in an FHL-1-dependent manner. This work demonstrates that FHL-1 can be assembled and remains active under micro-aerobic conditions and gives confidence this cellular system could be further harnessed for biotechnological applications where O_2 levels may fluctuate or be difficult to control.

5.2 Experimental

The *E. coli* K-12 strains utilised in this study were MG1655 (F^-, λ^-, *ilvG*$^-$, *rfb-50*, *rph-1* [25]) and MG16dZ (MG1655 Δ*fdhF* [218]). Strains were transferred from – 80 °C glycerol stocks, struck on LB-agar plates and incubated overnight at 37 °C. Before each aerobic experiment, a 50 mL starter culture of LB medium was prepared in a sponge-capped tube, inoculated with a single colony and incubated for 16 h (37 °C, 200 rpm) to a typical OD_{600} of 1.2. For anaerobic experiments, a static, sealed tube filled almost to the top with medium to limit headspace, was prepared. Ultimately, 20 mL aliquots of the starter cultures were harvested by centrifugation and the cell pellets suspended in 20 mL of fresh M9 minimal medium ready for the experimental phase. The M9 medium was also supplemented with 30 mM glucose and the anaerobic trace elements of 9 µM $NiCl_2$, 4 µM Na_2SeO_3 and 3.2 µM Na_2MoO_4. The rest of our M9 formulation is given in Section 2.2.1.

A combination of advanced non-invasive analytical spectroscopic techniques was used to monitor bacterial batch cultures *in situ* in a closed system, as described in Chapter 4 [138, 171]. First, 230 mL of M9 medium was prepared in the round-bottom flask with two side-arms. The flask was maintained at 37 °C using a temperature-controlled water bath under rapid stirring to enable efficient gas transfer. Next, the 20 mL anaerobic starter culture of *E. coli* prepared in M9 medium was added to the 230 mL of fresh M9 medium in the two-neck round-bottom flask giving a typical starting OD_{600} of 0.1 and pH of 6.9. The culture was supplemented with 30 mM D-glucose (final concentration) and, where appropriate, 20 mM deuterium (^{2}H or D)-labelled formate (Sigma 373842, 99 % D) or 20 mM ^{13}C-labelled formate (CK isotopes CLM-583, 99 % ^{13}C) as potassium salts (final concentrations). The flask was then sealed and purged of O_2 by alternating between evacuating the headspace and refilling with N_2 at least five times.

For continuous spectroscopic monitoring of aerobic experiments, a 20 mL aerobic LB starter culture, transferred to 20 mL M9 medium, was added to 230 mL fresh M9 medium in a two-neck round-bottom flask giving a typical starting OD_{600} of 0.1. Carbon sources were added as required and the flask was rapidly stirred at 37 °C. In this case, the headspace of the flask initially contained just air and was not purged with N_2 and O_2 levels in the closed system were monitored by CERS in addition to all other spectroscopic measurements.

While recording metabolic activity, from one neck of the flask, the 1425 mL headspace gas was cycled for gas-phase FTIR and Raman measurements by a peristaltic pump with a flow rate of 4.5 L h^{-1}. Production of $^{12}CO_2$, $^{13}CO_2$, acetaldehyde and ethanol were quantified by gas-phase FTIR spectroscopy (Mattson Research Series, 0.4 cm^{-1} spectral resolution) with a home-built, 6 m pathlength multiple-pass White cell, as described in Sections 3.2.4 and 3.3.3. Partial pressures were obtained by fitting experimental spectra to the sum of reference spectra from the HITRAN [8] and PNNL [84] databases. Gas-phase cavity-enhanced Raman spectroscopy (CERS) monitored O_2, N_2, $^{12}CO_2$, $^{13}CO_2$ and H_2, HD and D_2 isotopomers, as described in Sections 2.2.3 and 4.2.3. In the CERS experiment, the 40 mW 636 nm cw-diode laser was enhanced by around 8000 times in magnitude using an optical cavity [97, 98]. Scattered Raman light was analysed in a monochromator (Andor Shamrock SR163, DV420A-OE camera). Partial pressures were obtained from the Raman spectra after a calibration [98]. Using Henry's law, pressures were converted into concentrations in solution. Using the ideal gas law, its estimated that 10 % CO_2, 95 % acetaldehyde and 99.7 % ethanol were dissolved [171]. Under these conditions, less than 1 % of dissolved CO_2 was expected to be converted to carbonic acid and carbonates.

The liquid suspension was cycled from the second neck of the flask for *in situ* OD_{600} and liquid-phase Raman measurements by a second peristaltic pump (4.5 L h^{-1}). The suspension was circulated through a sealed borosilicate tube for recording liquid-phase Raman spectra using a home-built spectrometer with a 532.2 nm, 20 mW laser (Lasos, GL3dT) and a monochromator (Shamrock SR-750-A, DU420A-OE camera), as described in Sections 3.2.3 and 3.3.1 [138, 171]. No interfering fluorescence was noticeable in M9 minimal growth medium. The water bending vibration at 1630 cm^{-1} was used to normalise decreasing Raman intensities as the turbidity of the bacterial suspension increased. A fit of the 820 – 1200 cm^{-1} region to reference spectra yielded the concentrations of glucose and the monobasic and dibasic phosphate anions of the phosphate buffer and a fit of the 1300 – 1500 cm^{-1} region provided acetate and unlabelled and labelled formate concentrations [138, 171]. Although lactate has also some weak Raman peaks within the Raman spectral range, no lactate metabolism products were identified in this study above the detection limits, estimated to be in the low millimolar region (approximately 2 mM). Note that Raman scattering within the bacterial cells likely also contributes to the experimental spectra. However, as the sum volume of bacterial cells is much less than the volume of the liquid medium, it is assumed that the experimental spectra correspond mainly to species in solution. The liquid suspension cycling loop also contained a 1 cm optical pathlength glass cuvette where the scattering of a red laser pointer was continuously monitored to obtain OD_{600} data after a calibration.

At the end of the bacterial growth period, the cell suspension was harvested by centrifugation, washed and dried at 37 °C for 2 days to record the dry biomass (typically around 200 mg). The endpoint pH of the spent culture medium was recorded using a Mettler Toledo SevenMulti pH meter to corroborate the spectroscopically calculated values. The M9 medium phosphate buffer, composed of 47 mM HPO_4^{2-} and 22 mM $H_2PO_4^-$, absorbs H^+ from excreted acids during bacterial growth by shifting HPO_4^{2-} to $H_2PO_4^-$. Liquid-phase Raman measurements were used to calculate the concentrations of phosphate anions, which in turn were used to calculate the pH *in situ* using a modified Henderson-Hasselbalch equation, as described in Section 3.3.2 [137, 138].

All experiments conducted in this study were repeated at least in triplicate, with all repeats showing essentially the same behaviour. Figures in the Results and Discussion are presented as single representative experiments. Partial pressures p (mbar) were converted to number of moles n (mmol) by using the ideal gas law ($V = 1.425 \times 10^{-3}$ m^3, $T = 310$ K) and correcting for the dissolved percentage calculated by Henry's law. Note that n and p of CO_2 displayed in the figures is scaled up to correct for the 10 % dissolved in solution.

5.3 Results

5.3.1 Fermentation of Glucose Produces Equimolar H_2 and CO_2

First, mixed-acid fermentation was studied using the well-characterised *E. coli* K-12 strain MG1655 [25] as a model system. An anaerobic starter culture of MG1655 was used to inoculate fresh M9 medium supplemented with 30 mM glucose (*i.e*. 7.5 mmol glucose in the 250 mL flask). Growth characteristics and fermentation products were quantified by CERS, FTIR and liquid-phase Raman spectroscopy over 18 h at 37 °C, as shown in Figure 5.1. Overall, these fermentation data can be divided into at least three phases as defined by the behaviour of the endogenously-produced formate (Figure 5.1b). Following inoculation there is a typical lag phase lasting around 3 h (Figure 5.1d). Then, as growth commences, net export of formate dominates until the 9 h mark (Figure 5.1b, phase **A**), which coincides with the slowing of logarithmic growth (Figure 5.1d). During this first phase, net formate accumulation peaks at 4 mmol in the extracellular medium (Figure 5.1b, phase **B**) and this continues until the 15 h mark, by which time the cells have settled into stationary phase growth (Figure 5.1d). Finally, formate is exhausted (Figure 5.1b, phase **C**).

Using this experimental approach, the activity of FHL-1 is evident throughout the growth phases until formate is finally exhausted at 15 h (Figure 5.1a). Molecular H_2 and CO_2 are readily quantified in the gas-phase and their production kinetics map precisely together, culminating in 10 mmol each of H_2 and CO_2 being produced (Figure 5.1a).

Liquid-phase Raman spectroscopy allows the consumption of glucose to be followed, together with the accumulation of other fermentation products (Figure 5.1c). Acetate was produced to a final level of 11 mmol and 4 mmol ethanol was generated (Figure 5.1c). Interestingly, trace amounts of acetaldehyde, the enzymatic intermediate between acetyl-CoA reduction to ethanol using NADH, was observed in the FTIR data and accumulated at a peak value of 18 μmol in phase **B**. From 14 to 18 h, the remaining acetaldehyde was exhausted (Figure 5.1c).

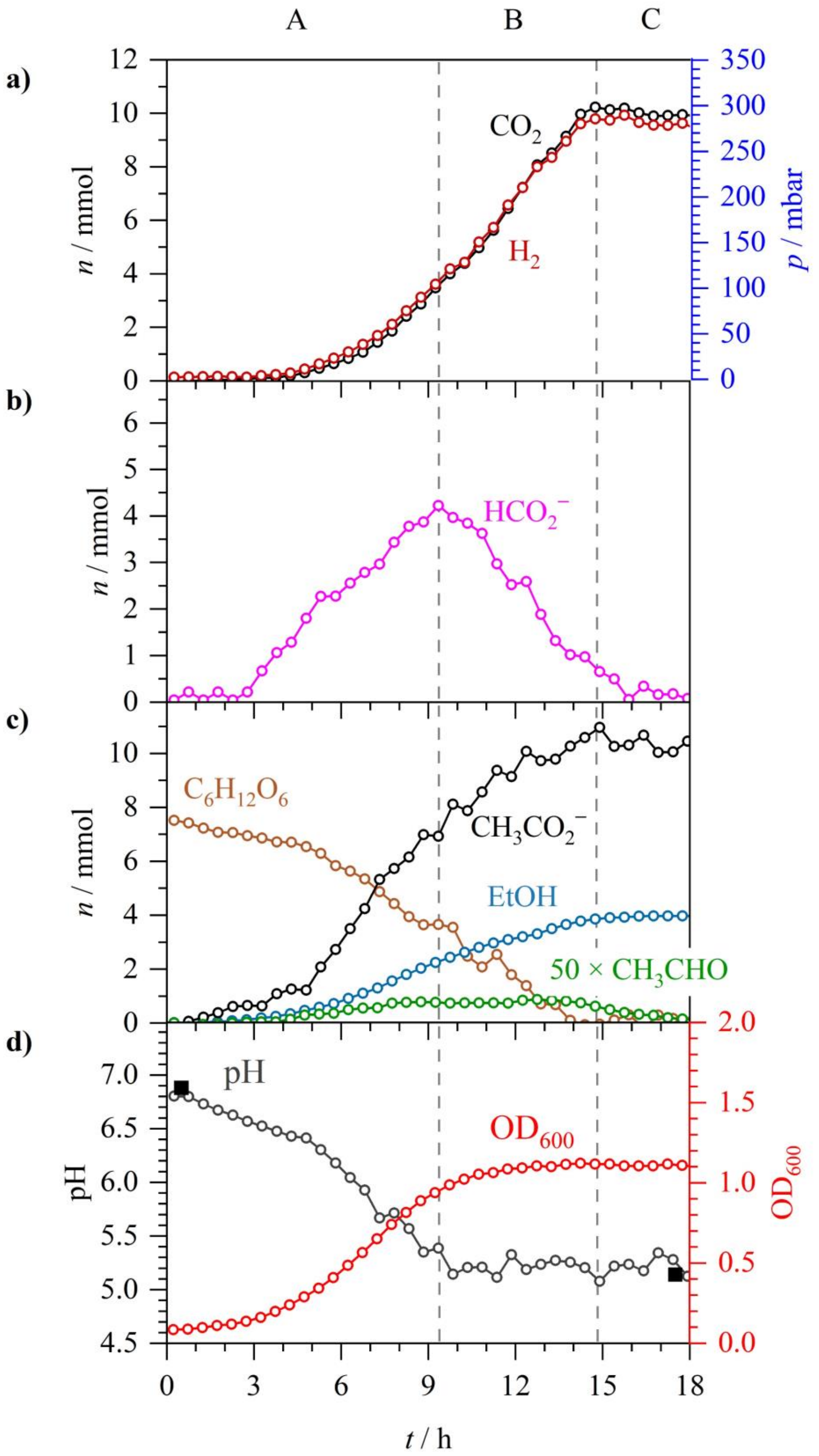

Figure 5.1 – Anaerobic fermentation by *E. coli* MG1655 during growth in M9 medium supplemented with 30 mM glucose. A to C denotes three distinct phases: net formate excretion (A), net formate consumption (B) and formate depletion (C). **a)** n and p of H_2 and CO_2. **b**) n of formate. **c)** n of acetaldehyde (× 50), acetate, ethanol and glucose. **d**) Spectroscopic pH (open circles), externally measured pH (solid squares) and OD_{600}.

5.3.2 The Fate of Exogenous Formate During Fermentation

One powerful aspect of Raman spectroscopy is the ability to differentiate between isotopically labelled compounds. Formate is amenable to D- or ^{13}C-isotope labelling studies due to the low natural abundances of deuterium (0.015 %) and carbon-13 (1.1 %). Figure 5.2 shows isotope shifts of the C-O stretching vibration for formate ($\Delta\tilde{\nu}_0$ = 1349 cm^{-1}), formate-^{13}C ($\Delta\tilde{\nu}_0$ = 1324 cm^{-1}) and formate-D ($\Delta\tilde{\nu}_0$ = 1322 cm^{-1}) in liquid-phase Raman spectra. The isotope shift opens the door to fermentation experiments where exogenously-added D- or ^{13}C-labelled formate could be readily distinguished from any endogenously-produced formate, which would remain unlabelled.

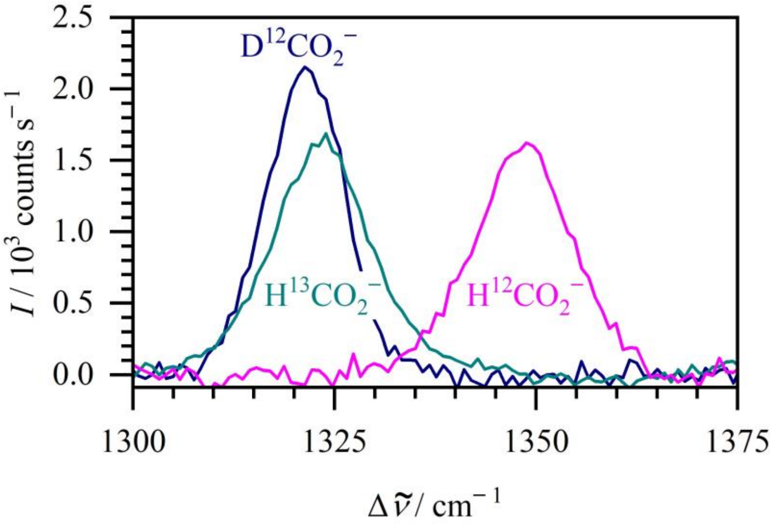

Figure 5.2 – Experimental liquid-phase Raman spectra of 100 mM unlabeled, D-labelled and ^{13}C-labelled formate.

Arguably one of the most compelling aspects of formate metabolism is the membrane transport processes at play in this biological system. In order to examine the metabolism of formate added exogenously at the beginning of the growth phase, 20 mM (5 mmol in the flask) formate-D (as a potassium salt), together with 30 mM unlabelled glucose was introduced into anaerobic batch cultures of *E. coli* MG1655 (Figure 5.3). Under these conditions, bacterial growth rates, and the amounts of acetate, ethanol and acetaldehyde produced, were comparable with the cells grown in the absence of exogenous formate (Figures 5.1 and 5.3). However, notable differences were observed in the formate, H_2, CO_2 and pH data (Figure 5.3).

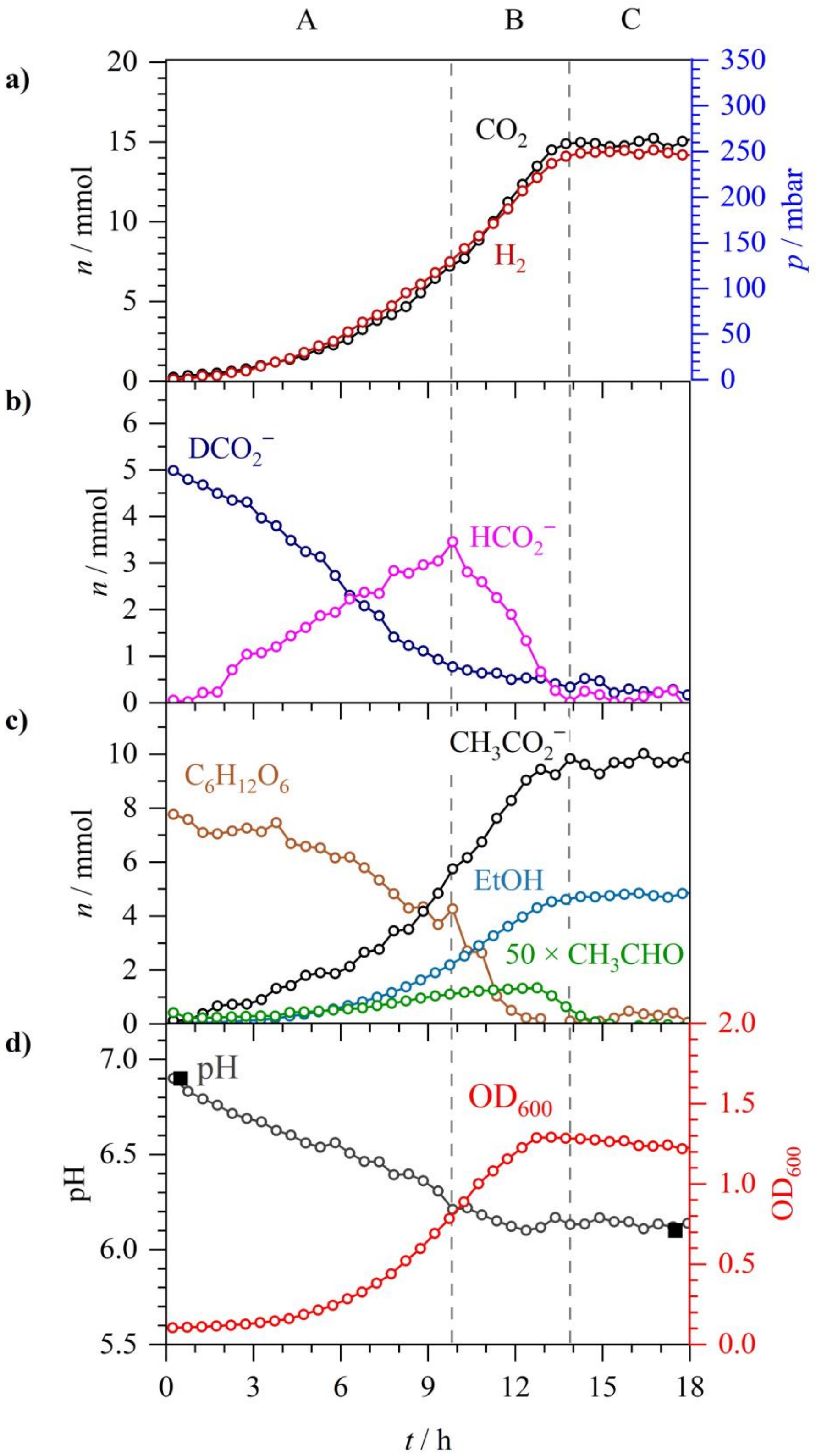

Figure 5.3 – Anaerobic fermentation by *E. coli* MG1655 during growth in M9 medium supplemented with 20 mM formate-D and 30 mM glucose. A to C denotes three distinct phases: net formate excretion (A), net formate consumption (B) and formate depletion (C). **a)** n and p of H_2 and CO_2. **b**) n of formate-D and formate. **c)** n of acetaldehyde (× 50), acetate, ethanol and glucose. **d**) Spectroscopic pH (open circles), externally measured pH (solid squares) and OD_{600}.

Metabolism of the external 5 mmol formate-D was observed to begin almost immediately (Figure 5.3b). Given the final amounts of H_2 and CO_2 produced in this experiment (15 mmol, Figure 5.3a) compared to the amount derived from the experiment without exogenous formate (10 mmol, Figure 5.1a), it is most likely that all the external formate-D was disproportionated to H_2 and CO_2 by FHL-1. Note that although the oxidation of formate-D would produce D^+ and CO_2, no detectable levels of HD or D_2 gas, which are also readily distinguished from H_2 by CERS, were observed.

Remarkably, despite the presence of exogenous formate-D, production, excretion and metabolism of endogenously produced unlabelled formate followed a familiar pattern (Figure 5.3b). In the initial phase, net export of formate was observed until around 10 h and peaked at around 3.5 mmol (Figure 5.3b, phase **A**). There then followed a net decrease in formate concentration as import and disproportionation continued until the 14 h mark (Figure 5.3b, phase **B**), by which time the FHL-1 reaction had ceased (Figure 5.3a) and the cells were in stationary phase (Figure 5.3d). Interestingly, at the 7 h timepoint, the extracellular concentrations of formate-D and unlabelled formate were identical (2.5 mmol), however the rates of excretion of endogenous formate and oxidation of formate-D continued largely unchanged (Figure 5.3b).

To explore further the relationship between exogenous and endogenous formate and the observed FHL-1 activity, a similar experiment using labelled formate-^{13}C was performed (Figure 5.4). Note that $^{13}CO_2$ can be distinguished from $^{12}CO_2$ by CERS or FTIR. Here, 20 mM (5 mmol) formate-^{13}C (as a potassium salt), together with 30 mM unlabelled glucose, was introduced into anaerobic batch cultures of *E. coli* MG1655 (Figure 5.4). The initial consumption of exogenous 5 mmol formate-^{13}C mirrored the production of 5 mmol $^{13}CO_2$, with the $^{13}CO_2$ data perfectly overlapping with the formate-^{13}C data if inverted (Figure 5.4). Production and excretion of endogenous unlabelled formate continued for 9 – 10 h in this case (Figure 5.4b) and peaked at 4 mmol before net uptake and oxidation was observed. This coincided with detectable levels of unlabelled $^{12}CO_2$ being generated (Figure 5.4a). Indeed, the sum of $^{13}CO_2$ and $^{12}CO_2$ overlapped almost exactly with the total H_2 production levels, indicating that FHL-1 activity was responsible for the generation of these compounds.

There were also notable differences in the final pH of the growth medium depending on the presence or absence of exogenous formate (Figures 5.1 and 5.3). Addition of potassium formate salt did not acidify the growth medium (Figure 5.3d), hence the pH in both experiments started at 6.9 (Figures 5.1d and 5.3d). However, in the presence of exogenous formate-D, the pH reduced from 6.9 to 6.1 over the course of the growth experiment (Figure 5.3d), compared to a drop in pH from 6.9 to 5.1 when the cells are grown with exogenous glucose only (Figure 5.1d).

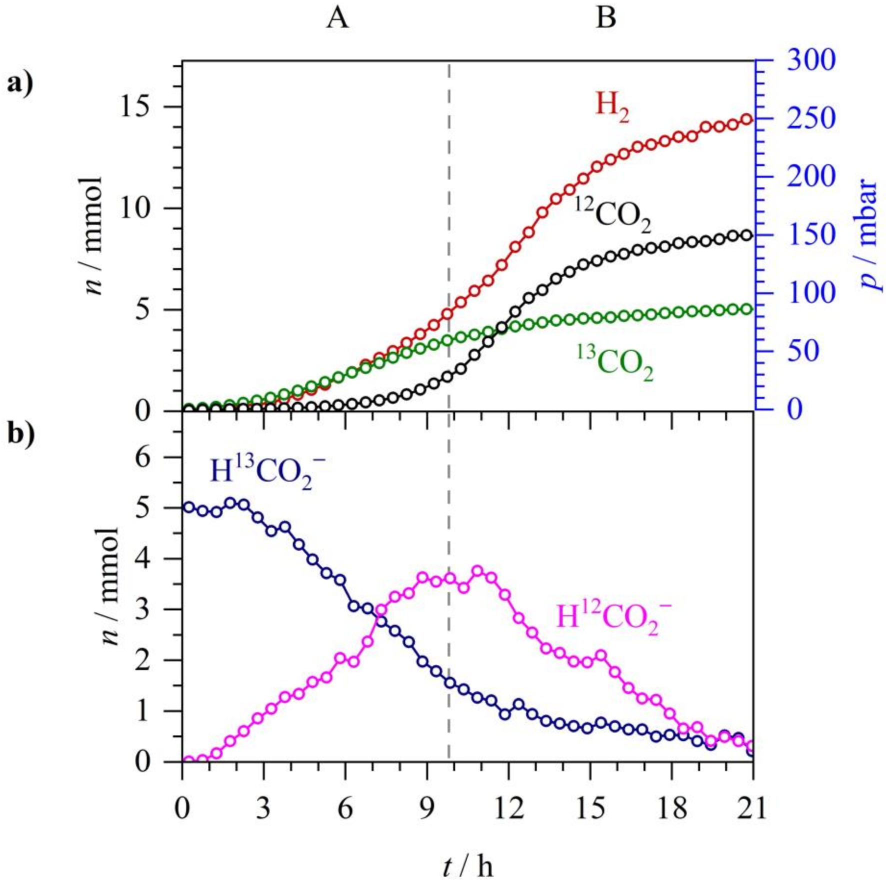

Figure 5.4 – Anaerobic fermentation by *E. coli* MG1655 during growth in M9 medium supplemented with 20 mM formate-^{13}C and 30 mM glucose. A and B denote two distinct phases: net formate excretion (A) and net formate consumption (B). **a)** *n* and *p* of H_2 and $^{12}CO_2$ and $^{13}CO_2$. **b)** *n* of formate-^{13}C and formate.

5.3.3 Metabolic Behaviour Under Micro-Aerobic Growth Conditions

To explore formate metabolism in aerobic cell cultures, first, an aerobic starter culture of *E. coli* MG1655 was prepared and used to inoculate 250 mL of M9 medium supplemented with 30 mM glucose. Note that this is a closed system that contains air in the vessel headspace but no way to replenish or regulate O_2 content. Over the course of 24 h, the cells were observed to grow, following an initial lag phase, to reach a peak OD_{600} value of 1.6 at around 9 h (Figure 5.5d). Cell density was then observed to decline slightly over time, suggestive of cell death phase following the stationary phase (Figure 5.5d). 8 mmol O_2 in the headspace was consumed, with an equal amount of CO_2 produced (Figure 5.5a).

Under these aerobic conditions, no detectable H_2 production was observed at any point of the experiment (Figure 5.5a). However, there was evidence of anaerobic pathways occurring alongside aerobic respiration (Figures 5.5b and 5.5c) strongly suggesting a micro-aerobic environment was present. Indeed, endogenous formate metabolism was clear in this data and Figure 5.5b could once again be readily divided into phases **A** (0 – 8 h), **B** (8 – 19 h) and **C** (> 19 h) based on this. Initial net formate production continued over 9 h and peaked at around 3 mmol (Figure 5.5b, phase **A**). Next, the accumulated formate was consumed over the following 10 h (Figure 5.5b, phase **B**), but no H_2 was produced.

The excretion of acetic acid and formate caused the culture medium pH to decrease from 6.9 to 4.9 (Figure 5.5d, phase **A**) with the ultimate production of 11 mmol acetate and 2 mmol ethanol (Figure 5.5c). Taken altogether, it can be concluded that this experimental system is ideally suited to the study of micro-aerobic growth conditions, where aspects of anaerobic metabolism (especially formate and ethanol production) are functional alongside aerobic respiration.

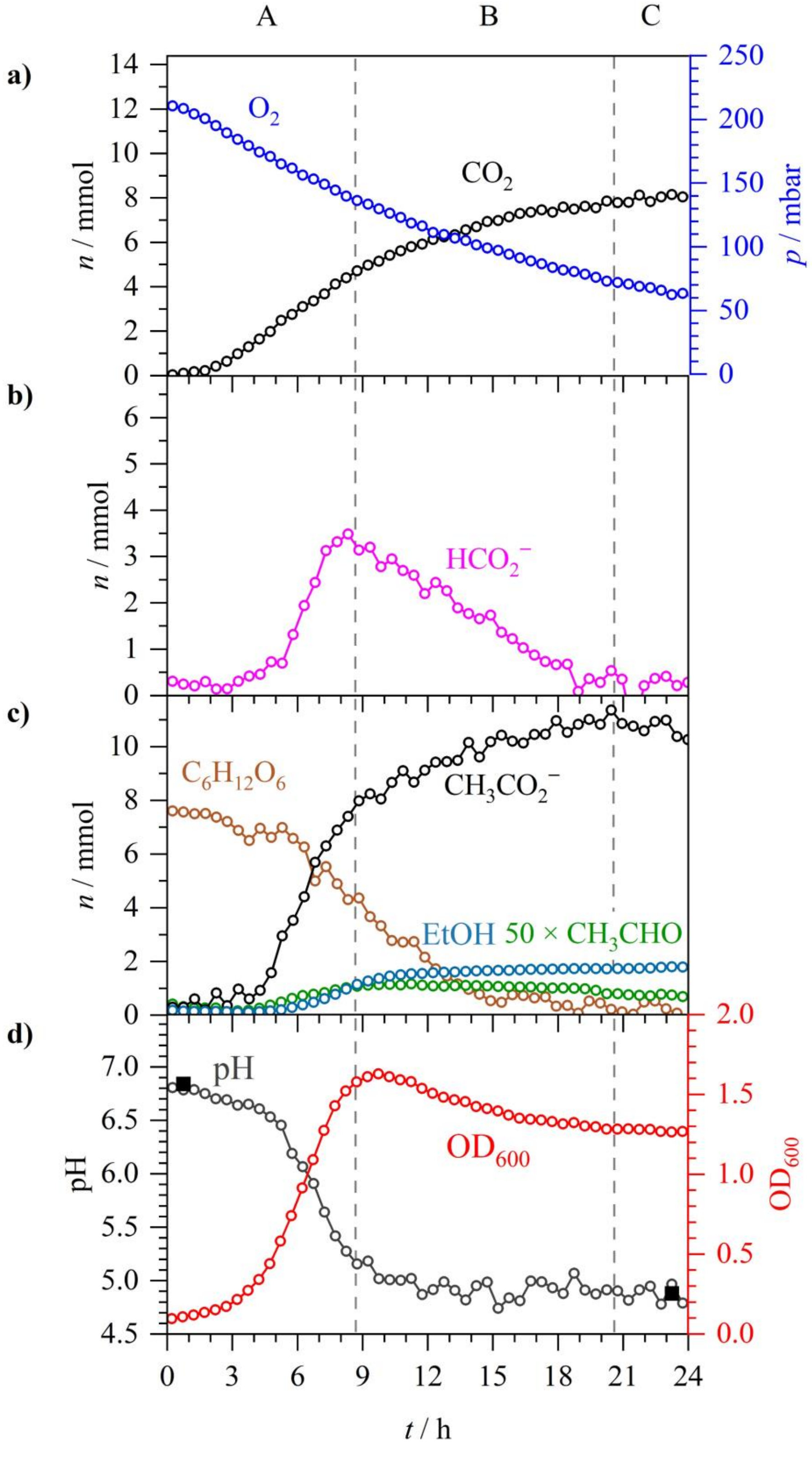

Figure 5.5 – Aerobic respiration by *E. coli* MG1655 during growth in M9 medium supplemented with 30 mM glucose. A to C denotes three distinct phases: net formate excretion (A), net formate consumption (B) and formate depletion (C). **a)** *n* and *p* of O_2 and CO_2. **b**) *n* of formate. **c)** *n* of acetaldehyde (× 50), acetate, ethanol and glucose. **d**) Spectroscopic pH (open circles), externally measured pH (solid squares) and OD_{600}.

5.3.4 Exogenous Formate Induces H_2 Production Under Aerobic Conditions

Next, the micro-aerobic growth system was tested in the presence of excess exogenous formate. An aerobic culture of *E. coli* MG1655 was prepared in M9 medium containing 20 mM formate-D and 30 mM glucose (Figure 5.6). Clear micro-aerobic physiology was observed, with formate, acetate and ethanol all being produced (Figure 5.6c), together with uptake of O_2 from the gas-phase (Figure 5.6a). As before, the observed endogenous formate metabolism could be divided into three phases. First, endogenous formate is produced and excreted by the cell (0 – 9 h), this time to a maximal level of 6 mmol (Figure 5.6b, phase **A**). Then, the endogenously-produced unlabelled formate was oxidised or otherwise metabolised away (9 – 17 h, Figure 5.6b, phase **B**) before a final phase was reached where formate was exhausted but other metabolic activities continued (Figure 5.6, phase **C**).

In this experiment, 5 mmol labelled formate-D was also added to the cultures from the outset. The exogenous labelled formate-D was consumed across phase **A** (Figure 5.6b). It is notable, however, that around the 5 h timepoint the levels of formate-D and unlabelled formate appeared equal at 3 mmol each (Figure 5.6b). The kinetics of unlabelled formate production and formate-D uptake do not change at this point.

Most surprisingly, the addition of exogenous formate induced the production of H_2 under aerobic conditions (Figure 5.6a). However, note that H_2 was not observed in the data until around 5 h into growth (Figure 5.6a). Indeed, almost all the 5 mmol exogenous formate-D are consumed by the end of phase **A**, while only 2 mmol of H_2 are produced in this time (Figure 5.6). An additional 4 mmol of H_2 are produced in phase **B**, which also does not match with the consumption of at least 6 mmol of unlabelled formate in that time.

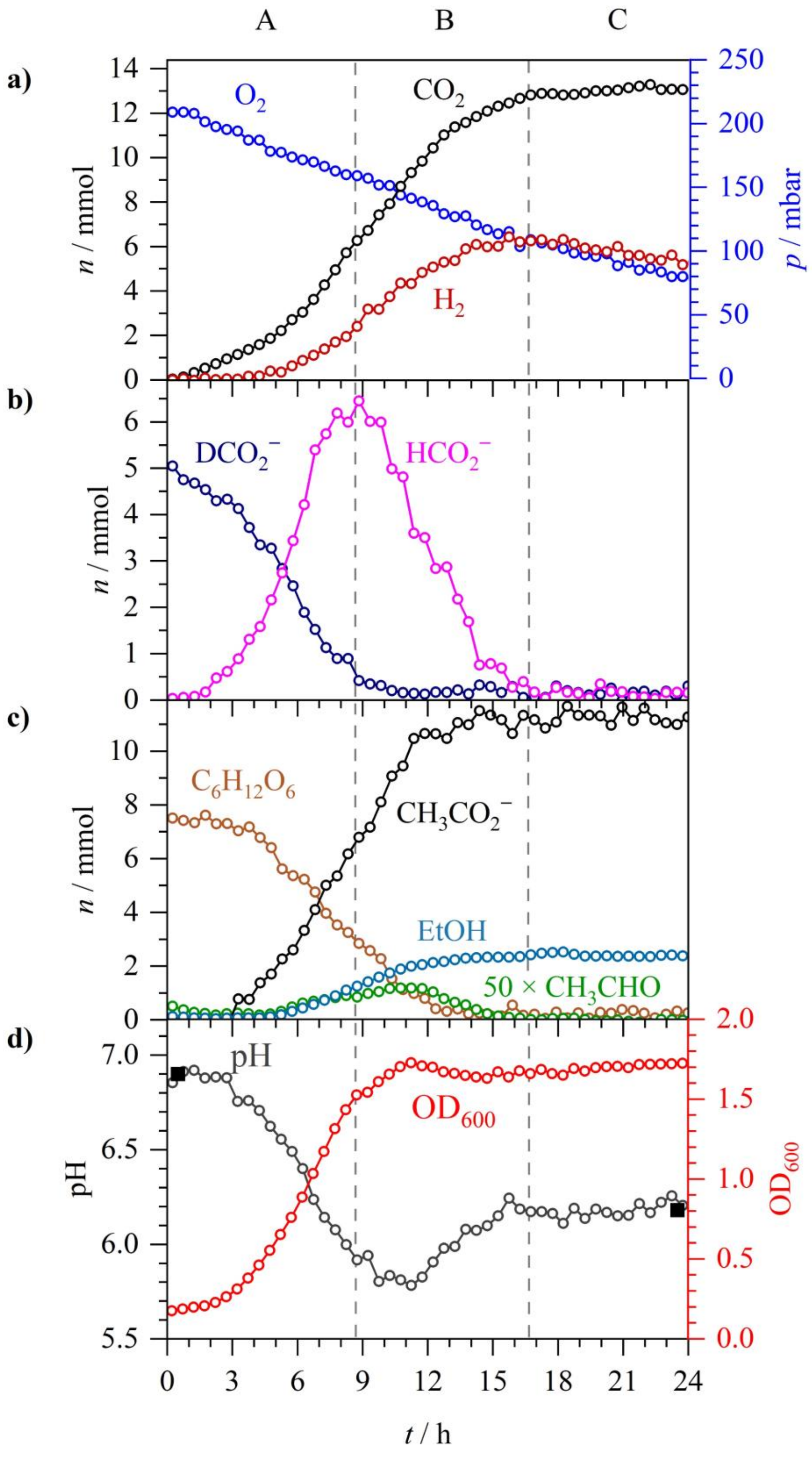

Figure 5.6 – Aerobic respiration by *E. coli* MG1655 during growth in M9 medium supplemented with 20 mM formate-D and 30 mM glucose. A to C denotes three distinct phases: net formate excretion (A), net formate consumption (B) and formate depletion (C). **a)** *n* and *p* of O_2, CO_2 and H_2. **b**) *n* of formate-D and formate. **c)** *n* of acetaldehyde (× 50), acetate, ethanol and glucose. **d**) Spectroscopic pH (open circles), externally measured pH (solid squares) and OD_{600}.

In order to test whether the aerobic H_2 production observed in the presence of exogenous formate was as a result of FHL-1 activity, a genetic approach was taken (Figure 6.7). The *E. coli* strain MG16dZ is a direct derivative of MG1655 carrying a complete deletion of the gene encoding the FDH-H component of FHL-1 [218]. An aerobic starter culture of *E. coli* MG16dZ was used to inoculate aerobic M9 medium supplemented with 20 mM formate-D and 30 mM glucose. Under these conditions, no detectable H_2 production was observed at any point of the experiment (Figure 5.7). This strongly suggests that the H_2 production induced by the addition of exogenous formate in the presence of O_2 (Figure 5.6) was as a result of FHL-1 activity.

The micro-aerobic growth curve for MG16dZ (Δ*fdhF*) was like the parent strain MG1655, having a short lag before peaking at an OD_{600} of 1.1 at the 12 h mark (Figure 5.7d). However, despite this, the metabolic rates of the *fdhF* mutant are noticeably slower overall (Figure 5.7). For example, formate metabolism by MG16dZ displayed only two clear phases, even after 42 h incubation. First, endogenous formate was produced from glucose across 0 – 12 h, peaking at 6.5 mmol (Figure 5.7b, phase **A**). Then the endogenous, unlabelled formate was slowly consumed over the following 20 h (Figure 5.7b, phase **B**). In addition, the majority (4 mmol) of the exogenous, labelled formate-D was consumed by 12 h incubation (Figure 5.7b, phase **A**), by which time the cells had already concluded exponential growth (Figure 5.7d).

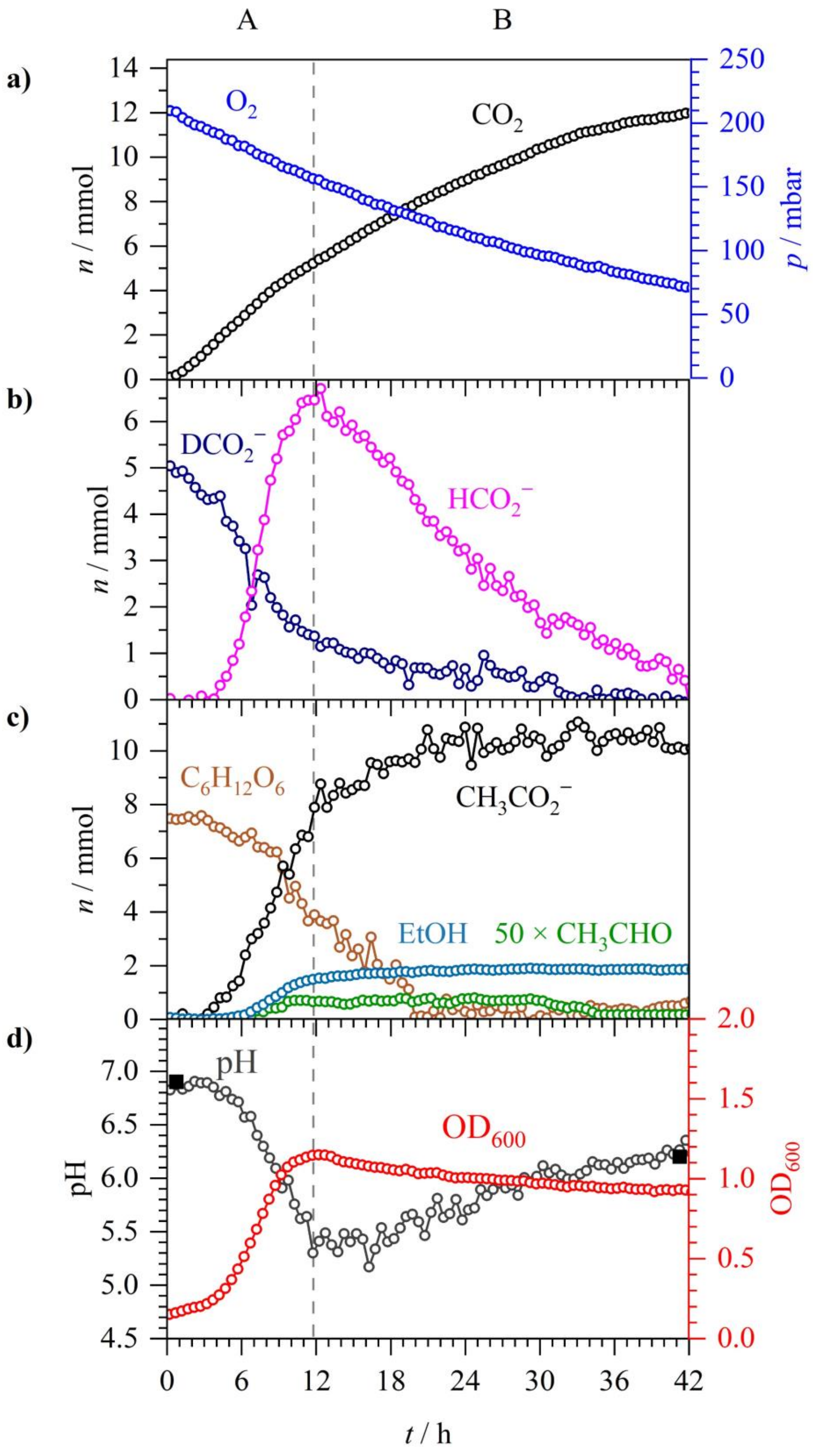

Figure 5.7 – Aerobic respiration by *E. coli* MG16dZ (Δ*fdhF*) during growth in M9 medium supplemented with 20 mM formate-D and 30 mM glucose. A and B denote two distinct phases: net formate excretion (A) and net formate consumption (B). **a)** *n* and *p* of O_2 and CO_2. **b**) *n* of formate-D and formate. **c)** *n* of acetaldehyde (× 50), acetate, ethanol and glucose. **d**) Spectroscopic pH (open circles), externally measured pH (solid squares) and OD_{600}.

5.4 Discussion

In this chapter, the metabolism of *E. coli* K-12 in fermentative and micro-aerobic growth has been studied using in-line, non-invasive spectroscopic techniques. This allowed the consumption of glucose to be correlated with microbial growth and the production of numerous compounds, including H_2 in the gas-phase, to be quantified in real-time. In addition, the ability of Raman spectroscopy to distinguish between isotopically-labelled compounds has allowed new insights into formate metabolism to be made.

5.4.1 Evidence for Formic Acid Efflux During Fermentation

The physiology of *E. coli* growing under fermentative conditions is largely well understood [52] and one critical environmental factor driving gene expression and other physiological changes is the external pH. Using this experimental set-up it was possible to follow pH changes spectroscopically by monitoring the ratio of HPO_4^{2-} to $H_2PO_4^{-}$ [137, 138]. During exponential growth under fermentative conditions (Figure 5.1, phase **A**), 8 mmol acetate and 4 mmol formate (no lactate or succinate was able to be quantified in this experimental set-up within the approximately 2 mM detection limit, though they are expected to be present) accumulated in the external medium (Figure 5.1). Concomitantly, the external pH decreased from 6.9 to 5.1 (Figure 5.1), which can be explained if acetate and formate are excreted as acetic acid and formic acid (*i.e.* co-transport of the anions with protons). Indeed, the efflux of 12 mmol (48 mM) acidic protons into the growth medium would be theoretically enough to overwhelm the 47 mM HPO_4^{2-} component of the phosphate buffer used in these experiments, thus preventing further spectroscopic pH measurements if additional acidic products were excreted. Fortunately, the pH remains almost constant at 5.1 (Figure 5.1d) despite a further 3 mmol acetic acid being excreted after the peak of formate production at the end of exponential growth (Figure 5.1, phase **B**). This is because the reimport and disproportionation of 4 mmol formic acid essentially balances the efflux of acetic acid.

These observations are important when considering the structure and function of the FocA formate channel, and the physiology of formate metabolism and pH homeostasis. It is worth considering that formate (not formic acid) is the product of the pyruvate formate lyase

(PFL) reaction at the cytoplasmic side of the membrane [219]. The PFL enzyme is anchored to, and possibly gating, the FocA channel in the cytoplasmic membrane such that it could be immediately excreted upon its synthesis [220, 221]. Efflux of formic acid (not simply formate) therefore requires co-transport of the anion with a new proton picked up from the cell cytoplasm. Such an event could not lead to charge separation across the membrane but would result in the net movement of a proton from the cytoplasmic (*n*-side) to the periplasmic (*p*-side) of the membrane. Any possible bioenergetic advantages linked to this efflux are probably negated as *E. coli* attempts to maintain the pH of its cytoplasm. Under a range of external pH and growth conditions, the *E. coli* cell cytoplasm is maintained at 7.4 – 7.8 [222] thanks to a combination of ion transport events and compatible solute regulation [223]. Indeed, the FHL reaction itself seems to balance the pH of the growth medium (Figure 5.1) by the influx of formic acid (as opposed to formate alone) and its subsequent disproportionation to H_2 and CO_2. The influx of formic acid is further highlighted in our experiments with exogenously-added formate salts (Figure 5.3 and discussed further below).

5.4.2 Separation of Formic Acid Influx and Efflux Pathways

The behaviour of formate, and its role in *E. coli* energy metabolism in general, has long been a source of intrigue in bacterial physiology. Endogenously-produced formic acid is initially excreted from the cell, presumably as *E. coli* has no real use for an excess of this C1 compound and it would perhaps be rapidly diluted, or metabolised away by other bacterial species, depending on the nature of the surrounding environment. Likewise, the presence of constitutively-expressed respiratory FDH-O originally posed a dilemma as endogenous formate is not made at all under fully aerobic conditions.

In this work, the experimental set-up clearly showed classic fermentative physiology where formic acid efflux was observed, and the compound initially accumulated until the end of exponential growth and was then metabolised away again (Figure 5.1b). In this case, net efflux of formic acid clearly continued as the external pH dropped from 6.9 to 5.5 (rather than stopping completely at a pH threshold) while H_2 production was initially recorded at pH 6.5 (Figure 5.1a) and continued until formate was exhausted (Figure 5.1b).

In total, the anaerobic fermentation produced near equimolar quantities of 10 mmol each of H_2 and CO_2 (Figure 5.1a), 10 mmol acetate (Figure 5.1c) and 4 mmol ethanol from

7.5 mmol glucose in the medium initially. It is likely that succinate and lactate were also produced but below the detection limits of the apparatus (*ca.* 2 mM). In theory, 7.5 mmol glucose could generate 15 mmol pyruvate from glycolysis. In turn, this could lead to 15 mmol acetyl-CoA (and 15 mmol formate) that could either be further reduced to ethanol or used for ATP production with an end-product of acetate. The combined totals of acetate and ethanol are close to the theoretical (Figure 5.1), however 15 mmol of formate would be expected to generate 15 mmol of H_2 and CO_2 *via* FHL-1, while only 10 mmol were recorded for each (Figure 5.1a). It is possible that some formate may be retained with the cells (either periplasm, cytoplasm or both) but at a level that cannot be efficiently oxidised by FDH-H (the K_m for formate for this enzyme is 10 mM [51]) or that it is being used for other biochemical pathways in the growing culture [224].

The ability of Raman spectroscopy to distinguish between isotopically-labelled compounds allowed some new observations of formate and H_2 metabolism. First, it is worth documenting that the addition of formate-D to the culture did not lead to HD or D_2 production. This is not altogether surprising as there would need to be an unusual mechanism of linking the FDH-H and Hyd-3 reactions within FHL-1 for this to be the case. Otherwise, the released D^+ is too dilute at 20 mM (5 mmol) compared to the concentration of the bulk H^+ in the aqueous phase (the concentration of pure H_2O is 55.5 M). Second, under these anaerobic conditions all the extra formate-D was disproportionated to H_2 and CO_2. This is evidenced by the fact that 15 mmol of both H_2 and CO_2 was recorded upon the addition of an extra 5 mmol of formate-D (Figure 5.3a) compared with 10 mmol each for the experiment with no exogenous formate (Figure 5.1a). Further corroboration was forthcoming in Figure 5.4a, where the addition of 5 mmol formate-^{13}C to the culture led to 5 mmol $^{13}CO_2$ being produced and an extra 5 mmol of H_2 overall. Moreover, a kinetic analysis of the $^{12}CO_2$ and $^{13}CO_2$ data shows that the rate of CO_2 production is consistent with being linearly dependent on the formate concentration and *E. coli* abundance (estimated by the OD_{600}) without any apparent preference for formate-^{13}C or unlabelled formate. As formate-^{13}C was more abundant than endogenous formate in the extracellular medium to begin with, $^{13}CO_2$ production was observed before $^{12}CO_2$ production. Then, as formate-^{13}C was consumed and endogenous formate was excreted, the rate of $^{13}CO_2$ production decreased while the rate for $^{12}CO_2$ increased (Figure 5.4a). This is possibly best viewed at the 7 h timepoint when there were equal amounts (3 mmol) formate-^{13}C and unlabelled formate in the extracellular medium (Figure 5.4b) and $^{12}CO_2$ and $^{13}CO_2$ have similar rates of production (Figure 5.4a).

The behaviours of the exogenously-added and endogenously-generated formate deserve some further discussion. Using isotopically-labelled formate, both the influx and efflux of formic acid can be observed at the same time (Figure 5.3 and 5.4). Indeed, the externally-added labelled formate and internally-produced unlabelled formate appear to behave as different substrates in this system, which could either be a subtle kinetic isotope effect or could be evidence for different molecular mechanism of uptake (influx) and export (efflux) of formate. For instance, export of endogenously-produced unlabelled formate displays essentially the same behaviour, with similar rates and maximal levels observed, regardless of the presence or absence of external formate-D (Figure 5.1 and 5.3). The maximum rate of formate efflux (normalised by the OD_{600}) in the absence of externally-added formate was calculated at 34 ± 3 μmol $OD_{600}{}^{-1}$ min^{-1}. When 5 mmol formate-D was added to the growth medium from the outset, the maximal rate of unlabelled formate efflux was calculated at 36 ± 7 μmol $OD_{600}{}^{-1}$ min^{-1}. For comparison, the maximum rate of formate-D influx was determined 111 ± 12 μmol $OD_{600}{}^{-1}$ min^{-1}, and the rate of re-import of unlabelled formate in the stationary phase was 13 ± 5 μmol $OD_{600}{}^{-1}$ min^{-1}. Indeed, the relatively high rates of external formate influx during exponential growth are remarkable. It is worth considering that influx of formic acid is intimately linked with FHL activity [225] and that FHL activity is intimately linked, by an unknown mechanism, to the ATP levels in the cell [226]. It seems clear, given these data, that glucose-replete fast-growing cells contain greater physiological FHL activity than cells in the stationary phase.

Taken altogether, this gives extra weight to the hypothesis that PFL (which generates the internal formate from pyruvate) is physically attached to the N-terminus of the FocA formate channel and is gating it in ‘efflux mode’ such that formate production and formic acid efflux are intimately linked [220]. Such a model would effectively maintain the cytoplasmic formate concentration at close to zero with the immediate efflux of the product linked to its synthesis. However, in the experimental system, there are already 5 mmol of formate-D (above the maximal level of 4 mmol that the ‘natural’ system can achieve under these conditions) outside the cell. The influx of exogenous formate-D is coupled directly to its disproportionation to H_2 and CO_2 by FHL-1 and this appears to occur in parallel to efflux.

It is worth considering how efflux and influx of formic acid could occur at the same time in such a cellular system. A large body of work points to the FocA membrane protein as being primarily responsible for both efflux and influx of formic acid [52]. It seems unlikely that a given individual protein could both export and import formic acid simultaneously.

Instead, it should be considered that a certain number of FocA channels in the cell could be gated for efflux only, for example those in physical contact with PFL, while a second pool of FocA channels could be gated for influx only. This perhaps also implies different routes of formate or proton translocation within the FocA protein under the different gated states. Indeed, site-directed mutagenesis of *focA* has identified amino acid residues that are important for formic acid influx, but not efflux. For example, substitution of *E. coli* FocA His-209 by either Asn or Gln locked the channel in efflux mode only [227]. This hypothesis would also stand if the monoculture of *E. coli* contained two distinct populations of cells, one carrying out formic acid efflux and another performing the FHL reaction linked to influx. Such bimodal phenotypic heterogeneity is common in bacterial populations [228].

In both experiments where exogenous formate was added (Figures 5.3 and 5.4), formic acid consumption and the production of H_2 and CO_2 began almost immediately with very little lag time. This was most likely because the starter cultures were prepared anaerobically, and the cells would have a certain level of FHL-1 already present. It is notable, however, that external medium pH does not become as acidic when spiked with exogenous formate compared with normal glucose fermentation conditions – in the former the pH decreases from 6.9 to 6.1 (Figure 5.3) and in the latter, the pH drops from 6.9 to 5.1 (Figure 5.1). This could be giving additional evidence as to how the FocA formate channel is working. A compelling model for FocA function is as an anion-proton symport system, where formic acid (HCOOH) would be either excreted or re-imported into the cell [229-231]. In such a model the efflux of formic acid would acidify the medium (as was seen in Figure 5.1) but, conversely, the subsequent influx of formic acid would de-acidify the medium and there may be clear evidence for that in Figure 5.3. Here, the addition of exogenous formate-D to the medium as a potassium salt did not affect the starting pH of the experiment, which remained steady at 6.9, as the formate-D anion is not an acid. Under the anion-proton symport model, influx of the 5 mmol extra, external formate-D would also bring with it 5 mmol of H^+ across the membrane into the cell from the bulk external medium, thus increasing the pH of the growth medium and helping to balance the pH of the external medium against the continued efflux of acetic acid and unlabelled formic acid.

5.4.3 Micro-aerobic Respiration

Following the fermentation experiments, attention then turned to the metabolism of formate under aerobic conditions. First, an *E. coli* starter culture already performing aerobic respiration was prepared and the experimental system was assembled with air in the culture headspace (210 mbar partial pressure is roughly 21 % O_2, Figure 5.5). Over the course of the experiment, 8 mmol of O_2 was consumed and 8 mmol of CO_2 was produced – an apparent respiratory quotient of 1.0 indicative of aerobic respiration of glucose. However, clear aspects of anaerobic metabolism were also evident, including acetate and ethanol production, as well as the efflux and influx of endogenous formic acid (Figure 5.5b). Indeed, formate efflux/influx behaviour was almost identical to that observed for the fermenting cells (Figure 5.1), where 10 mmol each of H_2 and CO_2 were also generated. In the presence of O_2, however, no H_2 was observed whatsoever (Figure 5.5). In this case, the formate was likely ultimately oxidised by the respiratory enzyme FDH-O in the periplasm [215], thus generating the 8 mmol of CO_2 observed. Moreover, if all the CO_2 production is attributable to formate respiration, then it follows that half of the O_2 consumption is attributable to formate oxidation in the periplasm. Taken altogether, in this experimental set-up, it can be concluded that the culture was clearly performing micro-aerobic respiration (Figure 5.5).

5.4.4 FHL-1 Activity is Inducible Under Micro-Aerobic Conditions

Having established a micro-aerobic growth environment, the final experiment involved the study of the physiology of external formate metabolism under these conditions. Somewhat surprisingly, the addition of exogenous formate-D to the culture at the outset led to the production of H_2 in an FHL-1-dependent manner (Figures 5.6 and 5.7). Unlike the anaerobic fermentation experiments (Figure 5.3), however, there was a notable 5 h delay in the onset of H_2 production (Figure 5.6). This is most likely because, using an aerobic starter culture the cells had to synthesise FHL-1 *de novo* in response to the external formate-D. Indeed, the formate-D was almost completely consumed by aerobic respiration before the H_2 production began (Figure 5.6). However, sufficient endogenous, unlabelled formate was produced that enabled the ultimate production of 6 mmol of H_2 and an extra 6 mmol of CO_2 *via* FHL-1 (Figures 5.6 and 5.7). Indeed, the ability of FHL-1 to function in the presence of 10 – 20 % O_2

in the headspace is quite remarkable, but, together with the obvious presence of numerous other O_2-sensitive enzymes, including PFL, the data is probably telling us that the O_2 tension in the cell cytoplasm is very much lower.

It is pertinent to note here that there is continued consumption of O_2 in stationary phase that is at roughly the same rate as consumption of the endogenous H_2 (Figure 5.6a, phase **C**). Conversely, under strict anaerobic conditions, the H_2 produced by FHL-1 remains largely steady (Figures 5.1 and 5.3). It is tempting to speculate that at least some of this activity represents an example of ‘hydrogen cycling’ where H_2 gas produced by FHL-1 is re-oxidised by the respiratory hydrogenases (Hyd-1 and/or Hyd-2) linked directly to the reduction of O_2 to water [55]. Note, however, that continued O_2 consumption up to 42 h was observed in the absence of H_2 (Figure 5.7) suggesting that other endogenous electron donors continue to be functional long after glucose is exhausted.

The H_2 production induced by exogenous formate under micro-aerobic conditions is undoubtedly due to FHL-1 (Figure 5.7). However, the isogenic *fdhF* mutant has a phenotype that exhibits surprising weaknesses compared to the parent strain. Oxidation of both exogenous and endogenous formate is very slow – for example, for external formate-D the MG1655 parent strain consumed 4 mmol over 9 h (Figure 5.3b) while for the FHL-1 mutant this process lasted 12 h (Figure 5.7b). Moreover, the growth medium of the mutant strain retained significant amounts (1 mmol) of endogenously-produced formate even after 42 h of incubation (Figure 5.7b).

The behaviour of formate and O_2 respiration was also different between the mutant and the parent strain. While glucose was abundant from 0 – 18 h, 8 mmol CO_2 was produced and O_2 decreased by 4 mmol, suggesting that all the O_2 respiration observed is linked to formate oxidation (Figure 5.7a). However, from 18 to 42 h the glucose was depleted and endogenous formate could no longer be produced, hence the 4 mmol formate remaining was slowly oxidised to increase CO_2 from 8 to 12 mmol, with O_2 decreasing from 8 to 4 mmol at the same time, suggesting additional endogenous electron donors were coming into play in the stationary phase.

5.4.5 Conclusion

In this chapter, the formate and H_2 physiology of *E. coli* has been examined by powerful, non-invasive Raman and FTIR spectroscopies. This project has produced further evidence that FHL-1 is part of a formic acid detoxification system involved in pH homeostasis. The data support an anion-proton symport model for formate transport across the cell membrane, and provide evidence for at least two separate routes, or mechanisms, for formic acid influx and efflux. Finally, there is evidence that FHL-1 can be assembled and functional under micro-aerobic conditions, which could remove some barriers to biotechnological applications.

Chapter 6

Concluding Remarks and Future Work

Existing and novel spectroscopic laser techniques, including cavity-enhanced Raman spectroscopy (CERS), photoacoustic detection in a differential Helmholtz resonator (DHR), White cell FTIR spectroscopy and liquid-phase Raman spectroscopy, have been developed and applied to monitoring different metabolic modes of *E. coli* batch cultures.

Due to low densities in the gas-phase, enhancement is needed for Raman spectroscopy. CERS couples excitation light from a low-power cw diode laser inside of an external Fabry-Pérot cavity, composed of two high-reflectivity supermirrors, with optical feedback to lock the laser wavelength to the optical cavity. The Raman signal of analyte gases inside the cavity is enhanced due to the longer interaction length from thousands of reflections as well as the optical resonator effect. CERS enables headspace gas-analysis with noise-equivalent (1 σ) detection limits of 32 ppmv H_2, 195 ppmv N_2, 265 ppmv O_2 and 240 ppmv CO_2 for 270 s integration time. With excellent selectivity and sensitivity, CERS can also distinguish isotopomers and isotopologues such as $^{13}CO_2$ and $^{12}CO_2$, as well as H_2, HD and D_2.

The DHR set-up is also capable of detecting O_2, $^{13}CO_2$ and $^{12}CO_2$ with excellent noise-equivalent (1 σ) detection limits for 16 s measurement time of 150 ppmv O_2 and 40 ppmv CO_2. The DHR has two identical chambers which produces out-of-phase photoacoustic absorption signals using a red laser for O_2 and a near-IR laser for CO_2 detection. Ultimately, differential detection doubles the photoacoustic signal while cancelling noise to a great extent. The DHR set-up is simpler and more cost-effective than CERS. However, CERS has the advantage of easier internal calibration using inert N_2 gas signals, as well as being able to detect other gases (H_2, N_2, CH_4, etc) without further modifications. Hence, the CERS set-up was used for fermentative studies, as the production of H_2 could not be monitored by the DHR set-up.

The CERS and DHR set-ups were compared when studying glucose-lactose diauxie, a classical *E. coli* experiment. With the addition of fully substituted ^{13}C-labelled glucose ($^{13}C_6H_{12}O_6$) and unlabelled lactose to the growth medium, gas-phase analysis of CO_2 isotopomers by both spectroscopic techniques enabled the distinction of glucose-lactose diauxie in real-time. Interestingly, a traditional Monod-style diauxic shift was not observed as there was no lag phase visible in the *in situ* OD measurements and there was a slight overlap between $^{13}CO_2$ production from ^{13}C-glucose and $^{12}CO_2$ production from unlabelled lactose.

This highlighted the importance of analysing bioreactors with multiple sensors as a single sensed variable (*i.e.* OD) on its own cannot characterise a bioprocess.

White cell FTIR and liquid-phase Raman spectroscopies were first applied to monitoring the mixed-acid fermentation of glucose by *E. coli*. Liquid-phase Raman detection affords noise-equivalent (1 σ) detection limits of 0.8 mM acetate, 0.4 mM formate, 0.5 mM glucose, 0.2 mM NO_3^-, 0.5 mM HPO_4^{2-} and 0.6 mM $H_2PO_4^-$ at 1 h integration time. The measurement of the phosphate buffer anions allows the spectroscopic, *in situ* pH determination of the bacterial culture *via* a modified Henderson-Hasselbalch equation. The White cell pathlength is variable between 4 – 8 m and enhances the sensitivity of gas-phase FTIR measurements. Noise-equivalent (1 σ) detection limits of at least 0.21 µbar acetaldehyde and 0.26 µbar ethanol are obtained in the gas-phase, corresponding to 3.2 µM acetaldehyde and 22 µM ethanol in solution, using Henry's law.

An analytical set-up was constructed, using CERS, FTIR and liquid-phase Raman spectroscopies together for complementary bioprocess analysis. The set-up was used for two isotopic labelling studies of *E. coli* metabolism: a ^{15}N-labelling study of NO_3^- and NO_2^- reduction and a ^{13}C- and D-labelling study of formate hydrogenlyase (FHL) activity in the absence and presence of O_2.

In the first study, anaerobic *E. coli* batch cultures were supplemented with $^{15}NO_3^-$, $^{15}NO_2^-$ and mixed $^{15}NO_3^-$ and $^{14}NO_2^-$. In a major pathway, NO_3^- was reduced to NH_4^+ *via* NO_2^-, with the bulk of NO_2^- reduction occurring after NO_3^- depletion. In a minor pathway, NO_2^- was reduced to N_2O *via* the toxic radical NO. The major pathway to NH_4^+ has been extensively studied by others, but trace N_2O production by *E. coli* is relatively overlooked. This study provided multiple insights into trace N_2O generation during NO_3^- and NO_2^- reduction. With its excellent FTIR detection sensitivities, N_2O served as a monitor for trace NO_2^- reduction, even when the cells were predominantly reducing NO_3^-. The analysis of N_2O isotopomers revealed that for mixed $^{15}NO_3^-$ and $^{14}NO_2^-$, $^{14}NO_2^-$ reduction occurred immediately, even before $^{15}NO_3^-$ reduction began. There is much still uncertain about NO generation and detoxification by *E. coli*, and further work is required to determine the enzymatic origin of these findings.

Finally, to further understand bacterial formate and H_2 metabolism, which holds great potential for biohydrogen production, aerobic and anaerobic *E. coli* cultures were supplemented with ^{13}C- or D-labelled formate. Anaerobically, formic acid was generated endogenously, excreted briefly from the cell and then taken up again to be disproportionated to H_2 and CO_2 by FHL. However, exogenously added D-labelled formate behaved differently as it was taken up immediately, independently and possibly by a different mechanism, by the cell and converted to H_2 and CO_2. This supports an anion-proton symport model for formic acid transport. In addition, when *E. coli* was grown in a micro-aerobic environment, aspects of formate and O_2 respiration occurred alongside anaerobic metabolism. While cells grew under micro-aerobic conditions and generated endogenous formic acid, no H_2 was produced. However, addition of exogenous formate at the outset of cell growth induced FHL biosynthesis and resulted in formate-dependent H_2 production in the presence of O_2, a finding that may hold great significance for removing some barriers to biotechnological applications.

Future work should include the further development and enhancement of these analytical spectroscopic techniques and their application to other novel bioprocesses. Although CERS has been proven to be a useful technique for monitoring bioprocesses, the lower sensitivity of Raman spectroscopy compared to direct absorption techniques is an inherent weakness. As Raman signals scale with optical power as well as with lower excitation wavelengths, the sensitivity of the current CERS set-up could be further improved by using a more powerful laser or one that emits in the UV.

The FTIR set-up uses a commercial spectrometer with a home-built White cell attachment, and, in truth, there are no reasonable physical improvements that could be implemented, outside the unnecessary effort to explore more sensitive long-path multiple-pass cell designs or purchasing a highly expensive new spectrometer with greater spectral resolution. Instead, effort is better focussed to improving and expanding on the spectral fitting routines introduced in this thesis. FTIR spectra contain a lot of valuable information but can be very complicated to analyse due to the abundance of water lines, overlapping spectral features and other interferences. The ‘white whale’ of analysing FTIR spectra in Chapter 4 was the inability to analyse NO. In principle it can be detected by FTIR spectroscopy, but low levels of NO are likely lost in water lines. However, if spectral analysis could be further improved to detect NO it would be a huge asset for any further studies of NO_3^- and NO_2^- reduction. Alternatively, there are other spectroscopic laser techniques for ultra-trace detection of NO such as laser induced fluorescence (LIF) or resonantly enhanced multi-photon ionisation (REMPI).

Liquid-phase Raman spectroscopy could be improved by replacing the green excitation laser with a longer wavelength (red or near-IR) to avoid fluorescence allowing the technique to be used to monitor different bioprocesses in coloured media, something not possible with the green set-up which is limited to colourless minimal media analysis. Furthermore, the Raman spectral analysis could be further optimised to detect other Raman-active species of interest, such as lactate, succinate and fumarate. Detection of these acids would also allow a more complete characterisation of mixed-acid fermentation. It is thought that these acids were produced under our experimental conditions but at concentrations below our detection limits. A more powerful excitation laser may allow detection of these species as well as being a necessity if changing to a longer excitation wavelength as this will decrease the Raman signal.

These spectroscopic techniques are widely applicable to a variety of bioprocesses. They could be used to continue the studies presented in this thesis, such as isotopically labelling growth substrates to identify preferential species and elucidate metabolic pathways, investigating the proposed N_2O reduction capability of *E. coli* K-12 in the presence of excess N_2O or further investigating the observed tolerance FHL activity has to micro-aerobic conditions. Concerns about climate change and dwindling petroleum reserves is increasing the search for alternate renewable fuels. The established analytical capabilities of the spectroscopic techniques described in this thesis are well-suited to monitoring bioethanol and biohydrogen production. Hence, monitoring bioprocesses such as lignocellulosic fermentation to produce bioethanol or biohydrogen production by green microalgae, cyanobacteria, photosynthetic bacteria or other fermentative bacteria is of particular interest. Further bioprocesses that could be monitored include hydrogenotrophic methanogenesis, where H_2 and CO_2 are used to generate CH_4, a molecular with a particularly large Raman cross-section. Furthermore, if efforts are made to prevent fluctuating CERS intensities then N_2 would no longer be needed as an internal calibrant, enabling the study of N_2 bioprocesses such as denitrification and nitrogen fixation. N_2 production could be monitored by using an inert argon atmosphere. If fluctuating CERS intensities cannot be prevented, another option would be to explore the silicon signals from the CERS cavity glass windows as an alternative internal calibrant. Some preliminary work analysing the silicon signals that are present as a slopping baseline in all CERS spectra (that is subtracted away using a vacuum spectrum) has already showed some promising and encouraging initial results.

There is no shortage of important bioprocesses that could be elucidated by these laser techniques. On-line, non-invasive data analysis by these cost-effective spectroscopic sensors has tremendous potential for bioreactor monitoring *in situ* and, with further development, they could easily supplement, or even supersede, more conventional methods. Future work demands further exploration of the full potential of these powerful analytical tools.

References

[1] J. M. Hollas (2013). *Modern Spectroscopy*. 4th Ed. Wiley, New York.

[2] A. Smekal (1923). *Zur Quantentheorie der Dispersion*. Naturwissenschaften. **11**, 873-875. https://doi.org/10.1007/BF01576902

[3] C. V. Raman, K. S. Krishnan (1928). *The Negative Absorption of Radiation.* Nature. **122**, 12-13. https://doi.org/10.1038/122012b0

[4] E. Smith, G. Dent (2019). *Modern Raman Spectroscopy: A Practical Approach*. 2nd Ed. Wiley, Hoboken, New Jersey.

[5] E. Fermi (1931). *Über den Ramaneffekt des Kohlendioxyds*. Z. Phys. **71**, 250-259. https://doi.org/10.1007/BF01341712

[6] A. E. Siegman (1986). *Lasers*. University Science Books, Mill Valley, California.

[7] G. Peach (1981). *Theory of the pressure broadening and shift of spectral lines*. Adv. Phys. **30**, 367-474. https://doi.org/10.1080/00018738100101467

[8] I. E. Gordon, L. S. Rothman, C. Hill, R. V. Kochanov, Y. Tan, P. F. Bernath, M. Birk, V. Boudon, A. Campargue, K. V. Chance, B. J. Drouin, J-M. Flaud, R. R. Gamache, J. T. Hodges, D. Jacquemart, V. I. Perevalov, A. Perrin, K. P. Shine, M-A. H. Smith, J. Tennyson, G. C. Toon, H. Tran, V. G. Tyuterev, A. Barbe, A. G. Császár, V. M. Devi, T. Furtenbacher, J. J. Harrison, J-M. Hartmann, A. Jolly, T. J. Johnson, T. Karman, I. Kleiner, A. A. Kyuberis, J. Loos, O. M. Lyulin, S. T. Massie, S. N. Mikhailenko, N. Moazzen-Ahmadi, H. S. P. Müller, O. V. Naumenko, A. V. Nikitin, O. L. Polyansky, M. Rey, M. Rotger, S. W. Sharpe, K. Sung, E. Starikova, S. A. Tashkun, J. Vander Auwera, G. Wagner, J. Wilzewski, P. Wcisło, S. Yu, E. J. Zak (2017). *The HITRAN2016 Molecular Spectroscopic Database*. J. Quant. Spectrosc. Radiat. Transf. **203**, 3–69. https://doi.org/10.1016/j.jqsrt.2017.06.038

[9] T. Escherich (1988). *The Intestinal Bacterial of the Neonate and Breast-Fed Infant*. Rev. Infect. Dis. **10**, 1220-1225. https://doi.org/10.1093/clinids/10.6.1220

[10] C. E. Clifton, J. P. Clearly (1934). *Oxidation-reduction Potentials and Ferricyanide Reducing Activities in Glucose-peptone Cultures and Suspensions of Escherichia coli*. J. Bacteriol. **28**, 561-569. https://doi.org/10.1128/jb.28.6.561-569.1934

[11] M. F. d'Herelle (1917). *Sur un microbe invisible antagoniste des bacilles dysentériques*. Res. Microbiol. **158**, 553-554. https://doi.org/10.1016/j.resmic.2007.07.005

[12] J. Lederberg, E. M. Lederberg (1952). *Replica Plating and Indirect Selection of Bacterial Mutants*. J. Bacteriol. **63**, 399-406. https://doi.org/10.1128/jb.63.3.399-406.1952

[13] I. R. Lehman, M. J. Bessman, E. S. Simms, A. Kornberg (1958). *Enzymatic Synthesis of Deoxyribonucleic Acid. I. Preparation of Substrates and Partial Purification of an Enzyme from Escherichia coli*. J. Biol. Chem. **233**, 163-170. https://doi.org/10.1016/S0021-9258(19)68048-8

[14] F. H. Crick, L. Barnett, S. Brenner, R. J. Watts-Tobin (1961). *General Nature of the Genetic Code for Proteins*. Nature. **192**, 1227-1232. https://doi.org/10.1038/1921227a0

[15] F. Jacob, D. Perrin, C. Sanchez, J. Monod (1960). *L'opéron: groupe de gènes à expression coordonnée par un opérateur*. C. R. Acad. Sci. Paris. **250**, 1727-1729. https://doi.org/10.1016/j.crvi.2005.04.005

[16] D. A. Jackson, R. H. Symons, P. Berg (1972). *Biochemical Method for Inserting New Genetic Information into DNA of Simian Virus 40: circular SV40 DNA Molecules Containing Lambda Phage Genes and the Galactose Operon of Escherichia coli*. Proc. Natl. Acad. Sci. USA. **69**, 2904-2909. https://doi.org/10.1073/pnas.69.10.2904

[17] S. N. Cohen, A. C. Chang, H. W. Boyer, R. B. Helling (1973). *Construction of Biologically Functional Bacterial Plasmids in vitro*. Proc. Natl. Acad. Sci. USA. **70**, 3240-3244. https://doi.org/10.1073/pnas.70.11.3240

[18] F. Sargent, R. G. Sawers (2022). *A paean to the ineffable Marjory Stephenson*. Microbiol. **168**, 3. https://doi.org/10.1099/mic.0.001160

[19] C. Tyrrell, P. S. Cohen (2015). *Commensal and Pathogenic Escherichia coli Metabolism in the Gut*. Microbiol. Spectr. **3**, 3. https://doi.org/10.1128/microbiolspec.MBP-0006-2014

[20] G. Na, Z. Lu, H. Gao, L. Zhang, Q. Li, R. Li, F. Yang, C. Huo, Z. Yao (2018). *The effect of environmental factors and migration dynamics on the prevalence of antibiotic-resistant Escherichia coli in estuary environments*. Sci. Rep. **8**, 1663. https://doi.org/10.1038/s41598-018-20077-x

[21] B. Merget, K. J. Forbes, F. Brennan, S. McAteer, T. Shepherd, N. J. C. Strachan, N. Holden (2022). *Influence of Plant Species, Tissue Type, and Temperature on the Capacity of Shiga-Toxigenic Escherichia coli To Colonize, Grow, and Be Internalized by Plants*. Appl. Environ. Microbiol. **85**, e00123-19. https://doi.org/10.1128/AEM.00123-19

[22] E. W. Trotter, M. D. Rolfe, A. M. Hounslow, C. J. Craven, M. P. Williamson, G. Sanguinetti, R. K. Poole. J. Green (2011). *Reprogramming of Escherichia coli K-12 Metabolism during the Initial Phase of Transition from an Anaerobic to a Micro-Aerobic Environment*. PLoS One. **6**, e25501. https://doi.org/10.1371/journal.pone.0025501

[23] V-M. N. Idalia, F. Bernardo (2017). *Escherichia coli as a Model Organism and Its Application in Biotechnology*. https://doi.org/10.5772/67306

[24] Z. W. El-Hajj, E. B. Newman (2015). *An Escherichia coli Mutant That Makes Exceptionally Long Cells*. J. Bacteriol. **197**, 1507-1514. https://doi.org/10.1128/JB.00046-15

[25] F. R. Blattner, G. Plunkett, C. A. Bloch, V. Burland, M. Riley, J. Collado-Vides, J. D. Glasner, C. K. Rode, G. F. Mayhew, J. Gregor, N. W. Davis, H. A. Kirkpatrick, M. A. Goeden, D. J. Rose, B. Mau, Y. Shao (1997). *The Complete Genome Sequence of Escherichia coli K-12*. Science. **277**, 1453-1462. https://doi.org/10.1126/science.277.5331.1453

[26] H. W. Smith (1975). *Survival of orally administered E. coli K12 in alimentary tract of man*. Nature. **255**, 500-502. https://doi.org/10.1038/255500a0

[27] K. A. Gray, L. Zhao, M. Emptage (2006). *Bioethanol*. Curr. Opin. Chem. Biol. **10**, 141-146. https://doi.org/10.1016/j.cbpa.2006.02.035

[28] M. Gares, S. Hiligsmann, N. K. Chaouche (2020). *Lignocellulosic biomass and industrial bioprocesses for the production of second generation bio-ethanol, does it have a future in Algeria?* SN Appl. Sci. **2**, 1680. https://doi.org/10.1007/s42452-020-03442-2

[29] D. N. Moysés, V. C. Reis, J. R. Almeida, L. M. Moraes, F. A. Torres (2016) *Xylose Fermentation by Saccharomyces cerevisiae: Challenges and Prospects*. Int. J. Mol. Sci. **17**, 207. https://doi.org/10.3390/ijms17030207

[30] V. Koppolu, V. K. Vasigala (2016). *Role of Escherichia coli in Biofuel Production*. Microbiol. Insights. **9**, 29-35. https://doi.org/10.4137/MBI.S10878

[31] M. Wang, G. Wang, Z. Sun, Y. Zhang, D. Xu (2019). *Review of renewable energy-based hydrogen production processes for sustainable energy innovation*. Glo. Energy Interconnect. **2**, 436-443. https://doi.org/10.1016/j.gloei.2019.11.019

[32] S. A. Ahmed, N. Rafa, M. Mofijur, I. A. Badruddin, A. Inayat, M. S. Ali, O. Farrok, T. M. Y. Khan (2021). *Biohydrogen Production From Biomass Sources: Metabolic Pathways and Economic Analysis*. Front. Energy Res. **9**, 753878. https://doi.org/10.3389/fenrg.2021.753878

[33] C. L. Kelly, C. Pinske, B. J. Murphy, A. Parkin, F. Armstrong, T. Palmer, F. Sargent (2015). *Integration of an [FeFe]-hydrogenase into the anaerobic metabolism of Escherichia coli*. Biotechnol. Reports. **8**, 94-104. https://doi.org/10.1016/j.btre.2015.10.002

[34] L. M. Rosales-Colunga, A. D. L. Rodríguez (2015). *Escherichia coli and its application to biohydrogen production*. Rev. Environ. Sci. Biotechnol. **14**, 123-135. https://doi.org/10.1007/s11157-014-9354-2

[35] W. J. Ingledew, R. K. Poole (1984). *The Respiratory Chains of Escherichia coli*. Microbiol. Rev. **48**, 222-271. https://doi.org/10.1128/mr.48.3.222-271.1984

[36] B. Erni (1989). *Glucose transport in Escherichia coli*. FEMS Microbiol. Rev. **5**, 13-23. https://doi.org/10.1111/j.1574-6968.1989.tb14096.x

[37] S. Steinsiek, K. Bettenbrock (2012). *Glucose Transport in Escherichia coli Mutant Strains with Defects in Sugar Transport Systems*. J. Bacteriol. **194**, 5897-5908. https://doi.org/10.1128/JB.01502-12

[38] W. D. Hollinshead, S. Rodriguez. H. G. Martin, G. Wang, E. E. K. Baidoo, K. L. Sale, J. D. Keasling, A. Mukhopadhyay, Y. J. Tang (2016). *Examining Escherichia coli glycolytic pathways, catabolite repression, and metabolite channeling using Δpfk mutants*. Biotechnol. Biofuels. **9**, 212. https://doi.org/10.1186/s13068-016-0630-y

[39] R. C. Eisenberg, W. J. Dobrogosz (1967). *Gluconate Metabolism in Escherichia coli*. J. Bacteriol. **93**, 941-949. https://doi.org/10.1128/jb.93.3.941-949.1967

[40] B. Cassey, J. R. Guest, M. M. Attwood (1998). *Environmental control of pyruvate dehydrogenase complex expression in Escherichia coli*. FEMS Microbiol. Lett. **159**, 325-329. https://doi.org/10.1111/j.1574-6968.1998.tb12878.x

[41] S. G. Henkel, A. T. Beek, S. Steinsiek, S. Stagge, K. Bettenbrock, M. J. T. de Mattos, T. Sauter, O. Sawodny, M. Ederer (2014). *Basic Regulatory Principles of Escherichia coli's Electron Transport Chain for Varying Oxygen Conditions*. PLoS One. **9**, e107640. https://doi.org/10.1371/journal.pone.0107640

[42] H. Erhardt, F. Dempwolff, M. Pfreundschuh, M. Riehle, C. Schäfer, T. Pohl, P. Graumann, T. Friedrich (2014). *Organization of the Escherichia coli aerobic enzyme complexes of oxidative phosphorylation in dynamic domains within the cytoplasmic membrane*. Microbiol. Open. **3**, 316-326. https://doi.org/10.1002/mbo3.163

[43] J. Rutter, D. R. Winge, J. D. Schiffman (2010). *Succinate dehydrogenase – Assembly, regulation and role in human disease*. Mitochondrion. **10**, 393-401. https://doi.org/10.1016/j.mito.2010.03.001

[44] J. Abramson, S. Riistama, G. Larsson, A. Jasaitis, M. Svensson-Ek, L. Laakkonen, A. Puustinen, S. Iwata, M. Wikström (2000). *The structure of the ubiquinol oxidase from Escherichia coli and its ubiquinone binding site*. Nat. Struct. Biol. **7**, 910-917. https://doi.org/10.1038/82824

[45] V. B. Borisov, R. B. Gennis, M. I. Verkhovsky (2011). *The cytochrome bd respiratory oxygen reductases*. Biochim. Biophys. Acta – Bioenerg. 1807, 1398-1413. https://doi.org/10.1016/j.bbabio.2011.06.016

[46] A. Grauel, J. Kägi, T. Rasmussen, I. Makarchuk, S. Oppermann, A. F. A. Moumbock, D. Wohlwend, R. Müller, F. Melin, S. Günther, P. Hellwig, B. Böttcher, T. Friedrich (2021). *Structure of Escherichia coli cytochrome bd-II type oxidase with bound aurachin D*. Nat. Commun. **12**, 6498. https://doi.org/10.1038/s41467-021-26835-2

[47] G. Unden, J. Bongaerts (1997). *Alternative respiratory pathways of Escherichia coli: energetics and transcriptional regulation in response to electron acceptors*. Biochim. Biophys. Acta. **1320**, 217-234. https://doi.org/10.1016/s0005-2728(97)00034-0

[48] D. P. Clark (1989). *The fermentation pathways of Escherichia coli*. FEMS Microbiol. Lett. **63**, 223-234. https://doi.org/10.1016/0378-1097(89)90132-8

[49] C. Thakker, I. Martínez, K-Y. San, G. N. Bennett (2011). *Succinate production in Escherichia coli*. Biotechnol. J. **7**, 213-224. https://doi.org/10.1002/biot.201100061

[50] C. Doberenz, M. Zorn, D. Falke, D. Nannemann, D. Hunger, L. Beyer, C. H. Ihling, J. Meiler, A. Sinz, R. G. Sawers (2014). *Pyruvate Formate-Lyase Interacts Directly with the Formate Channel FocA to Regulate Formate Translocation*. J. Mol. Biol. **426**, 2827-2839. https://doi.org/10.1016/j.jmb.2014.05.023

[51] G. Sawers (1994). *The hydrogenases and formate dehydrogenases of Escherichia coli*. Antonie van Leeuwenhoek. **66**, 57-88. https://doi.org/10.1007/BF00871633

[52] C. Pinske, R. G. Sawers (2016). *Anaerobic Formate and Hydrogen Metabolism*. EcoSal Plus. **7**(1). https://doi.org/10.1128/ecosalplus.ESP-0011-2016

[53] A. J. Finney, F. Sargent (2019). *Formate hydrogenlyase: A group 4 [NiFe]-hydrogenase in tandem with a formate dehydrogenase*. Adv. Microb. Physiol. **74**, 465-486. https://doi.org/10.1016/bs.ampbs.2019.02.004

[54] J. C. Boyington, V. N. Gladyshev, S. V. Khangulov, T. C. Stadtman, P. D. Sun (1997). *Crystal Structure of Formate DehydrogenaseH: Catalysis Involving Mo, Molybdopterin, Selenocysteine, and an Fe_4S_4 Cluster*. Science. **275**, 1305-1308. https://doi.org/10.1126/science.275.5304.1305

[55] F. Sargent (2016). *The Model [NiFe]-Hydrogenases of Escherichia coli*. Adv. Microb. Physiol. **68**, 433-507. https://doi.org/10.1016/bs.ampbs.2016.02.008

[56] K. Pandi, A. S. Chauhan, J. A. Gupta, A. S. Rathore (2020). *Microaerobic fermentation alters lactose metabolism in Escherichia coli*. Appl. Microbiol. Biotechnol. **104**, 5773-5785. https://doi.org/10.1007/s00253-020-10652-6

[57] C. M. Narayanan, V. Narayan (2019). *Biological wastewater treatment and bioreactor design: a review*. Sustain. Environ. Res. **29**, 33. https://doi.org/10.1186/s42834-019-0036-1

[58] M. Basan, S. Hui, H. Okano, Z. Zhang, Y. Shen, J. R. Williamson, T. Hwa (2015). *Overflow metabolism in Escherichia coli results from efficient proteome allocation*. Nature. **528**, 99-104. https://doi.org/10.1038/nature15765

[59] M. El-Mansi (2004). *Flux to acetate and lactate excretions in industrial fermentations: physiological and biochemical implications*. J. Ind. Microbiol. Biotechnol. **31**, 295-300. https://doi.org/10.1007/s10295-004-0149-2

[60] K. Han, H. C. Lim, J. Hong (1992). *Acetic acid formation in Escherichia coli fermentation*. Biotechnol. Bioeng. **39**, 663-671. https://doi.org/10.1002/bit.260390611

[61] R. A. Majewski, M. M. Domach (1990). *Simple constrained-optimization view of acetate overflow in E. coli*. Biotechnol. Bioeng. **35**, 732-738. https://doi.org/10.1002/bit.260350711

[62] S. J. Reyes, Y. Durocher, P. L. Pham, O. Henry (2022). *Modern Sensor Tools and Techniques for Monitoring, Controlling, and Improving Cell Culture Processes*. Processes. **10**, 189. https://doi.org/10.3390/pr10020189

[63] N. D. Lourenço, J. A. Lopes, C. F. Almeida, M. C. Sarraguça, H. M. Pinheiro (2012). *Bioreactor monitoring with spectroscopy and chemometrics: a review*. Anal. Bioanal. Chem. **404**, 1211-1237. https://doi.org/10.1007/s00216-012-6073-9

[64] T. R. Holzberg, V. Watson, S. Brown, A. Andar, X. Ge, Y. Kostov, L. Tolosa, G. Rao (2018). *Sensors for biomanufacturing process development: facilitating the shift from batch to continuous manufacturing*. Curr. Opin. Chem. Eng. **22**, 115-127. https://doi.org/10.1016/j.coche.2018.09.008

[65] H-Y. Goh, M. Sulu, H. Alosert, G. L. Lewis, G. D. Josland, D. E. Merriman (2020). *Applications of off-gas mass spectrometry in fed-batch mammalian cell culture*. Bioprocess Biosyst. Eng. **43**, 483-493. https://doi.org/10.1007/s00449-019-02242-2

[66] N. M. Dixon, D. B. Kell (1989). *The control and measurement of 'CO_2' during fermentations*. J. Microbiol. Methods. **3**, 155-176. https://doi.org/10.1016/0167-7012(89)90048-1

[67] V. Tarkiainen, T. Kotiaho, I. Mattila, I. Virkajärvi, A. Aristidou, R. A. Ketola (2005). *On-line monitoring of continuous beer fermentation process using automatic membrane inlet mass spectrometric system*. Talanta. **65**, 1254-1263. https://doi.org/10.1016/j.talanta.2004.08.051

[68] E. Heinzle (1992). *Present and potential applications of mass spectrometry for bioprocess research and control*. J. Biotechnol. **25**, 81-114. https://doi.org/10.1016/0168-1656(92)90111-L

[69] C-T. Yan, J-F. Jen (1992). *Determination of volatile fatty acids in landfill leachates by gas chromatography with distillation pretreatment*. Anal. Chim. Acta. **264**, 259-264. https://doi.org/10.1016/0003-2670(92)87013-B

[70] V. Diamantis, P. Melidis, A. Aivasidis (2006). *Continuous determination of volatile products in anaerobic fermenters by on-line capillary gas chromatography*. Anal. Chim. Acta. **573-574**, 189-194. https://doi.org/10.1016/j.aca.2006.05.036

[71] Y-C. Liu, F-S. Wang, W-C. Lee (2001). *On-line monitoring and controlling system for fermentation processes*. Biochem. Eng. J. **7**, 17-25. https://doi.org/10.1016/S1369-703X(00)00100-5

[72] P. v. Zumbusch, T. Meyer-Jens, G. Brunner, H. Märkl (1994). *On-line monitoring of organic substances with high-pressure liquid chromatography (HPLC) during the anaerobic fermentation of waste-water*. Appl. Microbiol. Biotechnol. **42**, 140-146. https://doi.org/10.1007/BF00170237

[73] A. Rehorek, K. Urbig, R. Meurer, C. Schäfer, A. Plum, G. Braun (2002). *Monitoring of azo dye degradation processes in a bioreactor by on-line high-performance liquid chromatography*. J. Chromatogr. A. **949**, 263-268. https://doi.org/10.1016/S0021-9673(01)01427-3

[74] L. Safo, S. Abdelrazig, A. Grosse-Honebrink, T. Millat, A. M. Henstra, R. Norman, N. R. Thomas, K. Winzer, N. P. Minton, D-H. Kim, and D. A. Barrett (2021). *Quantitative Bioreactor Monitoring of Intracellular Bacterial Metabolites in Clostridiumautoethanogenum Using Liquid Chromatography–Isotope Dilution Mass Spectrometry*. ACS Omega. **6**, 13518-13526. https://doi.org/10.1021/acsomega.0c05588

[75] A. N. Lane, T. W-M. Fan, R. M. Higashi (2008). *Isotopomer-Based Metabolomic Analysis by NMR and Mass Spectrometry*. Methods Cell Biol. **84**, 541-588. https://doi.org/10.1016/S0091-679X(07)84018-0

[76] M. R. Phelps, J. B. Hobbs, D. G. Kilburn, R. F. B. Turner (1995). *An autoclavable glucose biosensor for microbial fermentation monitoring and control*. Biotechnol. Bioeng. **46**, 514-524. https://doi.org/10.1002/bit.260460604

[77] M. Esti, G. Volpe, D. Compagnone, G. Mariotti, D. Moscone, G. Palleschi (2003). *Monitoring Alcoholic Fermentation of Red Wine by Electrochemical Biosensors*. Am. J. Enol. Vitic. **54**, 39-45. https://www.ajevonline.org/content/54/1/39

[78] C. Busse, P. Biechele, I. de Vries, K. F. Reardon, D. Solle, T. Scheper (2017). *Sensors for disposable bioreactors*. Eng. Life Sci. **17**, 940-952. https://doi.org/10.1002/elsc.201700049

[79] L. Rolinger, M. Rüdt, J. Hubbuch (2020*). A critical review of recent trends, and a future perspective of optical spectroscopy as PAT in biopharmaceutical downstream processing*. Anal. Bioanal. Chem. **412**, 2047-2064. https://doi.org/10.1007/s00216-020-02407-z

[80] A. P. Teixeira, R. Oliveira, P. M. Alves, M. J. T. Carrondo (2009). *Advances in on-line monitoring and control of mammalian cell cultures: Supporting the PAT initiative*. Biotechnol. Adv. **27**, 726-732. https://doi.org/10.1016/j.biotechadv.2009.05.003

[81] M. Rhiel, P. Ducommun, I. Bolzonella, I. Marison, U. von Stockar (2002). *Real-time in situ monitoring of freely suspended and immobilized cell cultures based on mid-infrared spectroscopic measurements*. Biotechnol. Bioeng. **77**, 174-185. https://doi.org/10.1002/bit.10134

[82] H. Kornmann, S. Valentionotti, P. Duboc, I. Marison, U. von Stockar (2004). *Monitoring and control of Gluconacetobacter xylinus fed-batch cultures using in situ mid-IR spectroscopy*. J. Biotechnol. **113**, 231-245. https://doi.org/10.1016/j.jbiotec.2004.03.029

[83] D. Landgrebe, C. Haake, T. Höpfner, S. Beutel, B. Hitzmann, T. Scheper, M. Rhiel, K. F. Reardon (2010). *On-line infrared spectroscopy for bioprocess monitoring*. Appl. Microbiol. Biotechnol. **88**, 11-22. https://doi.org/10.1007/s00253-010-2743-8

[84] S. W. Sharpe, T. J. Johnson, R. L. Sams, P. M. Chu, G. C. Rhoderick, P. A. Johnson (2004). *Gas-Phase Databases for Quantitative Infrared Spectroscopy*. Appl. Spectrosc. **58**,1452–1461. https://doi.org/10.1366/0003702042641281

[85] A. Knížek, K. Dryahina, P. Španěl, P. Kubelík, L. Kavan, M. Zukalová, M. Ferus, S. Civiš (2018). *Comparative SIFT-MS, GC–MS and FTIR analysis of methane fuel produced in biogas stations and in artificial photosynthesis over acidic anatase* TiO_2 *and montmorillonite*. J. Mol. Spectrosc. **348**, 152-160. https://doi.org/10.1016/j.jms.2017.10.002

[86] N. R. Abu-Absi, B. M. Kenty, M. E. Cuellar, M. C. Borys, S. Sakhamuri, D. J. Strachan, M. C. Hausladen, Z. J. Li (2011). *Real time monitoring of multiple parameters in mammalian cell culture bioreactors using an in-line Raman spectroscopy probe*. Biotechnol. Bioeng. **108**, 1215-1221. https://doi.org/10.1002/bit.23023

[87] T-H. Lee, J-S. Chang, H-Y. Wang (2013). *Rapid and in Vivo Quantification of Cellular Lipids in Chlorella vulgaris Using Near-Infrared Raman Spectrometry*. Anal. Chem. **85**, 2155-2160. https://doi.org/10.1021/ac3028118

[88] R. S. Jakubek, J. Handen, S. E. White, S. A. Asher, I. K. Lednev (2018). *Ultraviolet Resonance Raman Spectroscopic Markers for Protein Structure and Dynamics*. Analyt. Chem. **103**, 223-229. https://doi.org/10.1016/j.trac.2017.12.002

[89] S. E. J. Bell, G. Charron, E. Cortés, J. Kneipp, M. L. de la Chapelle, J. Langer, M. Procházka, V. Tran, S. Schlücker (2020). *Towards Reliable and Quantitative Surface-Enhanced Raman Scattering (SERS): From Key Parameters to Good Analytical Practice*. Angew. Chem. Int. Ed. **59**, 5454. https://doi.org/10.1002/anie.201908154

[90] P. St. J. Russell (2006). *Photonic-Crystal Fibers*. J. Light. Technol. **24**, 4729-4749. https://doi.org/10.1109/JLT.2006.885258

[91] S. Hanf, R. Keiner, D. Yan, J. Popp, T. Frosch (2014). *Fiber-Enhanced Raman Multigas Spectroscopy: A Versatile Tool for Environmental Gas Sensing and Breath Analysis*. Anal. Chem. **86**, 5278-5285. https://doi.org/10.1021/ac404162w

[92] S. Hanf, T. Bögözi, R. Keiner, T. Frosch, J. Popp (2015*). Fast and Highly Sensitive Fiber-Enhanced Raman Spectroscopic Monitoring of Molecular* H_2 *and* CH_4 *for Point-of-Care Diagnosis of Malabsorption Disorders in Exhaled Human Breath*. Anal. Chem. **87**, 982-988. https://doi.org/10.1021/ac503450y

[93] S. Wartewig, R. H. H. Neubert (2005). *Pharmaceutical applications of Mid-IR and Raman spectroscopy*. **57**, 1144-1170. https://doi.org/10.1016/j.addr.2005.01.022

[94] C. Niklas, H. Wackerbarth, G. Ctistis (2021). *A Short Review of Cavity-Enhanced Raman Spectroscopy for Gas Analysis*. Sensors (Basel). **21**, 1698. https://doi.org/10.3390/s21051698

[95] A. Weber, S. P. S. Porto, L. E. Cheesman, J. J. Barrett (1967). *High-Resolution Raman Spectroscopy of Gases with cw-Laser Excitation*. J. Opt. Soc. Am. A. **57**, 19-28. https://doi.org/10.1364/JOSA.57.000019

[96] H-B. Lin, A. J. Campillo (1995). *Radial profiling of microdroplets using cavity-enhanced Raman spectroscopy*. Opt. Lett. **20**, 1589-1591. https://doi.org/10.1364/OL.20.001589

[97] R. Salter, J. Chu, M. Hippler (2012). *Cavity-enhanced Raman spectroscopy with optical feedback cw diode lasers for gas phase analysis and spectroscopy*. Analyst. **137**, 4669-4676. https://doi.org/10.1039/C2AN35722D

[98] M. Hippler (2015). *Cavity-Enhanced Raman Spectroscopy of Natural Gas with Optical Feedback cw-Diode Lasers*. Anal. Chem. **87**, 7803–7809. https://doi.org/10.1021/acs.analchem.5b01462

[99] T. W. Smith, M. Hippler (2017). *Cavity-Enhanced Raman Spectroscopy in the Biosciences: In Situ, Multicomponent, and Isotope Selective Gas Measurements to Study Hydrogen Production and Consumption by Escherichia coli*. Anal. Chem. **89**, 2147–2154. https://doi.org/10.1021/acs.analchem.6b04924

[100] T. Frosch, R. Keiner, B. Michalzik, B. Fischer, J. Popp (2013). *Investigation of Gas Exchange Processes in Peat Bog Ecosystems by Means of Innovative Raman Gas Spectroscopy*. Anal. Chem. **85**, 1295-1299. https://doi.org/10.1021/ac3034163

[101] R. Keiner, T. Frosch, T. Massad, S. Trumbore, J. Popp (2014). *Enhanced Raman multigas sensing – a novel tool for control and analysis of* $^{13}CO_2$ *labeling experiments in environmental research*. Analyst. **139**, 3879-3884. https://doi.org/10.1039/C3AN01971C

[102] A. Sieburg, T. Jochum, S. E. Trumbore, J. Popp, T. Frosch (2017). *Onsite cavity enhanced Raman spectrometry for the investigation of gas exchange processes in the Earth's critical zone*. Analyst. **142**, 3360–3369. https://doi.org/10.1039/C7AN01149K

[103] A. Sieburg, S. Schneider, D. Yan, J. Popp, T. Frosch (2018). *Monitoring of gas composition in a laboratory biogas plant using cavity enhanced Raman spectroscopy*. Analyst. **143**, 1358-1366. https://doi.org/10.1039/C7AN01689A

[104] K. C. Utsav, J. A. Silver, D. C. Hovde, P. L. Varghese (2011). *Improved multiple-pass Raman spectrometer*. Appl. Opt. **50**, 4805-4816. https://doi.org/10.1364/AO.50.004805

[105] M. Hippler, C. Mohr, K. A. Keen, E. D. McNaghten (2010). *Cavity-enhanced resonant photoacoustic spectroscopy with optical feedback cw diode lasers: A novel technique for ultratrace gas analysis and high-resolution spectroscopy*. J. Chem. Phys. **133**, 044308. https://doi.org/10.1063/1.3461061

[106] E. D. Black (2001). *An introduction to Pound–Drever–Hall laser frequency stabilization.* J. Phys. **69**, 79-87. https://doi.org/10.1119/1.1286663

[107] J. M. Herbelin, J. A. McKay, M. A. Kwok, R. H. Ueunten, D. S. Urevig, D. J. Spencer, D. J. Benard, (1980). *Sensitive measurement of photon lifetime and true reflectances in an optical cavity by a phase-shift method*. Appl. Opt. **19**, 144-147. https://doi.org/10.1364/AO.19.000144

[108] A. O'Keefe, D. A. G. Deacon (1988). *Cavity ring-down optical spectrometer for absorption measurements using pulsed laser sources*. Rev. Sci. Instrum. **59**, 2544-2551. https://doi.org/10.1063/1.1139895

[109] A. O'Keefe, J. J. Scherer, J. B. Paul (1999). *cw Integrated cavity output spectroscopy*. Chem. Phys. Lett. **307**, 343-349. https://doi.org/10.1016/S0009-2614(99)00547-3

[110] G. D. Metcalfe, S. Alahmari, T. W. Smith, M. Hippler (2019). *Cavity-Enhanced Raman and Helmholtz Resonator Photoacoustic Spectroscopy to Monitor the Mixed Sugar Metabolism of E. coli*. Anal. Chem. **91**, 13096-13104. https://doi.org/10.1021/acs.analchem.9b03284

[111] J. D. van Elsas, A. V. Semenov, R. Costa, J. T. Trevors (2011). *Survival of Escherichia coli in the environment: fundamental and public health aspects*. ISME J. **5**, 173-183. https://doi.org/10.1038/ismej.2010.80

[112] G. Lambert, E. Kussell (2014). *Memory and Fitness Optimization of Bacteria under Fluctuating Environments*. PloS Genet. **10**, e1004556. https://doi.org/10.1371/journal.pgen.1004556

[113] E. Perrin, V. Ghini, M. Giovannini, F. Di Patti, B. Cardazzo, L. Carraro, C. Fagorzi, P. Turano, R. Fani, M. Fondi (2020). *Diauxie and co-utilization of carbon sources can coexist during bacterial growth in nutritionally complex environments*. Nat. Commun. **11**, 3135. https://doi.org/10.1038/s41467-020-16872-8

[114] J. Monod (1949). *The Growth of Bacterial Cultures*. Annu. Rev. Microbiol. **3**, 371-394. https://doi.org/10.1146/annurev.mi.03.100149.002103

[115] G. Aidelberg, B. D. Towbin, D. Rothschild, E. Dekel, A. Bren, U. Alon (2014). *Hierarchy of non-glucose sugars in Escherichia coli*. BMC Syst. Biol. **8**, 133. https://doi.org/10.1186/s12918-014-0133-z

[116] B. S. Dien, N. N. Nichols, R. J. Bothast (2002). *Fermentation of sugar mixtures using Escherichia coli catabolite repression mutants engineered for production of L-lactic acid*. J. Ind. Microbiol. Biotechnol. **29**, 221-227. https://doi.org/10.1038/sj.jim.7000299

[117] A. Solopova, J. van Gestel, F. J. Weissing, H. Bachmann, B. Teusink, J. Kok, O. P. Kuipers (2014). *Bet-hedging during bacterial diauxic shift*. PNAS Microbiol. **111**, 7427-7432. https://doi.org/10.1073/pnas.1320063111

[118] M. L. Siegal (2015). *Shifting Sugars and Shifting Paradigms*. PLoS Biol. **13**, e1002068. https://doi.org/10.1371/journal.pbio.1002068

[119] C. J. Joshua, R. Dahl, P. I. Benke, J. D. Keasling (2011). *Absence of diauxie during simultaneous utilization of glucose and xylose by Sulfolobus acidocaldarius*. J. Bacteriol. **193**, 1293-1301. https://doi.org/10.1128/JB.01219-10

[120] T. A. Desai, C. V. Rao (2009). *Regulation of Arabinose and Xylose Metabolism in Escherichia coli*. Appl. Environ. Microbiol. **76**, 1524-1532. https://doi.org/10.1128/AEM.01970-09

[121] E. M. Ammar, X. Wang, C. V. Rao (2018). *Regulation of metabolism in Escherichia coli during growth on mixtures of the non-glucose sugars: arabinose, lactose, and xylose*. Sci. Rep. **8**, 609. https://doi.org/10.1038/s41598-017-18704-0

[122] G. Busse, D. Herboeck (1979). *Differential Helmholtz resonator as an optoacoustic detector*. Appl. Opt. **18**, 3959-3961. https://doi.org/10.1364/AO.18.003959

[123] V. Zéninari, B. Parvitte, D. Courtois, V. A. Kapitanov, Y. N. Ponomarev (2003). *Methane detection on the sub-ppm level with a near-infrared diode laser photoacoustic sensor*. IR Phys. Technol. **44**, 253-261. https://doi.org/10.1016/S1350-4495(03)00135-X

[124] J. Rouxel, J-G. Coutard, S. Gidon, O. Lartigue, S. Nicoletti, B. Parvitte, R. Vallon, V. Zéninari, A. Glière (2016). *Miniaturized differential Helmholtz resonators for photoacoustic trace gas detection*. Sens. Actuators B Chem. **236**, 1104-1110. https://doi.org/10.1016/j.snb.2016.06.074

[125] S. Alahmari, X-W. Kang, M. Hippler (2019). *Diode laser photoacoustic spectroscopy of* CO_2*,* H_2S *and* O_2 *in a differential Helmholtz resonator for trace gas analysis in the biosciences and petrochemistry*. Anal. Bioanal. Chem. **411**, 3777-3787. https://doi.org/10.1007/s00216-019-01877-0

[126] T. Jochum, A. Fastnacht, S. E. Trumbore, J. Popp, T. Frosch (2017). *Direct Raman Spectroscopic Measurements of Biological Nitrogen Fixation under Natural Conditions: An Analytical Approach for Studying Nitrogenase Activity*. Anal. Chem. **89**, 1117–1122. https://doi.org/10.1021/acs.analchem.6b03101

[127] R. A. McClatchey, W. S. Benedict, S. A. Clough, D. E. Burch, R. F. Calfee (1973). *AFCRL Atmospheric Absorption Line Parameters Compilation*. AFCRL-Technical Report-0096. https://apps.dtic.mil/sti/citations/AD0762904

[128] R. Schermaul, R. C. M. Learner (1999). *Precise line parameters and transition probability of the atmospheric A band of molecular* $^{16}O_2$. J. Quant. Spectrosc. Radiat. Transf. **61**, 781-794. https://doi.org/10.1016/S0022-4073(98)00066-1

[129] R. Grosz, G. Stephanopoulos (1983). *Statistical mechanical estimation of the free energy of formation of E. coli biomass for use with macroscopic bioreactor balances*. Biotechnol. Bioeng. **25**, 2149–2163. https://doi.org/10.1002/bit.260250904

[130] G. Sezonov, D. Joseleau-Petit, R. D'Ari (2007). *Escherichia coli physiology in Luria-Bertani broth*. J. Bacteriol. **189**, 8746–8749. https://doi.org/10.1128/JB.01368-07

[131] C. G. Miller (1987). *Protein degradation and proteolytic modification*. In: Neidhardt FC (ed). *Escherichia coli* and *Salmonella typhimurium*. American Society for Microbiology, Washington, D. C. pp 680-691.

[132] A. Satanowski, B. Dronsella, E. Noor, B. Vögeli, H. He, P. Wichmann, T. J. Erb, S. N. Lindner, A. Bar-Even (2020). *Awakening a latent carbon fixation cycle in Escherichia coli*. Nat. Commun. **11**, 5812. https://doi.org/10.1038/s41467-020-19564-5

[133] Z. Li, M. Nimtz, U. Rinas (2014). *The metabolic potential of Escherichia coli BL21 in defined and rich medium*. Microb. Cell Fact. **13**, 45. https://doi.org/10.1186/1475-2859-13-45

[134] J. Wang, E. Atolia, Y. Savir, R. Escalante-Chong, M. Springer (2015). *Natural Variation in Preparation for Nutrient Depletion Reveals a Cost–Benefit Tradeoff*. PloS Biol. **13**, e1002041. https://doi.org/10.1371/journal.pbio.1002041

[135] L. Fernández-Coll, M. Cashel (2018). *Contributions of SpoT Hydrolase, SpoT Synthetase, and RelA Synthetase to Carbon Source Diauxic Growth Transitions in Escherichia coli*. Front. Microbiol. **9**, 1802. https://doi.org/10.3389/fmicb.2018.01802

[136] D. Chu, D. J. Barnes (2016). The lag-phase during diauxic growth is a trade-off between fast adaptation and high growth rate. Sci. Rep. **6**, 25191. https://doi.org/10.1038/srep25191

[137] M. Hippler, G. D. Metcalfe (2020). *Using Activities to Correct the Henderson-Hasselbalch Equation*. Bunsenmagazin. 102–105. https://doi.org/10.26125/y7p7-an56

[138] G. D. Metcalfe, T. W. Smith, M. Hippler (2020) *On-line analysis and in situ pH monitoring of mixed acid fermentation by Escherichia coli using combined FTIR and Raman techniques*. Anal. Bioanal. Chem. **412**, 7307–7319. https://doi.org/10.1007/s00216-020-02865-5

[139] K. Karimi, M. Tabatabaei, I. Sárvári Horváth, R. Kumar (2015). *Recent trends in acetone, butanol, and ethanol (ABE) production*. Biofuel. Res. J. **2**, 301–308. https://doi.org/10.18331/BRJ2015.2.4.4

[140] G. M. Walker, G. G. Stewart (2016). *Saccharomyces cerevisiae in the Production of Fermented Beverages*. Beverages. **2**, 30. https://doi.org/10.3390/beverages2040030

[141] C. Kirkpatrick, L. M. Maurer, N. E. Oyelakin, Y. N. Yoncheva, R. Maurer, J. L. Slonczewski (2001). *Acetate and formate stress: opposite responses in the proteome of Escherichia coli*. J. Bacteriol. **183**, 6466–6477. https://doi.org/10.1128/JB.183.21.6466-6477.2001

[142] P. K. Bunch, F. Mat-Jan, N. Lee, D. P. Clark (1997). *The IdhA Gene Encoding the Fermentative Lactate Dehydrogenase of Escherichia coli*. Microbiology. **143**, 187-195. https://doi.org/10.1099/00221287-143-1-187

[143] Y. K. Jung, S. Y. Lee (2011). *Efficient production of polylactic acid and its copolymers by metabolically engineered Escherichia coli*. J. Biotechnol. **151**, 94–101. https://doi.org/10.1016/j.jbiotec.2010.11.009

[144] S. Rittmann, C. Herwig (2012). *A comprehensive and quantitative review of dark fermentative biohydrogen production*. Microb. Cell Fact. **11**, 115. https://doi.org/10.1186/1475-2859-11-115

[145] S. Sivakesava, J. Irudayaraj, D. Ali (2001). *Simultaneous determination of multiple components in lactic acid fermentation using FT-MIR, NIR, and FT-Raman spectroscopic techniques*. Process Biochem. **37**, 371–378. https://doi.org/10.1016/S0032-9592(01)00223-0

[146] D. L. Doak, J. A. Phillips (1999). *In Situ Monitoring of an Escherichia coli Fermentation Using a Diamond Composition ATR Probe and Mid-infrared Spectroscopy*. Biotechnol. Prog. **15**, 529-539. https://doi.org/10.1021/bp990039b

[147] C. Koch, A. E. Posch, C. Herwig, B. Lendl (2016). *Comparison of Fiber Optic and Conduit Attenuated Total Reflection (ATR) Fourier Transform Infrared (FT-IR) Setup for In-Line Fermentation Monitoring*. Appl. Spectrosc. **70**, 1965–1973. https://doi.org/10.1177/0003702816662618

[148] J. W. Hall, B. McNeil, M. J. Rollins, I. Draper, B. G. Thompson, G. MacAloney (1996). *Near-Infrared Spectroscopic Determination of Acetate, Ammonium, Biomass, and Glycerol in an Industrial Escherichia Coli Fermentation*. Appl. Spectrosc. **50**, 102–108. https://doi.org/10.1366/0003702963906726

[149] S. A. Arnold, J. Crowley, N. Woods, L. M. Harvey, B. McNeil (2003). *In-situ near infrared spectroscopy to monitor key analytes in mammalian cell cultivation*. Biotechnol. Bioeng. **84**, 13–19. https://doi.org/10.1002/bit.10738

[150] C. Svendsen, T. Skov, F. W. J. van den Berg (2015). *Monitoring fermentation processes using in-process measurements of different orders*. J. Chem. Technol. Biotechnol. **90**, 244–254. https://doi.org/10.1002/jctb.4483

[151] K. Pontius, G. Praticò, F. H. Larsen, T. Skov, N. Arneborg, A. E. Lantz, M. Bevilacqua (2020). *Fast measurement of phosphates and ammonium in fermentation-like media: A feasibility study*. N. Biotechnol. **56**, 54–62. https://doi.org/10.1016/j.nbt.2019.11.006

[152] H. L. T. Lee, P. Boccazzi, N. Gorret, R. J. Ram, A. J. Sinskey (2004). *In situ bioprocess monitoring of Escherichia coli bioreactions using Raman spectroscopy*. Vib. Spectrosc. **35**, 131–137. https://doi.org/10.1016/j.vibspec.2003.12.015

[153] S. R. Gray, S. W. Peretti, H. H. Lamb (2013). *Real-time monitoring of high-gravity corn mash fermentation using in situ Raman spectroscopy*. Biotechnol. Bioeng. **110**, 1654–1662. https://doi.org/10.1002/bit.24849

[154] T. N. K. Zu, S. Liu, E. S. Gerlach, K. L. Germane, M. D. Servinsky, D. M. Mackie, C. J. Sund (2017). *Real-time metabolite monitoring of glucose-fed Clostridium acetobutylicum fermentations using Raman assisted metabolomics*. J. Raman Spectrosc. **48**, 1852–1862. https://doi.org/10.1002/jrs.5264

[155] S. M. Ewanick, W. J. Thompson, B. J. Marquardt, R. Bura (2013). *Real-time understanding of lignocellulosic bioethanol fermentation by Raman spectroscopy*. Biotechnol. Biofuels. **6**, 28. https://doi.org/10.1186/1754-6834-6-28

[156] J. A. Iversen, R. W. Berg, B. K. Ahring (2014). *Quantitative monitoring of yeast fermentation using Raman spectroscopy*. Anal. Bioanal. Chem. **406**, 4911–4919. https://doi.org/10.1007/s00216-014-7897-2

[157] C. Cannizzaro, M. Rhiel, I. Marison, U. von Stockar (2003). *On-line monitoring of Phaffia rhodozyma fed-batch process with in situ dispersive raman spectroscopy*. Biotechnol. Bioeng. **83**, 668–680. https://doi.org/10.1002/bit.10698

[158] M. I. Santos, E. Gerbino, E. Tymczyszyn, A. Gomez-Zavaglia (2015). *Applications of Infrared and Raman Spectroscopies to Probiotic Investigation*. Foods. **4**, 283-305. https://doi.org/10.3390/foods4030283

[159] C. Mohr, C. L. Spencer, M. Hippler (2010). *Inexpensive Raman Spectrometer for Undergraduate and Graduate Experiments and Research*. J. Chem. Educ. **87**, 326–330. https://doi.org/10.1021/ed800081t

[160] T. W. Smith (2017) *New applications of gas phase vibrational spectroscopies in biochemistry and microbiology*. PhD thesis, Department of Chemistry, University of Sheffield. https://etheses.whiterose.ac.uk/19391/

[161] M. D. Fontana, K. Ben Mabrouk, T. H. Kauffmann (2013). *Raman spectroscopic sensors for inorganic salts. In: Spectroscopic Properties of Inorganic and Organometallic Compounds: Techniques, Materials and Applications*. Volume 44. The Royal Society of Chemistry, pp 40–67.

[162] Q. Sun (2009). *The Raman OH stretching bands of liquid water*. Vib. Spectrosc. **51**, 213-217. https://doi.org/10.1016/j.vibspec.2009.05.002

[163] K. A. Syed, S-F. Pang, Y. Zhang, Y-H. Zhang (2013). *Micro-Raman observation on the* H_2PO4^- *association structures in a supersaturated droplet of potassium dihydrogen phosphate* (KH_2PO_4). J. Chem. Phys. **138**, 24901. https://doi.org/10.1063/1.4773585

[164] H. A. Wells, R. H. Atalla (1990). *An investigation of the vibrational spectra of glucose, galactose and mannose*. J. Mol. Struct. **224**, 385–424. https://doi.org/10.1016/0022-2860(90)87031-R

[165] K. Ito, H. J. Bernstein (1956). *The Vibrational Spectra of the Formate, Acetate and Oxalate Ions*. Can. J. Chem. **34**, 170-178. https://doi.org/10.1139/v56-021

[166] P. Debye, E. Hückel (1923). *Zur Theorie der Elektrolyte. I. Gefrierpunktserniedrigung und verwandte Erscheinungen*. Phys. Zeitschrift. **24**, 185–206. https://doi.org/10.1007/BFb0111753

[167] R. de Levie (2005). *On Teaching Ionic Activity Effects: What, When, and Where?* J. Chem. Educ. **82**, 878–884. https://doi.org/10.1021/ed082p878

[168] C. W. Davies (1962). *Ion Association*. Butterworths, Washington, D.C. p 41.

[169] R. Sander (2015). *Compilation of Henry's law constants (version 4.0) for water as solvent*. Atmos. Chem. Phys. **15**, 4399-4981. https://doi.org/10.5194/acp-15-4399-2015

[170] K. Noguchi, D. P. Riggins, K. C. Eldahan, R. D. Kitko, J. L. Slonczewski (2010). *Hydrogenase-3 contributes to anaerobic acid resistance of Escherichia coli*. PLoS One. **5**, e10132–e10132. https://doi.org/10.1371/journal.pone.0010132

[171] G. D. Metcalfe, T. W. Smith, M. Hippler (2021). *Advanced spectroscopic analysis and* ^{15}*N-isotopic labelling study of nitrate and nitrite reduction to ammonia and nitrous oxide by E. coli*. Analyst. **146**, 7021–7033. https://doi.org/10.1039/D1AN01261D

[172] M. Tiso, A. N. Schechter (2015). *Nitrate Reduction to Nitrite, Nitric Oxide and Ammonia by Gut Bacteria under Physiological Conditions*. PLoS One. **10**, e0119712. https://doi.org/10.1371/journal.pone.0119712

[173] J. Green, M. D. Rolfe, L. J. Smith (2014). *Transcriptional regulation of bacterial virulence gene expression by molecular oxygen and nitric oxide*. Virulence. **5**, 794–809. https://doi.org/10.4161/viru.27794

[174] V. Stewart (2003). *Nitrate- and nitrite-responsive sensors NarX and NarQ of proteobacteria*. Biochem. Soc. Trans. **31**, 1–10. https://doi.org/10.1042/bst0310001

[175] C. E. Vine, J. A. Cole (2011). *Nitrosative stress in Escherichia coli: reduction of nitric oxide*. Biochem. Soc. Trans. **39**, 213–215. https://doi.org/10.1042/BST0390213

[176] H. Corker, R. K. Poole (2003). *Nitric Oxide Formation by Escherichia coli: Dependence on nitrite reductase, the NO-sensing regulator Fnr and flavohemoglobin Hmp*. J. Biol. Chem. **278**, 31584–31592. https://doi.org/10.1074/jbc.M303282200

[177] M. S. Smith (1983). *Nitrous oxide production by Escherichia coli is correlated with nitrate reductase activity*. Appl. Environ. Microbiol. **45**, 1545–1547. https://doi.org/10.1128/aem.45.5.1545-1547.1983

[178] R. Metheringham, J. A. Cole (1997). *A reassessment of the genetic determinants, the effect of growth conditions and the availability of an electron donor on the nitrosating activity of Escherichia coli K-12*. Microbiology. **143**, 2647–2656. https://doi.org/https://doi.org/10.1099/00221287-143-8-2647

[179] S. O. Kim, Y. Orii, D. Lloyd, M. N. Hughes, R. K. Poole (1999). *Anoxic function for the Escherichia coli flavohaemoglobin (Hmp): reversible binding of nitric oxide and reduction to nitrous oxide*. FEBS Lett. 445, 389–394. https://doi.org/10.1016/S0014-5793(99)00157-X

[180] A. M. Gardner, R. A. Helmick, P. R. Gardner (2002). *Flavorubredoxin, an Inducible Catalyst for Nitric Oxide Reduction and Detoxification in Escherichia coli*. J. Biol. Chem. **277**, 8172–8177. https://doi.org/10.1074/jbc.M110471200

[181] J. Wang, C. E. Vine, B. K. Balasiny, J. Rizk, C. L. Bradley, M. Tinajero-Trejo, R. K. Poole, L. L. Bergaust, L. R. Bakken, J. A. Cole (2016). *The roles of the hybrid cluster protein, Hcp and its reductase, Hcr, in high affinity nitric oxide reduction that protects anaerobic cultures of Escherichia coli against nitrosative stress*. Mol. Microbiol. **100**, 877–892. https://doi.org/https://doi.org/10.1111/mmi.13356

[182] M. Kaldorf, K-H. Linne von Berg, U. Meier, U. Servos, H. Bothe (1993). *The reduction of nitrous oxide to dinitrogen by Escherichia coli*. Arch. Microbiol. **160**, 432–439. https://doi.org/10.1007/BF00245303

[183] V. Stewart (1988). *Nitrate respiration in relation to facultative metabolism in enterobacteria*. Microbiol. Rev. **52**, 190–232. https://doi.org/10.1128/mr.52.2.190-232.1988

[184] V. Bonnefoy, J. A. Demoss (1994). *Nitrate reductases in Escherichia coli*. Antonie Van Leeuwenhoek. **66**, 47–56. https://doi.org/10.1007/BF00871632

[185] V. Stewart, Y. Lu, A. J. Darwin (2002). *Periplasmic Nitrate Reductase (NapABC Enzyme) Supports Anaerobic Respiration by Escherichia coli K-12*. J. Bacteriol. **184**, 1314–1323. https://doi.org/10.1128/JB.184.5.1314-1323.2002

[186] H. Wang, C-P. Tseng, R. P. Gunsalus (1999). *The napF and narG Nitrate Reductase Operons in Escherichia coli Are Differentially Expressed in Response to Submicromolar Concentrations of Nitrate but Not Nitrite*. J. Bacteriol. **181**, 5303–5308. https://doi.org/10.1128/JB.181.17.5303-5308.1999

[187] J. Cole (1996). *Nitrate reduction to ammonia by enteric bacteria: redundancy, or a strategy for survival during oxygen starvation?* FEMS Microbiol. Lett. **136**, 1–11. https://doi.org/10.1111/j.1574-6968.1996.tb08017.x

[188] L. Chang, L. I-C. Wei, J. P. Audia, R. A. Morton, H. E. Schellhorn (1999). *Expression of the Escherichia coli NRZ nitrate reductase is highly growth phase dependent and is controlled by RpoS, the alternative vegetative sigma factor*. Mol. Microbiol. **34**, 756–766. https://doi.org/10.1046/j.1365-2958.1999.01637.x

[189] H. Wang, R. P. Gunsalus (2000). *The nrfA and nirB Nitrite Reductase Operons in Escherichia coli Are Expressed Differently in Response to Nitrate than to Nitrite*. J. Bacteriol. **182**, 5813–5822. https://doi.org/10.1128/JB.182.20.5813-5822.2000

[190] J. Mohn, B. Tuzson, A. Manninen, N. Yoshida, S. Toyoda, W. A. Brand, L. Emmenegger (2012). *Site selective real-time measurements of atmospheric* N_2O *isotopomers by laser spectroscopy*. Atmos. Meas. Tech. **5**, 1601–1609. https://doi.org/10.5194/amt-5-1601-2012

[191] P. Wunderlin, M. F. Lehmann, H. Siegrist, B. Tuzson, A. Joss, L. Emmenegger, J. Mohn (2013). *Isotope Signatures of N_2O in a Mixed Microbial Population System: Constraints on N_2O Producing Pathways in Wastewater Treatment*. Environ. Sci. Technol. **47**, 1339–1348. https://doi.org/10.1021/es303174x

[192] H. Moser, W. Pölz, J. P. Waclawek, J. Ofner, B. Lendl (2017). *Implementation of a quantum cascade laser-based gas sensor prototype for sub-ppmv H_2S measurements in a petrochemical process gas stream*. Anal. Bioanal. Chem. 409, 729–739. https://doi.org/10.1007/s00216-016-9923-z

[193] R. Keiner, M. Herrmann, K. Küsel, J. Popp, T. Frosch (2015). *Rapid monitoring of intermediate states and mass balance of nitrogen during denitrification by means of cavity enhanced Raman multi-gas sensing*. Anal. Chim. Acta. **864**, 39–47. https://doi.org/10.1016/j.aca.2015.02.007

[194] A. Blohm, S. Kumar, A. Knebl, M. Herrmann, K. Küsel, J. Popp, T. Frosch (2022). *Activity and electron donor preference of two denitrifying bacterial strains identified by Raman gas spectroscopy*. Anal. Bioanal. Chem. **414**, 601–611. https://doi.org/10.1007/s00216-021-03541-y

[195] M. B. Shinn (1941). *Colorimetric Method for Determination of Nitrate*. Ind. Eng. Chem. Anal. Ed. 13, 33–35. https://doi.org/10.1021/i560089a010

[196] I. L. Marr, A. Kindness, M. S. Cresser (1987). *Measurement of* $^{14}N : {}^{15}N$ *ratios by Fourier transform infrared spectrometry*. Analyst. **112**, 1491–1494. https://doi.org/10.1039/AN9871201491

[197] B. H. Bleakley, J. M. Tiedje (1982). *Nitrous Oxide Production by Organisms Other than Nitrifiers or Denitrifiers*. Appl. Environ. Microbiol. 44, 1342–1348. https://doi.org/10.1128/aem.44.6.1342-1348.1982

[198] T. M. Khlebodarova, N. A. Ree, V. A. Likhoshvai (2016). *On the control mechanisms of the nitrite level in Escherichia coli cells: the mathematical model*. BMC Microbiol. **16**, S7. https://doi.org/10.1186/s12866-015-0619-x

[199] J. van der Plas, K. J. Hellingwerf, H. G. Seijen, J. R. Guest, J. H. Weiner, W. N. Konings (1983). *Identification and localization of enzymes of the fumarate reductase and nitrate respiration systems of Escherichia coli by crossed immunoelectrophoresis*. J. Bacteriol. **153**, 1027–1037. https://doi.org/10.1128/jb.153.2.1027-1037.1983

[200] W. J. Dobrogosz (1966). *Altered End-Product Patterns and Catabolite Repression in Escherichia coli*. J. Bacteriol. **91**, 2263–2269. https://doi.org/10.1128/jb.91.6.2263-2269.1966

[201] N. J. Gilberthorpe, R. K. Poole (2008). *Nitric Oxide Homeostasis in Salmonella typhimurium: Roles of respiratory nitrate reductase and flavohemoglobin*. J. Biol. Chem. **283**, 11146-11154. https://doi.org/10.1074/jbc.M708019200

[202] C. E. Vine, S. K. Purewal, J. A. Cole (2011). *NsrR-dependent method for detecting nitric oxide accumulation in the Escherichia coli cytoplasm and enzymes involved in NO production*. FEMS Microbiol. Lett. **325**, 108–114. https://doi.org/10.1111/j.1574-6968.2011.02385.x

[203] L. Page, L. Griffiths, J. A. Cole (1990). *Different physiological roles of two independent pathways for nitrite reduction to ammonia by enteric bacteria*. Arch. Microbiol. **154**, 349–354. https://doi.org/10.1007/BF00276530

[204] R. H. Gillette, E. H. Eyster (1939). *The Fundamental Rotation-Vibration Band of Nitric Oxide*. Phys. Rev. **56**, 1113–1119. https://doi.org/10.1103/PhysRev.56.1113

[205] J. A. Cole (2021). *Anaerobic bacterial response to nitric oxide stress: Widespread misconceptions and physiologically relevant responses*. Mol. Microbiol. **116**, 29–40. https://doi.org/10.1111/mmi.14713

[206] A. Abou-Jaoudé, M. Chippaux, M-C. Pascal (1979). *Formate-Nitrite Reduction in Escherichia coli K12*. Eur. J. Biochem. **95**, 309–314. https://doi.org/10.1111/j.1432-1033.1979.tb12966.x

[207] J. S. McDowall, B. J. Murphy, M. Haumann, T. Palmer, F. A. Armstrong, F. Sargent (2014). *Bacterial formate hydrogenlyase complex*. Proc. Natl. Acad. Sci. **111**, E3948 LP-E3956. https://doi.org/10.1073/pnas.1407927111

[208] A. Pecher, F. Zinoni, C. Jatisatienr, R. Wirth, H. Hennecke, A. Böck (1983). *On the redox control of synthesis of anaerobically induced enzymes in enterobacteriaceae*. Arch. Microbiol. **136**, 131–136. https://doi.org/10.1007/BF00404787

[209] R. Rossmann, G. Sawers, A. Böck (1991). *Mechanism of regulation of the formate-hydrogenlyase pathway by oxygen, nitrate, and pH: definition of the formate regulon*. Mol. Microbiol. **5**, 2807–2814. https://doi.org/10.1111/j.1365-2958.1991.tb01989.x

[210] H. Abaibou, G. Giordano, M-A. Mandrand-Berthelot (1997). *Suppression of Escherichia coli formate hydrogenlyase activity by trimethylamine N-oxide is due to drainage of the inducer formate*. Microbiology. **143**, 2657–2664. https://doi.org/10.1099/00221287-143-8-2657

[211] G. Metcalfe, F. Sargent, M. Hippler (2022). *Hydrogen Production in the Presence of Oxygen by Escherichia coli K-12*. Microbiol. **268**, 3. https://doi.org/10.1099/mic.0.001167

[212] G. Unden, P. Dünnwald (2008). *The Aerobic and Anaerobic Respiratory Chain of Escherichia coli and Salmonella enterica: Enzymes and Energetics*. EcoSal Plus. **3**. https://doi.org/10.1128/ecosalplus.3.2.2

[213] V. B. Borisov, M. I. Verkhovsky (2015). *Oxygen as Acceptor*. EcoSal Plus. **6**. https://doi.org/10.1128/ecosalplus.ESP-0012-2015

[214] M. Jormakka, B. Byrne, S. Iwata (2003). *Formate dehydrogenase – a versatile enzyme in changing environments*. Curr. Opin. Struct. Biol. **13**, 418–423. https://doi.org/10.1016/S0959-440X(03)00098-8

[215] P. M. F. Sousa, S. T. N. Silva, B. L. Hood, N. Charro, J. N. Carita, F. Vaz, D. Penque, T. P. Conrads, A. M. P. Melo (2011). *Supramolecular organizations in the aerobic respiratory chain of Escherichia coli*. Biochimie. **93**, 418–425. https://doi.org/10.1016/j.biochi.2010.10.014

[216] G. Sawers, G. Watson (1998). *A glycyl radical solution: oxygen-dependent interconversion of pyruvate formate-lyase*. Mol. Microbiol. **29**, 945–954. https://doi.org/10.1046/j.1365-2958.1998.00941.x

[217] R. G. Sawers, S. P. Ballantine, D. H. Boxer (1985). *Differential expression of hydrogenase isoenzymes in Escherichia coli K-12: evidence for a third isoenzyme*. J. Bacteriol. **164**, 1324–1331. https://doi.org/10.1128/jb.164.3.1324-1331.1985

[218] C. M. Lamont, C. L. Kelly, C. Pinske, G. Buchanan, T. Palmer, F. Sargent (2017). *Expanding the substrates for a bacterial hydrogenlyase reaction*. Microbiology. **163**, 649–653. https://doi.org/10.1099/mic.0.000471

[219] J. Knappe, G. Sawers G (1990). *A radical-chemical route to acetyl-CoA: the anaerobically induced pyruvate formate-lyase system of Escherichia coli*. FEMS Microbiol. Rev. **6**, 383–398. https://doi.org/10.1111/j.1574-6968.1990.tb04108.x

[220] M. Kammel, D. Hunger, R. G. Sawers (2021). *The soluble cytoplasmic N-terminal domain of the FocA channel gates bidirectional formate translocation*. Mol. Microbiol. **115**, 758–773. https://doi.org/https://doi.org/10.1111/mmi.14641

[221] D. Hunger, M. Röcker, D. Falke, H. Lilie, R. G. Sawers (2017). *The C-terminal Six Amino Acids of the FNT Channel FocA Are Required for Formate Translocation But Not Homopentamer Integrity*. Front. Microbiol. **8**, 1616. https://doi.org/10.3389/fmicb.2017.01616

[222] J. L. Slonczewski, B. P. Rosen, J. R. Alger, R. M. Macnab (1981). *pH homeostasis in Escherichia coli: measurement by* ^{31}*P nuclear magnetic resonance of methylphosphonate and phosphate*. Proc. Natl. Acad. Sci. **78**, 6271–6275. https://doi.org/10.1073/pnas.78.10.6271

[223] R. D. Kitko, J. C. Wilks, G. M. Garduque, J. L. Slonczewski (2010). *Osmolytes Contribute to pH Homeostasis of Escherichia coli*. PLoS One **5**, e10078. https://doi.org/10.1371/journal.pone.0010078

[224] A. E. Marolewski, K. M. Mattia, M. S. Warren, S. J. Benkovic (1997). *Formyl Phosphate: A Proposed Intermediate in the Reaction Catalyzed by Escherichia coli PurT GAR Transformylase*. Biochemistry. **36**, 6709–6716. https://doi.org/10.1021/bi962961p

[225] L. Beyer, C. Doberenz, D. Falke, D. Hunger, B. Suppmann, R. G. Sawers (2013). *Coordination of FocA and Pyruvate Formate-Lyase Synthesis in Escherichia coli Demonstrates Preferential Translocation of Formate over Other Mixed-Acid Fermentation Products*. J. Bacteriol. **195**, 1428–1435. https://doi.org/10.1128/JB.02166-12

[226] K. C. Sasahara, N. K. Heinzinger, E. L. Barrett (1997). *Hydrogen sulfide production and fermentative gas production by Salmonella typhimurium require* F_OF_1 *ATP synthase activity*. J. Bacteriol. **179**, 6736–6740. https://doi.org/10.1128/jb.179.21.6736-6740.1997

[227] M. Kammel, O. Trebbin, C. Pinske, R. G. Sawers (2022). *A single amino acid exchange converts FocA into a unidirectional efflux channel for formate*. Microbiology. **168**. https://doi.org/https://doi.org/10.1099/mic.0.001132

[228] P. B. Rainey, H. J. E. Beaumont, G. C. Ferguson, J. Gallie, C. Kost, E. Libby, X-X. Zhang (2011). *The evolutionary emergence of stochastic phenotype switching in bacteria*. Microb. Cell Fact. **10**, S14 . https://doi.org/10.1186/1475-2859-10-S1-S14

[229] B. Suppmann, G. Sawers (1994). *Isolation and characterization of hypophosphite-resistant mutants of Escherichia coli: identification of the FocA protein, encoded by the pfl operon, as a putative formate transporter*. Mol. Microbiol. **11**, 965–982. https://doi.org/10.1111/j.1365-2958.1994.tb00375.x

[230] X. Lv, H. Liu, M. Ke, H. Gong (2013). *Exploring the pH-dependent substrate transport mechanism of FocA using molecular dynamics simulation*. Biophys. J. **105**, 2714–2723. https://doi.org/10.1016/j.bpj.2013.11.006

[231] K. Atkovska, J. S. Hub (2017). *Energetics and mechanism of anion permeation across formate-nitrite transporters*. Sci. Rep. **7**, 12027. https://doi.org/10.1038/s41598-017-11437-0